"The Effect of Low Velocity Impact Damage on the Performance of a Woven CFRP"

Mark Oxley B.Eng.(Hons), M.Phil., A.M.I.Mech.E.

Thesis submitted to the University of Sheffield for the Degree of Doctor of Philosophy in the Faculty of Engineering and Materials.

Department of Mechanical and Process Engineering,
University of Sheffield,
Mappin Street,
Sheffield,
S1 3JD.

October 1991

To June

Preface

This thesis is based on the findings of research carried out in the Department of Mechanical and Process Engineering, University of Sheffield. Except where specific reference is made to other work, the content of this thesis is original. No part of this thesis has been submitted to any other university for the award of any degree.

Mark Oxley

October 1991

Acknowledgements

I would like to express my gratitude to the following individuals and organisations who have provided assistance during the course of this work:-

- The Science and Engineering Research Council for generous financial support and for the award of a Research Studentship.

- My supervisors, Dr M.S. Found and Dr I.C. Howard for their guidance and advice during the course of the research work, and Prof K.J. Miller and Prof R.F. Boucher for the use of the facilities in the Department of Mechanical and Process Engineering.

- Lucas Aerospace, Fabrications Division, Burnley, especially Mr M.W. Jones, Mr C. Tempest and Mr C. Burrows for the supplies of high quality carbon fibre laminates and for the use of non-destructive testing facilities.

- The members of the Mechanical Engineering Workshop, particularly Mr M. Moore, Mr F. Loy and Mr J. Clark for help in preparing the specimens and setting up the experimental apparatus, and Mr D. Hallford for assisting with the photography.

- Mr B. Schofield, Chief Research Engineer, BAe Airlines Division for permission to use the computing facilities at BAe, Hatfield for the preparation of this thesis.

- Miss June Rutherford for her patience and encouragement and my friends and colleagues in the Composites Group, Messrs. Paterson, Harborne, Bell, Rezai, Kanyanga and Naeem for the valuable discussions we held.

Summary

A wide ranging study of the effects of low velocity impact on the performance of a quasi-isotropic, woven CFRP laminate has been conducted. The study considered the response of the laminate to constant velocity impact up to an incident energy of approximately 9J. The resulting damage, a complex network of delaminations, matrix cracking and fibre failure, was related to the incident energy and also to the residual static tensile and compressive strength of the material.

The growth of matrix cracking and delamination and also the reductions in tensile stiffness, measured locally over the impact damage site, were followed under constant amplitude zero-tension fatigue on specimens impacted at approximately 3J and 7J, representative of two characteristic damage states. The growth of matrix micro-cracking was found to be very rapid with numbers of cycles and was related to increases in tensile strength of plain, notched and impacted specimens, but substantial decreases in tensile stiffness. This type of fatigue related damage was observed to act as a 'pseudo-plastic' zone providing stress relieving around stress concentrations. No growth of this type of damage was noted in impacted specimens when the ratio of maximum fatigue stress to residual static strength was reduced to approximately 20%.

Growth of delamination was found to be related to the original impact damage and was only rapid towards the end of specimen life. The propagation of this type of damage under zero-tension fatigue was also apparently related to reduction in tensile stiffness.

The applicability of available 'equivalent flaw' models to the residual tensile and compressive strengths was investigated. In order to widen the applicability of the equivalent flaw approaches, a model has been suggested which predicts the fatigue strength of CFRP subjected to low velocity impact and subsequent zero-tension fatigue loading.

Nomenclature

The list below contains only notation and symbols which are frequently used throughout the thesis. Others are explained as they occur in the text.

A_c	C-Scan damage area.
A_d	Delamination damage area.
A_i	Impact damage area.
$[A_{ij}]$	Laminate in-plane stiffness matrix.
A_m	Micro-Cracking damage area.
A_{oc}	Threshold C-scan damage area for no static strength reduction.
A_{ox}	Threshold X-ray damage area for no static strength reduction.
A_x	X-Ray damage area.
$[B_{ij}]$	Laminate bending-stretching coupling matrix.
BVID	Barely visible impact damage.
c, c'	Half notch length of implanted flaw.
c_o, c'_o	Inherent flaw size.
C of V	Coefficient of variation.
CFRP	Carbon fibre reinforced plastics.
CRAG	Composites Research Advisory Group.
$[D_{ij}]$	Laminate bending stiffness matrix.
E_{nt}	Tensile modulus after n cycles fatigue.
E_{oc}	Compressive secant modulus of undamaged specimen.
E_{ot}	Tensile secant modulus of undamaged specimen.
E_{rt}	Residual tensile modulus of impacted specimen.
F	Force.
$F_{applied}$	Applied Loading.
F_s	Force - static loading of CFRP plate.
G	Strain energy release rate.
G_c	Critical strain energy release rate.

GRP	Glass fibre reinforced plastics.
h	Laminate thickness.
H_c	Composite fracture parameter.
K_{IC}	Critical stress intensity factor - mode I.
l_c^0	Back face crack length - 0° fibre direction.
l_c^{90}	Back face crack length - 90° fibre direction.
l_c^{mean}	Mean back face crack length.
LEFM	Linear elastic fracture mechanics.
$[M_{ij}]$	Bending moment resultants.
n	Number of fatigue cycles.
N_f	Number of cycles to failure.
$[N_{ij}]$	In-plane stress resultants.
NDT	Non-Destructive testing.
PEXR	Penetrant enhanced X-ray.
Q_x, Q_y	Transverse shear stress resultants.
r_f	Radius of front face damage.
R	Fatigue stress ratio.
S	Strain energy density factor.
S_{ij}	Laminate compliances.
t	Time, Laminate thickness.
U_i	Incident impact energy.
$\overline{U}_i$	Incident impact energy per unit thickness.
U_o	Threshold energy for initial damage/no strength reduction.
U_o'	Threshold energy for fatigue strength reduction.
U_s	Energy - static loading of CFRP plate.
w_i	Displacement - impact loading of CFRP plate.
w_{max}	Maximum central displacement.
w_s	Displacement - static loading of CFRP plate.
δ_r	Residual indentation depth.
ϵ_c	Compressive strain.

ϵ_{oc}	Compressive failure strain of undamaged specimen.
ϵ_{ot}	Tensile failure strain of undamaged specimen.
ϵ_t	Tensile strain.
ν_{xy}	Poisson's Ratio in the x-y plane.
ρ	Density.
σ	Direct stress.
σ_c	Compressive stress.
σ_{max}	Maximum fatigue stress.
σ_{nt}	Residual tensile strength after n fatigue cycles.
σ_o	Strength of undamaged specimen.
σ_{oc}	Compressive strength of undamaged specimen.
σ_{ot}	Tensile strength of undamaged specimen.
σ_r	Residual strength of damaged specimen.
σ_{rc}	Residual compressive strength of impacted specimen.
σ_{rt}	Residual tensile strength of impacted specimen.
σ_t	Tensile stress.
τ	Shear stress.
ϕ_h	Diameter of hole.

Contents

Chapter 1

Introduction

In many engineering applications the weight of a structure is an important design consideration. This is particularly true in the case of the aerospace industry where the high specific strength $\frac{\sigma_a}{\rho}$ and specific stiffness $\frac{E_a}{\rho}$ of carbon fibre reinforced plastics (CFRP) permit current and future generation aircraft the potential of significant improvements in performance over those with conventional aluminium alloy structures. In consequence of its anisotropic behaviour, CFRP also offers exciting design challenges and opportunities. Mechanical properties may vary considerably with direction and this can be used to great advantage by tailoring the material to suit the local and general loading conditions associated with a particular application.

Initially CFRP was proven in the aerospace environment by being used in simple secondary and tertiary panels and there are many examples currently in service on a wide variety of aircraft. These structures were of conservative design as weight savings could be easily achieved without the material being used to its full potential strength and stiffness and considerable experience has been gained, through these applications, of the advantages and more importantly the shortcomings of CFRP in service.

This 'honeymoon' period for CFRP is now over and in order to justify its further use it must find wider application on safety critical primary structures with design becoming more imaginative to take advantage of its unique properties. Unfortunately, due to inadequate understanding of the behaviour of composites,

the level of confidence within the aerospace industry is low and reinforced plastics are finding the jump from secondary to primary structures difficult. Large test programmes at coupon, sub-component and full-scale structure levels have to be undertaken which are prohibitively time-consuming and costly. Therefore, if composites are to progress towards their full potential, the importance of understanding the behaviour of CFRP, especially under adverse conditions, is plain.

It is recognised that perhaps the most worrying problem with the use of CFRP in a service environment is caused by impacts, particularly at low incident energies caused perhaps by a dropped tool during maintenance or small stones thrown up from the runway. Structural metallic materials are generally ductile and absorb large amounts of impact energy by plastic deformation. The dents caused by minor impacts are easily detected and, moreover can usually be safely ignored. For higher impact levels the damage is perfectly visible to the naked eye and decisions to repair or replace the damaged component are easily made.

Fibre reinforced plastics however are regarded as brittle and have little capacity for plastic deformation. Impact energy is absorbed in fracture processes which, in the case of thin laminated composites, normally consist of delamination between individual plies or groups of plies although fibre failure, matrix cracking and fibre/matrix debonding are often present. At high incident energies the damage, in terms of indentation and material crushing, is readily visible on the impacted surface of the composite, and in severe cases a hole may even be punched in the laminate. As with metallic materials it is relatively simple to determine the serviceability of the affected component and decide on repair or replacement.

Perhaps surprisingly, the problem of most concern exists with composites impacted at relatively low energies. Under these conditions, although quite high levels of damage may be present it is contained within the laminate and on the back face of the material which is often inaccessible to visual inspection. Damage of this type, not readily visible on the impacted surface, is termed barely visible impact damage (BVID) and can result in considerable reductions in mechanical performance of the material.

Detection of BVID is reasonably easy on a laboratory scale by destructive and

non-destructive testing (NDT) techniques. However it is evident that destructive examination is of no value on a service basis and in-field NDT systems are time-consuming and costly to use, in terms of out-of-service time of the aircraft, unless the position of the damage is detected in advance by visual examination. Special paint coatings have been devised for this purpose but, as detection of BVID cannot be guaranteed, it is of supreme importance that the effect of this type of damage on the performance of CFRP is fully investigated and understood and that allowance is made for undetected impact damage in the design process. In fact, current aerospace design standards reflect concern with BVID, regarding it as a worst case condition and design allowables are limited accordingly [18]. Increased understanding of the effects and behaviour under load of BVID, therefore would remove some of this concern and would allow more effective and imaginative use of composites.

The aims of the work reported here were to investigate the behaviour of a practical laminate under low energy impact and to determine the effects of BVID on the properties of the material under uniaxial static and fatigue loading conditions.

The Thesis is divided into ten chapters and the introduction is followed by a review of the available literature in Chapter Two. The aspects of impact behaviour of composites under low energy impact, examination techniques for the detection of impact damage and post-impact static and fatigue performance are considered. Chapter Three contains a description of the materials used in the experimental programme, the manufacture of the specimens and the equipment used to record the data necessary to achieve the aims of the study. Chapter Four gives a detailed description of the testing techniques used and Chapters Five, Six and Seven present the results and observations made during the experimental programme.

Chapter Eight describes the development of mathematical models proposed to describe the behaviour of the material under impact conditions and the analysis and discussion of the static and fatigue results is given in Chapter Nine in which the various models are fitted to the experimental results to illustrate their relative effectiveness.

The conclusions drawn from the investigation are given in Chapter Ten. Areas

of possible further research based on the current literature and the findings of this investigation are also suggested in this chapter.

References, Appendices, Tables of Results and Figures are grouped towards the back of the Thesis.

Chapter 2

Literature Review

2.1 Introduction

There has been a considerable volume of work conducted on the subjects of low velocity impact damage and post-impact performance of CFRP, reflecting the perceived importance of understanding impact damage to the successful use of CFRP in service. Available published work has been reviewed in this chapter as a background to the research programme reported later in the thesis.

2.2 The Behaviour of Laminated Composites under Low Velocity Impact Loading

Laminated composite materials may deform in a number of ways under the action of impact loads, depending on the impactor and material properties, the geometry of the impactor, the support conditions of the laminate and the velocity and energy of the impact event [19]. Typically, however over the range of energies required to cause barely visible impact damage (BVID) there are two primary causes of failure, namely contact stresses, and flexural stresses [20]. Although a number of workers [21], [22] have considered that tensile stress waves reflected from the back surface of the laminate can cause delamination failure, perhaps the most difficult to detect and therefore the most severe of the forms of damage caused by

impact, stress wave failures are only significant under high velocity ballistic impact conditions [20], [23], where inertia inhibits gross deformation of the material. The analysis of low velocity impact is complicated in the case of composite materials by the anisotropic nature of the laminates and the importance of both in-plane and out-of-plane stresses in causing failure. However providing effective stress analyses can be combined with appropriate failure criteria some prediction may be made of the failure modes caused by low velocity impact.

In order to understand the issue of impact damage in composite laminates, an accurate prediction of the response of the material to impact loading is necessary. It is therefore important to determine the contact force between the impactor and the surface of the laminate. The classical Hertzian Contact Law [24], [25] has been used by many workers and was derived from the contact of two frictionless, isotropic, elastic spheres such that:-

$$F = k\alpha^{\frac{3}{2}} \tag{2.1}$$

where F is the contact force, α is the relative approach of the bodies and k, dependent on the geometry and mechanical properties of the two bodies, is given by:-

$$k = \left[\frac{16}{9\pi^2}\frac{r_t r_p}{(k_t + k_p)^2(r_t + r_p)}\right]^{\frac{1}{2}} \tag{2.2}$$

where r_t and r_p are the radii of the two bodies and k_t and k_p are the stiffness parameters.

Of course, in the limiting case as $r_t \rightarrow \infty$, the analysis becomes that of contact between a spherical indentor and an isotropic half-space. The target is regarded as semi-infinite and localised contact stresses and deformations can be isolated from the general state of stress caused by the shape and deformation of the body as a whole.

The standard $\frac{3}{2}$ power law given in Equation 2.1 has been found by Willis [26] to be valid for the contact between a sphere and a transversely isotropic half-space and static indentation tests on $[0°, +45°, 0°, -45°, 0°]_{2S}$ laminates [27] have further

served to illustrate the effectiveness of the Hertz relationships for composites.

Static contact analysis can be directly applied to the examination of impact of elastic bodies providing that the duration of the impact event is much greater than the longest period of vibration of either body [26]. The analysis becomes quasi-static and vibrations can be ignored. This approach, which involves combining the dynamic solution of the problem of the impact of bodies with the static solution for pressure between bodies in contact, has been followed by Goldsmith [24], Johnson [25] and Timoshenko and Goodier [28] for an isotropic target and projectile and extended by Greszczuk [29] in an attempt to predict internal stresses and failure modes in semi-infinite targets of isotropic materials and quasi-isotropic composite materials under low velocity impact conditions. The analysis predicted maximum normal, radial and circumferential stresses on the impact surface directly below the centre of impact, whereas maximum shear stresses in the composite were predicted to occur at the edges of the contact area just below the impacted surface. Combining these results with a simple maximum stress criterion, for a quasi-isotropic composite material Greszczuk [29] suggested that:-

$$V_n = 31.2 \left(\frac{k_t^{*2}}{K_n}\right) (\sigma_{nA})^{\frac{5}{2}} \left(\frac{r_p}{m_p}\right)^{\frac{1}{2}} \tag{2.3}$$

where:-

V_n = Threshold damage velocity

k_t^* = Stiffness parameter

K_n = Material constant

σ_{nA} = Allowable stress in target

r_p = Radius of projectile

m_p = Mass of projectile

n = T,C,S (Tension, Compression, Shear)

Damage was found to initiate in the form of shear failure at the edges of the contact zone followed by compression/crushing and finally tensile failure.

Examination of Equation 2.3 suggests that the resistance to impact damage increases with increasing target strength and decreasing target modulus. Certainly

a combination of these properties would lead to the ability of the target material to absorb relatively large amounts of impact energy as elastic strain energy which would ultimately be returned to the impactor.

Chamis and Ginty [30] used an energy balance approach to obtain an expression for the threshold damage velocity V_n of a composite laminate impacted by a spherical projectile. Assuming that the incident impact energy of the impactor is entirely absorbed in creating delamination fracture surfaces they proposed that:-

$$V_n = \left[0.75 \left(\frac{S_{13_t} h_t}{\phi_p \rho_p}\right)\right]^{\frac{1}{2}} \tag{2.4}$$

where:-

S_{13_t} = Interlaminar shear strength of target

h_t = Thickness of target

ϕ_p = Diameter of projectile

ρ_p = Density of projectile

Comparing predictions from Equation 2.4 and values from the literature, Chamis and Ginty [30] concluded that their analysis provided a reasonable estimate of the projectile velocity necessary to cause initial delamination damage to a composite laminate.

The analyses presented above are attractive in their simplicity and they are useful in the study of contact stresses due to impact. However, the obvious limitation is that practical composites, in the form of thin laminates, rarely if ever conform to the ideal of being regarded as semi-infinite solids. In many cases the out-of-plane displacements and flexural vibrations can contribute significantly or even dominate failure processes under low velocity impact conditions. The contact force can again be determined by Hertz law. Tan and Sun [31] have found that the classical static indentation law expressed in Equation 2.1 is equally valid for low velocity impact of laminated composites although Sun [32] suggested modification to Equation 2.2 to account for the influence of transverse stiffness in the composite. However, unfortunately the examination of transient response complicates the study of low velocity impact considerably and much of the work in this area

inevitably relies on simplifying assumptions for the impact force and boundary conditions or on the use of finite element solutions.

Perhaps the simplest form of analysis for composites which considers the deflection of the target as significant in the production of low velocity impact damage is that due to Greszczuk and Chao [33]. Following the earlier work by Greszczuk [29], the impact event was considered to be quasi-static and stresses due to contact and plate bending were predicted by finite element techniques. This approach allowed the effect of a wide variety of physical parameters to be investigated with relative ease. The extent of the damage was determined by the use of a failure criterion for generally orthotropic solids and, in accordance with the previous analysis [29], resistance to impact was found to increase with increasing fibre and matrix strength and decreasing fibre and matrix modulus. Fibre reinforcement normal to the direction of damage propagation tended to arrest its progress, thus a cross-ply laminate was found to be more damage resistant than either unidirectional or quasi-isotropic material. Furthermore, dispersing plies of the same orientation through the thickness rather than grouping them together was found to improve impact resistance by providing effective barriers to the propagation of damage through the thickness. Thicker plates tended to resist damage more effectively than thin plates. Moreover for thin plates damage initiated at the bottom surface, governed by plate bending stresses, and spread through the thickness as impact velocity was increased. As plate thickness increased, bending stresses decreased and damage initiated from local contact stresses around the impact site, spreading from the top surface through the thickness.

Greszczuk and Chao [33] found that their theoretical predictions of damage and threshold damage velocities showed fair agreement with experimental results. A combination of this work with that of Gresczcuk [29] provides an easily understood insight into the factors which affect the development of low velocity impact damage in composites. However in these analyses the transient behaviour of the composite has been ignored and the problem has been reduced to that of static deflection. A more rigorous understanding of the deflection behaviour of the material under transverse impact loading including flexural vibrations must be obtained in order

that a full characterisation of the internal stresses can be conducted leading to more accurate predictions of internal damage.

The low velocity impact of a mass on a thin isotropic plate has been considered by Goldsmith [24]. For a Hertz type of contact the relative approach α in Equation 2.1 is now given by:-

$$\alpha = \left(\frac{F}{k}\right)^{\frac{2}{3}} = w_p - w_t(c) \tag{2.5}$$

where w_p is the displacement of the impactor given by:-

$$w_p = V_o t - \frac{1}{m_p}\int_0^t dt \int_0^t F dt \tag{2.6}$$

V_o = Initial velocity of impactor

m_p = Mass of impactor

t = Time

F = Force

and $w_t(c)$ is the plate deflection at the contact point and is found from the classical equation for out-of-plane displacement [34].

$$D\nabla^4 w_t + \rho h \frac{\partial^2 w_t}{\partial t^2} = F \tag{2.7}$$

D = Plate bending stiffness

ρ = Density of plate

h = Thickness of plate

However classical plate theory fails to adequately characterise the response of plates under impact loading where rapid transients and higher order modes of vibration may be present. Mindlin [35] showed that large discrepancies between classical theory and exact three-dimensional elasticity solutions could be effectively eliminated by applying corrections to account for rotatory inertia and transverse shear, non-inclusion of the latter giving rise to particularly large errors.

Corrections for transverse shear assume even greater significance when consideration is given to the low velocity impact of laminated plates. Most of the

analyses of fibre reinforced laminates employ classical lamination theory which ignores transverse shear deformation. In composite laminates, where the ratio of Young's modulus to shear modulus can be very large and the loading is essentially concentrated at a point, models using classical lamination theory can be unrealistically stiff and errors can be quite severe.

Lal [36] accounted indirectly for shear errors by proposing that the dynamic load/deflection response of a plate under transverse impact load could be represented by a series of springs accounting for indentation (Hertzian Contact), flexural and shear effects. Classical large deflection theory of plates [37] was used to predict load/deflection characteristics, the resulting equations being then modified to account for the progressive decrease in plate stiffness as a result of internal damage. Despite considering only the first mode of flexural vibration, Lal obtained good predictions of the impact response of clamped CFRP plates under low velocity impact.

Yang et al [38] followed a similar approach to Mindlin [35] and incorporated transverse shear and rotatory inertia terms into the two dimensional theory of motion for laminated plates. The theory was based on the following assumed displacement field:-

$$\begin{aligned} u(x,y,z,t) &= u^{\circ}(x,y,t) + z\psi_x(x,y,t) \\ v(x,y,z,t) &= v^{\circ}(x,y,t) + z\psi_y(x,y,t) \\ w(x,y,z,t) &= w^{\circ}(x,y,t) \end{aligned} \tag{2.8}$$

where:-

u, v, w = Displacements in the x, y, z directions

$u^{\circ}, v^{\circ}, w^{\circ}$ = Displacements of the mid-plane

ψ_x, ψ_y = Rotations in the x-z and y-z planes

which results in the following plate constitutive relationships:-

$$\begin{Bmatrix} N_x \\ N_y \\ N_{xy} \\ - \\ M_x \\ M_y \\ M_{xy} \end{Bmatrix} = \left[\begin{array}{ccc|ccc} A_{11} & A_{12} & A_{16} & B_{11} & B_{12} & B_{16} \\ A_{12} & A_{22} & A_{26} & B_{12} & B_{22} & B_{26} \\ A_{16} & A_{26} & A_{66} & B_{16} & B_{26} & B_{66} \\ - & - & - & + & - & - \\ B_{11} & B_{12} & B_{16} & D_{11} & D_{12} & D_{16} \\ B_{12} & B_{22} & B_{26} & D_{12} & D_{22} & D_{26} \\ B_{16} & B_{26} & B_{66} & D_{16} & D_{26} & D_{66} \end{array}\right] \begin{Bmatrix} \frac{\partial u^\circ}{\partial x} \\ \frac{\partial v^\circ}{\partial y} \\ \frac{\partial u^\circ}{\partial y} + \frac{\partial v^\circ}{\partial x} \\ - \\ \frac{\partial \psi_x}{\partial x} \\ \frac{\partial \psi_x}{\partial y} \\ \frac{\partial \psi_x}{\partial y} + \frac{\partial \psi_y}{\partial x} \end{Bmatrix} \tag{2.9}$$

and

$$\begin{Bmatrix} Q_y \\ - \\ Q_x \end{Bmatrix} = k \left[\begin{array}{cc|c} A_{45} & | & A_{55} \\ - & + & - \\ A_{44} & | & A_{45} \end{array}\right] \begin{Bmatrix} \frac{\partial w}{\partial x} + \psi_x \\ - \\ \frac{\partial w}{\partial y} + \psi_y \end{Bmatrix} \tag{2.10}$$

where:-

$[N_{ij}]$ = In-plane stress resultants

$[M_{ij}]$ = Bending moment resultants

$[A_{ij}]$ = Laminate in-plane stiffness matrix

$[B_{ij}]$ = Laminate bending-stretching coupling matrix

$[D_{ij}]$ = Laminate bending stiffness matrix

Q_x, Q_y = Transverse shear stress resultants

k = Shear correction factor

The equations of motion of the plate are:-

$$\begin{aligned} \frac{\partial N_x}{\partial x} + \frac{\partial N_{xy}}{\partial y} &= P\frac{\partial^2 u^\circ}{\partial t^2} + R\frac{\partial^2 \psi_x}{\partial t^2} \\ \frac{\partial N_{xy}}{\partial x} + \frac{\partial N_y}{\partial y} &= P\frac{\partial^2 v^\circ}{\partial t^2} + R\frac{\partial^2 \psi_y}{\partial t^2} \\ \frac{\partial M_x}{\partial x} + \frac{\partial M_{xy}}{\partial y} - Q_x &= R\frac{\partial^2 u^\circ}{\partial t^2} + I\frac{\partial^2 \psi_x}{\partial t^2} \\ \frac{\partial M_{xy}}{\partial x} + \frac{\partial M_y}{\partial y} - Q_y &= R\frac{\partial^2 v^\circ}{\partial t^2} + I\frac{\partial^2 \psi_y}{\partial t^2} \\ \frac{\partial Q_x}{\partial x} + \frac{\partial Q_y}{\partial y} + p &= P\frac{\partial^2 w^\circ}{\partial t^2} \end{aligned} \tag{2.11}$$

P = Lateral inertia

R = Impactor force

I = Rotatory inertia

p = Lateral loading

A combination of Equations 2.9 - 2.11 can be used to derive the equations of motion of laminated composite plates in terms of the displacement variables. The resulting set of equations were used successfully by Yang et al [38] and Whitney and Pagano [39] to analyse a number of composite plate bending and vibration problems. Sun and Lai [40] showed the applicability of this approach to plates subjected to impulsive loadings and this led naturally to its inclusion in a number of low velocity impact studies, notably those due to Sun and Chattopadhyay [41], Dobyns [42], Aggour and Sun [43], Humphreys and Goering [44] and Ramkumar and Chen [45]. Solutions for plate deformation, back face strains and transverse shear stresses have been obtained by these workers for a number of impact loading and boundary conditions. High shear stresses were predicted at the edges of the contact zone [42], [43] suggesting that matrix shear cracking and delamination due to contact stresses should initiate in this area. Ramkumar and Chen [45] obtained good qualitative agreement for the prediction of back face flexural matrix and fibre failure but predictions of the dimensions of internal delaminations, based on an assumed failure value for transverse shear stress $\frac{Q_x}{h}$, were less successful. Using a more sophisticated stress based failure criterion which allowed for the prediction of the presence and mode of failure, Humphreys and Goering [44] similarly predicted the initiation and propagation of matrix and fibre failure but again failed to accurately predict delamination damage. Significantly, Dobyns [42] showed that the low velocity impact response of the plate was very similar to the static response. This serves to confirm the effectiveness of the approach followed by Greszczuk and Chao [33] and may be an important result for CFRP which is regarded as largely insensitive to load rate.

The advantage of the above methods is that they are based on two-dimensional plate theory with corrections made for out-of-plane effects. As such they tend to be reasonably efficient in terms of intellectual effort or computing time, especially as it is almost invariably assumed that in-plane displacements are negligible compared

with transverse displacements and the plate is symmetric, thus eliminating bending/stretching coupling terms. However, it may be that if a more thorough assessment is to be made of damage caused by low velocity impact a three-dimensional analysis considering the effects of through thickness direct stress σ_z is unavoidable. There seems to be little information concerning the relative importance of transverse shear and direct stresses but Ross et al [46] and Wu and Springer [47] have both conducted three-dimensional transient finite element analyses in order to directly assess these effects. Ross et al [46] presented results for interlaminar shear stresses in cross-ply $[0_5^\circ, 90_5^\circ, 0_5^\circ]$ laminates, predicting the major axis of the delamination in the 0° direction and approximately the same delamination size at the two interfaces. These results did not agree well with experimental observations and, in view of this, it is difficult to justify the complexity of three-dimensional stress analysis in this case.

A more successful attempt to predict the dimensions of impact induced delaminations observed experimentally [48] has been described by Wu and Springer [47]. A number of existing failure criteria failed to accurately predict dimensions of the observed delaminations and a new criterion was proposed based purely on out-of-plane normal stresses. Wu and Springer [48] observed that the major axis of delamination was parallel to the fibre direction of the lower ply bounding it and therefore suggested that delamination could be characterised by two dimensions parallel and perpendicular to this direction. Applying dimensional analysis techniques to the variables known to affect the size of the delaminations Wu and Springer suggested that:-

$$\left(\frac{l_d}{l_o}\right) = C_1 \left(\frac{\sigma_{max} l_o^{\frac{1}{2}}}{K_{IC}}\right)^{C_2} (Q^*)^{C_3} \left(\frac{t_f}{t_m}\right)^{C_4} \left(\frac{D_{66}^B}{D_{66}^T}\right)^{C_5}$$

$$\left(\frac{w_d}{l_o}\right) = C_6 \left(\frac{\sigma_{max} l_o^{\frac{1}{2}}}{K_{IC}}\right)^{C_7} (Q^*)^{C_8} \left(\frac{t_f}{t_m}\right)^{C_9} \left(\frac{D_{66}^B}{D_{66}^T}\right)^{C_{10}} \qquad (2.12)$$

where:-

l_d = Length of delamination

l_o = Inherent flaw size

w_d = Width of delamination

σ_{max}=Maximum out-of-plane stress

K_{IC} = Mode I stress intensity factor

t_f = Duration of out-of-plane stresses

t_m = Time at which σ_{max} occurs

$D^B_{\theta\theta}$ = Flexural stiffness of lower ply bounding the delamination

$D^T_{\theta\theta}$ = Flexural stiffness of upper ply bounding the delamination

$Q^* = \frac{\Delta Q}{Q^B_{xx} - Q^T_{yy}}$

ΔQ = Difference in reduced stiffness of the two bounding plies

Q^B_{xx} = Reduced stiffness of the lower ply in the fibre direction

Q^T_{yy} = Reduced stiffness of the upper ply perpendicular to the fibre direction

$C_1 - C_{10}$ are constants, independent of material properties, lay-up and impact velocity. Wu and Springer [47] achieved reasonable accuracy in predicting the dimensions of delaminations between any two plies in rectangular laminates under a number of clamping conditions under low velocity impact.

2.3 Failure Modes and Detection of Impact Damage

2.3.1 Failure Modes Caused by Low Velocity Impact

Low velocity impact loadings on laminated composites usually result in the production of internal delaminations although matrix cracking, fibre/matrix debonding and fibre failure are often present. The magnitude and location of these types of damage depends on fibre and matrix properties, the geometry and mechanical properties of the impactor and the clamping/support conditions, making damage patterns unique to a given experiment. It is, therefore only possible to make

general observations concerning the failure modes which characterise low velocity impact damage in composite laminates.

The examination of internal failure modes in glass reinforced plastics is relatively straightforward due to their transparent nature and visual inspection methods have been reported by Sierakowski and Takeda [49], Takeda et al [50] and Critescu et al [51]. CFRP is, however opaque and such simple techniques cannot be applied. Furthermore studies by Bishop [52] and Dorey et al [53] have shown that for composites with brittle epoxy matrices any damage on the impact surface is almost invisible to the naked eye although Preston and Cook [54], Potter [55] and Caprino [56] have detected indentation, matrix and fibre failure at relatively low impact energies. By contrast back surface damage is often visible in the form of delamination, matrix cracking and fibre failure. However, in many practical applications this could not be used as an indication of impact damage as the laminate would be used as a load bearing skin and the back surface would be inaccessible to visual inspection. Low levels of surface damage can, however be associated with extensive internal damage, highly detrimental to the mechanical performance of the impacted component. It is therefore extremely important to use either destructive or non-destructive internal examination to study the extent and modes associated with low velocity impact damage.

The damage processes caused by impact loading on $\pm 45°, 0°$ CFRP laminates of varying flexural stiffness were studied in detail by Cantwell and Morton [22]. For laminates with low flexural stiffness large tensile stresses in the lowest ply initiated fibre/matrix debonding which extended up to the lowest interface where it was deflected to form a plane of delamination. The delamination extended until deflected upwards by matrix cracks, damage of this type extending progressively upwards and away from the plane of the impact as shown in Figure 2.1(a). Fibre failure was observed to be more extensive in the lower plies. At higher energies contact stresses at the edges of the contact area caused tensile and shear cracks to appear in the top surface ply which propagated until deflected at the upper interface to form a delamination. Damage in the form of matrix cracks and delaminations extended downwards and away from the contact zone as shown in

Figure 2.1(b). At high impact energies, therefore the total damage was considered to be the combination of low energy flexural damage and higher energy contact damage. For laminates with higher flexural stiffness, damage was similar but the sequence of events was reversed, initial contact failures preceding flexural or stress wave related failures. Similar relationships between matrix cracking and delamination have been observed by Boll et al [21], Clark [23] and Joshi and Sun for cross-ply [57] and quasi-isotropic [58] laminates. Joshi and Sun also achieved some success, at least for the simpler lay-up, in explaining failure patterns and especially the role of transverse shear in the initiation of matrix cracks in the upper plies by the use of two-dimensional finite element stress analysis.

Carbon fibre-reinforced plastics with brittle epoxy matrices have little capacity for plastic deformation and impact energy is absorbed as fracture surfaces are created. However the properties of the composite can be modified so that either only elastic deformations occur and a considerable amount of the energy imparted to the laminate is returned to the impactor or damage is restricted to a smaller area. The resistance to impact damage can be improved by the use of high strength/high strain fibres thus increasing the strain energy to failure of the reinforcement [33], [59]. It has further been suggested [60], [61] that glass and aramid fibres have better energy absorbing properties than carbon fibres and mixing them with carbon fibres to produce a hybrid composite would produce better impact properties. Reductions in delamination area can also be achieved by the use of woven fibres in the laminate [62], [63] to produce either a wholly woven laminate or a mixed-woven laminate (one containing a mixture of woven and non-woven plies).

The impact resistance of CFRP can also be improved by the optimisation of the fibre/matrix interface [60], or by altering the properties of the matrix materials. An extensive study of twenty-four different epoxy resin systems by Williams and Rhodes [64] has shown that improved impact resistance in terms of reduced internal damage area can be achieved by the use of a tougher matrix material and that use of a resin volume fraction of at least 40% allowed some plastic deformation of the resin between the fibres and led to further improvements. These results were confirmed by Boll et al [21] who further showed that, despite reduced damage

area, an increase in fibre breakage resulted from the use of tougher epoxies. The use of relatively tough thermoplastic matrices was investigated by Bishop [52] and Dorey et al [53] who obtained very similar results to those for toughened epoxies i.e a reduced area of delamination and matrix cracking but an increased incidence of fibre failure. A relatively recent idea, which combines the practical advantages of both types of resin system, is the use of thermoplastic interleaves between the plies in the laminate to improve resistance to impact damage [65].

Potter [55], [66] has observed that the delaminations at each interface show a characteristic double-lobe shape, the delamination mostly occurring at sites slightly removed from the centre of the impact. The orientation of delaminations has also been observed to depend strongly on the properties of the plies bounding the delamination, independant studies by Potter [55], [66], Wu and Springer [48], Shuart and Williams [67] and Clark [23] finding that the major axis of the damage coincided with the fibre direction of the lower ply. Not surprisingly delaminations do not tend to occur at interfaces where the fibre direction does not change [48], and Clark [23] has observed that in $0°, 90°, \pm 45°$ laminates the largest delaminations occurred at interfaces where the fibre direction change was the largest (i.e at $0°/90°$ and $+45°/-45°$ interfaces rather than $0°/\pm 45°$ or $90°/\pm 45°$ interfaces).

Clark [23] proposed a simple qualitative model which seems to successfully account for many of the delamination effects discussed above. The deflection of a pair of plies of different orientation under the action of an impact load was considered to give rise to peel stresses along a line coincident with the fibre direction of the lower ply and slightly away from the impact centre, whereas along a line perpendicular to the lower ply fibres the stresses would be such as to keep the plies together. Thus delamination is predicted in the direction of the lower ply and slightly removed from the impact centre. Furthermore Clark [23] suggested that the simple model could be extended to predict relative sizes of delaminations at different interfaces, the occurrence of matrix cracking due to tensile and shear stresses within the plies and the relationship between matrix cracks and delaminations at least for relatively simple cases.

2.3.2 Detection of Low Velocity Impact Damage

The methods of detection of impact damage, both destructive and non-destructive all have their merits and disadvantages and it is invariably necessary to use more than one examination technique to obtain an overall pattern of the failure. Extensive reviews of NDT have appeared in the literature [68], [69], [70] and these have suggested that there are five basic methods commonly used to detect damage in CFRP namely eddy-current testing, thermography, low-frequency vibration, ultrasonics and radiography. From a BVID standpoint eddy-current testing is able to detect matrix cracking [70] and fibre failure [69] but is insensitive to delamination [68]. Thermography is sensitive to delamination and impact damage [70] but is an extremely expensive technique and very sensitive to defect depth [68]. Low-frequency vibration methods (coin-tap being probably the most well known) is again sensitive to delamination [69] but is unable to detect damage away from the surface [68]. The NDT techniques which have, to date found most favour in the detection of low-velocity impact damage are ultrasonics (C-scan) and radiography (X-ray) and have been frequently used, with the destructive techniques of sectioning and deply, to characterise BVID. The relative merits of these four methods have been discussed by Cantwell and Morton [22].

Perhaps the method which yields the most detailed information about the internal damage in impacted CFRP laminates is the standard metallographic technique of sectioning and polishing followed by microscopic examination. Detailed internal patterns of matrix cracking, debonding, delamination and fibre fracture can be observed. Each section is two-dimensional but a fully three-dimensional image can be obtained by taking large numbers of slices in various directions as described by Boll et al [21] and Joshi and Sun [57], [58]. The main disadvantages of this method are that it is extremely time consuming and there is invariably a possibility of damaging the cross-sections during the cutting process. However, the examination of the cross-sections can be made easier by producing edge replicas of the damage as described by Liu et al [71].

Another destructive method, that of thermal deplying, has been developed by

Freeman [72]. Partial pyrolysis of the specimens loosens the contact between the plies and allows them to be unstacked with relative ease and thus with minimum damage. This technique has been found to be particularly useful in illustrating delamination size and shape and fibre failure within the laminate [22], [55], [66]. Although most of the matrix is lost in the process the use of suitable marker dyes can be used to highlight matrix failures [72].

Although the two methods described above provide great detail of the pattern of damage within the laminate caused by impact their great disadvantage lies in their destructive nature. After examination the specimens cannot be used to provide any further information and therefore the relationship between impact damage mechanisms and post-impact performance cannot be directly assessed.

There are two non-destructive examination techniques widely used in the study of impact damaged CFRP on a laboratory scale, namely ultrasonic C-scan and penetrant enhanced X-ray (PEXR).

Ultrasonic C-scan is only capable of illustrating damage perpendicular to the ultrasonic pulses. Its great advantage therefore lies in its ability to discern delaminations. Conventionally used, C-scan can only give an integrated picture of the overall damage through the thickness and cannot distinguish the depth of the damage into the laminate. However Potter [73] and Preuss and Clark [74] have described the successful generation of three-dimensional C-scan images by processing the amplitude and time of flight of the ultrasonic pulses and similar images have been produced by analysing backscatter signals from a transducer placed off-axis rather than normal to the laminate surface [21].

Fine detail can be provided by X-ray examination [18]. Unfortunately the X-ray absorption characteristics of carbon fibres and resin matrices are similar and a suitable X-ray opaque penetrant must be introduced to highlight damaged material [68], [75]. This technique can provide detailed information regarding internal delaminations and matrix cracks but can only be used when surface damage is present to allow passage of the penetrant. As with C-scan the extent of damage is presented on a two-dimensional image and the area has been reported [22] to be frequently less than for a C-scan, possibly reflecting difficulties in achieving

complete penetration of the fluid or diffraction of the X-rays.

2.4 The Behaviour of Impact Damaged CFRP under Static Loading

2.4.1 The Influence of Laminate Properties on Static Strength and Fracture

The issue of residual strength and stiffness of impact damaged CFRP is dominated by the type and extent of the induced damage and how that damage influences the load bearing capability of the material. The damage caused to laminated CFRP by low velocity impact loading has been shown in Sections 2.2 and 2.3 to consist mainly of a network of delaminations and matrix cracks around the impact site although fibre failures can occur. It is widely understood [76], [77] that damage of this type will be potentially most severe in components and structures which experience compressive loading. Under static load the strength and ultimate fracture is largely dependent on the fracture of the load bearing material aligned to the loading axis. Under tensile loading the effect of matrix cracking and delamination will be merely to degrade the effective transfer of load between matrix and fibre and between plies. Provided fibre failure has not occurred therefore the tensile load bearing capacity of the material will be little reduced and the strength of the impacted laminates will not be significantly less than that of the undamaged material [22]. Under compressive loading, however the support of the fibres and plies around the damage site is reduced, allowing buckling of the load bearing material and growth of the delaminations, usually in the transverse direction [59], [66] which will eventually lead to catastrophic failure. Relatively large reductions in compressive strength are to be expected therefore for laminates impacted under low velocity conditions.

The relationship between residual strength and impact energy was studied by Husman et al [78] and is illustrated in Figure 2.2. As impact energy and induced damage increase the residual strength decreases rapidly at first, then more slowly

to approximately half the undamaged strength over the BVID region. From there further reductions take the strength to a minimum of approximately one-third of the undamaged strength which represents initial penetration of the laminate. At this energy a hole is punched through the laminate and material removed from around the hole, especially by splitting out on the back face. If the impact energy is increased past this value the impactor passes cleanly through the laminate and the residual strength recovers to a value which represents the strength of the material containing a cleanly drilled hole of the same diameter as the impactor. Thus for high impact energies the residual strength of the laminate is independent of the energy of the impact. Experimental observations of this behaviour have been achieved by Dorey [59], [60].

Husman et al [78], however did not consider the behaviour of composites at very low energies. Subsequent investigations [56], [79], [80] recognised that strength would not decrease for very low impact energies as either no damage would be induced in the material or the damage would have negligible effect on the residual strength. This introduces the idea of a threshold damage energy and Dorey et al [53] and Tiu et al [81] found that this threshold occurred at a higher energy under tensile loading than under compressive loading for CFRP laminates with an epoxy resin matrix reflecting the higher energy input required to cause fibre rather than matrix failures.

The effect of material properties on the residual strength of impacted laminates is obviously closely linked with their influence on failure modes and extent of induced damage (Section 2.3.1). In general, changes in fibre and resin properties which reduce the level of matrix failure (matrix cracking and delamination) will lead to improvements in compressive properties but will have little influence on the tensile strength. Any changes in the laminate which reduce the incidence of fibre failure will be beneficial to both tensile and compressive strength.

Husman et al [78] investigated a number of different fibre (types I, II and III carbon and E-glass) and resin (epoxy and thermoplastic) combinations to determine the effects of constituent properties on the residual tensile strength after impact of $0°, 90°$ composites. Variations in matrix properties were found to have

little influence on the residual tensile strength of impacted materials but significant changes were noted with different fibre properties, fibres with a combination of high strength and high strain (i.e high strain energy to failure) providing the best results. The effects of resin on residual tensile and compressive properties were considered by Dorey et al [53] and Bishop [52]. Comparing $0°$,$90°$ and $\pm 45°$,$0°$ CFRP laminates with epoxy and a tougher thermoplastic PEEK matrix it was found, in accordance with Husman et al [78] that the residual tensile strength was little different between the two matrix systems but the less extensive delamination and greater resistance to damage growth provided by the tougher matrix led to much greater residual compressive strengths and higher threshold energies before initial reduction.

Laminate lay-up has a significant effect on residual properties of CFRP subject to impact. Bishop [52] noted that for $0°, 90°$ laminates, placing the load bearing $0°$ plies on the outside made them vulnerable to impact and residual strengths were less than if the $90°$ plies were the surface plies. Cantwell et al [82] explained differences in residual tensile behaviour in terms of impact induced failure modes. A threshold energy of approximately 2J was noted for laminates with $\pm 45°$ plies on the surfaces and a linear reduction from undamaged strength (i.e no threshold) for laminates with $0°$ surface plies. Placing the load bearing $0°$ plies on the surfaces, whilst increasing the flexural stiffness of the laminate puts them in the region of maximum impact induced contact stresses on the front face and maximum tensile flexural stresses on the back face. Reductions in tensile strength are dominated by fibre failure from low energies. The lower flexural stiffness and strength of laminates with outer $\pm 45°$ plies promotes large tensile strains in the lower plies and matrix shear cracks in these plies which do not affect tensile strength. At higher energies the cracks penetrate to the inner plies and act as stress concentrations on the $0°$ plies causing a large drop in strength. Eventually as the impact energy is increased the inner $0°$ plies fail and the rate of strength decrease reduces.

Altering the ply stacking sequence also changes the tensile notch sensitivity of the laminate. Potter [83] and Potter and Copley [84] noted that for notched unidirectional CFRP failure originated from the edge of the notch by longitudi-

nal splitting which eliminated the stress concentration. For laminates containing mainly plies at $\pm\theta^o$ (typically $\pm 45^o$) failure occurred by angle-ply splitting and delamination which tended to reduce the effect of the stress concentration on the laminate. Both of these failure modes were associated with lower notch sensitivity than tensile failure mode associated with laminates containing fibres in three or more directions. For these laminates axial plies carry most of the load but longitudinal splitting is inhibited by the presence of off-axis plies. Curtis and Bishop [62] and Bishop [63] attributed the better residual tensile strength after impact of $\pm 45^o$ CFRP laminates when compared with $0^o, 90^o$ laminates to the relative notch insensitivity of the angle-ply lay-up. However, this effect is unlikely to be entirely due to a notch sensitivity effect as the above discussion makes it clear that placing the load bearing fibres on the surface, as in the $0^o, 90^o$ material, is detrimental to the post-impact tensile behaviour of CFRP.

Similar crack blunting mechanisms have been observed under compressive loading [59]. However failure of impact damaged material under compressive loading tends to be associated with fibre and ply buckling. Under compressive loading Cantwell et al [85] noted that planes of delamination between surface 0^o plies and $\pm 45^o$ plies immediately below the surface caused local buckling of the load bearing outer plies which then did not contribute significantly to the strength of the laminate and strength losses were observed at very low energies. If $\pm 45^o$ plies were placed on the surface the load bearing 0^o material was unaffected by the initial delaminations at low impact energy. At higher energies delaminations propagated to the interior of the laminate causing progressive decoupling of the inner 0^o plies and subsequent reductions in strength.

The inclusion of woven material in the lay-up can have beneficial effects on the residual strengths after impact of CFRP. Results for woven $0^o, 90^o$ and $\pm 45^o$ and mixed-woven $0^o, \pm 45^o$ laminates were compared with equivalent non-woven laminates by Bishop [63], Curtis and Bishop [62] and Cantwell et al [82], [85], [86]. Impact damage was found to severely reduce the residual tensile strengths of $0^o, 90^o$ laminates and the reduction was more pronounced in the woven case. This effect was attributed to the inhibition of stress relieving mechanisms by the weave.

Tensile behaviour of multi-directional CFRP laminates containing notches shows that localised failures can occur at the notch tip giving rise to stable damage zones of matrix cracks and delaminations [87], [88]. These zones act as stress relievers in the same way as plastic zones in metals and the notch sensitivity is reduced from the value predicted by elastic analysis.

Under compressive loading, however the performance of the $0°, 90°$ was superior in the woven case due to the reduced area of delamination. Woven $\pm 45°$ laminates were found to be less sensitive to impact due to the relative notch-insensitivity of this lay-up. For more damaged non-woven laminates small reductions in both residual tensile and compressive strengths were noted but the effect of impact on woven material was negligible. For mixed-woven laminates the residual strengths under tensile and compressive loading were significantly better at higher impact energies than non-woven lay-ups. The reduced area of damage, containment of $45°$ cracking and better properties of the woven $45°$ layers account for these improvements and the use of woven $45°$ material offers great improvements to the impact resistance of CFRP.

2.4.2 Delamination Growth and Residual Strength Models

The failure analysis of impact damaged material under the influence of external loads is made extremely difficult by the patterns of interrelated damage present around the impact site and thus far no studies have successfully predicted damage by direct methods. However, as low velocity impact damage is characterised mainly by the presence of internal delaminations, the study of idealised delaminations has been attempted by a number of workers as an introduction to the problem. Wang [89] applied a fracture mechanics approach to the solution of delamination problems, consideration of the stress singularity at the crack tip leading to expressions for the stress intensity factors for opening mode and in-plane and out-of-plane shear (K_I, K_{II}, K_{III}) and the strain energy release rate G. The effect of fibre orientation, ply thickness and crack length for $[+\theta, -\theta]_S$ laminates were studied by numerical examples and were found to significantly influence delamina-

tion crack behaviour. The numerical work was not validated against experimental data. However the formulae developed by Wang [89] were not associated with any specific cases and could be useful in delamination and impact studies using a strain energy release rate approach. Wang [89] considered that, in these cases a fully three-dimensional analysis would be essential in obtaining complete information.

Although the formulae developed in [89] are intended for hand calculation the complex nature of the stress field around the delamination front means that stress analysis is most easily accomplished using finite element techniques [90], [91], although Jones et al [90] noted that the finite element analysis of three-dimensional delamination damage constituted a particularly difficult problem. Low velocity impact can produce asymmetric and unbalanced laminates above and below the plane of the delamination, coupling bending, twisting and stretching deformations. They considered that each ply must be modelled separately to obtain through-thickness peel stresses (σ_z) and interlaminar shear stresses (τ_{xz} and τ_{yz}) and that fine meshes are needed at the delamination front, the obvious disadvantage being that the problem can rapidly become excessively large. Chester and Pavier [91] took a more simplified approach, using plate elements to model the plies around the delamination and using a relatively coarse mesh. Recognising that this approach did not allow for detailed modelling of stresses at the delamination front, they nevertheless suggested that the variability in composite fracture data justified the inaccuracy.

Once the stress analysis has been performed a failure criterion must be used to assess the severity of the delamination damage. Baker et al [92] considered that the two criteria showing most promise were the strain energy release rate approach, as used by Wang [89], and the strain energy density approach.

Using strain energy release rate is, at first sight an attractive solution. For two-dimensional problems the forces and displacements between nodes at the crack tip can be assessed with relative ease from the finite element analysis. Failure is assumed to occur when G, the strain energy release rate reaches a critical value G_c, the fracture toughness of the material. However, for three-dimensional impact

damage/delamination problems Baker et al [92] noted that the damage growth would be mixed-mode (i.e $G = G_I, G_{II}, G_{III}$) due to action of peel and interlaminar stresses around the delamination front and that there would be considerable difficulty in assessing G without prior knowledge of the delamination shape and growth behaviour. Nevertheless this approach was used by Chester and Pavier [91] to assess damage growth and the load at which growth was initiated for specimens containing idealised rectangular delaminations under compressive loading. The crudeness of their finite element mesh allowed them to decide on the point of initiation by calculating G at each point on the delamination front and releasing nodes around the point of maximum G to give an increment of delamination growth. Calculations of G were compared with G_c to give a load level for growth initiation. Chester and Pavier [91] noted that, in their studies delamination was predicted and observed to grow laterally under nearly pure mode I opening. Predictions of delamination growth and initiation showed good agreement with experimental observations given that the coarseness of the finite element mesh controlled the size of each growth increment.

The strain energy density criterion is capable of predicting the way in which damage will grow and is therefore useful for delamination problems where the direction of growth is not known in advance. According to this method failure occurs when the strain energy density factor S reaches a critical value S_c where:-

$$S_c = r_c \left(\frac{dW}{dV}\right)_c \tag{2.13}$$

Both $\left(\frac{dW}{dV}\right)_c$, the critical strain energy density and r_c, the radius of a spherical core region surrounding the crack tip are material properties. The location along the delamination front of minimum strain energy corresponds to fracture or crack extension [93] such that:-

$$\frac{\partial S}{\partial \theta} = 0 \quad \text{and} \quad \frac{\partial^2 S}{\partial \theta^2} > 0 \quad \text{at} \quad \theta = \theta_o \tag{2.14}$$

Therefore rapid crack growth occurs when S_{min} reaches the critical value i.e:-

$$S_{min} = S_c \quad \text{at} \quad \theta = \theta_o \tag{2.15}$$

Jones et al [90] used this appoach to analyse the growth of artificially introduced rectangular delaminations of different sizes in CFRP laminates under compressive loading. The discrepancies between predicted and observed strains to initiate delamination growth were about 20% - 50%, results which were regarded as promising given problems with the experimental techniques.

The direct approach to the assessment impact damage by finite element analysis combined with fracture mechanics has shown encouraging results although it is in its relatively early stages of studying idealised delaminations. It is evident, however that the prediction of damage growth and strength of delaminated composites is a very involved procedure and it may well prove extremely difficult to extend such methods to more realistic impact induced damage, the stress analysis in particular requiring considerable resources.

An alternative method to predicting residual tensile and compressive strength which has achieved some popularity is one which draws an analogy between the damage produced by low velocity impact loading and artificially implanted flaws of known size. Accepted fracture mechanics approaches can then be employed to produce expressions relating impact parameters to residual strength of the impacted material.

Chamis and Ginty [30] noted that low velocity impact damage induced a similar strength degredation in CFRP as a circular drilled hole, and proposed to simulate the state of damage by a specimen containing a hole under a combined direct and shear load. Using available expressions for stress concentration factors around circular holes they determined the stress state around the damaged area.

A more popular method of determining strength reduction in impacted laminates by an equivalent implanted flaw has been the semi-empirical method followed by Husman et al [78], Lal [96], [97], Caprino [56] and Avva [80].

Husman et al [78] noted that if a tensile specimen was subjected to low velocity impact the resulting strength would be lower than the undamaged strength. The same result could be obtained by introducing a slit or hole of known size into the

specimen. Thus residual strength of impact damaged specimens could be analysed in terms of a fracture mechanics approach used for composite materials containing flaws. Using the expression for critical strain energy release rate for an orthotropic material containing a slit, determined by Sih et al [94]:-

$$G_{IC} = K_{IC}^2 \left\{ \left(\frac{S_{11}S_{22}}{2} \right) \left[\left(\frac{S_{22}}{S_{11}} \right)^{\frac{1}{2}} + \frac{2S_{12} + S_{66}}{2S_{11}} \right] \right\}^{\frac{1}{2}} \tag{2.16}$$

where:-

S_{ij} = Laminate compliances

G_{IC} = Critical strain energy release rate

K_{IC} = Critical stress intensity factor

and the inherent flaw model developed by Waddoups et al [95]:-

$$\sigma_r = \sigma_o \left(\frac{c_o}{c + c_o} \right)^{\frac{1}{2}} \tag{2.17}$$

where:-

σ_r = Residual strength

σ_o = Undamaged strength

c_o = Inherent flaw size

c = Half notch length of implanted flaw

c can be expressed in terms of the kinetic energy of the impact and the work required to fracture an undamaged specimen. This approach leads to the expression for residual strength of impacted specimens:-

$$\sigma_r = \sigma_o \left(\frac{U_s - K\overline{U}_{ke}}{U_s} \right)^{\frac{1}{2}} \tag{2.18}$$

K = Effective damage constant

$\overline{U}_{ke}$ = Kinetic energy/unit thickness imparted to specimen

U_s = Work/unit volume required to break undamaged specimen.

Thus residual strength of impacted specimens can be predicted as a function of the kinetic energy of the impact by performing just two simple experiments, namely static tensile tests on undamaged and impact damaged specimens. It

should be noted that the expression 2.18 could also be generated by assuming that the equivalent implanted flaw took the form of a circular drilled hole. The application of this model is limited to low velocity impact. The model predicts continuous reduction in strength with increasing impact energy, reaching zero when $U_s = K\overline{U}_{ke}$, whereas in reality the strength of an impacted laminate never vanishes. For high impact velocities above the penetration threshold the residual strength is that of a drilled hole of the same diameter as that of the impactor. This relationship is illustrated in Figure 2.2.

Good agreement was obtained by Husman et al between the expression 2.18 and experimental results for symmetric $[0^o, 90^o]$ laminates under low velocity impact. Furthermore consideration of the expression suggests that as U_s increases for a given $\overline{U}_{ke}$ the residual strength will increase (i.e materials containing fibres with a higher strain energy to failure have better impact resistance). This result is in full accordance with the experimental observations obtained by Husman et al [78] and many other workers.

Lal [96], [97] used a very similar approach to that of Husman et al [78] , assuming that impact damage could be considered analogous to an equivalent implanted slit. As static tensile strength is largely dependent on the strength of the fibre reinforcement in a laminate Lal obtained the equivalent slit length c directly from fibre breakage energy and strain energy release rate:-

$$c = \frac{U_f}{2hG_{IC}} \tag{2.19}$$

h = Thickness of laminate

U_f = Fibre breakage energy

Thus Equation 2.17 becomes:-

$$\sigma_r = \sigma_o \left(\frac{c_o}{\frac{U_f}{2hG_{IC}} + c_o} \right)^{\frac{1}{2}} \tag{2.20}$$

Fracture mechanics tests can be conducted to obtain c_o, σ_o and U_f can be obtained from the difference between absorbed impact energy and the energy required to produce delaminations (delaminations are ignored in the analysis as having little

or no influence on the *tensile* strength of the composite). Lal [96] obtained good agreement between expression 2.20 and test results on $[45°, 0°, -45°, 90°]_S$ CFRP laminates. Again, examination of the analysis suggests that impact resistance of laminates can be improved by increasing the strain to failure of the material.

Caprino [98] modified the basic fracture mechanics equations for notched composites to account for the pseudo-plastic zone of micro damage around the notch such that:-

$$\sigma_r = \sigma_o \left(\frac{c_o}{c}\right)^m \tag{2.21}$$

m = Constant

This relationship was extended [56] to the study of the residual strength of impact damaged composites, Caprino [56] suggesting that the continuous reduction in strength with increasing notch size meant that for any impact energy and damage zone size there was an equivalent hole in terms of residual strength such that:-

$$\sigma_r = \sigma_o \left(\frac{U_o}{U}\right)^\alpha \tag{2.22}$$

U = Impact energy

α = Constant

U_o is the energy producing a damage corresponding to equivalent hole size c_o and represents the maximum energy level that the material can support without reduction in strength. U_o and α are constants dependent on the impact test geometry that can be determined experimentally. Caprino [56] confirmed by experiment the conclusion reached by Crivelli-Visconti et al [99] that under low velocity impact conditions CFRP could be considered rate insensitive and the constants U_o and α could be determined by simple static tests.

Good agreement was obtained between the predictions made by equation 2.22 and experimental measurements on $[0°, \pm 45°]_{2S}$ CFRP laminates and the validity

of the assumption that the material was rate insensitive for the velocity range under consideration was confirmed. However Caprino noted, like Husman et al [78] that the model predicted continuous strength reduction and was therefore only valid for energies below the penetration threshold. Application of the model to data available in the literature suggested that the model was equally effective in predicting residual compressive strength of impacted CFRP.

Tiu et al [81] recognised the effectiveness of the Caprino Model in predicting both the residual tensile and compressive strength of impacted CFRP but highlighted the limitation caused by having to determine the constants U_o and α from experimental results. At least one of these, namely the threshold energy for damage induced strength reduction, U_o could be determined from a static finite element analysis in conjuction with the Tsai-Hill failure criterion. Tiu et al confirmed the accuracy of the Caprino approach under tensile and compressive loading for quasi-isotropic 24-ply CFRP and the finite element model predicted U_o reasonably close to experimental values. The effectiveness of this approach lies in its ability to assess the effects of material properties, loading and clamping conditions on the damage threshold energy analytically without the need for extensive test programmes.

Avva [80] accounted for the existence of a threshold energy below which there would be no strength reduction due to impact by proposing that the dimensions of a through thickness crack used to model the damage would be proportional to the difference between the applied impact energy and the threshold value such that:-

$$c = k(\overline{U} - \overline{U}_o) \tag{2.23}$$

k = Constant

$\overline{U}$ = Impact energy/unit thickness

$\overline{U}_o$ = Threshold energy/unit thickness

Using the avarage stress criterion developed by Whitney and Nuismer [100], [101] for laminates containing a notch:-

$$\sigma_r = \sigma_o \left[\frac{1 - \left(\frac{c}{c+a_o}\right)}{1 + \left(\frac{c}{c+a_o}\right)} \right]^{\frac{1}{2}} \tag{2.24}$$

a_o = Characteristic dimension adjacent to discontinuity

Avva suggested the expression:-

$$\sigma_r = \sigma_o [2K(\overline{U} - \overline{U}_o) + 1]^{-\frac{1}{2}} \tag{2.25}$$

K= Constant

K and $\overline{U}_o$ have to be obtained from experimental results on a few specimens. The effectiveness of the proposal was illustrated by Avva [80] and Avva et al [79] for residual tensile and compressive strengths of impacted $[\pm 45°, 0°, 90°]_{2S}$ CFRP laminates.

2.5 The Behaviour of Impact Damaged CFRP Under Fatigue Loading

The behaviour of low velocity impact damaged CFRP under the action of repeated loading has received relatively little attention and most of the work has consisted of experimental data and qualitative attempts to understand the observed phenomena.

Perhaps the most significant body of work is that due to Cantwell et al [82], [85], [86] who conducted detailed studies of the effects of ply stacking sequence and the introduction of woven plies into the laminates on the zero-tension [82], [86] and zero-compression [85], [86] fatigue performance of CFRP laminates containing low velocity impact damage.

The effect of introducing woven plies into CFRP laminates to produce a mixed-woven material was assessed initially [86] by a consideration of $[+45°, -45°, 0°_2,$ $-45°, +45°, 0°_2]_S$ laminates and a similar lay-up in which the $(+45°, -45°)$ ply pairs were replaced by a single $\pm 45°$ woven ply. For the non-woven laminates significant improvements in residual tensile strength after zero-tension fatigue and in

residual compressive strength after zero-compression fatigue were noted despite large increases in damage area under fatigue. For mixed-woven laminates under zero-tension fatigue residual tensile strength was improved by fatigue and had little dependence on the initial impact energy. Interestingly the mixed-woven laminates suffered further reductions in residual compressive strength due to zero-compression cycling.

This study was extended to the investigation of different stacking sequences of non-woven and mixed-woven laminates under zero-tension [82] and zero-compression [85] fatigue. Three lay-ups comprising various combinations of $+45°$, $-45°$ and $0°$ fibres were investigated together with their mixed-woven equivalents. All laminates exhibited considerable increases in residual tensile strength after zero-tension fatigue and Cantwell et al [82] suggested a mechanism for stress relieving of the damage area based on evidence from microscopically examined cross-sections of the laminates. It was discussed in Section 2.4.1 that in laminates with $\pm 45°$ plies on the surfaces, impact induced matrix cracks acted as stress concentrations on the internal $0°$ material causing large strength reductions. Under fatigue loading these cracks propagated in the $\pm 45°$ material and were deflected at the interfaces with $0°$ plies to form local delaminations. This process reduces the stress concentrating effect of the damage on the load bearing $0°$ material and leads to increased strength after fatigue. For the laminates with $0°$ plies on the outside it was noted that, despite the strength reduction under impact loading being more dependent on fibre failure, matrix cracking played a similar role in improving residual tensile strength after fatigue. For mixed-woven laminates matrix cracks originated in resin-rich areas in the weave and grew rapidly at the interface between woven and non-woven plies, increasing residual strength to a greater degree than for non-woven laminates.

Cantwell, Morton and Curtis [85] found that the residual compressive strength of impact damaged mixed-woven laminates was further reduced by zero-compression fatigue loading. The mechanism for damage growth under fatigue was similar to that observed for zero-tension fatigue, matrix cracking being initiated in the resin-rich zones in the weave and then growing to the interface with $0°$ mate-

rial. In this case however the influence on residual strength was different. The production of local delaminations at the interface served to reduce the support of the load-bearing 0° fibres under compressive loading leading to reductions in residual strength. Clear results were not obtained for non-woven laminates and in two cases improved residual compressive strength was observed. Although no explanation could be supplied to account for this effect Rosenfeld and Gause [102] have observed similar improvements in compressive strength despite considerable damage growth under compressive fatigue.

Ramkumar [77] investigated the effect of two different levels of impact induced damage, namely internal delamination of a given size with and without attendant cracking on the surfaces of the laminate on the fatigue performance of two multi-directional CFRP laminates. Zero-tension, zero-compression and fully reversed loadings were conducted and the growth of damage monitored using ultrasonic techniques. A measure of the relative fatigue resistance of the two types of damage was achieved by measuring the maximum stress level that could be applied to the specimens for 10^6 cycles without causing failure. Under all fatigue conditions the growth of delamination was observed to be the predominant mode of failure and final failure of the specimens occurred when the delamination reached the edges of the specimens. For both laminates under both impact conditions zero-compression loading was found to be the most detrimental to the fatigue performance and zero-tension was the least damaging. Furthermore delamination with attendant surface cracking was more severe than delamination alone.

Potter investigated low velocity impact damage and subsequent fatigue growth in plain [66] and tapered thickness [18], [55] CFRP laminates by ultrasonic C-scan, PEXR, fractography, and in the case of compression loading shadow Moiré fringe techniques to observe the buckling of delaminated plies. Although residual tensile strengths after tensile fatigue were improved for impact damaged material, NDT studies showed that, even in the presence of the stress concentration caused by the tapered material, no damage growth was observed from the damage site. Under compressive fatigue loading however lateral delamination growth was observed, the growth rate being initially slow but building towards failure as illustrated in Figure

2.3. Furthermore it was shown that the damage after fatigue retained the characteristic double-lobe shape of impact induced delaminations discussed in Section 2.3.1 and that substantial delamination growth under fatigue was restricted to one interface near the laminate surface. Towards the end of fatigue life delamination growth occurred at interfaces deeper into the laminate and Potter [66] suggested that this might indicate the final collapse of the laminate.

The effect of altering the sequence impact/fatigue or fatigue/impact was shown by Avva, Vala and Jeyaseelan [79] to be important to the fatigue life of CFRP under tension-tension cycling. Impacted specimens of $[\pm 45°, 0°, 90°]_{2S}$ CFRP were subjected to fatigue to determine the fatigue life. Alternatively specimens were fatigued to a predetermined number of cycles and then impacted. Specimens that survived were then fatigued until failure. In terms of fatigue life of the specimens the sequence impact followed by fatigue was found to be more detrimental and Avva et al [79] interpreted this result by suggesting that the relative damage under this sequence was more severe.

The effects of simulated service loadings on low velocity impact damaged CFRP have been observed in related studies by Clark and van Blaricum [76] and by Saunders and van Blaricum [103]. Data of this type is more useful in analysing the service performance of damaged laminates than the relatively simple constant amplitude data usually reported.

Clark and van Blaricum [76] investigated the growth of impact induced damage in $\pm 45°, 0°$ CFRP laminates. Damage was observed, by shadow Moiré techniques, to grow mainly in the 90° direction to failure suggesting that growth was controlled by delamination along $+45°$ and $-45°$ plies, net growth being in the lateral direction. Damage growth rate was seen to increase as the damage progressed and seemed to be related to damage width by a simple power law. Time-of-flight C-scanning, reported by Saunders and van Blaricum [103] showed that the most significant delamination growth was in layers close to the back face of the laminate, where the largest delaminations had been produced by the initial impact. Some delamination growth was observed between more central plies and these shifted to adjacent interfaces by through ply cracking. These results are in close agreement

with those observed by Potter [66], suggesting that the orientation of the plies bounding a growing delamination strongly influence the direction of growth.

Clark and van Blaricum [76] suggested that longitudinal stiffness could be used to give a good indication of the onset of failure in specimens subject to fatigue loading. Sudden decreases in stiffness to 95% of the original value were observed at the start of fatigue, followed by a slow and steady drop to 90% over the majority of the life. A sudden decrease to 85% corresponded with a rapid increase in delamination size just before final failure. Thus, although no relationship between delamination size and specimen stiffness seemed to exist, stiffness measurement could be used to predict imminent specimen failure.

2.6 Discussion

The considerable volume of work conducted in recent years on the subject of low velocity impact damage and post-impact performance of CFRP has undoubtably been due to concern that, despite being difficult to detect, BVID can seriously reduce the load bearing capabilities of composite structures. Current design allowables are set low to account for the presence of notches and impact damage and with greater emphasis being laid on the use of bonded rather than mechanically fastened joints, impact damage is likely to become the limiting factor on the effective use of composites.

Numerous experimental studies have successfully identified the issues influencing the resistance of laminates to low velocity impact and it should be possible to design a material to maximise this property by the correct choice of fibre, matrix and lay-up. The laminate behaviour and stresses which cause the characteristic failure patterns are well understood and analytical work has been used to predict load/deflection characteristics and internal stresses by the combination of classical contact theory and modified laminate theory. The use of existing failure criteria has predicted fibre failure and matrix cracking but the successful prediction of the major feature of the damage zone, namely delamination has so far proved largely elusive.

A similar situation exists for the post-impact behaviour of CFRP. The issues affecting residual strength under tensile and compressive loading have been addressed by experimental work and are, of course closely related to the impact resistance of the material. Direct analysis is made extremely difficult by the complex nature of the laminates, the interrelated damage modes and stress field around the impact site. Analytical studies are still in the early stages of considering idealised delaminations and, given the so far modest success of this work, it seems that the successful prediction of impact induced delamination, delamination growth and failure in composites containing 'real' damage may be some way in the future and may depend on the use of costly and time-consuming three-dimensional finite element analyses.

However, several models do exist to predict the residual strength of impact damaged CFRP. The damage site is considered analogous to an implanted through-thickness notch of known dimensions. Accepted fracture mechanics approaches are then taken to predict the residual strength. Although these models in effect ignore the reality of the damage site and need some experimental results to obtain the correct expressions, they seem to be extremely successful in predicting both residual tensile and compressive strengths of low velocity impact damaged material with the minimum of experimental input. These models are easily applied and will suffice until more direct approaches to the problem reach fruition.

In contrast to the large amount of work conducted on the impact behaviour and post-impact static performance, the fatigue behaviour of impact damaged composites has recieved little attention. A body of opinion exists that suggests that, as strain allowables are so low to account for the presence of BVID, fatigue of the composite will not occur under practical loading conditions. However, this opinion seems not to backed up by practical experience and it would seem imperative to at least test this assumption by experimental means. Experimental studies have been conducted into the fatigue of impacted CFRP and have highlighted some interesting results. Increases in strength after fatigue compared with unfatigued material have been obtained, delamination growth has been observed and changes in longitudinal stiffness have been used to predict specimen failure. However, the

work in this area has been rather disjointed and it is inevitably difficult to to obtain a global view of the issues based on a relatively small amount of experimental work.

The purpose of the present study was therefore to study the overall behaviour of a practical quasi-isotropic carbon fibre reinforced epoxy matrix laminate under the range of impact energies required to cause BVID. The experimental programme ranged from impacting the laminates by drop-weight, through characterising the damage sites by destructive and non-destructive testing to determining the behaviour of the impacted material under static and fatigue loading. It was hoped that this comprehensive study would provide greater insight into the interrelation of the factors governing the behaviour of CFRP under these loading conditions. Particular emphasis was given to the study of fatigue strength and damage growth under fatigue loading for specimens impacted at different energy levels, as this seemed to be the area in the literature where more study was required.

Wherever possible, existing models were fitted to existing data to further verify (or disprove) their applicability and a simple model has been proposed which, it is hoped can be used to predict fatigue strength with the minimum of experimental effort.

Chapter 3

Materials, Specimens and Equipment

3.1 Introduction

This chapter describes the materials used throughout the experimental programme. It discusses the specimen design specifications and methods of preparation, and the equipment and test machines used during impact and post-impact testing. Ancillary apparatus and equipment are described in Chapter 4 on experimental work under the appropriate sections.

The standards used throughout this work are set out in the publications of the Composites Research Advisory Group (CRAG) and numerous references are made to these recommendations where appropriate. The initial CRAG document was made available in 1984 [104] and was updated during the course of the work in 1985 and 1988. Any recommended revisions that would not seriously affect the experimental results were incorporated in to the programme.

3.2 Materials

The CFRP laminates were prepared by Lucas Aerospace, Fabrications Division, Burnley using Ciba-Geigy 914 pre-preg sheets. The full pre-preg designation was Fibredux 914C-833-40% (Toray 300-3000 woven), this indicating a Toray 300 car-

bon fibre with 3000 filaments per tow in a Ciba-Geigy 914 epoxy resin matrix system with a 40% nominal resin content by weight. Cured ply properties are given in Table 3.1 [105].

The laminates were manufactured using conventional autoclave temperature/-pressure moulding techniques to the manufacturers specification to prepare final material with a cured thickness of approximately 2.4mm and a nominal fibre volume fraction of 55 - 60%. Details of the recommended cure cycle are given in Appendix A.

The weave style of carbon fibre, which is illustrated in Figure 3.1, was a five-harness-satin weave and the ply lay-up was an eight-ply quasi-isotropic $[0°/90°, \pm 45°_2, 0°/90°]_S$.

The quality of the prepared laminates was inspected by the manufacturers to commercial standards using ultrasonic C-Scan before being supplied to Sheffield University for further testing. Details of the quality control standards relevant to flat CFRP laminates are given in Appendix B.

The material used for the end-tabs of post-impact static and fatigue specimens was a two-ply chopped-strand-mat glass-fibre polyester made by a simple hand lay-up method. Each GRP laminate was checked thoroughly to ensure that the thickness was consistent within acceptable limits, and areas found to contain troughs or ridges were not used to produce specimen end-tabs.

3.3 Specimens

3.3.1 Design

The CRAG recommendations for the drop-weight impacting of CFRP laminates specify a minimum spacing between adjacent impact centres and between impact centres and the edges of the laminate of 100mm. These restrictions combined with those imposed by the need to remove specimens for post-impact testing meant that, in order to make the most economical use of the material available, the laminates were impacted as a whole. A typical laminate plan showing the impact-centre

positioning is shown in Figure 3.2.

CRAG also specify the dimensions of post-impact compression specimens. This design, illustrated in Figure 3.3 was also used for static tension and fatigue testing of impacted specimens.

3.3.2 Preparation

The detailed preparation of the laminates for impact testing is given in Appendix C.

Preparation of specimens for post-impact static and fatigue testing was conducted in accordance with the CRAG recommendations. The laminates were cut so as to ensure that the impact damage was in the centre of the specimen gauge section. Cutting was done using a diamond impregnated slitting wheel which was cleaned at regular intervals to keep it free from grit and dust. To achieve the best possible cut edge a slow, uniform material feed rate was maintained throughout the cutting process. Steel spacers and cutting guides were used to ensure that the edges were parallel and that the specimens were of the correct width.

The GRP end-tabs and specimen end faces were abraded with 320 Grade wet-or-dry paper and then treated with Genklene to remove dust and grease. The tabs were then bonded to the end faces using Ciba-Geigy Araldite 2001 two-pack epoxy resin adhesive. The specimens were then clamped over the end faces, using steel jigs designed for the purpose, and placed in a curing oven for 3 hours at 80°C.

3.4 Equipment

3.4.1 Impact Testing Equipment

The apparatus used for impact testing of the laminates was designed and manufactured so as to keep the test as closely as possible in accordance with the CRAG recommendations. The overall experimental set-up is shown in Figure 3.4.

The clamping of the laminate proved to be the most problematical aspect of the equipment design. The standards specify clamping between two rings of

internal diameter 100mm but also impacting of the laminate as a whole. Therefore clamping has to be largely achieved at the edges of the laminate, not an ideal situation considering the dimensions of the material.

A frame was devised which clamped the two rings to the laminate by using the stiffness of the frame itself. Carefully chosen dimensions meant that as the frame was assembled around the laminate, it squeezed the two rings together on either side of the area to be impacted. The two rings could be easily moved within the frame to impact at different sites.

After a series of trials an optimum design was achieved which included the addition of six cap screws which could be screwed down on to the top ring and which reacted, via secondary frames, on to the top bars of the primary frame. To ensure consistent and even clamping the six cap screw were torqued to the same value of 10Nm. This solution to the problem of clamping is illustrated in Figure 3.5.

The laminates were impacted using a 12.7 mm diameter spherical nosed impactor manufactured from 25.4 mm diameter steel rod sectioned in approximately 100 gramme sections. These could be fastened together with grub screws to vary the mass of the impactor and hence the incident impact energy.

The impactor was dropped from a height of one metre through a perspex guide tube, held vertical by a series of clamps, to strike the material in the centre of the clamped section.

The instrumentation employed during the impact tests was designed to measure plate deflection and plate strains during the impact event. A diagram of the experimental apparatus is given in Figure 3.6.

The deflection of the laminate was measured using a capacitance method which is described in more detail in Appendix D. The displacement signal was taken via a Tektronix Type-Q transducer and strain gauge pre-amplifier to a Hitachi VC-6020 digital storage oscillascope.

Strain measurement was by Micro-Measurements EA-06-060RZ-120 three-element strain gauge rosette or by EA-06-060LZ-120 linear strain gauge. The output from the gauges was taken to a bank of Micro-Measurements P3500 digital strain

indicators and thence to the storage oscillascopes. A maximum number of two oscillascopes were available, therefore the displacement and a maximum of three strain signals could be recorded for each test.

The four signals could be plotted after the test using a Philips PM-8141 X-Y recorder. The slowest possible plotting speed available gave the maximum detail reproduction of the recorded signals.

3.4.2 The Mayes S100 Machine

The static tests of impacted specimens were conducted using a Mayes S100 screw driven servo-electric machine of 100kN capacity (Figure 3.7) which could be driven in load, displacement or strain control. The digital read-out, used to monitor load or displacement, was accurate to $\pm 0.005\%$ of full scale and $\pm 0.01\%$ of reading. The load and displacement signals could be connected to an external plotter, thus facilitating the production of continuous test plots to failure. The maximum fatigue frequency of 100 cycles/minute meant that this machine was unsuitable for fatigue testing of impacted specimens.

3.4.3 The Schenck Hydropuls PSA 1006 Machine

Fatigue testing was conducted using a Schenck PSA 1006 servo-hydraulic machine rated at 100kN static and ± 80kN fatigue either side of a zero mean value. This machine is illustrated in Figure 3.8. Cycling could be performed in either load or displacement control up to a maximum frequency of 100Hz using either sinusoidal, triangular or square waveforms. The accuracy limits for this machine were ± 0.05kN for load, ± 0.005mm for displacement and ± 0.05Hz for frequency.

Flat faced testing grips were designed for use with the Schenck machine and adaptors manufactured allowing the grips to be also used on the Mayes. The design was a simple modification of an earlier one developed for the testing of narrower plain specimens of CFRP [3]. This type of grip was easy and quick to manufacture but has the disadvantage that it does not have any self-alignment . A careful programme of tests consisting of instrumenting the grips and testing

with gauged specimens to check for bending had to be devised to achieve sufficient accuracy of alignment. Thereafter each specimen was carefully aligned in the grips before testing, a depth gauge being used to check that the specimen was vertical and the clamping screws being all torqued to the same value of 20Nm.

Chapter 4

Experimental Work

4.1 Introduction

This chapter describes the programme of testing and the experimental techniques chosen to achieve the aims of the work. The test programme was split into four parts. The first part covered the impacting of the laminates and the second, the examination of the damage caused by impact. The third and fourth parts concerned the static tensile and compressive testing and fatigue testing of impact damaged specimens.

The programme was devised in such a way as to achieve the aims of the research within material and equipment availability. The primary restriction on the work was the difficulty in obtaining laminates of commercial quality in sufficient quantities.

4.2 Test Programme

4.2.1 Impacting of Laminates

Impacting of the CFRP laminates was done primarily to provide specimens for further study under static and fatigue test programmes although the laminates were instrumented for the measurement of plate deflection and strains. Initially impacting was conducted at energies ranging from 0.98J to 8.83J in approximately

1J intervals to provide specimens for both the damage study programme and the static testing programme. The fatigue test programme only required specimens impacted at selected levels and so later laminates were only impacted at three different energies, 2.94J, 6.87J and 8.83J. These levels were chosen as representing the threshold value for strength reduction, the energy at which damage was readily visible on both faces of the laminate and the maximum energy considered in this study.

A number of static tests were also conducted under conditions as close to those of the impact tests as possible. These tests were essentially bending tests of clamped, circular plates under the action of a central load, and also served to calibrate some of the apparatus used to record the impact events.

4.2.2 Examination of Impact Damage

Impact damage was examined with the aid of both destructive and non-destructive testing (NDT) techniques in order to obtain an overall picture of internal and external failure mechanisms associated with BVID. Techniques used included measurement of residual indentation on the impacted face, ultrasonic C-scan, penetrant enhanced X-ray (PEXR), and microscopic examination both internally and externally. C-Scan was only available through Lucas Aerospace and was therefore only used on a limited basis as a commercial datum against which to assess the effectiveness of more readily available techniques. C-Scan on a larger scale would have tied laminates up, thereby seriously delaying the experimental programme. Internal examination was also only used on a limited basis as it involved sectioning the specimens, thus rendering them useless for further testing.

Initially all specimens were examined before testing in order to obtain detailed information of damage at all impact levels up to 8.83J. Selected specimens were then chosen for comparison purposes as each new laminate was impacted, providing information on the variability of the results.

4.2.3 Static Testing

The aims of the static test programme were to determine the material properties of the laminates, to determine the relationship between incident impact energy and static strength and to study the behaviour of low energy impact damage under static loading conditions. At least three tensile and compressive tests were conducted at each impact level so that an indication of variability was obtained. Due to the large number of laminates impacted for the static test programme, at least one undamaged specimen was tested from each sheet to ensure that the basic material properties were comparable. Specimens with centrally drilled holes ranging in diameter from 2.5mm to 38.5mm were tested for the purposes of the verification and development of residual flaw approaches to the prediction of residual strength after impact. Furthermore a hole size of 12.7mm could be used to assess the severity of the damage over the range of impact energy chosen, as it represents a theoretical infinite impact energy in which the impactor (12.7mm diameter nose) would penetrate the laminate without causing splitting out of the back face or any other damage other than the production of the hole.

Material properties and the state of straining adjacent to the impact damage were studied using either linear strain gauges or three element rosette gauges on both the impact and back face of the specimens.

4.2.4 Fatigue Testing

The aims of the fatigue test programme were to obtain the S-N data for the material, to study the growth of damage originating from the impact site and to determine the change of physical properties under fatigue loading.

As in the case of static testing, specimens from a number of different laminates were impacted for the fatigue test programme. Therefore to obtain realistic baseline S-N data for the material fatigue tests were conducted on undamaged specimens from nine different laminates representing the material used in the majority of the programme.

Due to the limited availability of material three impact energies were chosen for

study under fatigue loading conditions. 2.94J was representative of a low energy impact where the static properties of the material were just beginning to be affected by the impact, 6.87J was a higher impact level where damage was readily visible on both faces of the laminate and 8.83J was the maximum energy chosen in this study. S-N data was collected for these impact levels and a study of the damage growth and change of physical properties was undertaken for specimens impacted at 2.94J and 6.87J.

The measurement of physical property changes and progression of damage had to be non-destructive, therefore localised stiffness changes were recorded at the impact site under a non-damaging load and PEXR was used to track damage so that only one specimen need be used for each fatigue test.

Measurement of stiffness could be achieved in three different ways. A localised strain reading adjacent to the damage could be obtained, an overall specimen displacement could be found from machine actuator displacements or localised displacement over the impact area could be found using a clip gauge. The first method would have been the most accurate and reliable but fatigue loading caused the damage to grow under the strain gauge causing it to debond. The second method would be the least accurate and would possibly not pick up stiffness changes due to localised damage growth from the initial impact site. This method is also prone to error due to elastic extension of the grips and to movement of the specimens in the grips. The third method proved to be the most suitable and was chosen for the experimental programme.

The specimens were tested under zero-tension loading (i.e stress ratio R=0) at a frequency of 5Hz sinusoidal waveform with the maximum stress chosen to be a given percentage of the static tensile strength. Specimens were removed from the machine at intervals during the predicted fatigue life of the specimen so that examination of damage and localised displacement readings could be taken.

The testing frequency chosen was, according to the CRAG document, the maximum recommended frequency for testing specimens with a significant proportion of 45° fibres. Higher frequencies would cause an unacceptable degree of heating of the specimen.

4.3 Experimental Procedure

4.3.1 Impacting of Laminates

Impact testing of laminates was achieved using a drop-weight method, the equipment for which is described in Section 3.4.1. A steel impactor was dropped from a fixed height of one metre through a perspex guide tube on to a circular clamped section of laminate 100mm in diameter, this test method being in accordance with the CRAG recommendations.

Firstly the laminate was prepared as outlined in Appendix C, and then carefully fixed in the clamping frame at the required position. All necessary connections were then made to the pre-amplifier, oscillascopes and strain indicators. The frame was placed below the guide tube and a plumb-line suspended through the centre of the tube. This ensured that the guide tube was vertical, thus minimising any frictional effects between the impactor and the tube when the impactor was released, and allowed the clamped section of the laminate to be accurately lined up with the tube so that the impact was achieved centrally. When satisfactory alignment had been obtained the plumb-line was removed.

The impactor of required mass was then placed in the guide tube at the correct height and when the recording apparatus had been set to trip on impact, the impactor was released. After striking the laminate the impactor was caught to prevent secondary impact. The laminate was then carefully removed from the frame to prevent further damage.

Calibration of the capacitance displacement transducer had to be conducted under static conditions as close to those of the impact test as possible. This meant conducting a static plate bending test of the CFRP laminate under the same clamping conditions.

The clamping frame was adapted to fit the bed of the Mayes S100 testing machine and an adaptor was designed so that the loading nose of the impactor could be mounted in the standard grips described in Section 3.4.3. A static load/deflection test was conducted so that the deflection measured on the oscillascope could be related to the central displacement as indicated by the DVM on the

Mayes. This method had the advantage of also providing a static load/deflection characteristic for the CFRP plate.

4.3.2 Examination of Impact Damage

External damage was examined on the front (impact) face and back face with the unaided eye and using Olympus Model VMZ stereo and Model CHC microscopes giving the capability of up to ×500 magnification. Sketches of the overall damage site were made at low magnification (×10 - ×40) using the stereo microscope and details were identified with the aid of the CHC model at higher magnifications (×50, ×100 and ×500). Photographs were also obtained using a standard 35mm SLR camera equipped with a close-up lens. Once the main features of the damage sites had been identified, dimensions were recorded with the aid of a travelling microscope and vernier scale.

The extent of the indentation made on the surface of the laminate by the impactor was measured by placing each specimen impact face upwards on surface plates and running a dial gauge across the surface until a minimum was detected. A datum level was obtained over the undamaged surface by placing the gauge at selected positions over the surface.

Internal damage was examined using C-scan, X-ray and sectioning/microscopy techniques. The most widely used technique for NDT of composites is ultrasonic C-scan. Unfortunately this method was only available on a limited basis through Lucas Aerospace. C-Scan was therefore used as a means of assessing the effectiveness of examination methods more readily available against a commercial standard. Results were provided by Lucas in the form of C-scan traces with one attenuation level of 6dB above the reference level of undamaged material used to illustrate the damage.

Damage areas were assessed from the C-scan traces by simply tracing round the indicated area of damage and transferring the tracing to a sheet of graph paper. The squares contained within the boundary of the tracing were then counted. Although this method was very tedious and time consuming it was found to give

reliable and accurate results.

X-Radiography was conducted using a Hewlett-Packard Faxitron (model 438-55A) X-ray cabinet. Due to the similarity of absorption of X-rays by carbon fibres and the epoxy resin matrix and the difficulty in detecting delaminations due to the low effect on overall absorption it was decided that an X-ray opaque penetrant had to be used.

Penetrant enhanced X-ray (PEXR) can be successfully accomplished using a number of high density organic penetrants such as di-iodomethane, di-iodobutane, dibromomethane, and tetrachloroethene. Investigations by Clark [75] and Stone and Clark [68] have shown that inorganic zinc iodide solution gives comparable results to the others mentioned. It is readily available, simple to use and has been shown [22] to give good contrast between damaged and undamaged material. Thus far no data has been produced to suggest that zinc iodide solution has any detrimental effects on the performance of CFRP. The only great disadvantage of PEXR is that it requires surface damage to be present in order that the penetrant can work its way in to the internal damage.

Penetrant solution was made up of a mixture of zinc iodide powder, water, propan-2-ol and Kodak Photoflo in the proportions outlined in Table 4.1. The ingredients were mixed and warmed to ensure a uniform solution which was then ready for use.

There are essentially four ways to introduce the penetrant. Firstly the entire specimen can be immersed in penetrant and left to soak. Secondly a 'dam' can be built around an area of surface damage and again left to soak. Thirdly penetrant can be introduced directly into the damage using a syringe and lastly the penetrant can be worked into the damage by using a brush. For the present study the final technique was used as good penetration could be achieved more rapidly and this method was considerably more economical with the penetrant. Penetrant was painted over both faces and edges of each specimen and worked in with a brush for a period of about five minutes. As an added precaution this task was generally performed on the day before the X-rays were to be taken and the penetrant was left on the specimen overnight. Zinc iodide solution does not readily evaporate

from the damage area and so X-ray could be performed any time after application. Prior to X-ray the excess penetrant was removed with tissue.

The specimens were placed directly on top of Agfa-Gevaert D4 film, cut to size so as to give full reproduction of the specimen gauge section. Experience showed that a voltage of 18kV with a current of 3mA and an exposure time of 80 seconds gave excellent contrast on the film. The negatives were then developed for 7 minutes in a 1:4 solution of developer and fixed in a 1:5 fixer solution for 5 minutes.

X-Ray damage areas were assessed in a similar way to those given by C-scan traces. The negatives were placed on a sheet of glass and back-lit so that accurate tracings of the damage could be obtained. The tracing was then transferred to graph paper where the area was measured by counting the squares.

Both X-ray and C-scan NDT show damage in the plies and between the plies as an accumulated two-dimensional image. Neither technique provides information of through thickness position of damage. Although three-dimensional ultrasonic scans have been accomplished [73], [74] and three-dimensional X-rays can be achieved by observing stereo pairs of images, these methods were unavailable for the present study.

Damage through the thickness of the laminate was examined using microscopy techniques. 50mm squares of material were cut around each impact site and then cut, using a diamond impregnated slitting wheel, normal to the required direction of study, and away from the centre of impact so that cutting damage would not occur on the cross-section to be studied. The specimens were placed in a glass mould and set in a block of polyester resin which was allowed to cure slowly as a normal accelerated cure cycle caused cracking of the resin.

After cure the resin block was cut down to the CFRP surface and then carefully ground and polished down to the required cross-section using a polishing wheel and wet-or-dry paper ranging from 120 grade to 1200 grade with water as a lubricant. To achieve the required standard of finish for microscopy purposes the polishing was concluded with diamond paste of 5 micron and 1 micron grade and using oil as a lubricant.

In order to remove dust and excess oil from the polished surface the resin block was placed face downwards in a beaker of Genklene which was then placed in an ultrasonic cleaning bath for about 2 minutes. Excess Genklene was driven off using a warm air source.

The polished cross-sections were then examined using an Olympus Model CHC microscope and photographs were taken using a similar microscope adapted for use with a SLR camera. The magnifications available for the photographs were $\times 12.5$, $\times 25$ and $\times 125$.

4.3.3 Static Testing

In order to investigate the state of straining around the impact site and to determine stiffness and Poisson's Ratio of the material, strain gauges were used both remote from and adjacent to the damage. Reference was made to the relevant X-ray to ensure accurate placing of the gauges. Strain readings were taken with Micro-Measurements P3500 strain indicators and continuous load-strain plots were obtained using either Philips PM-8141 or Bryans 50000 X-Y plotters. Where continuous plotting of results could not be achieved, a single strain indicator was used in conjunction with a Micro-Measurements SB-1 switch and balance unit which allowed large numbers of strain readings to be recorded but only during tests interrupted at certain load levels.

After calibration of the equipment, the specimens were clamped in to the grips using a torque wrench which ensured even clamping of the specimen over the end tabs. Tests were conducted in load control on the Mayes S100 machine at a constant loading rate set to cause failure within 30 to 90 seconds in the case of continuous tests.

To accurately assess the compressive properties of the CFRP laminates guides had to be used to eliminate buckling of the specimens. The anti-buckling guides were developed from a design illustrated in the CRAG report and are shown in Figure 4.1. In order to reduce friction between the guides and the specimen and possible unwanted damage to the specimen, low friction PTFE tape was placed

between the specimen and the faces of the guides.

4.3.4 Fatigue Testing

Fatigue testing was conducted using the Schenck PSA 1006 machine. As this machine is capable of testing specimens of widely different mass, stiffness and damping characteristics it was necessary to conduct preliminary tests with dummy specimens so that the feedback control loop could be set to give the correct actuator response to the command signal. This ensured an accurate sinusoidal waveform for the fatigue test programme.

Before the start of fatigue testing each specimen was X-rayed and the local displacement across the damage area was recorded using a clip gauge, calibrated for displacement using a barrel micrometer. The gauge was held by two notched studs, as shown in Figure 4.2, to give a gauge length of approximately 45mm. The specimen was loaded to a level which would not cause damage and the strain output from the clip gauge was measured using a P3500 strain indicator.

Each specimen was bolted into the grips on the Schenck using a torque wrench and a frequency of 5Hz and sinusoidal waveform were selected. Load control was selected so that any changes in the stiffness of the specimen under fatigue loading would be compensated for and a constant load amplitude would be maintained. Firstly the mean load of 0.5 of the maximum was selected. The sinusoidal load signal was then applied and slowly increased in amplitude until the required maximum and minimum loads were achieved. Care was taken to ensure that the specimen was not subjected to any compressive loading. The Schenck machine has a tendency to allow the load to 'drift' from the parameters set at the beginning of the test. Therefore the load levels were checked at frequent intervals during the test and corrections made to the mean load or amplitude of the waveform as appropriate.

Zinc iodide X-ray penetrant was applied to both surfaces and edges of the specimens at regular intervals during fatigue loading, the cyclic opening/closing of the damage being very effective in drawing the penetrant into the damaged

areas. Great care was taken to ensure that it did not come into contact with either the grips or the machine itself due to its highly corrosive nature. After each specimen had reached a predetermined number of cycles it was removed from the machine and left overnight with penetrant on its surfaces. Excess penetrant was then removed and the specimen X-rayed using the technique described in Section 4.3.2.

After X-ray the local displacement around the damage area was measured using the technique described earlier. The specimen was then replaced for further fatigue. This cycle of fatigue, X-ray and local displacement measurement was continued until either the specimen failed by complete separation of the gauge length, or it reached 10^6 cycles without failure, after which it was designated a 'run-out' and removed from the Schenck. Run-out specimens were then tested for residual tensile strength on the Mayes.

Chapter 5

Experimental Results and Observations. Low Velocity Impact Loading and Examination of Failure Modes

5.1 Introduction

The results obtained and observations made during the experimental programme for both low velocity impact and examination of the resulting damage zones are presented in this chapter. As in most cases more than one specimen was tested under any given set of conditions, only representative results illustrating typical behaviour are presented.

5.2 Low Velocity Impact Loading

5.2.1 Static Load/Deflection Behaviour of CFRP Plates

Typical static load/deflection behaviour for a 100mm diameter clamped CFRP plate loaded centrally through a 12.7mm spherical nosed indenter is shown in

Figure 5.1. The behaviour was approximately linear up to an applied load of 1.5kN after which the stiffness, given by $\frac{F_a}{w_c}$ decreased with increasing load. The test was halted at a load of approximately 2kN, the readings taken from the oscillascope becoming unstable as the load/deflection curve levelled off. The first obvious indication of failure was found to be clearly audible cracking sounds which occurred at an applied load of approximately 1.5kN. Thus it can be seen that first audible indications of failure coincided closely with the onset of reducing bending stiffness of the plate.

The values of load and deflection at the onset of reducing stiffness (and consequently at first audible failure) for this and the other plates tested under these conditions are given in Table 5.1. The energy required to cause initial failure under static loading was assessed by the area under the load/deflection curve up to first failure and these values are also presented in Table 5.1. These values should be considered alongside the later work on impact induced damage in order to verify or disprove the assumption that a direct analogy can be made between static and low velocity impact loading.

5.2.2 Impact Behaviour of CFRP Plates

Displacement/time and strain/time traces for a 4.91J impact on a 100mm diameter clamped CFRP plate are given in Figure 5.2. These were typical for many of the impacts from 0.98J - 8.83J. If the assumption is made that the impact event was quasi-static, then the period of the displacement could be taken as equal to the duration of impact. The duration of the impact events therefore ranged from 1.2ms - 1.3ms for a 0.98J impact to approximately 3.5ms for the higher impact energies of 7.85J and 8.83J.

Maximum plate deflection, occurring at approximately half the impact duration, is given in Table 5.2 and plotted against impact energy in Figure 5.3. The curve shows a gently increasing slope from approximately 1.7J impact upwards indicating that the rate of increase of central displacement with incident impact energy increases from this point. This may reflect the greater levels of damage

and hence reducing local and bending stiffness of the plate with increasing energy, implying a threshold energy for initial damage of approximately 1.7J. This was only 3% higher than the threshold energy under similar static loading conditions which seems to support the use of static testing to simulate impact tests in determining this property. However, the maximum central displacement under impact loading equating to an incident energy of 1.7J was approximately 1.9mm (Figure 5.3), whereas under static loading initial failure occurred at a central displacement of approximately 2.3mm, a discrepancy of 17%. Therefore, although the static/dynamic analogy seemed to hold for threshold energy, the measured response of the plate under the two loading conditions was appreciably different.

Not surprisingly for this case in which the gauges were placed along the 0° fibre direction on the top and bottom surfaces at the same axial position, the strain/time traces were virtually a mirror image of each other. The maximum magnitude strains in this case were -1450$\mu\epsilon$ on the impact face and 2450$\mu\epsilon$ on the back face. The higher tensile stress could suggest the presence of an in-plane tensile stress superimposed on the plate bending strains, possibly caused by the clamped boundary conditions. However, in view of the fact that the gauges were placed adjacent to the predicted contact zone, this effect could have been due in part to localised tensile strains at the edges of the contact indentation.

It should be noted that the results gained from this part of the study should be treated with some caution. In many cases, especially at the higher incident energies, the use of this type of strain gauge so close to the impact zone proved to be inappropriate. Extensive back face damage served to disbond the gauges in many cases and therefore reduced the number of valid results. Also, at energies above 5.89J, there was a tendency for the damaged material splitting out from the back face to contact the fixed plate of the displacement transducer, thus shorting out the capacitor and rendering the displacement/time traces invalid. The operation and accuracy of the transducer depended critically on the separation of the capacitor plates and although some small alterations could be made, a compromise had to be reached whereby some of the results at the higher impact energies had to be discarded as being illegible. Therefore, although the capacitance transducer

showed some promise, it would require considerable study to enable this method of displacement measurement to be reliable and accurate.

5.3 Failure Modes under Low Velocity Impact Loading

5.3.1 Front Face Damage

Damage on the impact face of the laminates was visible to the naked eye, from an incident impact energy of 1.96J, as either a circular area of material, light brown in colour compared with the dark brown, almost black appearance of the sheet as a whole or as an indentation in the surface, circular in plan view. The lightened area showed up under the microscope as superficial surface damage comprising resin cracking and flaking away of the surface resin from the body of the specimen. For impact energies of 4.91J and above the indentation was clearly visible to the naked eye and, from 6.87J upwards a well defined rim was evident around the indentation. Microscopic examination of the indentation revealed small amounts of cracking on the surface from 3.93J following 0° and 90°, the fibre directions in this face. From 6.87J upwards the view of the damage site was confused by surface cracking and missing surface resin in a circular area around the point of impact.

The radius and indentation depth of the front face damage region are presented in Tables 5.3 and 5.4. The data for front face damage radius (Table 5.3) suggests that it was possible to detect damage at incident impact energies as low as 1.96J although reasonably confident observations were only made in the region 3.93J - 4.91J and above. For the 4.91J impact 71% of the impacts were detectable and for 5.89J and above very nearly 100% detection was achieved, the notable exception being an isolated impact at 6.87J. Residual indentation depth measurement (Table 5.4) achieved 100% success from 3.93J reflecting the greater accuracy of the experimental techniques involved, although the threshold for initial detection was higher at 2.94J.

It must be noted that an important feature of the data for front face damage

radius was the high variability as shown in Figure 5.4. The nature of the impact tests meant that it was unusual to impact more than one specimen per laminate at any given energy. Where multiple tests were conducted it can be seen that the variability in damage radius within a single laminate was comparatively low. In that the method of impacting the sheets and measuring the damage remained constant throughout the programme, the results suggest that the severity of this type of damage is very sensitive to changes in the properties of the laminates (it may be that the damage produced on the front face is an indication of laminate hardness and can therefore be used as a simple mechanical method for assessing cure).

In addition to this the measurement of damage radius depended on accurately pin-pointing the edges of the observable damage. This was extremely difficult, even when the observations were aided by the use of a microscope, especially at low incident impact energies where the damage region could be very difficult to pick up accurately. Even at higher energies where the rim of the indentation was sharper, accurately determining the radius of the damaged region was difficult if the illumination of the subject was not optimised.

In comparison, the data for residual indentation (Figure 5.5) was more consistent. The slope of the indentation/energy curve increases gently with impact energy reflecting greater levels of induced damage. At an incident energy of approximately 7J the curve seems to jump suddenly to a higher level of indentation, this region being also marked by a higher than normal variability. This seems to suggest that an important change in damage mode had taken place. Although this was not visible on the surfaces of the laminate, microscopic examination of the sectioned impact zones showed this change clearly. A more detailed discussion is given in Section 5.3.3.2.

The observation of front face damage proved to be an extremely unreliable method of assessing the presence and severity of BVID. Even on a laboratory scale it was extremely difficult to observe the damage and the variability of measurements means that it would be no easy task to relate experimental observations of front face damage to impact energy and therefore to assess possible reductions

in post-impact performance.

5.3.2 Back Face Damage

Visible damage on the back face of the specimens tended to follow the 0° and 90° fibre directions as shown in Figure 5.6, although some off-axis cracking was observed in the surface resin at lower impact energies. The threshold energy level for the initiation of visible damage on this face was 1.96J, only about 33% of the impacts at this level producing noticeable failures. All impacts above this level produced damage which was quite readily visible. Impacts of 2.94J - 4.91J produced an area of material which was raised above the general surface level of the laminate. This observation illustrates fibre distortion and, in view of the inability of CFRP to sustain plastic deformation, fibre failure is implied if not directly observed. For impacts of 5.89J and above areas of surface material were split-out from the surface so that fibre failure could be observed in both 0° and 90° directions.

The dimensions of the damaged regions are given in Tables 5.5 and 5.6 and plotted against impact energy in Figures 5.7 and 5.8. In an attempt to ascertain whether the weave style of the fibres had influenced the back face damage the 0° and 90° dimensions are plotted against each other in Figure 5.9, each point on the curve representing a single specimen. The slope of the curves, representing $\frac{l_c^{90}}{l_c^0}$ ranged from 0.71 to 1.29. However, the latter figure was obtained from limited experimental data and the mean gradient, taking the laminates as a whole, was 0.99 indicating that overall the split lengths were similar in both directions, despite the fact that the unwoven fibre length was four times greater in the 0° direction on this face. The fibre directions therefore seem to have influenced the directions of the back face splits but the weave style of the fibres appears to have had little or no effect on the split length on the back face.

Again a major feature of the data for back face damage is the extremely high variability which means that, although damage dimension increases approximately linearly with impact energy, study of damage on this face is of limited value as an

accurate indication of the severity of BVID and thus its effect on the performance of the material. In common with the data for front face damage radius the variability seems to arise from changes in properties of the laminate. Some explanation can be gained from a close study of the results for front face damage (Figure 5.4) and back face damage (Figures 5.7 and 5.8). For a given impact energy, the minimum front face damage radius is found for laminates LE6170/A1/1 and LE6170/A1/2 and the *maximum* damage dimension on the back face in both 0° and 90° is found for these same two laminates. This seems to suggest that the variability in front and back face damage dimension between laminates could be due to changes in laminate flexural stiffness. In Chapter 2 it was stated that under low velocity impact conditions failure was largely caused by tensile flexural stresses towards the back face and contact stresses towards the impact face. This suggests that the two laminates under consideration were the most compliant of those tested, back face failure being enhanced and front face failure being suppressed. For the stiffer laminates the reverse was true. In view of the variability in the results it is perhaps fortunate that it would be unlikely that back face damage would be used in service as an indication of the state of the material after impact as in most cases the back face of the impacted CFRP would be hidden from view within the structure.

5.3.3 Internal Damage

5.3.3.1 C-Scan and X-Ray

Outlines of typical C-scan traces and representative X-rays are shown in Figures 5.10 and 5.11. The two methods gave similar results, the edges of the projected damage roughly following ±45° directions. However, whereas the C-scan tended to just show the general area of damage, the PEXR technique proved capable of distinguishing fine detail within the damage area.

For the X-rays the dark shaded areas on the prints show general penetration of the zinc iodide solution over a large area. These areas could therefore be interpreted as illustrating the presence of delamination although through thickness

position of the damage was not clear, this method in common with C-scan providing a two-dimensional projected image of a three-dimensional damage region. Individual matrix cracks were identified from the X-rays in 0°, 90° and ±45° directions from an impact energy of 1.96J upwards. The most well defined cracks followed the 0° and 90° directions and corresponded closely to the crack patterns observed on the back face of the specimens, penetration of X-ray opaque fluid being better on the surfaces. Internal damage was less distinct but still readily visible within the damage area at lower impact energies. For impacts above 4.91J the intensity of the image of the main damage area masked the fine detail of matrix cracking except for at the edges of the delamination where a regular network of 0°, 90° and ±45° matrix cracks was visible.

The data relating X-ray and C-scan area to incident impact energy is presented in Tables 5.7 and 5.8 and indicates a threshold energy for detectable damage for both methods of approximately 1.96J, only 33% of C-scan and 50% of the X-ray traces showing damage at this level. Damage was detected for all impacts above this level. Both C-scan area and X-ray area increased linearly with incident impact energy over the range of energies under investigation as shown in Figures 5.12 and 5.13. It is interesting to note Figure 5.14 which represents a batch of specimens which were C-scanned *and* X-rayed before further testing thus enabling a direct comparison of the two NDT methods to be made. Although the thresholds for initially observing damage were very similar the X-ray always produced a smaller trace than the C-scan. It is unclear why this should be so as both methods should yield a 1:1 ratio of real damage size to trace size. However this phenomenon has been observed by Cantwell and Morton [22] who suggested that it was possibly due to either incomplete penetration of the X-ray enhancing fluid or to diffraction of the X-rays.

The variability of the results for X-ray and C-scan results was considerably less than those for front face or back face damage. This is despite the fact that in most cases the specimens were examined for external as well as internal damage so that the difference in reliability of the damage detection methods cannot be attributed to a different batch of specimens. It must therefore be concluded that

non-destructive examination of internal damage was a more reliable indication of the state of impacted CFRP than visual inspection of either surface even when the surface damage was enhanced by favourable lighting conditions and the use of optical microscopes. For a relatively complex eight-ply quasi-isotropic woven laminate it proved impossible to use X-rays of this type to provide information on the positions of the observed damage through the thickness. The intensity of the image may provide some clues as would the orientation of the observed crack patterns but these would only be of limited value and, especially in the former case, would be extremely unreliable. Stereo X-ray pairs would have to be used in order to ascertain the through-thickness distribution of impact damage.

5.3.3.2 Sectioning/Microscopy

Sectioning impacted specimens and examining the polished cross-sections was used to illustrate the types and positions of internal damage through the laminate thickness. The specimens were sectioned across a plane perpendicular to the 0° fibre direction so that it was possible to observe fibre failure in the 90° direction, matrix cracking in 0°, ±45° and 90° directions and delamination at all interfaces. An important feature of the damage site, resulting from the woven nature of the material, was that delamination was observed not only at the interfaces between plies, but also within individual plies between the warp and weft fibre tows.

At incident impact energies of 0.98J and 1.96J no damage was visible as illustrated by Figure 5.15 for a 0.98J impact. However, at 2.94J damage already seemed to be fairly evenly distributed throughout the thickness, there being a slight suggestion of a greater density of matrix cracks and delaminations below the mid-plane of the specimens. In the upper plies the main form of damage was small delaminations which seemed to be isolated, not obviously connected by matrix cracking which was rare in the region (Figure 5.16). Below the mid-plane the delaminations tended to be more severe and were connected by matrix cracks running across the plies (Figure 5.17). Features of the delaminations which were of particular interest were that, although they occurred between plies they tended to be more prevalent within the plies at the warp/weft interfaces. It also appeared

that the weave played a significant role in the propagation of impact induced damage, some delaminations at ply interfaces being deflected by the cross-overs into adjacent plies as warp/weft delaminations (Figure 5.18). Importantly, in terms of residual strength, fibre failure was observed in the lowest ply (the back face ply) so for this material it would seem that the production of matrix failure and fibre failure were almost coincident.

As the impact energy was increased both the extent and density of the damage increased. Also, the distribution of the damage tended to be less uniform, greater amounts of damage being observed towards the back face of the specimens. For the 3.93J impact delamination was observed at the majority of interfaces, the exceptions being those between the top surface ply (the impact face ply) and the $\pm 45^{\circ}$ ply below it and between the two central $0^{\circ}/90^{\circ}$ plies. The greatest density of matrix cracks was observed in the $\pm 45^{\circ}$ material behind a region of fibre failure in the back face ply, this area being directly below the centre of the impact. The distribution of damage up to 3.93J suggests that tensile bending stresses towards the back face of the specimens are dominant in producing the impact damage.

Important changes in the damage zone could be observered for the 4.91J impact. At this energy delamination was observed at *every* interface. However the damage zone was dominated by a large delamination at the lowest interface. This delamination had, in places been deflected at tow cross-overs to produce delaminations in the adjacent $\pm 45^{\circ}$ plies (Figure 5.19), or by matrix cracks (Figure 5.20) which propagated the damage through the thickness. Fibre failure was observed in the back face ply, again associated with a dense region of matrix cracks in the $\pm 45^{\circ}$ material just behind it, and in the two central $0^{\circ}/90^{\circ}$ plies (Figure 5.21) Also at the 4.91J level it was becoming clear that contact stresses were becoming important to the overall damage pattern. A compressive buckling 'kink zone' was observed in the impact face ply, slightly removed from the centre of the impact site (Figure 5.22)

For impact energies greater than 4.91J delaminations could be observed at every interface but by far the largest delamination existed at the lowest interface. The severity and density of the damage was greatest towards the back face of

the specimen and the influence of tow cross-overs and matrix cracks in deflecting delaminations into adjacent plies was easily visible. For a 5.89J impact fibre failure was evident in the back face ply and the two central plies below the centre of the impact. In the impact face ply two fibre failure zones had also occurred, but in a region slightly removed from the impact centre. This ply also exhibited the kink zone first seen for a 4.91J impact. Important features at the 6.87J impact level were large delaminations in the $\pm 45^{\circ}$ plies above and below the mid-plane of the specimen and between the $\pm 45^{\circ}$ and central $0^{\circ}/90^{\circ}$ plies. The occurrence of fibre failure was similar to that in the 5.89J specimen except that no kink zones were observed, these being replaced by two regions of fibre failure removed from the centre of impact (Figure 5.23). The occurrence of front face fibre failure could lead to localised loss of stiffness around the contact zone and could therefore account for the sudden increase in residual indentation depth noted at approximately 7J (Figure 5.5).

The impact at 7.85J was similar to the 6.87J and 5.89J impacts but the impact at 8.83J showed a significant change. In places, below the impact centre, the damage was so severe that in places in the lower $\pm 45^{\circ}$ material, the back face $0^{\circ}/90^{\circ}$ and the lower of the two central $0^{\circ}/90^{\circ}$ plies, material had effectively separated from the body of the specimen and had been deflected vertically downwards from the undamaged position (Figure 5.24). This level of damage suggests that an impact of approximately 9J marks the onset of penetration of the laminate by the impactor.

Chapter 6

Experimental Results and Observations. Post-Impact Static Loading

6.1 Introduction

The results obtained and observations made during the experimental programme for post-impact static loading are presented in this chapter. As for Chapter 5, where more than one specimen was tested under a given set of conditions, only representative results are presented to illustrate typical behaviour.

6.2 Tensile Loading of Undamaged Specimens

6.2.1 Mechanical Properties

The static tensile results for undamaged material are presented in Table 6.1. The values for mean failure stress and axial strain were 421.9MPa and 8582$\mu\epsilon$. The value of modulus, 47.7GPa was the secant modulus at 0.25% axial strain and the

value of Poisson's Ratio, 0.31 was calculated from:-

$$\nu_{xy} = -\frac{\epsilon_y}{\epsilon_x} \quad \text{at} \quad \epsilon_x = 0.25\%$$

6.2.2 Stress/Strain Behaviour

The material exhibited linear stress/strain behaviour up to final failure as shown in Figure 6.1. It had previously been noted [6] that for a similar material with only a slightly different lay-up of $[\pm 45°, 0°/90°, \pm 45°, 0°/90°]_S$ a clearly defined 'knee-point' indicating a reduction in stiffness appeared in the curve at around 5500 - 6500$\mu\epsilon$. This is generally taken to be an illustration of first-ply failure of the material. For the present material no such indication was evident. However the first audible indication of failure, loud cracking noises, occured at approximately 70 - 80% of the tensile strength which translates to 6000 - 6900$\mu\epsilon$. Isolated cracking noises were also noted at considerably lower stress levels, just after the start of the test, but these were unlikely to be indications of failure in the CFRP and probably originated from the GRP end-tabs or the glue-line between the specimen and tabs as the specimen 'settled in'.

6.2.3 Examination of Failed Specimens

A typical failure of an undamaged tensile specimen is shown in Figure 6.2. The primary failure plane was perpendicular to the line of action of the applied stress as would be expected for a quasi-isotropic material under uniaxial loading. All damage was confined to a small region around the separation, this being confirmed by the use of PEXR on the failed specimens (Figure 6.3). Close visual examination of the failure site revealed splitting parallel to the fibre direction in the 0°, 90° and ±45° plies and a small amount of fibre pull-out in the 0° and ±45° plies, but the overall picture was of a plane fracture surface.

The majority of the specimens failed across a plane away from the end-tabs as required by CRAG, only a small number failing adjacent to the tabs. However, as the results from these specimens were not significantly different to those of 'legitimate' specimens, the results were regarded as valid.

6.3 Tensile Loading of Impacted Specimens

6.3.1 The Impact Energy/Residual Strength Relationship

The relationship between incident impact energy and residual tensile strength is presented in Table 6.2 and Figure 6.4. Between 0J (undamaged) and 1.96J the mean residual tensile strength fell to about 95% of the undamaged value i.e from 421.9MPa to 402.9MPa. However all of the specimens tested at 0.98J and 1.96J had strengths which fell within the scatter band for undamaged material. Impacts of less than 1.96J therefore seem to have had little or no effect on the residual tensile strength of this material.

Examination of Figure 6.4 suggests that the threshold impact energy for significant tensile strength reduction lay in the range 2 - 2.5J, specimens impacted at 2.94J, the lowest energy after this range, showing a mean tensile strength of 344.9MPa, 82% of the undamaged value. The scatter at this level was considerably larger than for either higher or lower energies which illustrates the fact that this impact level was on the steepest part of the residual strength characteristic and close to the threshold energy, small variations in the impact event leading to large variations in residual strength. This impact level was seen to have caused the first observable occurrence of fibre failure in the laminate (Section 5.3.3.2), fibre failure being largely responsible for reductions in residual tensile strength. Between 2.94J and 3.93J a rapid reduction in strength took place from 82% to 65% of the undamaged value. Thereafter the rate of strength degredation was reduced so that over the range 3.93J - 8.83J the strength only fell a further 10% to 55% of the undamaged value. At the higher impact energies there was a slight recovery of strength from a mean value of 222.2MPa at 7.85J to 232.1MPa at 8.83J. The minimum strength of impacted CFRP would occur at low penetration energies and would be below that of the 12.7mm drilled hole as discussed in Section 2.4.1. It was apparent both from the study of the impact damage and from Figure 6.4 that the impact energy resulting in the minimum strength was higher than those

considered in this study. Hence there was no obvious explanation for the observed recovery of tensile strength and this effect was probably due to variability in the material.

6.3.2 Stress/Strain Behaviour

The axial stress/strain behaviour adjacent to the impact damage site on the back face of specimens impacted at 1.96J and 3.93J are shown in Figure 6.5. The behaviour was linear up to final failure but the strains were typically 5% higher and 18% higher than remote axial strains for the 1.96J and 3.93J specimens respectively. The curves for 4.91J (Figure 6.6) show that axial strain was higher on the back face than the impact face for all applied stress levels. Over the linear part of the curves strains on the impact face were approximately 5% lower than remote values and 22% higher than remote values on the back face, these results apparently reflecting the fact that impact damage was largely grouped towards the back face of the specimens. A knee-point occurred in the back face strain curve only at a remote stress of approximately 230MPa, 86% of the eventual failure stress. This may have been an indication that the impact damage was beginning to propagate under the applied stress or that the impact induced delaminations had produced a non-symmetric laminate around the impact site and that localised bending was taking place, although neither of these was observed experimentally. The curves for 5.89J (Figure 6.7) were similar to those for a 4.91J specimen and strain adjacent to the damage site on the back face over the linear part of the characteristic was approximately 32% higher than remote values. The axial strains on the impact face adjacent to the damage were similar to remote strains up to approximately 46% of the specimen strength and thereafter started to increase above remote values. A sharp knee-point occurred in the two near-damage curves at approximately 86% of the failure stress, this effect being more pronounced on the impact face. A significant difference, in terms of tensile loading, between the damage zone at 5.89J and the ones for lower energies was zones of fibre failure in the impact face (Section 5.3.3.2) which would explain the detection of damage on this face, hith-

erto unobserved. This damage would seem to have started to propagate at an applied stress approximately 86% of the eventual failure stress. The stress/strain behaviour adjacent to the damage on the back face for 7.85J and 8.83J specimens is shown in Figures 6.8. For these two impact energies the strains were approximately 19% higher than remote values over the linear part of the characteristics and knee-points indicating that damage propagation occurred at 87% and 75% of the specimen strength respectively. In view of previous results the fact that near damage strains on the back face were only 19% higher than remote values for the two highest impact energies was unusual. The only obvious difference between these tests and previous tests on lower impact energies was that linear strain gauges were used for the tests on lower energies and three element rosettes were used in the latter two. It was therefore impossible to place the two types of gauge at exactly the same position which would seem to have been vital to the production of consistent results.

6.3.3 Examination of Failed Specimens

The tensile fracture surface for impacted specimens was similar to that for non-impacted specimens for impact energies up to 4.91J there being no special features associated with the presence of impact damage. Two of the three specimens impacted at 0.98J failed across a region closely associated with the impact, one failing closer to the end-tabs and away from the damage site. These results indicated that, despite evidence of the impact at this level having been 'invisible' (see Section 5.3), it may have produced sufficient damage to provide a stress concentration which precipitated fracture of the specimen. However, the strengths of all three 0.98J specimens lay within the scatter band for undamaged material and were moreover not significantly different from each other. Therefore a 0.98J impact could have influenced the failure of the material if not the tensile strength.

Again at 1.96J two of the three tensile specimens failed across the impact site. Interestingly, the remote failure was of the only specimen in which impact damage was not detected by any of the methods described in Section 4.3.2. The

other two specimens showed damage detectable visually on the back face and internally by PEXR. This result suggested that for damage at the 1.96J level to have influenced the failure it should have been detectable. However, as in the case of 0.98J specimens there seemed to be little difference between the strengths of specimens with detectable and non-detectable damage and the strengths of both groups again lay within the scatter band for undamaged material. Again this level of impact damage provided sufficient damage to influence the failure but not necessarily the tensile strength. For impacts of 2.94J and above the tensile failures were invariably across the impact site.

Typical fractures for tensile specimens impacted at 4.91J, 6.87J and 8.83J are shown in Figures 6.9 - 6.11 and were typical of the failures at higher impact energies. The fracture surfaces showed a region of fibre and tow pull-out at the impact site, towards the back face of the specimen reflecting both the presence and through-thickness position of the impact induced delaminations. The fractures of 6.87J specimens and above showed greater levels of fibre and tow pull-out over the full width of the specimen illustrating the higher levels of impact damage prior to tensile loading. As in the case of tensile loading of undamaged specimens the damage caused by the tensile loading and subsequent fracture was confined to a small region around the final separation. PEXR showed that impact damage was easily distinguishable from the tensile damage and that the only effect of the loading on the impact damage was a slight growth in the transverse direction before final failure (Figure 6.12).

6.4 Compressive Loading of Undamaged Specimens

6.4.1 Mechanical Properties and Stress/Strain Behaviour

The static compression results for undamaged material are given in Table 6.3. Although the mean values for compressive strength and 0.25% secant modulus, at

416.3MPa and 46.9GPa were 98 - 99% of the tensile values, the mean strain to failure was approximately 58% higher for the compressive specimens due to the non-linear stress/strain behaviour which is illustrated for a typical specimen in Figure 6.13. The curve showed gently decreasing slope up to an applied stress of between 70% and 85% of the compressive strength. Thereafter there was a large drop in indicated specimen stiffness to approximately 22GPa, just less than half of the initial stiffness. This 'knee-point' could indicate first failure of the specimen but unlike the tensile tests no audible failure of the specimen was present to confirm the observed behaviour. Alternatively the apparent large drop in stiffness could be due to instability of the specimen (i.e buckling) just before final failure. As the anti-buckling guides appeared to be efficiently restraining the specimens up to final failure it must be concluded that either the knee-point was a legitimate indication of initial compressive failure or that localised buckling was taking place which could not be prevented using this design of anti-buckling guide.

6.4.2 Examination of Failed Specimens

A typical failure of an undamaged compression specimen is shown in Figure 6.14. Although it is difficult to identify individual failure modes in a compression failure as inevitably the two parts of the failure surface are driven together when final failure occurs, some buckling of the surface plies was evident around the fracture and an examination of the edges showed overlapping wedges of material, typical of compressive shear failure [7]. PEXR of failed specimens showed that damage was confined to a small region around the final separation, although in some cases small isolated regions of damage appeared to have been initiated away from the fracture surface. These did not seem to have propagated beyond the edges of the anti-buckling guides (Figure 6.15). Perhaps more significantly in one case a damage region was detected in a region between the anti-buckling guides and the end-tabs. This damage had not propagated to failure and fracture had occurred in a region supported by the guides.

A number of specimens failed in the clearance gap between the end-tabs and

anti-buckling guides. The results from these tests were discarded as the compressive strength of these specimens was sometimes considerably lower than the strength of specimens which failed in the centre section, supported by the guides. These results served to highlight the fact that perhaps this design of anti-buckling guides may not have been entirely suitable for the testing of specimens which contain no obvious stress concentration. The guides themselves may have been a source of stress concentration and may have led to premature failure of the specimens.

The compressive strength of specimen LE5932/A1/5/5 seemed unduly low at 302.2MPa but, as this specimen failed in the central supported section, it was regarded as a valid result.

6.5 Compressive Loading of Impacted Specimens

6.5.1 The Impact Energy/Residual Strength Relationship

The relationship between incident impact energy and residual compressive strength (Table 6.4 and Figure 6.16) was similar to that between impact energy and residual tensile strength in that there was an initial region in which residual strength was largely unaffected by impact energy. This was followed by a rapid drop in strength and, at the higher energies, a slower rate of decrease with increasing impact energy.

Between 0J and 1.96J the mean strength increased from 416.3MPa to 443.6 MPa, a rise of 6.6% but the strength values for all tests conducted on 0.98J and 1.96J specimens fell within the scatter band for undamaged material so that this was unlikely to be a significant result. Between 1.96J and 2.94J the strength dropped rapidly to 78% of the undamaged value and comparison of this trend with the residual tensile strength results suggests that the threshold impact level for significant strength reductions was slightly lower in the case of compressive loading. This result was not surprising as compressive strength would be influenced

by matrix failure which was observed at 1.96J (Section 5.3), a lower impact energy than that observed to cause initial fibre failure, the dominant factor in tensile strength reduction. After the initial rapid reduction the compressive strength reduced less rapidly from 78% to 53% over the range 2.94J - 8.83J. Over the 9J range of impacts selected for the present study the strength reduction under post-impact tensile and compressive loading was, therefore approximately the same at 55% and 53% respectively. However under compressive loading due to the higher strength of the 12.7mm hole specimens the strength of the impacted specimens fell below that of a hole specimen between 7.85J and 8.83J.

6.5.2 Stress/Strain Behaviour

The axial stress/strain behaviour for a specimen impacted at 2.94J is shown in Figure 6.17. The behaviour was essentially linear up to 55% of the strength with remote and back face near-damage strains being similar and the impact face near-damage being slightly lower. At 55% of the strength the back face near-damage strain showed a knee-point with reduction in slope of the curve. This would usually taken as representing the propagation of the impact damage leading to final failure but the other two curves for remote strains and for near-damage strain on the impact face indicated a 'reversed knee-point' with an increase in slope. This behaviour suggested buckling of the specimen as a whole but was confusing as the remote gauge was on the same face as the back face gauge adjacent to the damage. The buckled shape of the specimen may have been such as to cause higher than expected strains at one position on the back face and lower than expected strains at another location (i.e the specimen took up an '*S*' rather than a '*C*' shape). Similar behaviour existed for the 3.93J specimen (Figure 6.18), with a knee-point at 62% of strength, but the reversed knee-point was less well defined in this case, possibly due to the lower loading involved for the specimens impacted at higher energies. Figure 6.19 shows the stress/strain behaviour adjacent to the damage on the back face for a 4.91J impact with strains being typically 8% lower than remote strains over the initial part of the characteristic and a knee-point at 76%

of strength. For a 5.89J specimen (Figure 6.20) remote and near-damage strains on the impact face were similar, showing approximately linear behaviour up to failure. The near-damage strains on the back face were approximately 17% higher than remote strains over the initial portion of the curve and showed a knee-point at approximately 72% of the strength. These trends suggested that the buckling behaviour observed for the lower impact energies was eliminated and that the knee-point in the near-damage strains on the back face was a legitimate indication of damage progression around the impact site. For 6.87J the remote stress/strain behaviour was linear to failure (Figure 6.21) but the two adjacent gauges showed similar behaviour, indicating a knee-point behaviour at approximately 54% on the impact face and 64% on the back face. The strain on the back face was higher at failure. For a 8.83J specimen (Figure 6.22) strains on the back face adjacent to the damage over the initial part of the characteristic were typically 20% higher than remote strains and the knee-point occurred at 55% of the compressive strength.

It was noted by sectioning/microscopy (Section 5.3.3.2) that a major feature of the impact damage at 6.87J was the presence of large delaminations both towards the impact face and back face which may explain the similar strain behaviour on both faces and the possibility of picking up damage propagation on both faces of the specimens. For specimens impacted at lower energies the stress/strain behaviour reflected the fact that the impact induced damage tended to be more extensive towards the back face.

Comparing these results with those for tensile loading it would seem that, although the strain response adjacent to the impact site showed a pronounced knee-point and damage could be detected on both faces at the higher impact energies, the strain gauges were not as efficient under compressive loading at indicating the presence of damage. The difference between remote strain values and those adjacent to the damage was generally less and in one case the near damage strain on the back face was lower than remote values over the initial part of the characteristic. In a further three cases the near-damage strain on the impact face was consistently lower than remote values. These results were unusual as it would be expected that the impact damage (predominantly delamination) would be more

severe under compressive loading, causing high compressive strains. However, it may be that localised buckling may have been causing the superposition of tensile bending strains on the axial compressive strains, in effect lowering the compressive strain adjacent to the damage.

It also seemed likely that the specimens were being influenced by the anti-buckling guides, those impacted at energies below approximately 4J not being restrained adequately against buckling. It is difficult to quantify the effects of the anti-buckling guides without the aid of a parametric study of different designs. Furthermore, in the case of impacted material, it would of course be impossible to use short gauge length specimens which would be unaffected by buckling. Evidence has been given (Section 6.4.2) that the guides could act to restrict the spread of delamination. However it is difficult to envisage a design of anti-buckling guide which, whilst efficiently restraining the specimen against out-of-plane buckling displacements, could permit the free development of delamination damage which, in the case of impacted materials, is often accompanied by out-of-plane deformation of the plies bounding the delamination. Despite the obvious disadvantages of this type of anti-buckling guide outlined above, the residual compressive strength characteristic (Figure 6.16) showed that the specimens which seemed to be measureably influenced by the guides did not exhibit unusual residual strength behaviour.

6.5.3 Examination of Failed Specimens

The fracture surface of impacted specimens was similar to that for non-impacted specimens for impact energies up to 4.91J, as in the case of tensile testing. All of the specimens impacted at 0.98J failed across the impact site and only one of the 1.96J specimens failed in the gap between the end-tabs and anti-buckling supports. However all of the specimens tested at these levels had compressive strengths which lay within the scatter band for undamaged material. These results seemed to confirm those found for tensile loading in that at low impact energies (below the threshold value), even though damage was undetectable, it may have provided sufficient of a stress concentration to influence the failure if not the strength of

the material. For impacts of 2.94J and above all failures were across the impact site. Fractures for 4.91J and above were similar to those of lower energies when viewed from the impact face and the sides. However the back face showed a well defined area of localised buckling at the impact site as illustrated in Figure 6.23, which shows the compressive failure on the back face of an 8.83J specimen. This reflected the presence of the major impact induced delamination which was towards the back face of the specimens. PEXR of the failed specimens showed that compressive damage was confined to a small region around the final separation (Figure 6.24). There was no evidence of failure at any sites remote from the final fracture surface and the confusion of the failure meant that PEXR failed to show any special features of the fractures associated with the impacts.

Chapter 7

Experimental Results and Observations. Post-Impact Fatigue Loading and Residual Static Strength Testing

7.1 Introduction

The results obtained and observations made during the experimental programme for both post-impact fatigue testing and residual strength testing of run-out specimens is presented in this chapter. Where more than one specimen was tested under any given set of conditions, only representative results are presented.

7.2 Post-Impact Fatigue Loading

7.2.1 Zero-Tension Fatigue Loading of Undamaged Specimens

7.2.1.1 S-N data

The fatigue S-N data for undamaged material is given in Table 7.1 and Figure 7.1 illustrates the baseline S-N curve for the material. Variability was assessed by repeat tests at 348.1MPa ($7300\mu\epsilon$) and 274.2MPa ($5700\mu\epsilon$), values which represented 82.5% and 65% of the undamaged tensile strength. No tests were conducted above a peak stess value of 348.1MPa as this made the tests too short to be regarded as valid (the peak stress could not be attained with any accuracy before failure of the specimen occurred). It can be seen from Figure 7.1 that the variability of the fatigue data was high (N_f ranged from 1.4×10^5 to 1×10^6 cycles for an applied load σ_{max} of 274.2MPa), this being regarded as a normal aspect of fatigue testing for both metals and composites. However, previously reported work on this material [3] found appreciably lower variablity under zero-tension, zero-compression and fully-reversed loading. This was thought to represent the high quality of the laminates and the fact that specimens were taken from only one or two sheets of material. The variability of the fatigue results in the present study was probably due to the fact that specimens were taken from nine different sheets of material in order that the baseline data should be fully representative of all the material tested under fatigue loading. In view of this variability it is usually suggested [106] that only a straight line representation of the data is justified and a linear regression analysis was performed on the data.

7.2.1.2 Development of Damage

The development and spread of damage as followed by PEXR began early in the specimen life with isolated transverse cracking throughout the gauge length. The density of these cracks, especially at the specimen edges, increased with fatigue cycles and the weave style in the $0°/90°$ plies became easily visible which suggested

that the X-ray fluid was being absorbed at specific damage sites on the surfaces and that the development of fatigue damage in this material was influenced by the cross-overs in the weave. Towards the end of the fatigue life the intensity of the X-ray image at the edges of the specimens suggested the presence of large quantities of penetrant and hence of edge delamination. Visual examination of the edges showed that, at this stage the delamination was readily visible to the naked eye and had mostly developed between $0°/90°$ and $\pm 45°$ plies, the interfaces where the largest interlaminar stresses would be produced. Also at this stage matrix cracking was detected by PEXR in the body of the specimen especially in the $\pm 45°$ directions and, to a more limited extent in the $0°$ direction. It was not clear when damage in the $\pm 45°$ material developed as it may be that penetrant could only reach these sub-surface plies late in the life when surface damage and edge damage had become comparatively severe. The X-ray for a typical fatigued specimen in which edge delamination, matrix cracking and highlighting of the weave are illustrated is presented in Figure 7.2.

7.2.1.3 Examination of Failed Specimens

The failure of a high stress/low cycle fatigue specimen (Figure 7.3) was very similar to that of a static tensile specimen (Figure 6.2), being basically a plane failure with small amounts of fibre and tow pull-out at the fracture surface. However a low stress/high cycle failure (Figure 7.4) showed very much more damage over the whole of the specimen, damage not being confined to the region around the final separation. This was confirmed by PEXR on the failed specimen although the extent of the damage was clearly visible to the naked eye. The levels of delamination, splitting between fibres and pull-out were higher and the bonding between individual fibre tows had been degraded around the fracture surface. The largest areas of delamination had occurred at the interfaces between $0°/90°$ and $\pm 45°$ plies. The level of damage under low stress fatigue reflected the accumulation of damage before final failure.

7.2.2 Zero-Tension Fatigue Loading of Impacted Specimens

7.2.2.1 S-N Data

Fatigue S-N data for specimens impacted at 2.94J, 6.87J and 8.83J and for specimens with a 12.7mm drilled hole is presented in Tables 7.2 - 7.5. Over the range of cycles under consideration (approximately 10^3 - 10^6) the performance of undamaged material was superior to that of damaged specimens as shown in Figure 7.5.

At the high stress/low cycle end of the S-N curves the fatigue performance of the impacted specimens reflected the tensile strength i.e the 2.94J specimens had the best performance and the 8.83J specimens had the worst. The specimens with a 12.7mm hole had a fatigue performance inferior to that of the impacted material for low numbers of cycles.

However the gradients of the curves were greatly different and led to some reversals in this behaviour. The gradient of an S-N curve in part represents the resistance of the material to fatigue loading and, for the damaged material the trend was for the slope of the fatigue curves to reduce with increasing impact energy, indicating that, as the level of impact damage in the material increased, the resistance to zero-tension fatigue loading also increased. The ultimate expression of this trend were the results for specimens containing a drilled hole, representing an 'infinite' impact energy, for which some specimens ran to the 10^6 cycles run-out at a maximum fatigue stress equal to the mean residual tensile strength of the specimens. This behaviour was not unique to this hole size/specimen size combination as previously reported work [4] on 25mm wide specimens of the same material containing 4mm diameter holes produced similarly impressive resistance. As part of the present study, in order to check how widespread this behaviour was, a limited number of static tensile and zero-tension fatigue tests were conducted on different hole sizes in 50mm wide specimens and the results are presented in Tables 7.6 and 7.7. For hole sizes of 2.5mm, 10mm and 25mm specimens cycled at a maximum stress equal to the tensile strength the specimens either ran to

10^6 cycles and were run-out or ran to between 10^5 and 10^6 cycles before failing. Only for the largest hole size of 38.5mm did the specimens fail to reach 10^5 cycles (the maximum number reached was approximately 2×10^4 cycles). The impressive fatigue performance of specimens containing holes is thought to be due to the production of stress relieving crack mechanisms at the notch tip reducing the effect of the hole as a stress concentration [107], [108]. For the largest hole size the ligaments of material between the edges of the hole and the edges of the specimen were less than 6mm wide and it seems probable that there was a direct interaction between the stress concentration and the specimen edges such that the normal stress relieving mechanisms were less effective.

The differences in resistance to zero-tension fatigue meant that if the S-N data for 8.83J specimens was extrapolated to 10^6 cycles the performance of these specimens became superior to that of 6.87J specimens after approximately 1.3×10^4 cycles and superior to that of 2.94J specimens after approximately 2.9×10^5 cycles.

The resistance of the specimens to fatigue is shown by Figure 7.6 which represents the fatigue stress normalised with respect to the static strength of the specimens. For the specimens containing stress concentrations (i.e the impacted specimens and the specimens containing holes) the ratio of zero-tension fatigue strength at n cycles to residual static tensile strength $\frac{\sigma_{at}}{\sigma_{rt}}$ increased with incident impact energy. All of the curves shown in Figure 7.6 should pass through $\frac{\sigma_{max}}{\sigma_{rt}} = 1.0$ at $\log N_f = -0.3$ (a static tensile test can be thought of as a zero-tension test with $N_f = \frac{1}{2}$) and, although there was no fatigue data between $\log N_f = -0.3$ - 3.0, examination of the curves for 2.94J and 6.87J impact specimens suggests that as impact energy was increased then the threshold number of cycles for the onset of significant strength reductions due to fatigue loading was also increased. It is difficult to assess a threshold for the 8.83J impact level due to the flatness of the S-N curve but the specimens containing the holes do not show a threshold, there being no strength reduction due to fatigue over the range of cycles under consideration. For the specimens tested, resistance to zero-tension fatigue was increased with increasing impact energy.

It is important to note that at the highest impact energy of 8.83J the specimens

were beginning to behave in a similar way to specimens containing a 12.7mm drilled hole under zero-tension fatigue loading. Although the static strength reduction due to the impact was not as great as that due to a hole of the same diameter as the impactor, the fatigue curves for the two types of specimen were both very flat indicating a similar resistance to fatigue cycles.

7.2.2.2 The Effect of Fatigue Cycles on Specimen Stiffness

The data relating localised stiffness changes to numbers of applied fatigue cycles is given in Tables 7.8 - 7.29. Typical relationships between stiffness ratio $\frac{E_{at}}{E_{rt}}$ and fatigue cycle ratio $\frac{n}{N_f}$ are shown for a 2.94J specimen in Figure 7.7 and for a 6.87J specimen in Figure 7.8. The trends for both impact levels were similar. For a 2.94J specimen the stiffness ratio fell gently to approximately 80% at a cycle ratio of 0.8. Thereafter the stiffness fell rapidly to zero over the final fifth of the specimen life. For a 6.87J specimen the stiffness drop was slightly larger at 30% over the first 80% of the specimen life. Again the stiffness fell rapidly over the final fifth of the life. These trends were similar for all failed specimens independent of the stress level at which the specimens were cycled.

2.94J specimens reaching the run-out of 10^6 cycles (i.e those cycled at approximately $\frac{\sigma_{max}}{\sigma_{rt}} \leq 0.5$) showed measureable falls in stiffness ratio at the run-out until $\frac{\sigma_{max}}{\sigma_{rt}}$ was dropped to 0.20 ($\epsilon_{max} = 1400\mu\epsilon$). For 6.87J specimens which reached the run-out (i.e those cycled at approximately $\frac{\sigma_{max}}{\sigma_{rt}} \leq 0.6$), measurable reductions in stiffness at the run-out occurred until $\frac{\sigma_{max}}{\sigma_{rt}}$ was dropped to 0.25 ($\epsilon_{max} = 1300\mu\epsilon$). This is illustrated in Table 7.30.

7.2.2.3 The Effect of Fatigue Cycles on Impact Damage

The propagation of impact damage under zero-tension fatigue loading was followed by PEXR of the specimens at intervals during the fatigue life. This technique showed that, under fatigue loading, two distinct areas of damage developed.

The presence of relatively large amounts of X-ray opaque penetrant showed up as a white area on the X-ray negative. This denoted the presence of delamination. Surrounding this area was an area showing up grey on the negative, illustrating

the more limited presence of the penetrant. A typical X-ray of a cycled specimen is shown in Figure 7.9 and these areas can be clearly seen. Some run-out specimens were sectioned across the 'grey' area both parallel and perpendicular to the loading direction, set in resin and polished as described in Section 4.3.2. Examination of these sections revealed that these grey areas comprised small through-thickness matrix cracks, mainly in the 90° and ±45° plies but also to a more limited extent in the 0° plies as shown in Figures 7.10 and 7.11. Typically, these cracks did not penetrate beyond the ply boundaries and closer examination of the X-rays did not show any noticeable characteristic of crack length or density. It was interesting to observe that in some cases these micro-cracks tended to be more prevalent in the resin-rich areas at tow cross-overs (Figure 7.10). Although it was by no means true in all the specimens examined that the greater density of micro-cracks had been produced in these areas compared to the plies as a whole it may serve to explain the apparent highlighting of the weave in the 0°/90° plies observed for undamaged specimens under fatigue loading (Figure 7.2).

Data relating micro-damage growth area to number of applied fatigue cycles is given in Tables 7.8 - 7.29. It proved to be extremely difficult to assess quantitavely the growth of micro-damage with fatigue cycles due to the rapid growth rate of this type of damage. Even at relatively low applied loads which would cause run-out of the specimens at 10^6 cycles, micro-damage had propagated to the extremities of the specimens before the specimen had been removed for the first X-ray. The edges and end-tabs of the specimens provided the barriers to free damage growth and the criterion for damage growth data to be valid was that the damage should not have reached these barriers. This, unfortunately meant that little data was available to assess the free growth of micro-damage under fatigue loading and it was impossible to ascertain the number of cycles required before this type of damage reached the edges of the specimens. However typical growth curves for both impact levels are shown in Figures 7.12 - 7.15. Figures 7.12 and 7.13 represent specimens cycled at $\frac{\sigma_{max}}{\sigma_{ut}} = 0.80$ and the initial rapid growth of micro-damage is evident until the damage reached the edges of the specimens and was constrained to grow in the longitudinal direction only. Similar behaviour existed for specimens cycled at a

lower level. Figures 7.14 and 7.15 represent specimens cycled at $\frac{\sigma_{max}}{\sigma_{rt}} = 0.45$, both specimens reaching the run-out. Figure 7.14 suggests that there was a roughly linear relationship between micro-damage area and fatigue cycles up to the point where damage reached the specimen edges. However, as this specimen was the only one tested to reveal more than one data point in this region no attempt was made to devise such a relationship.

A typical series of micro-damage growth areas is illustrated in Figure 7.16 for a 2.94J specimen and in Figure 7.17 for a 6.87J specimen. Both figures represent specimens cycled at $\frac{\sigma_{max}}{\sigma_{rt}} = 0.45$ for which the specimens were run-out. For both impact conditions (2.94J and 6.87J) the micro-damage growth was mainly in the direction transverse to the direction of the applied load, although some damage growth was evident in all directions giving rise to a general spread of damage. This growth pattern and the dimensions of the specimens meant that micro-damage first reached the edges of the specimens after which growth was confined to the direction parallel to the applied load. For all failed specimens micro-damage was observed to have grown to the full width and in most cases to the full gauge length as well before final fracture. However this type of damage does not seem to have contributed significantly (if at all) to fatigue failure as some specimens sustained 100% micro-damage and attained the run-out. Interestingly, the use of X-ray penetrant during the fatigue process proved useful in providing a qualitative assessment of the position and extent of micro-damage. The opening and closing action of the damage under cyclic loading resulted in the formation of small clusters of bubbles on the surfaces of the specimens. X-ray proved that the patterns of bubbles bore a very close relationship to the areas of micro-damage. It may well be therefore that a simple soap solution, applied to the specimen, could be used to give an approximate idea of the spread of micro-damage under fatigue loading.

Cycling the specimens at different percentages of the residual tensile strength showed that a value of $\frac{\sigma_{max}}{\sigma_{rt}} = 0.20$ was the maximum value that both the 2.94J and 6.87J specimens could sustain for 10^6 cycles with no growth of micro-damage as illustrated in Table 7.31. These values represent maximum strain levels of $1400\mu\epsilon$ for 2.94J specimens and $1000\mu\epsilon$ for 6.87J specimens. These results suggested that,

even though micro-damage may not have contributed to the failure of the specimens, the specimen stiffness, which showed measureable falls above approximately $\frac{\sigma_{max}}{\sigma_{rt}}$ =0.20 - 0.25 was affected by the presence and growth of micro-cracking. Relationships between mechanical properties and damage growth under fatigue loading are discussed in more detail in Chapter 9.

Delamination growth was more easily assessed quantitavely than micro-cracking due to its slower growth rate and the greater intensity of the X-ray image. For specimens impacted at 2.94J and 6.87J and then subjected to zero-tension fatigue the delamination area was always surrounded by an area of micro-damage as shown in Figures 7.9 and 7.18. Again the edges and end-tabs of the specimens provided the barriers to free delamination growth and were used as the criteria for delamination growth data to be valid. Delamination growth data is given in Tables 7.8 - 7.29 and 7.32 - 7.37.

Typically for a 2.94J impact specimen delamination spread fairly evenly in all directions as shown in Figure 7.19 but some X-rays showed a slight tendency for a preferred growth direction parallel to the applied load as shown by the elongated central damage region in Figure 7.20. Examination of the series of X-rays following damage under fatigue cycles showed that delamination growth was not only associated with the impact damage area. Delamination was also observed at the edges of the specimens apparently growing independently of the impact induced delamination, and it appeared that the two regions of delamination, namely those associated with the impact and the specimen edges coalesced rather than the impact delamination growing to the edges of the specimens (Figure 7.21). After the two delamination areas joined final failure of the specimens soon followed but no failures were observed before delamination was observed at the specimen edges. The appearance of delaminations at the specimen edges could therefore be usually taken as a reliable indication of imminent specimen failure.

A typical delamination growth curve for 2.94J specimens is shown in Figure 7.22. Initially the growth rate was slow but increased over the final part of the specimen life. The final rapid growth of the delamination area represented the final collapse of the specimen and was closely related to the rapid drop in specimen

stiffness at the end of the specimen life.

For a 6.87J impact specimen delamination again spread parallel and perpendicular to the applied load but the largest growth occurred in the $\pm 45°$ directions so that the original diamond shaped delaminations caused by impact (Figure 5.11) developed lobes in these directions as illustrated in Figure 7.23. Later in the specimen life areas of delamination showed up on the X-rays at the edges of the specimen along lines at $\pm 45°$ through the centre of the impact as shown in Figure 7.24. These edge delaminations were also visible to the naked eye. (This phenomenon has been observed by Sturgeon [108] for specimens containing holes and was attributed to damage propagating from the holes along the $\pm 45°$ fibre directions causing delaminations at the specimen edges). As in the case of 2.94J specimens, X-ray showed that the impact induced delamination and the edge delamination coalesced before final fracture (Figure 7.25).

A typical delamination growth curve for 6.87J specimens is shown in Figure 7.26. The general shape was similar to that for a 2.94J specimen in that the initial growth was relatively slow and increased towards failure. However the initial growth rate was higher for the higher impact energy.

For specimens which reached the run-out without failure the values for growth of delamination area over 10^6 cycles are given in Table 7.38. The data shows that it was necessary to drop the value of $\frac{\sigma_{max}}{\sigma_{rt}}$ to approximately 0.45 for both impact levels to arrest the growth of delamination. This represents applied strain levels of $3300\mu\epsilon$ for 2.94J specimens and $2300\mu\epsilon$ for 6.87J specimens.

7.2.2.4 Examination of Failed Specimens

In contrast to the fatigue failures for undamaged material for which high stress/low cycle failures were similar to static tensile failures, the fractures for impact damaged specimens were significantly different to static failures even for high stress tests.

For a high stress/low cycle failure of a 2.94J specimen (Figure 7.27) the major features of the fractures were large delaminations at the interfaces between $0°/90°$ and $\pm 45°$ material. This was visible at the edges of the specimens and is illus-

trated by the region of ±45° material which had pulled out from the specimen on separation. Significantly no delamination was evident between plies of the same orientation i.e the two ±45° ply pairs and the central 0°/90° ply pair. The 0° fibre tows had failed in a relatively plane manner perpendicular to the direction of the applied load with little splitting down between the fibres as shown in Figure 7.28. Splitting parallel to the fibres was visible in the 90° tows and the ±45° tows leading to a jagged appearance of the failed material (Figure 7.29). Pull-out of the ±45° tows was evident and the 0° tows showed a significantly greater pull-out length over the central part of the fracture surface, the area of the initial impact damage. Behind the fracture surface the bonding between the tows had been degraded and ±45° and 90° tows had been pulled apart. On the surfaces cracks were observed to follow the line of the weave so that in effect the bonding between warp tows, weft tows and between warp and weft material had been degraded.

For a low stress/high cycle failure of a 2.94J specimen (Figure 7.30) the damage existed over the full width and gauge length of the specimen. Viewed from the edges, delamination was evident at every interface and between 0°/90° and ±45° material extended over the *full* gauge length. Delamination was less severe between the ±45° ply pairs. Plies had been separated almost over the full width and gauge length. Splitting down between fibres was evident in the 90° and ±45° tows leading to a jagged fracture appearance in the ±45° material. Significantly delamination was observed at the specimen edges between the warp and weft fibres in the individual plies. As for a high stress/low cycle failure most 0° tows showed plane failure surfaces perpendicular to the line of the applied load with little splitting. However a few showed a jagged appearance with associated parallel splitting. The pull-out of 0° fibre tows existed in some cases from the fracture surface to the end tabs. Behind the fracture surface the bonding between tows had been degraded over the full gauge length and ±45° tows and 90° tows had been pulled apart.

The high stress/low cycle failure of a 6.87J specimen (Figure 7.31) can be directly compared with the 2.94J specimen as both had been cycled at $\frac{\sigma_{max}}{\sigma_{rt}}$=0.80. Despite the fact that the 6.87J specimen had survived a higher number of cy-

cles before failure than the 2.94J specimen (25291 as opposed to 8338) the level of damage exhibited by the fracture surface was noticeably lower for the 6.87J specimen. This observation echoes the greater resistance to zero-tension fatigue of the specimens impacted at the higher energy, discussed in Section 7.2.2.1 and shown by Figure 7.6. The only major area of delamination was between the $\pm 45^{\circ}$ ply pair nearest the back face and the $0^{\circ}/90^{\circ}$ plies on either side. This perhaps reflected the through thickness position of the impact induced damage and would confirm similar observations by Potter [66] and Saunders and van Blaricum [103]. Delamination was less prevalent towards the front face of the specimen. The 0° tow pull-out length was smaller than for a 2.94J specimen but all other types of damage were similar. Parallel splitting was evident mainly in the $\pm 45^{\circ}$ and 90° tows leading to a jagged fracture appearance in the tow failures. Some splitting was found in the 0° tows but the fractures of these tows was mainly relatively smooth and perpendicular to the direction of the applied load. Again degredation of bonding in the weave was evident behind the fracture surface.

The low stress/high cycle failure of a 6.87J specimen (Figure 7.32) showed less extensive damage than the equivalent failure of a 2.94J specimen. Delamination was evident over the full gauge length at every interface except those between the two $\pm 45^{\circ}$ ply pairs, where delamination appeared to be limited to a small region around the fracture surface. In the $0^{\circ}/90^{\circ}$ plies delamination appeared to have occurred between the warp and weft material. Parallel splitting was evident in all fibre directions and the failures of $\pm 45^{\circ}$ tows showed the jagged appearance discussed previously. Again the 0° tows failed in a relatively plane manner. Degredation of the bonding between warp and weft tows had again occurred over the full gauge length but in this case only seemed to be severe towards the edges of the specimen, leaving a central area almost unaffected by this type of damage.

In summary, the types of failure mode observed from the fractured fatigue specimens at both 2.94J and 6.87J impact levels were similar, comprising delamination (both between plies and within each ply), matrix splitting between fibres, fibre failure and debonding between warp and weft material. The positions of the dominant delaminations were observed to be closely related to the positions of the

original impact induced damage. Not surprisingly, the overall degree of damage was greater in specimens at both impact energies which had been subjected to low stress/high cycle fatigue, reflecting the higher levels of fatigue damage accumulation before final separation. Comparing the 2.94J and 6.87J specimens, it was noted that for equivalent fatigue conditions the overall degree of accumulated fatigue damage was lower in the specimens which had been subjected to the higher initial impact energy. This confirmed the observation made in Section 7.2.2.1 that, for the specimens tested, the resistance to zero-tension fatigue loading increased with incident impact energy (Figure 7.6).

7.3 Residual Strength of Impact/Fatigue Specimens

Specimens which had survived 10^6 cycles zero-tension fatigue without fracture were tested for residual tensile strength and the results are presented in Tables 7.39 - 7.42. Plots of residual tensile strength ratio after 10^6 cycles against maximum fatigue stress ratio are shown in Figures 7.33 - 7.36. In these figures the value of $\frac{\sigma_{at}}{\sigma_{rt}}$ at $\frac{\sigma_{max}}{\sigma_{rt}} = 0$ represents the static tensile strength of an un-cycled specimen and the scatter band of static tensile results is presented in order to assess the significance of any changes in strength due to fatigue. The value of $\frac{\sigma_{max}}{\sigma_{rt}}$ at $\frac{\sigma_{at}}{\sigma_{rt}} = 0$ is a value extrapolated from the relevant S-N curve (Figure 7.6) as being the maximum fatigue stress required to just cause failure at 10^6 cycles (i.e the fatigue strength at 10^6 cycles). Due to the variability in the fatigue data these values should only be regarded as approximate.

Each point on the residual strength curves represents only one test and it is therefore difficult to draw firm conclusions from this data, given the high variability shown by the fatigue results. However, Figure 7.33 shows that, even for undamaged material zero-tension fatigue can improve the tensile strength of the material. This suggested the presence of residual stresses and/or stress concentrations within the plain material which were masked by stress relieving mechanisms

in the same way that the residual strength of specimens containing more obvious stress concentrations could be improved by cycling [86], [108]. It is unlikely that the laminates are entirely free of curing stresses and stress concentrations in woven material could be provided by the tow cross-overs. It was noted in Section 7.2.1.2 that X-rays of cycled undamaged specimens showed that the weave was highlighted by the presence of penetrant in micro-cracks in the resin-rich areas at cross-overs. This would suggest that fatigue damage of this type was capable of acting as a stress reliever at these points, thereby improving the tensile strength.

Improvements in tensile strength after fatigue were more pronounced in the case of impact damaged specimens (Figures 7.34 and 7.35) and specimens containing holes ($U_i = \infty$) (Figure 7.36) suggesting that micro-damage, observed to propagate from the impact site (Figures 7.9 and 7.18) was effective in masking the stress concentration. For some specimens showing strength improvements, X-ray showed that micro-damage had propagated to the edges and end-tabs of the specimens and was not localised around the impact site. Thus despite the presence of extensive amounts of micro-cracking the tensile strength of impacted specimens was not inferior to that of un-cycled material but was, in fact noticeably better. The presence of some types of fatigue damage were therefore beneficial to the tensile performance of impacted material. It was interesting to note that improvements in tensile strength after 10^6 cycles were observed even at very low fatigue stresses (i.e $\frac{\sigma_{max}}{\sigma_{rt}} = 0.15$ for both 2.94J and 6.87J specimens) even though propagation of micro-damage was not observed by X-ray in specimens cycled below $\frac{\sigma_{max}}{\sigma_{rt}} = 0.20$. This result suggested the production of stress relieving damage and that either the extent of the damage growth was too little to be resolved by the methods chosen, being highly concentrated around the impact site, or that the type of damage produced at these stress levels was effectively invisible to PEXR (possibly too small to allow passage of sufficient quantities of penetrant). An alternative explanation could be the presence of another type of stress relieving (e.g limited plasticity in the matrix) but this could not be confirmed.

Interestingly, in the curves for both 2.94J and 6.87J impact specimens (Figures 7.34 and 7.35) there appears to be a 'dip' in the residual tensile strength behaviour

at a value of $\frac{\sigma_{max}}{\sigma_{rt}} = 0.35$. This effect suggested that the stress relieving damage modes, present in specimens cycled at, $\frac{\sigma_{max}}{\sigma_{rt}} < 0.35$ were dominated by a strength degrading damage mode which was present in specimens cycled at $\frac{\sigma_{max}}{\sigma_{rt}} = 0.35$. This new damage mode was itself then overridden by another stress relieving mechanism, present in specimens cycled at $\frac{\sigma_{max}}{\sigma_{rt}} > 0.35$, which again increased the residual tensile strength. This double stress relieving fatigue behaviour for impact damaged specimens is difficult to conceptualise. All specimens were cycled to $n = 10^6$ cycles before being tested for residual strength. Therefore any damage present in specimens cycled at $\frac{\sigma_{max}}{\sigma_{rt}} < 0.35$ should also be present in specimens cycled at $\frac{\sigma_{max}}{\sigma_{rt}} = 0.35$. Equally there should be additional damage modes present, due to cycling at the higher stress level, to cause the strength reduction. Furthermore, any damage present in specimens cycled at $\frac{\sigma_{max}}{\sigma_{rt}} = 0.35$ should be present in specimens cycled at $\frac{\sigma_{max}}{\sigma_{rt}} > 0.35$ with additional stress relieving damage modes superimposed. Examination of the X-rays for run-out specimens around this applied stress level showed no obvious characteristic differences which could account for a 'double stress relieving' behaviour. In that each point on these curves represents only one test it can only be suggested that the strength dip is due to natural variability in the results and it may be coincidence that such a dip should occur at the same value of $\frac{\sigma_{max}}{\sigma_{rt}}$ for both 2.94J and 6.87J specimens.

The rapid fall in residual tensile strength for specimens cycled at $\frac{\sigma_{max}}{\sigma_{rt}}$ values just below those causing failure at 10^6 cycles (i.e for specimens just reaching the run-out) reflected the rapid growth in delamination damage over the final collapse phase of the specimen life. There was a narrow band of applied fatigue stress $\frac{\sigma_{max}}{\sigma_{rt}}$ between catastrophic failure at 10^6 cycles and no appreciable delamination growth at 10^6 cycles. The value of $\frac{\sigma_{max}}{\sigma_{rt}}$ for no observable delamination growth for both 2.94J and 6.87J impact levels was approximately 0.45 so that for a 2.94J specimen cycling at $0.45 < \frac{\sigma_{max}}{\sigma_{rt}} < 0.51$ and for a 6.87J specimen $0.45 < \frac{\sigma_{max}}{\sigma_{rt}} < 0.56$ should result in run-out but with a measureable growth in delamination area and possible strength reductions. It can be seen from Figures 7.34 and 7.35 that this was not necessarily the case. The only significant strength reductions at 10^6 cycles were for a 2.94J specimen cycled at $\frac{\sigma_{max}}{\sigma_{rt}} = 0.50$ ($\epsilon_{max} = 3600\mu\epsilon$) and for a 6.87J specimen

cycled at $\frac{\sigma_{max}}{\sigma_{rt}} = 0.60$ ($\epsilon_{max} = 3100\mu\epsilon$). This latter test should, ideally have led to failure before the run-out and the result must be regarded as symptomatic of the inevitable variability in fatigue testing. Nevertheless both of these tests showed appreciable damage growth at the run-out, the delamination having spread to the full width over the full gauge length in the case of the 2.94J specimen and over the full width over nearly the full gauge length for the 6.87J specimen. The other specimens in the regions of run-out with delamination growth showed considerably less damage growth at the run-out. In these cases the delamination had not reached the edges and the growth was at the most 14% of that shown by the specimens showing strength reductions at 10^6 cycles (Table 7.38).

These observations led to the conclusion that a limited amount of delamination growth could be sustained by the specimens without any significant loss of tensile strength. Large amounts of delamination were accompanied by significant reductions in residual tensile strength. However these large damage growths were at the end of the specimen life and were therefore associated with the final collapse of the specimens. It was therefore probable that the tensile strength was influenced to a greater extent by the other failure modes (e.g fibre failure) which occurred at this period of the specimen life.

Chapter 8

Development of Model

8.1 Introduction

In Chapter 2 a number of existing models were presented which attempted to predict the residual static tensile and compressive strength of laminates containing damage caused by low velocity impact loading. These semi-empirical 'equivalent flaw' models can be easily applied given a minimum amount of experimental data and have been found to be successful for a wide variety of materials and laminate lay-ups.

It is the purpose of this chapter to present a similar argument to that proposed in support of these models in an attempt to deduce a relationship capable of predicting the fatigue strength of laminates subjected to low velocity impact and subsequent zero-tension fatigue loading.

8.2 The Caprino Residual Static Strength Model

It is a relatively recent approach to the understanding of the resistance to fracture of materials containing defects to study the stress-strain, displacement and energy conditions at the tip of the defect when it begins to grow [109]. This is the basis of fracture mechanics. Of primary importance is the critical stress and strain at the crack tip when the crack begins to propagate in a brittle, catastrophic manner. This critical state can be described by a critical stress intensity factor K_C.

Linear elastic fracture mechanics (LEFM), as applied to homogeneous, isotropic materials provides the following expression for the critical fracture stress of an infinitely wide sheet containing a notch of length $2c$ [98].

$$\sigma_r = K_{IC}(\pi c)^{-\frac{1}{2}} \tag{8.1}$$

K_{IC} is a material parameter known as the fracture toughness, which is experimentally determined and the exponent, $-\frac{1}{2}$ is the order of the mathematical singularity at the crack tip. For a flaw in an orthotropic plate the value of K_{IC} is the same as for an isotropic material [94].

For LEFM to be a valid analysis tool it is important that elasticity conditions at the crack tip dominate, Equation 8.1 being derived under the assumption that the material is linearly elastic up to fracture. In fact, for CFRP containing notches this is not the case. Although the material has little capacity for the plastic flow and yielding effects present in ductile metals, relaxing of high local stresses and absorption of fracture energy have been observed to take the form of a 'pseudo-plastic', sub-critical damage zone of cracks and delaminations [88]. A direct application of LEFM to composites is, therefore generally considered to be inappropriate [110].

Mar and Lin [111], [112] proposed that the fracture of fibre reinforced composite materials was governed by the expression:-

$$\sigma_r = H_c(2c)^{-m} \tag{8.2}$$

where H_c, the composite toughness or composite fracture parameter, is a property of the material and laminate lay-up and has dimensions of $stress \times (length)^m$. The exponent, m is the order of the singularity of a crack with its tip at the interface of two dissimilar materials and is a function of the shear modulus and Poisson's Ratio for the fibre and matrix.

No material is entirely free from flaws and therefore the value of c in Equation 8.2 will never be zero. Caprino [98] suggested that, in the absence of an artificially implanted flaw, the failure of the material was precipitated by an inherent flaw of

dimension $2c_o$. Therefore for 'plain' material Equation 8.2 can be written:-

$$\sigma_o = H_c(2c_o)^{-m} \tag{8.3}$$

Combining Equations 8.2 and 8.3, Caprino suggested the following two-parameter model for predicting the residual strength of notched laminates:-

$$\frac{\sigma_r}{\sigma_o} = \left(\frac{c_o}{c}\right)^m \qquad c \geq c_o \tag{8.4}$$

where c_o and m are determined from experimental data.

The damage zone caused by low velocity impact on a CFRP laminate is extremely complex, typically comprising a combination of fibre failure, delamination and matrix cracking. Caprino [56], recognising the considerable difficulty in analysing the influence of the impact damage on the residual strength of the laminate in any direct manner, attempted to extend the applicability of the simple model outlined above to predict the residual strength of laminates damaged by low velocity impact loading (i.e containing BVID).

If a specimen containing impact induced damage is loaded to failure then, for $U_i \geq U_o$, its strength would be less than or equal to the undamaged strength (Figures 6.4 and 6.16). This result could be achieved by implanting a flaw of known dimension in the specimen. Therefore, *in terms of residual strength*, whatever applied impact energy U_i and consequent level of damage, a notch of appropriate dimension c could be found giving the same strength reduction. Caprino [56] expressed the relationship between c and U_i as a simple power law, giving:-

$$c = kU_i^n \qquad n > 0 \tag{8.5}$$

and

$$c_o = kU_o^n \qquad n > 0 \tag{8.6}$$

Substitution of Equations 8.5 and 8.6 into Equation 8.4 gives, for impact damaged specimens under static loading:-

$$\frac{\sigma_r}{\sigma_o} = \left(\frac{U_o}{U}\right)^{\alpha} \qquad \alpha = mn \tag{8.7}$$

where U_o, the threshold energy for no strength reduction and α, the parameter which determines the rate of residual strength degredation with impact energy must be obtained from experimental data.

The Caprino residual strength model has been found to give excellent correlation with experimental data for CFRP specimens impacted at low velocities [56], [81].

8.3 The Fatigue Strength Model

If there is considerable difficulty in analysing the complex state of damage caused by low velocity impact directly [56], then this must be equally if not more true for the damage zone produced by the combined effects of impact and fatigue loading. A useful design tool for CFRP would therefore be a simple relationship which, from a minimum of experimental data, would be capable of predicting the fatigue strength σ_n of laminates subjected to impact and subsequent fatigue loading.

The model proposed for the prediction of the fatigue strength of CFRP subjected first to low velocity impact and then to zero-tension fatigue loading (R=0) is based on the Mar-Lin Fracture Model and Caprino's simple approach to the prediction of residual strength of CFRP damaged by impact loading only.

For a specimen tested under constant amplitude fatigue loading, the residual static strength is dependent on the stress ratio R, the applied fatigue stress σ_{max} and the number of applied fatigue cycles n. Of course, for zero-tension fatigue R is a constant and the preceding statement can then be expressed as:-

$$\sigma_{rt} = f(\sigma_{max}, n) \tag{8.8}$$

If the specimen is un-cycled Equation 8.8 becomes:-

$$\sigma_{rt}\,|_{n=0} = f(\sigma_{max}, 0) = \sigma_{ot} \tag{8.9}$$

Because of the accumulation of damage with applied cycles during fatigue loading the residual static tensile strength of the specimen is progressively degraded (i.e $\sigma_{rt} < \sigma_{ot}$) and it may be assumed that fatigue failure occurs when the residual tensile strength σ_{rt} is reduced to the maximum applied fatigue stress σ_{max}. *The final fatigue half cycle before failure can therefore be considered equivalent to a static tensile test.* This condition occurs when $n = N_f$ and therefore Equation 8.8 must satisfy the condition:-

$$\sigma_{rt} = f(\sigma_{max}, N_f) \tag{8.10}$$

It is a common design requirement that a material should be able to withstand a minimum number of cycles without failure. This may, for example be representative of a number of flights for a composite component on an aircraft. It is therefore important to be able to specify the maximum applied fatigue stress that the material is able to support in attaining that life. Thus, if N_f is specified as a required constant, Equation 8.8 can be expressed as:-

$$\sigma_{rt} = \sigma_{max} \qquad \text{at} \qquad n = N_f \tag{8.11}$$

where the value of σ_{rt} at $n = N_f$ is the zero-tension fatigue strength of the material.

If a specimen containing impact induced damage is loaded to failure under constant amplitude zero-tension fatigue, then its fatigue strength at a given number of cycles n would be less than the fatigue strength of an undamaged specimen subjected to the same number of cycles, i.e:-

$$\sigma_{rt}\,|_{U_i=x} \leq \sigma_{rt}\,|_{U_i=0} \qquad x \geq 0 \tag{8.12}$$

This has been shown experimentally in Figure 7.5. In this case the final half fatigue cycle can be considered equivalent to a static tensile test of a specimen degraded by a combination of impact damage and fatigue damage or, in the case of $U_i = 0$, fatigue damage only.

Similar strength reductions could also be obtained by a static tensile test of a specimen containing a notch of known dimension c'. Therefore, in terms of fatigue

strength at n cycles, whatever initial applied impact energy U_i and consequent level of damage, an 'equivalent' notch of appropriate dimension c' could be found resulting in the same strength reduction, i.e:-

$$c' = f(U_i) \tag{8.13}$$

If the relationship between U_i and c' can be expressed as a power law then:-

$$c' = k' U_i^p \tag{8.14}$$

and:-

$$c'_o = k' U_o'^p \tag{8.15}$$

U'_o is the impact energy below which there would be the same fatigue strength reduction as an undamaged specimen at n cycles (i.e the impact has no influence on the fatigue strength). As U_i increases, so does c' if a cumulative failure law with applied impact energy is valid, therefore $p > 0$.

Equations 8.14 and 8.15 are equivalent to expressions 8.5 and 8.6 for specimens subjected to impact loading only. However due to the accumulation of damage under fatigue loading:-

$$\sigma_{nt}\,|_{U_i=a} \leq \sigma_{rt}\,|_{U_i=a} \qquad \text{and} \qquad \sigma_{nt}\,|_{U_i=0} \leq \sigma_{ot} \tag{8.16}$$

therefore:-

$$c' \geq c \qquad \text{and} \qquad c'_o \geq c_o \tag{8.17}$$

Applying the Mar-Lin Fracture Model, in terms of residual strength Equation 8.2 becomes:-

$$\sigma_{nt}\,|_{U_i=a} = H_C(\pi c')^{-m} \tag{8.18}$$

and:-

$$\sigma_{nt}\,|_{U_i=0} = H_C(\pi c'_o)^{-m} \tag{8.19}$$

which, when combined result in the expression:-

$$\frac{\sigma_{nt}\,|_{U_i=x}}{\sigma_{nt}\,|_{U_i=0}} = \left(\frac{c'_o}{c'}\right)^m \qquad c' \geq c'_o \tag{8.20}$$

Substitution of Equations 8.14 and 8.15 into Equation 8.20 then yields the following expression:-

$$\frac{\sigma_{nt}\,|_{U_i=x}}{\sigma_{nt}\,|_{U_i=0}} = \left(\frac{U'_o}{U_i}\right)^{\xi} \qquad \xi = mp \tag{8.21}$$

For $n = 0$ (i.e un-cycled specimens) Equation 8.21 is equivalent to the Caprino residual static strength model presented in Equation 8.7.

The above relationship can be used to predict the zero-tension fatigue strength at n cycles of specimens damaged by low velocity impact. U'_o, the threshold energy and ξ, the parameter governing the rate of reduction in fatigue strength with impact energy must be determined from experimental data.

Equation 8.21 is unique to a given number of cycles, n. However, given a minimum of S-N data it could be used to generate a series of expressions for any required fatigue life, enabling a suite of design curves of $\frac{\sigma_{nt}|_{U_i=x}}{\sigma_{nt}|_{U_i=0}}$ against U_i to be produced. The application of Equation 8.21 to experimental data generated in this work is discussed in Section 9.5.

The expression is only valid for;-

$$U_i \geq U'_o$$

and, like Caprino's residual static strength model [56] predicts continuous reduction of σ_{nt} with increasing U_i. Moreover, the accuracy of the design curves produced from this expression is limited by the variability of the fatigue data. In practical applications there would have to be some assessment of fatigue variability to establish confidence limits for the prediction. Nevertheless, the proposed model has the capability of considerably reducing the amount of testing required to assess the fatigue performance of CFRP containing low velocity impact damage which, in view of its 'invisibility', currently restricts the effective use of the material.

Chapter 9

Analysis and Discussion of Results

9.1 Introduction

Individual results and sections of the present study have been discussed in Chapters 5, 6 and 7. It is the purpose of this chapter to employ some of the existing models presented in Chapter 2 to describe the behaviour of the material under post-impact static loading, to examine the effectiveness of the fatigue strength model proposed in Chapter 8 and to provide an overview of the results and a discussion of the work as a whole.

9.2 Impact of CFRP Plates - The Static/ Dynamic Analogy

Crivelli-Visconti et al [99] suggested that, over the range of impact velocities and energies required to cause low velocity impact damage, CFRP was insensitive to the rate of loading. For simply supported rectangular specimens impacted over the range of incident energies 0 - 3J (impact velocities 0 - 5.13ms^{-1}) it was concluded [99] that the applied energy U_i determined the residual tensile strength of the specimens independent of whether that energy was applied statically or dynamically.

Furthermore, it was shown that the overall force/displacement behaviour of the laminates was unaffected by loading rate.

Tiu et al [81] showed that for CFRP 100mm diameter clamped sections of laminate the threshold energy U_o could be predicted with reasonable accuracy using a static, two-dimensional finite element analysis coupled with an appropriate failure criterion, further confirming the static/dynamic analogy for impacted CFRP.

The significance of the static/dynamic analogy is, perhaps best illustrated in the work by Caprino [56]. Caprino [56] used the data generated in [99] to show that the residual strength curves for impacted and statically loaded specimens were almost coincident, suggesting that the parameters U_o and α in the Caprino Model (Section 2.4.2) could be determined by static tests. The test philosophy used by Caprino [56] was that, by producing a static force/displacement curve, the value of elastic energy at first failure could be equated to U_o and the total applied energy would be given by the area under the curve. Residual strength tests would then allow the parameter α to be determined. It proved possible to generate accurate residual strength data and to produce a Caprino type predictive model using only static tests, showing that the use of instrumented impact testing may be eliminated in the attempt to predict the residual mechanical properties of CFRP subject to low velocity impact. It would therefore be valuable to further confirm or disprove the static/dynamic analogy for CFRP laminates impacted under clamping and loading conditions specified by the CRAG recommendations, which are widely used at present as a test standard.

In the present case it was not possible to measure the dynamic load/deflection of the CFRP plates so a direct comparison between static and dynamic behaviour cannot be made. However, dynamic displacement measurements were recorded (Section 5.2.2) and it is therefore possible to make an indirect correlation. Furthermore it is possible to compare the threshold energy U_o, measured under static and dynamic loading conditions.

Under static loading the typical load/deflection behaviour has been illustrated in Figure 5.1. U_o was assessed by the area under the curves at first failure which was detected audibly and indicated by the loss of bending stiffness on the curves.

Using these criteria, first failure was indicated at approximately 1.65J.

Under dynamic impact conditions first failure could be indicated by an examination of the damage zones or by loss of static strength although the criteria for determining U_o are not strictly the same and neither can therefore be used for an accurate comparison of static and dynamic behaviour. It is possible that damage may be present and detectable at an energy lower than that required to influence the static strength or bending stiffness of the plate. However, under static loading reductions in plate stiffness and the first audible indications of failure were almost coincident (Section 5.2.1) and it is probable that the damage detected audibly should be visible, at least by sectioning and microscopic examination. Therefore, of the two criteria for comparison between static and dynamic behaviour of CFRP plates, examination of damage zones for first failure is considered to be the more accurate. Damage was first detected at the 1.96J impact level (Section 5.3) but as impacts were only conducted at approximately 1J intervals it seems unwise to use this as a comparison other than as a rough indication that first failure occurred between incident energies of 0.98J and 1.96J, values 41% lower and 19% higher than the value of U_o suggested by static loading. Residual static strengths were not significantly influenced by the presence of impact damage until U_i reached 2.94J (Sections 6.3.1 and 6.5.1).

Under impact conditions maximum plate deflection was plotted against impact energy in Figure 5.3. This curve showed gently increasing slope from an incident energy of approximately 1.7J, indicating that the rate of increase of maximum displacement increased with incident energy from this point. This trend may have reflected the greater levels of damage and hence reducing bending and local stiffness of the plate, implying that the 1.7J impact level represented the threshold impact level for initial damage U_o. This value was only 3% higher than the threshold energy under static conditions, which seemed to support the use of static testing to simulate low velocity impact tests for CFRP. However, examination of the central displacements at first failure showed for static loading (Figure 5.1) a value of approximately 2.3mm, whereas under similar dynamic conditions the central displacement at first failure was only 1.9mm (Figure 5.3), a discrepancy

of 17%. This suggested that the static and dynamic load/deflection behaviour of CFRP plates were not the same for these clamping and loading conditions, the dynamic bending stiffness of the plate being apparently greater than the bending stiffness under static loading. This may have been due to inertia of the system under the dynamic loading condition inhibiting the gross bending behaviour of the plate. Therefore, although the static/dynamic analogy seems to hold for the measurement of threshold energy U_o, the measured response of the plates under the two loading conditions was considerably different. This is, nevertheless a valuable result in that comparisons could be made of the resistance to initial impact damage of different material systems and laminates by the use of relatively straightforward static tests.

9.3 Correlation of Impact Damage and Residual Static Strength

The significance of low velocity impact damage in CFRP laminates is in the effect that it has on the post-impact mechanical properties of the material. Therefore the effectiveness of the destructive and non-destructive methods of damage detection should be measured against this criterion, i.e the NDT method must be capable of detecting damage before any serious reductions in the performance of the material have occurred. Detected damage is presented with residual static tensile and compressive strengths in Tables 9.1 and 9.2 for the quantitative NDT methods.

Direct correlation between impact damage and residual static strength was, of course impossible for the destructive sectioning/microscopy examination technique. However this method gave the most detailed view of the state of damage in the impacted specimen. In terms of residual strength, the significant failure modes of matrix cracking, delamination and fibre failure were observed at the 2.94J impact level, a value below which no significant reductions in either tensile or compressive strength were detected. Sectioning/microscopy therefore seemed to be an effective method of damage examination and, moreover was the only method ca-

pable of illustrating the internal failure mechanisms directly. This method would, therefore be valuable in indicating the values of impact energy U_o at the onset of static strength reductions. However, use of this technique alone must be restricted to qualitative assessment of the damage state and its likely effect on the residual strength of the material. If the damage were to be closely correlated with the residual strength, being used in a predictive capacity, then some assessment would have to be made of the extent and distribution of fibre failure, matrix cracking and internal delaminations, factors which all influence the residual tensile and compressive strength of the material to a greater or lesser extent. This would require a large number of slices through the damage area to be made which would be impossibly time-consuming and completely impractical. Despite its value sectioning/microscopy must therefore be restricted to the laboratory due to these constraints, and of course its destructive nature.

The other methods available for damage detection in this programme, namely by front face and back face visual examination, residual indentation depth measurement, X-ray and C-scan did not directly assess the overall damage mechanisms and their influence on the residual static strength. These methods relied on the measured dimension being characteristic of an overall damage state and must therefore be restricted to one particular material under one particular set of loading and clamping conditions.

Examination of front face damage did not (with one exception) reveal any measureable damage until the residual tensile strength of the impacted specimens had fallen to approximately 60% of the undamaged value. Under compressive loading the corresponding value was approximately 70%. Thus, the material had lost a large part of its inherent strength before any indication of the occurrence of an impact was noticed. This was for specimens under relatively ideal conditions where the existence and position of damage was known, the specimens were well lit and the damage was examined with the aid of a microscope. The variabilty and unreliability of the method as illustrated in Table 9.1 and Figure 5.4 also mean that an accurate relationship between detected front face damage and residual static strength would be, at best difficult. In view of these points it would be difficult to

justify any suggestion that any damage could be detected visually and subsequently measured under normal service conditions over the 0 - 9J BVID impact range considered in this study. Serious reductions in post-impact performance could occur undetected and therefore examination of front face damage radius should be discounted for this material as a measure of the severity of low velocity impact loading. Simple visual examination of the impacted surface of a structure will always be used as a first indication of the presence of damage. It is, therefore vital that the front (impact) face of the material should show damage before the mechanical properties of the material are degraded significantly. In practical terms, therefore either the allowable stress and strain limits for this material must be kept low enough to account for the presence of undetected damage of this severity or the material must not be used in an area susceptible to low velocity impact.

Measurement of residual indentation depth showed a 100% detection rate for specimens having a residual tensile strength below 70% of the undamaged value and for specimens having a residual compressive strength below 80% of the undamaged value. These are both 10% higher than the values found for measurement of front face damage radius and moreover this method proved less prone to inaccuracies and variability. Nevertheless, using this method, specimens showing significant strength reductions were being assessed as undamaged. The method is also very much a 'point' technique and in service would be difficult and time consuming to operate and would probably require detailed prior knowledge of impact locations to be effective. In view of the above discussion on front face damage, this is unlikely. Moreover, it would also rely heavily on surface quality as the measured indentations were of the order of 0.3 - 0.4mm at the maximum energy considered in the present study. It is unlikely that this degree of surface quality could be assured on any real composite structure and therefore it seems unlikely that any measurement of front face indentation depth could be used as a practical NDT method for composites.

Back face cracks proved easily visible to the naked eye for all significant strength reductions and for some tensile strength reductions which were not below the variability band for undamaged specimens. On first consideration therefore this

method seems to be promising, it proving possible to detect damage before the residual properties of the material were significantly affected by the impact. However, as stated in Section 5.3.2 this method was particularly prone to variability (Figures 5.7 and 5.8) and it would therefore be unwise to use back face crack length as a quantitative indication of the damage state and hence likely residual performance of the material. However the presence of back face cracking could be reliably used as a qualitative indication of impact damage in the knowledge that if damage of this type were not present then any impact would not have seriously reduced the static tensile or compressive performance of the material. Its presence, moreover could lead to the use of more sophisticated and accurate NDT in localised areas. However, in the majority of service applications it is likely that the back face of the laminate would be hidden from view and would therefore be of no use in the inspection procedure.

Not surprisingly the two most sophisticated NDT methods used, namely C-scan and X-ray proved the most reliable. C-scan proved capable of detecting damage before any significant compressive strength reductions were observed and X-ray had a similarly impressive performance in detecting damage before tensile strength reductions took place. Limited data makes any further assumption not possible but it is likely from a consideration of the results in Section 5.3.3.1 that C-scan and X-ray would have similar performance against both loading conditions.

Due to the effectiveness of X-ray and its consistent results it is possible to generate relationships between X-ray damage area A_x and residual strength ratio $\frac{\sigma_r}{\sigma_o}$. Examination of the residual strength curves (Figures 6.4 and 6.16) and the relationship between incident impact energy and X-ray area (Figure 5.13) suggest that a simple power law may be assumed for the relationship between residual strength and X-ray damage area, i.e:-

$$\sigma_r = cA_x^n \tag{9.1}$$

where c and n are constants to be experimentally determined. Of course as residual strength reduces with increase in X-ray area, $n < 0$.

There must be an impact resulting in a detectable damage area A_{cx} which does

not result in a reduction in static strength, i.e:-

$$\sigma_o = cA_{os}^n \tag{9.2}$$

Combining Equations 9.1 and 9.2 results in the expression:-

$$\frac{\sigma_r}{\sigma_o} = \left(\frac{A_s}{A_{os}}\right)^n \tag{9.3}$$

Suitable treatment of the experimental data results in the two expressions for the relationship between X-ray damage area and residual tensile and compressive strength of impacted specimens. A_{os} represents the minimum detectable area before strength reductions occur. In a practical situation therefore it would be desirable to maximise A_{os} so that relatively large and detectable damage zones occur before strength reductions become significant. The coefficient n determines the rate of strength reduction with X-ray area and its absolute value should therefore be minimised. n clearly depends on the type of damage produced by the impact and therefore on the material and clamping/loading conditions. It would also depend on the subsequent loading condition (tension or compression) as the failure modes in each case would be different. Husman et al [78] suggested that the minimum residual strength σ_r is attained at low penetration energies, the impact producing a hole with significant damage around it. It is possible that this energy also produces the maximum A_s. Above this energy σ_r recovers to the value of a drilled hole and is thereafter independent of the impact energy U_i. A_s may also reduce to a value independent of U_i at high velocities. This suggests that expression 9.3 may be valid for a wide range of energies. However, failure modes under low velocity and high velocity impact are different [19] and therefore n will change between the two conditions. It is therefore recommended that expressions of the form 9.3 are only applied to low velocity impact cases.

For tensile loading:-

$$\frac{\sigma_{rt}}{\sigma_{ot}} = \left(\frac{A_s}{8.40}\right)^{-0.17} \tag{9.4}$$

and for compressive loading:-

$$\frac{\sigma_{rc}}{\sigma_{oc}} = \left(\frac{A_o}{17.54}\right)^{-0.21} \tag{9.5}$$

These expressions have been plotted, along with the experimental data, in Figures 9.1 and 9.2 and provide the facility of being able to predict the residual tensile and compressive strength of the material from the X-ray NDT output. A minimum amount of experimental data is required to evaluate A_{oc} and n. Undoubtably similar expressions could be generated for C-scan traces but a quantitative approach is not justified in the present case due to the lack of sufficient C-scan data. However, a direct comparison of C-Scan and X-Ray areas was made for a single batch of specimens (Section 5.3.3.1) which revealed that the threshold energies for initial observation of damage were similar for the two methods whilst C-Scan gave a larger trace for all energies above this value. In conseqence, if similar expressions to Equations 9.4 and 9.5 were generated from adequate C-scan data, it is probable that threshold areas A_{oc} and A_{oc} would be similar but that the absolute value of n in Equation 9.3 would be lower for the C-scan, reflecting the larger area of the trace for a given impact energy and residual strength reduction.

9.4 Residual Static Strength Models

9.4.1 Introduction

The equivalent flaw models for the prediction of residual static strength of impact damaged laminates are discussed in Section 2.4.2. They are primarily intended for the prediction of residual tensile strength (only Caprino [56] applied similar relationships to tensile and compressive data, achieving good predictions for both loading cases), but as their effectiveness depends mainly on the fact that residual strength decreases with increasing incident impact energy and therefore for each impact energy there is an equivalent flaw size, the models should be equally applicable to the prediction of residual tensile and compressive strength. This approach has been taken in the current study.

In each case the model is semi-empirical, containing constants which can be

determined by suitable examination of the experimental data obtained. Each proposed expression is first manipulated to give a simple linear relationship of the form:-

$$y = mx + c$$

and the experimental data is then plotted on this basis. Linear regression analysis is then used to give a best fit to the data and suitable treatment of the gradient m and the intercept c will then yield the empirical constants which, when applied to the original model will give the best fit curve to the residual strength data.

For the Husman, Lal and Avva models residual strength after impact is related to the impact energy per unit thickness $\overline{U}_i$. In order to make the predictions due to these models as effective as possible the mean $\overline{U}_i$ has been obtained by dividing the incident impact energy by the mean thickness of the specimens tested at that energy U_i.

9.4.2 The Husman Model

The model developed by Husman et al [78] states that the residual strength of an impacted material is related to the impact energy by the expression:-

$$\sigma_r = \sigma_o \left(\frac{U_s - K\overline{U}_{ke}}{U_s} \right)^{\frac{1}{2}} \tag{9.6}$$

σ_r = Residual strength of impacted material

σ_o = Strength of undamaged material

K = Effective damage constant

$\overline{U}_{ke}$ = Kinetic energy/unit thickness imparted to specimen

U_s = Work/unit volume required to break undamaged specimen.

Simple manipulation of this expression results in:-

$$\left(\frac{\sigma_r}{\sigma_o}\right)^2 = 1 - \frac{K\overline{U}_{ke}}{U_s} \tag{9.7}$$

which is of the required linear form and which will yield the relevant constant K if $\left[\left(\frac{\sigma_r}{\sigma_o}\right)^2 - 1\right]$ is plotted against $\overline{U}_i$ ($\overline{U}_i$ is equivalent to $\overline{U}_{ke}$). The data for residual

tensile and compressive strength is presented in Figure 9.3. No threshold for initial strength reduction is assumed for the Husman model so that all the data has been included in the analysis.

The mean energy per unit volume required to break an undamaged specimen can be obtained from the area under relevant tensile and compressive curves, examples of which are given in Figures 6.1 and 6.13, and were for a tensile test 1.77Jmm^{-3}, and for a compressive test 3.50Jmm^{-3}.

Analysis of the residual static strength data by a Husman analysis yields the two expressions for residual tensile and compressive strength. For tensile strength:-

$$\begin{aligned} \frac{\sigma_{rt}}{\sigma_{ot}} &= \left(\frac{1.77 - 0.39\overline{U}_i}{1.77}\right)^{\frac{1}{2}} \\ &= (1 - 0.22\overline{U}_i)^{\frac{1}{2}} \end{aligned} \tag{9.8}$$

and for compressive strength:-

$$\begin{aligned} \frac{\sigma_{rc}}{\sigma_{oc}} &= \left(\frac{3.50 - 0.84\overline{U}_i}{3.50}\right)^{\frac{1}{2}} \\ &= (1 - 0.24\overline{U}_i)^{\frac{1}{2}} \end{aligned} \tag{9.9}$$

These expressions are plotted with the experimental data in Figures 9.4 and 9.5 and a numerical indication of the difference between the experimental results and the Husman predictions is given in Tables 9.3 and 9.4. It is evident from an examination of the data and particularly from the 'best fit' curves that the Husman Model does not provide a particularly accurate representation of the experimental data. The experimental trend, as described in detail in Section 2.4.1, is for little or no drop in strength up to a threshold energy value followed by a rapid strength drop, levelling out to a more gentle fall up to the penetration threshold. Even though Husman suggests that the model is only valid for impact energies up to the penetration threshold, the shape of the Husman prediction is almost the opposite of the observed relationship. The threshold energy below which there is little or no drop in strength is not accounted for and, more importantly the

rate of drop in strength increases with impact energy rather than the other way around. The theoretical curves therefore merely cross the experimental data in two places, the differences beween the predicted and experimentally determined strength becoming as large as 36% for compressive data at the highest energy in the present study. The experimental trend obtained in the present study seems from the literature to be fairly general and it must therefore be concluded that the Husman Model is not adequate in predicting the residual tensile or compressive strength of these CFRP laminates subjected to low velocity impact loading.

9.4.3 The Lal Model

The residual strength model due to Lal [96], [97] and that suggested by Husman [78] are both based on the inherent flaw model for laminates containing a notch, developed by Waddoups et al [95]. However the form used by Lal results in:-

$$\sigma_r = \sigma_o \left(\frac{c_o}{\frac{U_f}{2hG_{IC}} + c_o} \right)^{\frac{1}{2}} \tag{9.10}$$

h = Thickness of laminate

U_f = Fibre breakage energy

Again examination of the above expression yields the linear equation:-

$$\left(\frac{\sigma_o}{\sigma_r}\right)^2 = \frac{U_f}{h} \frac{1}{2G_{IC}c_o} + 1 \tag{9.11}$$

No data was available for G_{IC} and c_o but if the above expression is simply treated in a 'curve fitting' fashion, to examine the form of the expression, the constant $\frac{1}{2G_{IC}c_o}$ can be evaluated from a linear regression analysis of the results.

Under static tensile loading the strength is largely influenced by the presence of fibre damage. The data can be analysed in its present form if the energy required to cause fibre failure U_f is considerably greater than that required to cause delamination U_d and other matrix failure U_m (i.e if $U_d + U_m \ll U_f$ then $U_i \approx U_f$). Data presented by Dorey [19] suggests that this assumption is valid.

Under compressive loading the strength is influenced to a greater extent by the presence of delamination and matrix damage as well as fibre failure so that the equivalent slit size is dependent on U_i directly.

The tensile and compressive data used in obtaining the Lal constants is plotted in Figure 9.6. Again, as Lal does not consider a threshold energy value all the available experimental data is used in obtaining the theoretical expressions. Analysis by a Lal technique yields the following two expressions. For tensile loading:-

$$\frac{\sigma_{rt}}{\sigma_{ot}} = \left(0.72\overline{U}_i + 1\right)^{-\frac{1}{2}} \tag{9.12}$$

and for compressive loading:-

$$\frac{\sigma_{rc}}{\sigma_{oc}} = \left(0.72\overline{U}_i + 1\right)^{-\frac{1}{2}} \tag{9.13}$$

These two expressions, along with the experimental data, are plotted in Figures 9.7 and 9.8 and a quantitative indication of the accuracy of fit is given in Tables 9.5 and 9.6. The data shows that this 'ideal' fit follows the form of the residual strength/impact energy data very well above the threshold for initial strength reduction for both tensile and compressive loading. Above this threshold the difference between predicted and experimental values is at most approximately 5%; below the error can be as large as approximately 26%. However, it must be stressed that this fit is based on assumed values for G_{IC} and c_o, obtained indirectly through the curve fitting process. G_{IC} and c_o values could be obtained from tensile and compressive fracture mechanics tests on slitted specimens. Lal [96], [97] conducted a tensile study in this way and achieved good correlation between experimental data and expression 9.10.

9.4.4 The Caprino Model

The residual strength model developed by Caprino [56] states that:-

$$\sigma_r = \sigma_o \left(\frac{U_o}{U}\right)^{\alpha} \tag{9.14}$$

U = Impact energy

α = Constant

Unlike the Husman and Lal models, simple rearrangement of this expression does not yield a linear expression that can be plotted to obtain the constants. However, taking logs on both sides of the equation gives the equation:-

$$\log \frac{\sigma_r}{\sigma_o} = \alpha \log U_o - \alpha \log U \tag{9.15}$$

an expression of the required form.

Caprino [56] suggested that his model was only valid for impact energies above the threshold for strength reduction. Examination of the experimental data for tensile (Table 6.2 and Figure 6.4) and compressive (Table 6.4 and Figure 6.16) loading suggests that only experimental points for energies of 2.94J and above for tensile and 1.96J and above for compressive testing should be included in the analysis. The resulting analysis plots are given in Figure 9.9 which provide the expressions for tensile loading:-

$$\frac{\sigma_{rt}}{\sigma_{ot}} = \left(\frac{1.27}{U_i}\right)^{0.33} \tag{9.16}$$

and for compressive loading:-

$$\frac{\sigma_{rc}}{\sigma_{oc}} = \left(\frac{1.87}{U_i}\right)^{0.43} \tag{9.17}$$

These two expressions are plotted with the experimental data in Figures 9.10 and 9.11 and a quantitative indication of the accuracy of fit is given in Tables 9.7 and 9.8. This data shows that the expressions follow the form of the residual strength/impact energy data very well. At no point over the range of application of the model does the difference between predicted and measured strengths exceed 10%, these higher errors occurring near the threshold where the experimental data itself is more scattered. Below the threshold the model does not apply and a horizontal line is drawn from $U_i = 0$ to $U_i = U_o$. The general nature of Equation 9.14 means that to a certain extent the expression can be made to fit any data

reasonably well, the accuracy of fit depending on the amount of experimental data used in the determination of U_o and α. Also some idea of the value of U_o must be obtained before the analysis is conducted. Examination of Equations 9.16 and 9.17 yields the surprising result that, for the Caprino model $U_{ot} < U_{oc}$ despite the fact that the experimental data does not support this result. In the tensile loading case it is apparent that the form of the expression cannot adequately follow the very rapid drop in residual tensile strength at approximately 2.94J. This leads to the error in assessing U_{ot} whereas the gentler fall at U_{oc} allows the power law to follow the experimental data more closely.

9.4.5 The Avva Model

The model proposed by Avva [80] states that:-

$$\sigma_r = \sigma_o[2K(\overline{U} - \overline{U}_o) + 1]^{-\frac{1}{2}} \tag{9.18}$$

K= Constant

As in the case of the Husman and Lal models, simple rearrangement gives the linear expression necessary for analysis. This produces:-

$$\left(\frac{\sigma_o}{\sigma_r}\right)^2 = 2K(\overline{U} - \overline{U}_o) + 1 \tag{9.19}$$

As in the case of the Caprino model this expression is only valid for energies above the threshold and only this data has been included in the analysis. The graphs of $\left(\frac{\sigma_o}{\sigma_r}\right)^2$ against $\overline{U}_i$ are given in Figure 9.12 and linear regression analysis provides the constants. For impacted material under tensile loading:-

$$\begin{aligned} \frac{\sigma_{rt}}{\sigma_{ot}} &= \left[0.71(\overline{U}_i - 0.10) + 1\right]^{-\frac{1}{2}} \\ &= (0.71\overline{U}_i + 0.93)^{-\frac{1}{2}} \end{aligned} \tag{9.20}$$

and under compressive loading:-

$$\frac{\sigma_{rc}}{\sigma_{oc}} = \left[0.87(\overline{U}_i - 0.58) + 1\right]^{-\frac{1}{2}} \qquad (9.21)$$
$$= (0.87\overline{U}_i + 0.50)^{-\frac{1}{2}}$$

The two expressions, along with the experimental data, are plotted in Figures 9.13 and 9.14 and a quantitative indication of the accuracy of fit is given in Tables 9.9 and 9.10. As in the case of the Caprino model, above the experimentally obtained threshold energy U_o the fit is very good, errors not exceeding 10%. However the prediction of U_o is significantly worse than that obtained by the Caprino approach and the same restrictions apply to the use of the model. Again the most serious deficiency in the Avva model is its inability to follow the rapid decrease in residual tensile strength at the threshold energy.

9.4.6 Discussion

The static tensile and compressive data for impacted specimens, together with the residual strength curves predicted by the four models considered above are presented in Figures 9.15 and 9.16.

Of the eqivalent flaw models available, only that developed by Husman [78] does not appear to be adequate in describing the residual strength behaviour of this material.

The Lal Model [96], [97] is the only one of the four which does not require a 'best fit' to at least a sensible minimum of the residual strength data in order to find the constants in the analytical expression. This model has been treated in a fairly superficial manner in the present study due to the lack of relevant fracture mechanics data. However the form of the expression is such as to provide a good fit to the data above the threshold energy for initial strength reductions, whilst ignoring the presence of that value.

In view of the common roots of the Husman and Lal models it is perhaps surprising that the forms of the two predicted curves are substantially different. The Husman model predicts increasing rate of residual strength reduction with

impact energy whereas the opposite is true for the Lal model. The difference lies in the calculation of the equivalent slit length c. For the Husman model [78]:-

$$c \propto \frac{1}{U_* - \overline{U}_i}$$

whereas for the Lal model [96], [97]:-

$$c \propto \overline{U}_i$$

which influences the form of the final expressions.

The Caprino Model [56] and the Avva Model [80] provide a similar good fit to the experimental data and are both relatively simple to apply. Both allow for the presence of the threshold energy, although this value must be, to a certain extent known *a priori* to obtain the best fit. Both models have problems, in the present case, of following the rapid fall in tensile strength just after the threshold, this leading to an error in determining the threshold energy U_i. The estimation of this value by the Avva Model is significantly worse than that by a Caprino approach. It is therefore suggested that, of the models currently available and despite its deficiencies, the Caprino Model provides the best estimation of the residual tensile and compressive strength of CFRP containing low velocity impact damage. This technique shows the most potential for useful development and is deserving of further study.

9.5 The Fatigue Strength Model

In Chapter 8, the application of a residual flaw approach to the prediction of zero-tension fatigue strength of CFRP specimens damaged by low velocity impact was discussed. The approach taken, via the Mar-Lin Fracture Model for notched composites, resulted in the expression:-

$$\frac{\sigma_{nt}\,|_{U_i=s}}{\sigma_{nt}\,|_{U_i=0}} = \left(\frac{U_o'}{U_i}\right)^{\epsilon} \tag{9.22}$$

σ_{nt} = Fatigue strength at n cycles

U_i = Incident impact energy

U_o' = Threshold energy for fatigue strength reduction

ξ = Constant

It is proposed that this model is capable of assessing the fatigue performance of CFRP containing BVID from a minimum of experimental data. U_o' and ξ are dependent on initial impact damage and the subsequent form of the fatigue loading and are therefore functions of material properties, impact conditions and fatigue stress ratio R.

Simple manipulation of Equation 9.22 results in the expression:-

$$\log\left(\frac{\sigma_{nt}\,|_{U_i=x}}{\sigma_{nt}\,|_{U_i=0}}\right) = \xi \log U_o' - \xi \log U_i \tag{9.23}$$

which is linear and can be used to determine the constants U_o' and ξ. The data required for this analysis is obtained from the relevant S-N curve (Figure 7.5) and is presented in Table 9.11. This information is used to generate the curves shown in Figure 9.17. Examination of the gradient and intercept of these curves reveals the following suite of expressions which can be used for the prediction of zero-tension fatigue strength of CFRP specimens containing low velocity impact damage:-

$$\begin{aligned}
\text{If } \; n = 10^3, \;\; & \frac{\sigma_{10^3 t}\,|_{U_i=x}}{\sigma_{10^3 t}\,|_{U_i=0}} = \left(\frac{2.17}{U_i}\right)^{0.32} \\
n = 10^4, \;\; & \frac{\sigma_{10^4 t}\,|_{U_i=x}}{\sigma_{10^4 t}\,|_{U_i=0}} = \left(\frac{1.19}{U_i}\right)^{0.24} \\
n = 10^5, \;\; & \frac{\sigma_{10^5 t}\,|_{U_i=x}}{\sigma_{10^5 t}\,|_{U_i=0}} = \left(\frac{0.87}{U_i}\right)^{0.28} \\
n = 10^6, \;\; & \frac{\sigma_{10^6 t}\,|_{U_i=x}}{\sigma_{10^6 t}\,|_{U_i=0}} = \left(\frac{0.49}{U_i}\right)^{0.29}
\end{aligned} \tag{9.24}$$

Of course n can be chosen to be any value specified for a particular application and a suitable expression can be generated. For comparison the Caprino Model, for specimens containing low velocity impact damage only, can be stated as:-

$$\text{If} \quad n = 0 \qquad \frac{\sigma_{0t}\,|_{U_i=\infty}}{\sigma_{0t}\,|_{U_i=0}} = \frac{\sigma_{rt}}{\sigma_{ot}} = \left(\frac{1.27}{U_i}\right)^{0.33} \tag{9.25}$$

Equations 9.24 are plotted, along with the experimental data, in Figure 9.18. The horizontal lines in this figure represent specimens containing a 12.7mm diameter hole, the theoretical 'infinite' impact energy. It can be seen from Figure 9.18 that the Equations 9.24 fit the experimental data very well, an observation to be expected perhaps since U_o' and ξ are determined by experiment.

The limits of applicability of the model are that $U_i \geq U_o'$ and that there should be a continuous reduction in σ_{nt} with U_i. It can be seen from the trends expressed in Equations 9.24 that, as n is increased U_o' decreases, the exception being an increase in U_o' between $n = 0$ and $n = 10^3$. In Section 9.4.4 it was stated that that the Caprino Model was unable to follow the rapid fall in tensile strength of impact damaged specimens at the threshold point, this error leading to a low estimate of U_o. Examination of the experimental data in Figure 9.10 suggests that a realistic value for U_o' at $n = 0$ (i.e U_o) would be approximately 2.5J. This value follows the trend observed by U_o' for $n > 0$.

U_o' represents the maximum impact energy that the material can sustain without experiencing a reduction in fatigue strength above that experienced by an undamaged specimen subjected to the same number of cycles. Impact damage has been shown to exist in a specimen without influencing its static tensile strength (Section 9.3). However, if the specimen is subjected zero-tension fatigue cycles the damage can propagate and may therefore degrade the fatigue strength of the material to a greater extent than non-impacted material. As the number of applied fatigue cycles increases this influence will tend to increase. Therefore, as n increases the maximum impact energy required to cause no decrease in fatigue strength due to the impact will decrease.

Examination of the S-N curves (Figure 7.5) reveals that, due to the increasing resistance to zero-tension fatigue with impact energy, the criterion that there should be a continuous reduction in σ_{nt} with U_i does not hold true for all U_i at all n. As n is increased the upper limit of applicability for Equation 9.22 is reduced. Nevertheless, the model will predict a 'safe' low fatigue stress if this upper limit is

unknown and exceeded. Overall, considering Figure 9.18, the range of U_i covered by the model tends to shift to the left, to lower impact energies.

The accuracy of the above technique is restricted by the quality of the fatigue data and in practical situations some idea should be gained of the statistical variability of the experimental results used to generate the empirical constants.

Equations 9.24 can be generated from a minimum of fatigue data on undamaged and impacted material and are capable of predicting the fatigue strength σ_{nt} of impacted specimens at a given impact energy and a required number of cycles. They can therefore be used to set maximum allowable stress limits for the material.

9.6 PEXR as an Indication of the Damage State Caused by Impact and Zero-Tension Fatigue Loading

Penetrant enhanced X-ray (PEXR) proved to be an invaluable method for following the initiation and propagation of fatigue damage in both undamaged and impacted CFRP specimens, it proving possible to observe the spread of matrix cracking and delamination, the two dominant damage mechanisms before final collapse.

On a superficial level, the method illustrated the patterns of damage on the specimen surfaces by bubbling as air was drawn in and out of the surface cracks, the patterns of bubbles bearing a strong resemblance to the micro-damage area (Section 7.2.2.3). However this technique is only useful in illustrating surface and edge damage and the bubble pattern/micro-damage correlation would probably be less convincing if the surface plies were $\pm 45^\circ$ or unidirectional 0° rather than the $0^\circ/90^\circ$ woven plies of the specimens in the present study, which are more susceptible to matrix failure. It is also doubtful whether PEXR would follow the propagation of damage adequately without the presence of surface and/or edge damage to allow the passage of penetrant to the sub-surface plies. The value of this technique in detecting impact and fatigue damage in practical composite

structures of a significant size is, therefore limited as access to the damaged area may well be restricted to the impact face, often the least damaged face of the material under low velocity impact loading (Section 5.3).

PEXR illustrated, for both undamaged and impacted specimens, the importance of the resin-rich zones and tow cross-overs (obviously both characteristics of a woven material) as sites for the initiation of matrix cracking (Figure 7.2). Not only does a resin-rich zone constitute an area of weakness in the laminate, but in the case of a woven composite this weak area coincides with a stress concentration associated with the deformation of the fibres at the tow cross-overs. These two factors combine to produce regions which are preferred for the initiation of fatigue damage within the material.

In the case of undamaged specimens the sites of selective absorption of penetrant, associated with tow cross-overs, were evenly distributed throughout the specimen gauge length reflecting the absence of an obvious local material or induced macro-flaw. Although a thorough investigation of the spread of damage by PEXR was not conducted in the case of undamaged specimens it was evident that the intensity and extent of the X-ray image increased with fatigue cycles as the matrix cracks spread and increased in density, allowing the presence of greater quantities of penetrant.

The influence of interlaminar edge stresses is illustrated by the greater density of matrix cracks at the specimen edges and also by the development of edge delamination towards the end of the specimen life (Figure 7.2) although both of these effects could be partially due to the influence of stress concentrations at the cut edges of the specimens.

Although the later stages of fatigue damage development in undamaged materials were not observed, Schulte [113] suggested that, in woven fabric material under tension-tension fatigue (R=0.1) the final collapse mechanism is dominated by the production of internal delaminations at the intersections of matrix cracks in adjacent layers followed by fibre failure at the undulations in the 0° plies.

Taken in isolation, the development of matrix cracking at the tow cross-overs seems to be beneficial to the tensile strength of the material, providing a 'pseudo-

plastic' zone of stress relieving damage (Section 7.3). Material which is observed to contain only fatigue induced micro-damage can therefore be regarded as 'safe' from the point of view of tensile strength, if not from that of tensile modulus or compressive properties which tend to be degraded by the presence of matrix cracks, as discussed in Section 9.8. However, the absence of any other type of damage *must not* be taken as an indication that the material is being cycled at a 'safe' maximum stress level. Micro-damage of the form discussed here is, for all applied stress levels, the first to propagate, being followed by more damaging modes such as delamination and eventually fibre failure.

For prior impact damaged material PEXR is an ideal method for following the spread of fatigue damage, the ruptured surfaces of the laminate providing excellent passage for the penetrant to the internal damage zones.

Under zero-tension fatigue loading three distinct areas of fatigue related damage were observed to develop in the impacted specimens. The first 10 - 20% of the fatigue life for both 2.94J and 6.87J was characterised by the rapid growth of matrix cracking mainly in the direction perpendicular to the applied load, propagating along the 90° material in the 0°/90° plies, although limited matrix cracking in the 0° and ±45° materials gave rise to general spread of fatigue damage from the original impact site (Figures 7.16 and 7.17). The likely mechanism for such damage growth is for the transverse matrix cracks to be deflected into adjacent layers at the ply interfaces and also at the interfaces between warp and weft material within each ply. Longitudinal cracking could also be induced in the 0°/90° plies due to the Poisson's mis-match between the two fibre directions tending to produce a transverse tensile stress in the 0° material.

Generally speaking, by 20% of specimen life, matrix cracking had propagated from the impact site to the edges of the specimens, although the rate of growth of this type of damage was lower for the 6.87J specimens than for the 2.94J specimens for a given fatigue stress ratio suggesting that matrix failure of this type is influenced by σ_{max} rather than $\frac{\sigma_{max}}{\sigma_{rt}}$. Matrix cracking continued to grow at a reduced rate throughout the rest of the specimen life, the damage area being constrained to grow in the direction parallel to the applied load, whilst still containing matrix

cracking in all fibre directions.

The first 85 - 90% of the specimen life for both 2.94J and 6.87J specimens is also characterised by steady delamination growth from the original impact site, although the rate of delamination area growth over this range of fatigue cycle ratio $\frac{n}{N_f}$ is, in this case faster for the 6.87J specimens (Section 7.2.2.3). In the case of 2.94J specimens the tendency was for the X-ray to show dominant delamination growth parallel to the direction of the applied load (Figure 7.20), an observation supported by work by Cantwell et al [82] on zero-tension fatigue of impacted non-woven CFRP laminates and by Ramani and Williams [114] for notched laminates under similar loading conditions. In both cases the delamination growth was observed to be bounded by longitudinal splitting. This observation was not made in the present case.

For the 6.87J specimens the tendency was for the X-ray to show delamination growing at $\pm 45°$ to the direction of the applied load (Figure 7.23) suggesting that, although delamination may be growing in other directions, the dominant growth is at these orientations. This observation has also been made by Clark [23], Clark and van Blaricum [76] and Saunders and van Blaricum [103]. Saunders and van Blaricum [103] have further suggested that over the period of controlled delamination growth, that growth is generally confined to the interfaces at which the largest impact induced delamination took place and is influenced by the orientation of the plies bounding those delaminations. This observation is supported by the present work, at least in the case of 6.87J specimens. The most noticeable feature of the damage zone caused by a 6.87J impact (Section 5.3.3.2) were delaminations between the $+45°$ and $-45°$ material in the angle-ply layers. Delamination would therefore seem to grow in these specimens predominantly by a process of shearing between the warp and weft material in the $\pm 45°$ plies.

It is less evident why the preferred growth direction for delaminations in the 2.94J specimens should be parallel to the direction of applied loading. Furthemore, unlike the case of 6.87J specimens there is no clear correlation between the original impact damage (Section 5.3.3.2) and the subsequent growth patterns under zero-tension loading. However it is evident that the development of delamination under

fatigue loading is closely dependent on the types and positions of the original impact damage and therefore, to some extent on the impact energy.

Over the final 10 - 15% of the fatigue life the rate of growth of delamination area with fatigue cycles increases dramatically for 2.94J specimens representing the final collapse of the specimen towards eventual separation (Section 7.2.2.3). Lack of experimental data in this final region of the fatigue life for 6.87J specimens prevents any firm conclusion being made about collapse of these specimens, although it is likely that a similarly impressive increase in delamination growth rate would occur at this time. It is evident from Figure 9.19 for 2.94J specimens that the growth of delamination damage area A_d with fatigue cycle ratio is independent of the applied stress ratio $\frac{\sigma_{max}}{\sigma_{rt}}$. This effect can also be seen in the curve for 6.87J specimens (Figure 9.20) although there is considerably greater scatter in this case. This suggests that delamination area A_d can be used to characterise the specimen under zero-tension fatigue conditions, detected delamination area being used to predict the remaining life of the specimens. The forms of Figures 9.19 and 9.20 suggest that a hyperbolic, exponential or quadratic relationship exists between fatigue cycle ratio and delamination damage area and expressions of the following form were investigated:-

$$A_d = A + B\cosh\left(\frac{n}{N_f - n}\right)$$

$$A_d = A + Be^{\frac{n}{N_f - n}}$$

$$A_d = A + B\left(\frac{n}{N_f - n}\right)^2$$

Best fit analyses were employed to determine the constants A and B for each expression and the resulting curves are shown in Figures 9.21 and 9.22. Hyperbolic and exponential expressions are almost coincident in each case, the squared relationship providing a smoother transition from controlled to rapid delamination growth which fits the experimental data rather better. The best fit quadratic expressions are for a 2.94J impact energy:-

$$A_d = 138.32 + 2.30\left(\frac{n}{N_f - n}\right)^2 \qquad (9.26)$$

and for a 6.87J impact energy:-

$$A_d = 356.54 + 24.91\left(\frac{n}{N_f - n}\right)^2 \tag{9.27}$$

However, it can be seen from Figures 9.21 and 9.22 that none of the curves provide an adequate representation of the experimental results, in particular missing the controlled slow growth of delamination over the first 85 - 90% of the fatigue life. This is particularly poor for the 6.87J specimens as the initial growth rate of delamination is higher. It is therefore suggested that the growth of delamination damage must be characterised by experiment.

However, in the case of the 2.94J the flatness of the curve over the period of controlled delamination growth means that it would be difficult to determine the difference between A_d at, say $\frac{n}{N_f} = 0.2$ and 0.8 experimentally. The only area of the characteristic where there is an appreciable change of delamination area with fatigue cycle ratio is over the final collapse part of the specimen life where the severity of the damage is evident visually without the aid of PEXR and where the only conclusion that can be drawn about fatigue life is that the catastrophic failure of the specimen is imminent. For 6.87J specimens the steeper curve over the region of controlled delamination growth (Figure 9.20) means that it should be possible to predict $\frac{n}{N_f}$ from A_d but in this case the larger scatter would make any prediction at best uncertain and therefore unsafe.

This leads to the conclusion that, for these specimens damaged by low velocity impact loading and subsequent zero-tension fatigue, the area of the impact damage zone, as determined by PEXR, cannot be used reliably to assess the fatigue life of the material.

From a fatigue cycle ratio $\frac{n}{N_f}$ of 30 - 40% the first signs of edge delamination began to appear in specimens impacted at both energies (Figures 7.20 and 7.24). At first sight these areas seem to be unconnected with the central impact delamination growth. However, in the case of 2.94J specimens edge delamination tended to form at the edges on a line perpendicular to the applied load (i.e on the same level as the impact damage). This may be due to a redistribution of load to the specimen edges as a result of the central impact locally reducing the

specimen stiffness. In the case of 6.87J edge delamination appeared along lines drawn at $\pm 45^{\circ}$ through the original impact centre (Figure 7.24). It is evident that the growth of edge delamination and impact delamination are not unconnected. Work by Sturgeon [108] on zero-tension fatigue of specimens containing drilled holes may provide some explanation of the observations made in the case of the 6.87J. Fatigue damage, propagating from the central stress concentration along $\pm 45^{\circ}$ directions, was seen to induce delaminations where the developing damage intersected the edges. Obviously, in the case of the 2.94J specimens, where the predominant direction of damage propagation is parallel to the applied load, the damage would not intersect the edges and produce this effect.

It is noticeable that final failure of any of the specimens does not occur before delamination growing from the impact site and that associated with the specimen edges coalesce and the integrity of the specimens is lost over a large part of the gauge length (Figures 7.21 and 7.25), this result echoing similar work by Ramkumar [77] on non-woven materials. The final, rapid growth of delamination over the last 10 - 15% of the specimen life is associated with the joining of the two types of delamination before final separation.

For impacted material at both levels the presence of micro-cracking is beneficial to the residual tensile strength, providing a stress relieving mechanism and, in effect masking the stress concentrating effects of the impact damage zone. However, micro-damage growth is often accompanied by delamination growth later in the specimen life and which eventually leads to final failure. Delamination growth is largely unnoticeable over the majority of the specimen life and is only useful as an indication of imminent catastrophic failure. Therefore, it must be concluded that, if PEXR is to be used as an NDT technique under conditions where the amplitude of the loading is unknown, then for impacted material under zero-tension loading a 'no damage growth' criterion should be observed for the determination of safe operating strain levels.

9.7 Residual Stiffness as an Indication of the Damage State Caused by Impact and Zero-Tension Fatigue Loading

Perhaps the most significant mechanical properties of engineering materials are strength, stiffness and life. Measurement of strength or life during fatigue damage development is not feasible due to the destructive nature of the required tests. Stiffness can be measured frequently throughout the life of an individual specimen and is therefore a possible NDT method which could be used to establish residual strength and life of fatigue loaded composites.

Numerous workers have attempted to establish a relationship between axial stiffness and fatigue cycle ratio for various lay-ups of both woven and non-woven CFRP under tension and compression dominated fatigue loading. Noteable amongst these have been Schulte [113], Jamison et al [115] and Camponeschi and Stinchcomb [116] for undamaged specimens, Shimokawa and Hamaguchi [117] and Gibbins and Stinchcomb [118] for notched specimens and Saunders and van Blaricum [103] for impact damaged CFRP under compression dominated fatigue. Shimokawa and Hamaguchi [117] observed that for woven CFRP specimens containing notches, the relationship between stiffness ratio and fatigue cycle ratio was independent of the applied stress level. This suggests that stiffness ratio $\frac{E_{at}}{E_{rt}}$ can be used to charaterise the material under fatigue loading, being used as a non-destructive indication of fatigue life.

The relationship between stiffness ratio $\frac{E_{at}}{E_{rt}}$ and fatigue cycle ratio $\frac{n}{N_f}$ has been discussed in Section 7.2.2.2. It was found that after initial gentle reductions in stiffness up to 80% of the specimen life, there was a rapid fall to zero (Figures 7.7 and 7.8). Thus the specimens appear to be exhibiting a form of 'sudden death' behaviour, whereby the stiffness does not fall appreciably over most of the life and then reduces rapidly as the specimen reaches catastrophic failure (both sudden death and steady degredation behaviour has been observed by the above workers). Moreover, there is some evidence that the specimens are exhibiting the 'three

phase' stiffness reduction behaviour noted by other workers for plain [113], [115] and notched [117] specimens, i.e:-

- *Phase I.* Initial rapid reduction in stiffness over the initial part of the specimen life (typically the first 5 - 20%).
- *Phase II.* Steady slow reduction in stiffness over the majority of the life (typically up to $\frac{n}{N_f}$ = 85 - 95%).
- *Phase III.* Final rapid reduction in stiffness towards final failure (typically over the final 5 - 15%).

For both 2.94J and 6.87J specimens *Phase I* and *Phase II* are not distinct, the subtle decrease in slope between the two not being detectable in the experimental scatter.

The trends described above are similar for all failed specimens at both impact levels and are apparently independent of the maximum fatigue stress to which the specimens are subjected, supporting the observations of Shimokawa and Hamaguchi [117]. This is illustrated in Figures 9.23 and 9.24. The results suggest, for a given impact condition, energy and material, there is an unique relationship between axial stiffness ratio $\frac{E_{at}}{E_{ri}}$ and fatigue cycle ratio $\frac{n}{N_f}$, providing the opportunity to use stiffness as a non-destructive means to predict the zero-tension fatigue life of the specimens. As in the case of delamination damage area (Section 9.6), the forms of the curves do not lend themselves to the generation of simple analytical expressions and the characteristic should be determined experimentally.

Scatter in the stiffness results is relatively high, especially in the case of the 2.94J impact specimens (Figure 9.23). As well as normal fatigue variability this is probably due, as in the case of post-impact static tensile loading (Section 6.3.1), to the fact that this impact level is near the threshold level below which the specimen behaviour is largely unaffected by the impact. Small variations in the impact event around this energy level may give rise to large variations in post-impact behaviour.

As in the case of delamination growth however the curves are relatively flat over the region of most use (i.e the first 80% or so of the specimen life). Couple this

with the experimental scatter and it is evident that axial stiffness measurement would make a very unreliable NDT method for use in obtaining information about the structural integrity impacted CFRP under zero-tension loading. The only part of the characteristic where there is an appreciable change in stiffness with fatigue cycles is over the last 20% of the life where the only conclusion that can be obtained is that the material is about to fail catastrophically. It can therefore be seen that axial stiffness would be difficult to justify as a means to predict the fatigue life of impacted specimens loaded under zero-tension fatigue.

9.8 The Relationship between Stiffness Change and Internal Damage in Fatigue Loaded Specimens

It is evident from an examination of the delamination growth curves (Figures 9.19 and 9.20), the stiffness ratio curves (Figures 9.23 and 9.24) and the general discussion in Chapter 7 that there is a strong correlation between the growth of impact induced delamination under constant amplitude zero-tension fatigue loading and residual tensile stiffness of the specimens tested in this study.

Residual stiffness could be influenced by four damage parameters, namely fibre/matrix debonding, matrix cracking, delamination and fibre failure. It was not possible with PEXR to observe fibre failure, nor to distinguish between debonding and matrix failure so the discussion here will concentrate on the relationship between observable damage modes and axial stiffness ratio.

Specimens impacted at both 2.94J and 6.87J and cycled at a stress level below approximately $\frac{\sigma_{max}}{\sigma_{rt}} = 0.45$ show no delamination growth up to the run-out at 10^6 cycles (Section 7.2.3.3). Despite this, axial stiffness ratio $\frac{E_{at}}{E_{rt}}$ at $n = 10^6$ shows a measureable decrease until the applied stress level is reduced to $\frac{\sigma_{max}}{\sigma_{rt}} \leq 0.20$ - 0.25 (Section 7.2.2.2), a value which corresponds closely with the minimum applied stress level required to cause propagation of matrix cracking. The tensile stiffness of impacted specimens can therefore be degraded by the sole presence of matrix

cracking in the laminate. Matrix cracking is observed for the specimens in all fibre directions and all plies; stiffness reductions may be related to the proportion of plies at each orientation. However, it is impossible to ascertain the influence of matrix failure in each direction on specimen stiffness without the aid of experimental data on simpler lay-ups (e.g unidirectional, cross-ply, angle-ply).

For specimens cycled at $\frac{\sigma_{max}}{\sigma_{rt}} = 0.45$ the specimens reached the run-out of 10^6 cycles and showed stiffness reductions of approximately 30% for the 2.94J impact level, and 20% for the 6.87J specimens (Table 7.30). Compare these appreciable losses in stiffness with the improvements in tensile strength for the same specimens (Tables 7.40 and 7.41). The 6.87J specimen cycled at $\frac{\sigma_{max}}{\sigma_{rt}} = 0.35$ showed a larger reduction in stiffness but this was against the experimental trend shown for all other applied stress levels and is therefore likely to be due to an isolated experimental error. The levels of matrix cracking present in the run-out specimens cycled at $\frac{\sigma_{max}}{\sigma_{rt}} = 0.45$ are likely to be the most severe occurring in isolation (i.e without the presence of other types of damage), as specimens loaded at a higher stress or at the same stress for a greater number of cycles would be likely to see the initiation and subsequent growth of delamination. It is therefore suggested that, under zero-tension loading, the maximum tensile stiffness reduction for specimens containing only matrix cracking would be approximately 30% for 2.94J impact specimens and 20% for the 6.87J specimens.

In the two impact cases, the delamination growth curves (Figures 9.19 and 9.20) and the residual stiffness curves (Figures 9.23 and 9.24) are almost a mirror image of one another. In the former case a slow rise in delamination over the first 85 - 90% of the specimen life is followed by a rapid growth towards failure. In the latter case a slow fall in specimen stiffness over the first 80% of the life is followed by a rapid fall towards failure. In the case of residual stiffness of a 6.87J specimen there seems to be an initial more rapid degredation over the first 20% of the specimen life, although this is not distinct. This is not matched by the relevant delamination growth curve and may therefore be due to some other damage mechanism. It is possible to characterise the three phases of stiffness reduction discussed in Section 9.7 in terms of the damage mechanisms at each

stage.

The initial rapid fall in stiffness over the first 20% of the specimen life for 6.87J is caused by the combination of steady delamination growth from the impact site plus the initial rapid growth of micro-cracking in the matrix material observed over the first 10 - 20% of the life. The latter damage would, of course not be indicated on the delamination growth curve (Figure 9.20). For the 2.94J specimens, although the damage mechanisms are the same there is no distinct indication of this initial rapid fall in stiffness (Figure 9.23). In both cases it is difficult to be confident of such subtle effects, due to experimental variability. It has been noted that the initial growth of matrix cracking tended to be more rapid in the case of the 2.94J specimens (Section 9.6). An initial drop of stiffness may have been over a smaller percentage of the life and would possibly be missed by the experimental techniques. Furthermore, although the initial rate of increase in delamination area was approximately the same in both cases (Figures 9.19 and 9.20), if the suggestion that initial delamination growth is confined to the interfaces where the largest impact induced delamination occur (Section 9.6) is correct, then delamination growth under fatigue loading would be more easily detected in the 6.87J specimens. This argument may also apply to the growth of micro-cracking which is observed to propagate from the impact site.

The gentle fall in stiffness over *Phase II* is characterised by the steady, slow growth of the impact induced delamination. The delamination growth rate for 6.87J specimens (Figure 9.20) over this region is greater than that for the 2.94J specimens (Figure 9.19) and this is reflected in the higher rate of loss of specimen stiffness with applied fatigue cycle ratio over this region. Although edge delamination initiation and growth is also a feature of this phase of damage development, there are no distinct indications of its presence in the residual stiffness curves. Edge delamination has previously been shown [119] to influence longitudinal stiffness and its apparent lack of influence in the present case may be entirely due to the fact that stiffness is being measured locally across the damage site rather than globally by the use of LVDTs [119]. At the end of *Phase II* the stiffness ratio of the specimens is approximately 80% for the 2.94J specimens and 70% for the

6.87J specimens. This is the reverse of the effect shown for matrix cracking only. Matrix cracking appears to have a more severe effect on the stiffness of a 2.94J specimen, whereas delamination influences the stiffness of a 6.87J specimen to a greater degree. This observation is reflected in the rate of growth for the two types of damage at the each impact energy. Direct comparison between the two impact energies should, strictly not be made in the case of the delamination growth as the mechanisms for growth and the positions of the fatigue induced delamination growth are by no means the same in the two cases.

Phase III, the final rapid fall in specimen stiffness towards final failure over the last 10 - 15% of the specimen life, is apparently similar for both impact conditions and is characterised by the rapid growth of the impact induced delamination, its coalescence with the edge delaminations and subsequent fibre failure at final separation. For a fatigue test of constant amplitude as specimen stiffness decreases, applied strain will increase with cycles, giving rise to the observed rapid loss of specimen stiffness at this stage.

The trends discussed above suggest a that a linear relationship between delamination area and stiffness ratio could exist for impacted specimens loaded under zero-tension fatigue. This has certainly been observed for edge delaminated specimens [115], [119]. Figures 9.25 and 9.26 show the plots of delamination damage area against stiffness ratio for 2.94J and 6.87J specimens. In the case of 6.87J specimens (Figure 9.26) there is undoubtably a suggestion of a linear relationship for a delamination area greater than approximately 250mm^2, which is independent of the applied fatigue stress level. However, any trends are masked to a large extent by variability in the data and in the case of the 2.94J specimens no attempt can be made to draw a relationship. This is, to some degree due to the experimental methods and the material behaviour. The criterion for the acceptance of valid delamination growth data was that the damage should not have reached the specimen edges. This obviously limited the acceptable data with the specimens being only 50mm wide. Furthermore, as delamination area did not alter appreciably over the majority of the specimen life and then grew rapidly towards failure it proved extremely difficult to collect data over the final part of the specimen life,

when delamination area and stiffness were changing to a greater extent. Noting the experimental limitations and the possibility of a linear relationship between delamination area and stiffness ratio, it must be concluded that there is no unique relationship between these two variables for the materials and conditions tested in this work.

Chapter 10

Conclusions and Recommendations for Further Work

10.1 Conclusions

This programme of work has been an extensive study of the effects of low-velocity impact on a woven CFRP and the influence of the induced damage on the post-impact static and fatigue performance of the material. The following conclusions can be drawn from the study:-

10.1.1 Impact Loading

- The resistance to initial impact of CFRP plates, as measured by the threshold incident impact energy can be obtained from static load/deflection behaviour provided that the clamping and loading conditions are equivalent.
- Visual examination of a CFRP material is unreliable as a means to indicate the presence of low velocity impact damage and/or degredation of post-impact mechanical properties.

- Both C-scan and X-ray are capable of detecting impact damage before significant strength reductions are encountered. Residual static tensile and compressive strength can be determined from X-ray damage areas by expressions of the form:-

$$\frac{\sigma_r}{\sigma_o} = \left(\frac{A_s}{A_{os}}\right)$$

10.1.2 Post-Impact Static Loading

- For undamaged (plain) material and material impacted at low energies, the CRAG face-supporting anti-buckling guides are not suitable for the accurate determination of static compression behaviour.

- Low velocity impact damage can exist in a CFRP material without degrading its static tensile or compressive strength.

- Of the equivalent flaw approaches to the determination of residual static strength of impacted CFRP currently available, the Caprino Model provides the most accurate predictions.

10.1.3 Post-Impact Fatigue Loading

- For undamaged (plain) material under zero-tension fatigue loading, the tow cross-overs between warp and weft material are preferred sites for the initiation of fatigue damage as through-thickness matrix cracks. Fatigue damage of this type increases the tensile strength of woven CFRP.

- For impacted material, the resistance to zero-tension fatigue loading increases with increasing impact energy.

- For impacted material under zero-tension fatigue loading two distinct zones of damage develop from the impact site, a zone of delamination being surrounded by a zone of through-thickness matrix cracks.

- For impacted material, fatigue damage under zero-tension loading is initiated from the impact site as through-thickness matrix cracking growing primarily

in a direction perpendicular to that of the applied load. The rate of growth with fatigue cycles for this type of damage is greater in specimens impacted at a lower incident energy.

- For impacted material, the presence of fatigue induced matrix cracking increases the tensile strength of the material. This same damage can significantly degrade the tensile modulus.

- The maximum fatigue stress ratio that the material can sustain for 10^6 cycles, showing no damage growth, is independent of the initial incident impact energy.

- The propagation of delamination under zero-tension fatigue loading is closely dependent on the damage modes and through-thickness position of the original impact damage.

- The rate of growth of delamination area with zero-tension fatigue cycle ratio for impact damaged material is higher in specimens impacted at higher incident energies.

- For material impacted at a given incident energy, the growth of delamination area with fatigue cycle ratio is independent of the applied fatigue stress ratio.

- For impacted material under zero-tension fatigue loading, delamination growth can be used as a criterion for indicating imminent catastrophic failure.

- The maximum fatigue stress ratio that the material can sustain for 10^6 cycles, showing no delamination growth, is independent of the initial incident impact energy.

- For material impacted at a given incident energy, the change in axial stiffness ratio with fatigue cycle ratio is independent of the applied fatigue stress ratio.

- For impacted material under zero-tension fatigue loading, axial stiffness ratio can be used as a criterion for indicating imminent catastrophic failure.

- the maximum fatigue stress ratio that the material can sustain for 10^6 cycles, showing no axial stiffness reduction, is independent of the initial incident impact energy.

- The zero-tension fatigue strength of material containing low velocity impact damage can be determined from an expression of the form:-

$$\frac{\sigma_{nt}\,|_{U_i=s}}{\sigma_{nt}\,|_{U_i=0}} = \left(\frac{U_o'}{U_i}\right)^{\xi}$$

10.2 Recommendations for Further Work

At present, in practical engineering applications of CFRP, design allowable strain limits are set artificially low to account for the presence of impact damage. Thus BVID is, perhaps the single most important technical issue restricting the effective use of the material.

Adequate experience now exists for materials and laminates to be optimised for impact resistance and post-impact static behaviour and sufficient research is being conducted to improve materials.

The major deficiency in this area is the lack of adequate analysis techniques for the determination of accurate interlaminar shear and direct stresses. This limits the ability to analytically determine the severity of impact damage and the post-impact static properties. Several models currently exist which successfully predict residual strength of impacted material. However, these rely on the generation of experimental data and are, therefore severely restricted in their breadth of applicability. Although they may depend on complex three-dimensional analyses, advances in computer software and hardware capability make the detailed finite element study of delaminated composites a possibility. Ultimately it may be possible to predict impact and post-impact behaviour from a knowledge of material properties and laminate lay-up.

It is widely recognised that the behaviour of a composite material depends on its lay-up. Present studies have been conducted entirely on practical quasi-isotropic woven laminates. The information gained from this study should be

extended and verified to other laminate configurations and simpler lay-ups should be studied in order to gain a more fundamental understanding of the material behaviour, for example the influence of the ply lay-up on the propagation of delamination under fatigue loading.

The current study has concentrated on zero-tension fatigue loading, perhaps the least damaging for impacted laminates. Before studies can be contemplated on zero-compression, fully reversed and service spectrum loadings the issue of the use of anti-buckling guides should be resolved. A study should be conducted of the performance of impacted CFRP under static compression and compression-dominated fatigue loading using different designs of anti-buckling guide.

There is a considerable jump from simple coupon testing to a full structure under service loading and some thought should be given as to how coupon tests can be related to the full structure, maybe via the intermediate step of considering the use of small, representative structural components.

Published Work

Found,M.S., Howard,I.C., Oxley,M. "The Effect of Low-Velocity Impact Damage on the Fatigue Performance of a Woven Carbon-Fibre-Reinforced Plastic." Proceedings of The Institution of Mechanical Engineers, Fourth International Conference, Fibre Reinforced Composites FRC'90, 1990, pp 245-252.

References

[1] Found,M.S., Howard,I.C., Oxley,M. "The Fatigue Behaviour of CFRP For Aerospace Applications." Lucas Aerospace Contract Report No. 1, University of Sheffield, 1984.

[2] Found,M.S., Howard,I.C., Oxley,M. "The Fatigue Behaviour of CFRP For Aerospace Applications." Lucas Aerospace Contract Report No. 2, University of Sheffield, 1985.

[3] Found,M.S., Howard,I.C., Oxley,M. "The Fatigue Behaviour of CFRP For Aerospace Applications." Lucas Aerospace Contract Report No. 3, University of Sheffield, 1986.

[4] Found,M.S., Howard,I.C., Oxley,M. "The Fatigue Behaviour of CFRP For Aerospace Applications." Lucas Aerospace Contract Report No. 4, University of Sheffield, 1986.

[5] Found,M.S., Howard,I.C., Oxley,M. "The Fatigue Behaviour of CFRP For Aerospace Applications." Lucas Aerospace Contract Report No. 5, University of Sheffield, 1987.

[6] Oxley,M. M.Phil. Thesis, University of Sheffield, 1986.

[7] Hull,D. "An Introduction to Composite Materials." Cambridge Solid State Science Series, 1981.

[8] Tsai,S.W., Hahn,H.T. "Introduction to Composite Materials." Technomic Publishing Co. Inc. 1980.

[9] Piggott,M.R. "Load Bearing Fibre Composites." Pergamon Press, 1980.

[10] Langley,M. "Carbon Fibres in Engineering." McGraw-Hill, 1973.

[11] Gill,R.M. "Carbon Fibres in Composite Materials." Iliffe, 1972.

[12] Introduction to Fibre Reinforced Plastics. University of Sheffield, 1984.

[13] Hoskin,B.C., Baker,A.A. (Eds). "Composite Materials for Aircraft Structures." AIAA, 1986.

[14] Gerharz,J.J., Schütz,D. "Literature Research on the Mechanical Properties of Fibre Composite Materials - Analysis of the State of the Art, v1." RAE Library Translation 2045, 1980.

[15] Foreign Object Impact Damage to Composites. ASTM STP 568, 1975.

[16] Instrumented Impact Testing of Plastics and Composite Materials. ASTM STP 936, 1986.

[17] Moon,F.C. "Wave Propagation and Impact in Composite Materials." in Composite Materials v7: Structural Design and Analysis, Part 1. Academic Press, 1975.

[18] Potter,R.T. "The Interaction of Impact Damage and Tapered-Thickness Sections in CFRP." Composite Structures v3, 1985, pp 319-339.

[19] Dorey,G. "Impact and Crashworthiness of Composite Structures." in Structural Impact and Crashworthiness v1. Elsevier Applied Sciences, 1984.

[20] Sjöblom,P.O., Hartness,J.T., Cordell,T.M. "On Low-Velocity Impact Testing of Composite Materials." J. Comp. Mat. v22, 1988, pp 30-52.

[21] Boll,D.J., Bascom,W.D., Weidner,J.C., Murri,W.J. "A Microscopy Study of Impact Damage of Epoxy-Matrix Carbon-Fibre Composites." J. Mat. Sci. v21, 1986, pp 2667-2677.

[22] Cantwell,W.J., Morton,J. "Detection of Impact Damage in CFRP Laminates." Composite Structures v3, 1985, pp 241-257.

[23] Clark,G. "Modelling of Impact Damage in Composite Laminates." Composites v20, 1989, pp 209-214.

[24] Goldsmith,W. "Impact." Edward Arnold, 1960.

[25] Johnson,K.L. "Contact Mechanics." Cambridge University Press, 1985.

[26] Willis,J.R. "Hertzian Contact of Anisotropic Bodies." J. Mech. Phys. Solids v14, 1966, pp 163-176.

[27] Yang,S.H., Sun,C.T. "Indentation Law for Composite Laminates." ASTM STP 787: Composite Materials Testing and Design, 1982, pp 425-449.

[28] Timoshenko,S., Goodier,J.N. "Theory of Elasticity." Engineering Societies Monographs, 1951.

[29] Greszczuk,L.B. "Response of Isotropic and Composite Materials to Particle Impact." ASTM STP 568: Foreign Object Impact Damage to Composites, 1975, pp 183-212.

[30] Chamis,C.C., Ginty,C.A. "Fiber Composite Structural Durability and Damage Tolerance: Simplified Predictive Methods." NASA Technical Memorandum No. 100179, 1987.

[31] Tan,T.M., Sun,C.T. "Use of Statical Indentation Laws in the Impact Analysis of Laminated Composite Plates." J. App. Mech. v52, 1985, pp 6-12.

[32] Sun,C.T. "An Analytical Method for Evaluation of Impact Damage Energy of Laminated Composites." ASTM STP 617: Composite Materials Testing and Design, 1977, pp 427-440.

[33] Greszczuk,L.B., Chao,H. "Impact Damage in Graphite Fibre-Reinforced Composites." ASTM STP 617: Composite Materials Testing and Design, 1977, pp 389-408.

[34] Graff,K.F. "Wave Motion in Elastic Solids." Oxford Engineering Science Series, 1975.

[35] Mindlin,R.D. "Influence of Rotatory Inertia and Shear on Flexural Motions of Isotropic, Elastic Plates." J. App. Mech. v18, 1951, pp 31-38.

[36] Lal,K.M. "Low Velocity Transverse Impact Behaviour of Eight-Ply Graphite-Epoxy Laminates." J. Reinforced Plastics and Composites v2, 1983, pp 216-225

[37] Timoshenko,S., Woinowsky-Krieger,S. "Theory of Plates and Shells." Engineering Societies Monographs, 1959.

[38] Yang,P.C., Norris,C.H., Stavsky,Y. "Elastic Wave Propagation In Heterogeneous Plates." Int. J. Solids and Structures v2, 1966, pp 665-684.

[39] Whitney,J.M., Pagano,N.J. "Shear Deformation in Heterogeneous Anisotropic Plates. J. App. Mech. v37, 1970, pp 1031-1036.

[40] Sun,C.T., Lai,R.Y.S. "Exact and Approximate Analysis of Transient Wave Propagation in an Isotropic Plate." AIAA J. v12, 1974, pp 1415-1417.

[41] Sun,C.T., Chattopadhyay,S. "Dynamic Response of Anisotropic Plates Under Initial Stress due to Impact of a Mass." J. App. Mech. v42, 1975, pp 693-698.

[42] Dobyns,A.L. "Analysis of Simply-Supported Orthotropic Plates Subject to Static and Dynamic Loads." AIAA J. v19, 1981, pp 642-650.

[43] Aggour,H., Sun,C.T. "Finite Element Analysis of a Laminated Composite Plate Subjected to Circularly Distributed Central Impact Loading." Computers and Structures v28, 1988, pp 729-736.

[44] Humphreys,E.A., Goering,J. "Development of an Analytical Procedure to Calculate Damage Accumulation in Composites during Low Velocity Impact." NASA-CR-166086, 1983.

[45] Ramkumar,R.L. Chen,P.C. "Low-Velocity Impact Response of Laminated Plates." AIAA J. v21, 1983, pp 1448-1452.

[46] Ross,C.A., Malvern,L.E., Sierakowski,R.L., Takeda,N. "Finite Element Analysis of Interlaminar Shear Stress due to Local Impact." ASTM STP 864: Recent Advances in Composites in the United States and Japan, 1985, pp 355-367.

[47] Wu,H.Y.T., Springer,G.S. "Impact Induced Stresses, Strains and Delaminations in Composite Plates." J. Comp. Mat. v22, 1988, pp 533-560.

[48] Wu,H.Y.T., Springer,G.S. "Measurements of Matrix Cracking and Delamination Caused by Impact on Composite Plates." J. Comp. Mat. v22, 1988, pp 518-532.

[49] Sierakowski,R.L., Takeda,N. "An Investigation of In-Plane Failure Mechanisms in Impacted Fibre-Reinforced Plates." Composite Materials: Proc. Japan-U.S. Conference, Tokyo, 1981.

[50] Takeda,N., Sierakowski,R.L., Malvern,L.E. "Microscopic Observations of Cross-Sections of Impacted Composite Laminates." Composites Technology Review v4, 1982, pp 40-44.

[51] Critescu,N., Malvern,L.E., Sierakowski,R.L. "Failure Mechanisms in Composite Plates Impacted by Blunt-Ended Penetrators." ASTM STP 568: Foreign Object Impact Damage to Composites, 1975, pp 159-173.

[52] Bishop,S.M. "The Mechanical Performance and Impact Behaviour of Carbon-Fibre Reinforced PEEK." Composite Structures v3, 1985, pp 295-318.

[53] Dorey,G., Bishop,S.M., Curtis,P.T. "On the Impact Performance of Carbon Fibre Laminates with Epoxy and PEEK Matrices." Composites Science and Technology v23, 1985, pp 221-237.

[54] Preston,J.L., Cook,T.S. "Impact Response of Graphite-Epoxy Flat Laminates using Projectiles that Simulate Aircraft Engine Encounters." ASTM STP 568: Foreign Object Impact Damage to Composites, 1975, pp 49-72.

[55] Potter,R.T. "The Effects of Impact Damage in Tapered Thickness CFRP Laminates." RAE Technical Report No. 85087, 1985.

[56] Caprino,G. "Residual Strength Prediction of Impacted CFRP Laminates." J. Comp. Mat. v18, 1984, pp 508-518.

[57] Joshi,S.P., Sun,C.T. "Impact Induced Fracture in a Laminated Composite." J. Comp. Mat. v19, 1985, pp 51-66.

[58] Joshi,S.P., Sun,C.T. "Impact-Induced Fracture in a Quasi-Isotropic Laminate." J. Composites Technology and Research v9, 1987, pp 40-46.

[59] Dorey,G. "Impact Damage in Composites - Development, Consequences and Prevention." Proc. ICCM VI/ECCM II v3, 1987, pp 3.1-3.26.

[60] Dorey,G. "Fracture Behaviour and Residual Strength of Carbon Fibre Laminates Subjected to Impact Loads." AGARD CP 163, 1974, Paper B.3.

[61] Dorey,G., Sidey,G.R., Hutchings,J. "Impact Properties of Carbon Fibre/Kevlar 49 Fibre Hybrid Composites." Composites v9, 1978, pp 25-32.

[62] Curtis,P.T., Bishop,S.M. "An Assessment of the Potential of Woven Carbon Fibre-Reinforced Plastics for High Performance Applications." Composites v15, 1984, pp 259-265.

[63] Bishop,S.M. "A Review of the Strength and Failure of High-Performance Woven Carbon Fibre-Reinforced Plastics." RAE Technical Report No. 86036, 1986.

[64] Williams,J.G., Rhodes, M.D. "Effect of Resin on Impact Damage Tolerance of Graphite/Epoxy Laminates." ASTM STP 787: Composite Materials Testing and Design, 1982, pp 450-480.

[65] Madan,R.C. "Composite Transport Wing Technology Development." NASA-CR-178409, 1988.

[66] Potter,R.T. "Some Fractographic Investigations of Compressive Failures in Carbon-Fibre Reinforced Plastics." RAE Technical Report No. 86049, 1986.

[67] Shuart,M.J., Williams,J.G. "Compression Behaviour of ±45° Dominated Laminates with a Circular Hole or Impact Damage." AIAA J. v24, 1986, pp 115-122.

[68] Stone,D.W.E., Clarke,B. "Non-Destructive Evaluation of Composite Structures- An Overview." Proc. ICCM VI/ECCM II v1, 1987, pp 28-59.

[69] Cawley,P., Adams,R.D. "Defect Types and Non-destructive Testing Techniques for Composites and Bonded Joints." Materials Science and Technology v5, 1989, pp 413-425.

[70] Mahoon,A. "The Role of Non-Destructive Testing in the Airworthiness Certification of Civil Aircraft Composite Structures." Composites v19, 1988, pp 229-235.

[71] Liu,D., Lillycrop,L.S., Malvern,L.E., Sun,C.T. "The Evaluation of Delamination - An Edge Replication Study." Experimental Techniques v11, 1987, pp 20-25.

[72] Freeman,S.M. "Characterisation of Lamina and Interlaminar Damage in Graphite/Epoxy Composites by the Deply Technique." ASTM STP 787: Composite Materials Testing and Design, 1982, pp 50-62.

[73] Potter,R.T. "Environmental Effects on the Post-Impact Compressive Strength of CFC." RAE Technical Memo. Mat./Str. 1088, 1987.

[74] Preuss,T.E., Clark,G. "Use of Time-of-Flight C-Scanning for Assessment of Impact Damage in Composites." Composites v19, 1988, pp 145-148.

[75] Clarke,B. Private Communication, 1984.

[76] Clark,G., van Blaricum,T.J. "Load Spectrum Modification Effects on Fatigue of Impact-Damaged Carbon Fibre Composite Coupons." Composites v18, 1987, pp 243-251.

[77] Ramkumar,R.L. "Effect of Low-Velocity Impact Damage on the Fatigue Behaviour of Graphite Epoxy Laminates." ASTM STP 813: Long Term Behaviour of Composites, 1983, pp 116-135.

[78] Husman,G.E., Whitney,J.M., Halpin, J.C. "Residual Strength Characterisation of Laminated Composites Subjected to Impact Loading." ASTM STP 568: Foreign Object Impact Damage to Composites, 1975, pp 92-114.

[79] Avva,V.S., Vala,J.R., Jeyaseelan,M. "Effect of Impact and Fatigue Loads on the Strength of Graphite/Epoxy Composites." ASTM STP 893: Composite Materials Testing and Design, 1986, pp 196-206.

[80] Avva,V.S. "Impact Initiated Damage in Laminated Composites." AFOSR-TR-82-1038, 1982.

[81] Tiu,W.P., Gott,J., Breckell,T.H., Jones,L. "Residual Static Strength Prediction of Impacted Composite Laminates." Proc. Int. Conf. on Computer Aided Design in Composite Material Technology, 1988, pp 337-351.

[82] Cantwell,W.J., Curtis,P.T., Morton,J. "Impact and Subsequent Fatigue Damage Growth in Carbon Fibre Laminates." Int. J. Fatigue v6, 1984, pp 113-118.

[83] Potter,R.T. "The Structural Significance of Failure Mode in Notched Fibre Reinforced Plastics under Tension." RAE Technical Report No. 82009, 1982.

[84] Potter,R.T., Copley,S.M. "The Effects of Fibre Lay-Up on the Tensile Notch Sensitivity of CFRP Laminates. RAE Technical Report No. 81156, 1981.

[85] Cantwell,W.J., Morton,J., Curtis,P.T. "A Study of the Impact Resistance and Subsequent Zero-Compression Fatigue Performance on Non-Woven and Mixed-Woven Composites." Structural Impact and Crashworthiness v2, 1984, pp 521-531.

[86] Cantwell,W.J., Curtis,P.T., Morton,J. "Post-Impact Fatigue Performance of

Carbon-Fibre Laminates with Non-Woven and Mixed-Woven Layers." Composites v14, 1983, pp 301-305.

[87] Potter,R.T. "On the Mechanism of Tensile Fracture in Notched Fibre Reinforced Plastics." Proc. R. Soc. Lond. A361, 1978, pp 325-341.

[88] Mandell,J.F., Wang,S.S., McGarry,F.J. "The Extension of Crack Tip Damage Zones in Fibre Reinforced Plastic Laminates." J. Comp. Mat. v9, 1975, pp 266-287.

[89] Wang,S.S. "Fracture Mechanics for Delamination Problems in Composite Materials." J. Comp. Mat. v17, 1983, pp 210-223.

[90] Jones,R., Broughton,W., Mousley,R.F., Potter,R.T. "Compression Failures of Damaged Graphite Epoxy Laminates." Composite Structures v3, 1985, pp 167-186.

[91] Chester,W.T., Pavier,M.J. "Predictive Modelling of Damage in CFRP: Delaminations in Carbon-Epoxy." Cambridge Consultants Report C2448-R-03b, 1987.

[92] Baker,A.A., Jones,R., Callinan,R.J. "Damage Tolerance of Graphite/ Epoxy Composites." Composite Structures v4, 1985, pp 15-44.

[93] Sih,G.C., Chen,E.P. "Cracks in Composite Materials." v6 in the Series Mechanics of Fracture. Martinus Nijhoff, 1981.

[94] Sih,G.C., Paris,P.C., Irwin,G.R. "On Cracks in Rectilinearly Anisotropic Bodies." Int. J. Fracture v1, 1965, pp 189-203.

[95] Waddoups,M.E., Eisenmann,J.R., Kaminski,B.E. "Macroscopic Fracture Mechanics of Advanced Composite Materials." J. Comp. Mat. v5, 1971, pp 446-454.

[96] Lal,K.M. "Residual Strength Assessment of Low Velocity Impact Damage of Graphite-Epoxy Laminates." J. Reinf. Plastics and Composites v2, 1983, pp 226-238.

[97] Lal,K.M. "Prediction of Residual Tensile Strength of Transversely Impacted Composite Laminates." Structures and Solid Mechanics, NASA CP-2245, 1982.

[98] Caprino,G. "On the Prediction of Residual Strength for Notched Laminates." J. Mat. Sci. v18, 1983, pp 2269-2273.

[99] Crivelli-Visconti,I., Caprino,G., Di Ilio,A., Carrino,L. "Impact Tests on CFRP: a Static-Dynamic Analogy." Proc. 4th Int. SAMPE Conf., 1983.

[100] Whitney,J.M., Nuismer,R.J. "Stress Fracture Criteria for Laminated Composites Containing Stress Concentrations." J. Comp. Mat. v8, 1974, pp 253-265.

[101] Nuismer,R.J., Whitney,J.M. "Uniaxial Failure of Composite Laminates Containing Stress Concentrations." ASTM STP 593: Fracture Mechanics of Composites, 1975, pp 117-142.

[102] Rosenfeld,M.S., Gause,L.W. "Compression Fatigue Behaviour of Graphite/Epoxy in the Presence of Stress Raisers." ASTM STP 723: Fatigue of Fibrous Composite Materials, 1981, pp 174-196.

[103] Saunders,D.S., van Blaricum,T.J. "Effect of Load Duration on the Fatigue Behaviour of Graphite/Epoxy Laminates Containing Delaminations." Composites v19, 1988, pp 217-228.

[104] Curtis,P.T. Ed. "CRAG Test Methods for the Measurement of the Engineering Properties of Fibre-Reinforced Plastics." RAE Technical Report No. 84102, 1984. Updated as RAE TR85099, 1985 and RAE TR88012, 1988.

[105] "High Temperature Resistant Prepregs of Unidirectional Carbon, Glass and Aramid Fibre." Ciba-Geigy Fibredux 914 Information Sheet No. FTA.49d, 1981. Updated as Information Sheet No. FTA.49e, 1984.

[106] Owen,M.J. "Fatigue Testing of Fibre Reinforced Plastics." Composites v1, 1970, pp 346-355.

[107] Bevan,L.G. "Axial and Short Beam Shear Fatigue Properties of CFRP Laminates." Composites v8, 1977, pp 227-232.

[108] Sturgeon,J.B. "Fatigue of Multi-Directional Carbon Fibre-Reinforced Plastics." Composites v8, 1977, pp 221-226.

[109] Miller,K.J. "An Introduction to Fracture Mechanics." in Mechanical and Thermal Behaviour of Metallic Materials. Soc. Italiana di Fisica, 1982.

[110] Awerbuch,J., Madhukar,M.S. "Notched Strength of Composite Laminates: Predictions and Experiments - A Review." J. Reinf. Plastics and Composites v4, 1985.

[111] Mar,J.W., Lin,K.Y. "Fracture Mechanics Correlation for Tensile Failure of Filamentary Composites with Holes." J. Aircraft v14, 1977, pp 703-704.

[112] Mar,J.W., Lin,K.Y. "Fracture of Boron/Aluminum Composites with Discontinuities." J. Comp. Mat. v11, 1977, pp 405-421.

[113] Schulte,K. "Fatigue Damage Development in Carbon Fibre Reinforced Composites." Proceedings of the Institution of Mechanical Engineers, International Conference, Fatigue of Engineering Materials and Structures, 1986, pp 321-327

[114] Ramani,S.V., Williams,D.P. "Notched and Unnotched Fatigue Behaviour of Angle-Ply Graphite/Epoxy Composites." ASTM STP 636: Fatigue of Filamentary Composite Materials, 1977, pp 27-46.

[115] Jamison,R.D., Schulte,K., Reifsnider,K.L., Stinchcomb,W.W. "Characterisation and Analysis of Damage Mechanisms in Tension-Tension Fatigue of Graphite/Epoxy Laminates." ASTM STP 836: Effects of Defects in Composite Materials, 1984, pp 21-55.

[116] Camponeschi,E.T., Stinchcomb,W.W. "Stiffness Reduction as an Indicator of Damage in Graphite/Epoxy Laminates." ASTM STP 787: Composite Materials Testing and Design, 1982, pp 225-246.

[117] Shimokawa,T., Hamaguchi,Y. "Distributions of Fatigue Life and Fatigue Strength in Notched Specimens of a Carbon Eight-Harness-Satin Laminate." J. Comp. Mat. v17, 1983, pp 64-76.

[118] Gibbins,M.N., Stinchcomb,W.W. "Fatigue Response of Composite Laminates with Internal Flaws." ASTM STP 787: Composite Materials Testing and Design, 1982, pp 305-322.

[119] O'Brien,T.K. "Characterisation of Delamination Onset and Growth in a Composite Laminate." ASTM STP 775: Damage in Composite Materials, 1982, pp 140-167.

[120] Kanyanga,S.B. Ph.D. Thesis, University of Sheffield, 1988.

[121] Naeem,M. Ph.D. Thesis, University of Sheffield, 1988.

Appendix A

Cure Cycle Requirements for Ciba-Geigy Fibredux 914C-833-40% (Toray T300-3000 Woven) CFRP Laminates

The CFRP laminates used in the test programme were prepared to commercial standards using the following cure cycle.

- Apply a minimum vacuum of 832 bar to the component and heat at a rate of $\frac{1}{2}$°C - 5°C/minute up to 120°C±5°C and hold the component at this temperature for a dwell period of 30 ± 5 minutes.
- At a period, 15 ± 5 minutes into the dwell, pressurise the autoclave. When the autoclave pressure reaches 210 ± 34kPa, vent the vacuum to atmosphere and continue pressurisation until the pressure ranges between 550kPa and 690kPa.
- At the completion of the dwell period heat the component at a rate of $\frac{1}{2}$°C - 5°C/minute up to 175°C±5°C and maintain at this temperature for between 60 minutes and 75 minutes.

- Cool the structure at a rate of $\frac{1}{2}$°C - 5°C/minute until the component temperature has fallen below 60°C and release pressure.

- Post cure the structure in an air circulating oven for between 240 minutes and 255 minutes at 190°C±5°C. If necessary, support the structure during the post cure operation.

The cure cycle was controlled from calibrated thermocouples and monitoring equipment. Where possible the thermocouples were buried within the trim areas of the components, or alternatively within the tool where it had been demonstrated that it was representative of the thermal behaviour of the component.

Appendix B

Acceptance Criteria for Laminated Structures

The CFRP laminates used in the test programme were inspected by the manufacturers to commercial standards. The relevant parts of the standard are as follows.

- Delamination is acceptable within the body of a component up to a maximum diameter of 15mm without repair subject to relevant size and location requirements.
- Edge delamination is acceptable, subject to repair providing:-
    1. The delamination does not extend into the body of a component by more than 6mm and is of a length not greater than 25mm when investigated by NDT techniques.
    2. The minimum allowable distance between defects is not greater than 75mm.
- Void volume fraction shall be controlled to less than than 2%.
- Surface inclusions are acceptable up to a maximum size of $30mm^2$.
- Indentations are acceptable up to a maximum size of $30mm^2$.

- Fabric distortion is acceptable in local areas up to a maximum size of 100mm in length providing laminate thickness within the defect area is within the thickness and thickness tolerance of the remainder of the component. There shall be no more than one defect of this type in a 350mm × 350mm area and the defect shall be applicable to a single ply only.

- Ridges produced from resin curing either in tool face scratches, or nitches formed by creases in bagging films are acceptable to a height of 1mm.

- Blisters are unacceptable.

- Chipping at edges shall not extend more than 3mm into the component or be of a depth greater than a fibre tow. When measured along the edge of a component, not more than 25% of the edge shall be chipped within a 150mm length.

- The tool faces of components shall be smooth, continuous and free of all defects, except those allowed by the specification.

- The bag faces of components vary in texture dependent on the manufacturing techniques and the type of bagging materials used. The surface texture shall be agreed between the Design, Quality and Materials Departments.

- The tool faces of components shall be of uniform colouration. Surface staining on the tool face of components caused by transference of release agent shall be rejectable. The staining shall be removed by appropriate methods. Other sources of staining shall be reported.

- The bag face of components shall be uniform in colour. Staining shall be reported.

- Fibre plucking caused by inadequate component release from the tool shall be cause for rejection.

- Exposed weave effects at the component tool surface shall be rejected and subject to repair.

- Visual examination of surface texture of machined edges shall show the edge to be smooth and free from resin pull-out or fibre pull-out.

Appendix C

Preparation of Laminates for Impact Testing

Each circular section of the laminate to be impacted was prepared as follows. Strain gauges were not used for all tests, in which case this procedure was greatly simplified.

- Each disc was marked out on both faces of the laminate. The centre of each disc was marked to permit accurate placing of any strain gauges and to aid alignment of the disc for impacting.
- The back face of the disc was lightly abraded using 320 grade wet-or-dry paper and then treated with Genklene to remove dust and grease. These operations provided a key for the strain gauges and conductive paint.
- The strain gauges were applied at the required positions using standard procedures and concluding with an application of Micro-Measurements M-Coat A polyurethane protective strain gauge coating. This coating was allowed to dry thoroughly before proceeding. The application of M-Coat A was vitally important as it provided some measure of electrical insulation between the gauges and conductive paint.
- A piece of Mylar tape was applied over the strain gauges, leaving the terminal strip uncovered. A second piece of tape was applied over the terminal strip.

These were cut to size and the excess removed. This operation provided a second barrier between the conductive paint and the gauges.

- A thin, complete layer of RS Components Aerosol RFI/EMI Shielding (conductive paint) was sprayed on to the back face of the impact discs and allowed to dry thoroughly.

- The Mylar tape was removed from the terminal strip, and the M-Coat A scraped from the terminals leaving them exposed.

- A thin strip of Mylar tape was placed just below the terminal strip to insulate the exposed ends of gauge wire.

- After baring the ends of suitable lengths of Micro-Measurements 136-AWP strain gauge wire, they were soldered to the gauge terminals in the usual fashion. The fine gauge wire was chosen as it would lie within the capacitor gap of the dislacement transducer when assembled and it was desirable to disrupt the capacitor as little as possible. The gauge wire was taped to the underside of the CFRP laminate as a protection against it being pulled off, making sure that the bared ends of wire did not contact each other or the conductive paint coating. The wires were paired and marked as it would be impossible to trace them to source when outside the capacitor.

- The CFRP laminate was clamped in the frame (Figure 3.5) at the desired position, and the gauge wires passed out of the capacitor. All wires were secured against pulling off and all necessary connections were made to the recording apparatus.

Experience with this system proved it to be very delicate and it was found that considerable frustration could be averted by frequently checking for correct operation of the strain gauges throughout the above operations.

Appendix D

The Capacitance Displacement Transducer

The use of a variable capacitance displacement transducer for the impact testing of CFRP laminates arose from the requirements of a rapid response from a transducer which would not interfere with the impact test itself. Simple mechanical transducers (e.g. LVDTs) would have been subject to 'bounce' resulting from slow response and would not have followed the rapid changes in displacement during an impact event adequately.

The capacitor was set up between a fixed plate and a moveable plate with air as the dielectric. The fixed plate was chosen to be a circular sheet of aluminium foil, whilst the moveable plate was the CFRP sheet itself with a suitable conductive film applied to its bottom surface. Impact of the laminate would cause relative movement of the capacitor plates, causing a change in capacitance as a measurable displacement signal.

The equation relating capacitance to the areas and separation of the capacitor plates is:-

$$C = \frac{\epsilon_o \epsilon_r (n-1) a}{d}$$

where:-

C = capacitance

ϵ_o = permittivity of free space

ϵ_r = relative permittivity of dielectric

n = number of plates

a = area of plates

d = distance between plates

Thus to make C as large as possible and hence more easily measured:-

- The area of the plates must be as large as possible with the restriction that they must be smaller than 100mm diameter to fit inside the clamping rings.
- The spacing between the plates must be as small as possible with the restriction that the plates must not touch when the top plate was impacted at the higher energies.

Realistically the diameter of the fixed plate could only be approximately 85mm to allow for the unrestricted passage of the strain gauge wires out of the capacitor and a capacitance of around 10pF was required for measurement. Using the above equation the spacing of the plates was found to be about 5mm.

Simple calculation using Hertzian Contact Theory to calculate an upper bound load for the maximum impact energy and then applying large deflection theory of plates gave a maximum predicted deflection of 3.2mm. Thus allowing for variables not accounted for in the calculations i.e. plate failure, non-ideal clamping it was felt that 85mm diameter plates at a spacing of 5mm provided a sound basis for the design.

The experimental programme was left to illustrate whether this combination of dimensions was the ideal solution for the transducer.

A perspex plug was designed to be fixed inside the bottom clamping ring which fixed the undisturbed capacitor gap at 5mm, and the aluminium foil was glued to its top surface (Figure D1). Conductive paint was applied to the bottom surface of the CFRP laminate as described in Appendix C and electrical connections were made to the foil and to the bottom clamping ring of the frame which was in electrical contact with the paint layer.

Tables

Interlaminar Shear Strength	63 MPa
Ultimate Flexural Strength (warp)	835 MPa
Ultimate Flexural Strength (weft)	865 MPa
Flexural Modulus (warp)	60 GPa
Flexural Modulus (weft)	58 GPa
Ultimate Tensile Strength (warp)	620 MPa
Ultimate Tensile Strength (weft)	620 MPa
Tensile Modulus (warp)	62 GPa
Tensile Modulus (weft)	62 GPa

Table 3.1. Cured Ply Properties of Fibredux

914C-833-40% (Toray T300-3000 Woven) [105].

Zinc Iodide Powder	60g
Water	10ml
Propan-2-ol	10ml
Kodak Photoflo	0.5ml

Table 4.1. Recipe for Zinc Iodide X-Ray Penetrant [75].

Specimen	Load F_s (kN)	Central Displacement w_s (mm)	Energy U_s (J)
LE6170/A1/2/CAL1	1.23	2.19	1.35
LE6170/A1/2/CAL2	1.25	2.42	1.51
LE6169/A1/B4/CAL1	1.65	2.39	1.97
LE6169/A1/B4/CAL2	1.27	1.99	1.26
LE6169/A1/A4/CAL1	1.52	2.53	1.92
LE6169/A1/A4/CAL2	1.50	2.52	1.89
Mean	1.40	2.34	1.65
C of V	0.13	0.09	0.19

Table 5.1. Static Loading of Clamped CFRP Plates. Values of Load, Deflection and Energy at First Failure.

Incident Impact Energy U_i (J)	Specimen	Maximum Central Displacement w_{max} (mm)	Mean w_{max} (mm)	C of V
0	-	0	0	-
0.98	LE6170/A1/2/1	1.35	1.80	0.36
	LE6170/A1/2/10	2.25		
1.96	LE6170/A1/2/11	1.86	2.00	0.10
	LE6169/A1/B1/2	2.15		
2.94	LE6170/A1/2/3	2.37	2.15	0.10
	LE6170/A1/2/12	2.03		
	LE6169/A1/B2/1	2.00		
	LE6169/A1/B2/3	1.93		
	LE6169/A1/B2/5	2.44		
	LE6169/A1/B2/7	2.30		
	LE6169/A1/B2/9	2.30		
	LE6169/A1/B2/11	1.85		
	LE6169/A1/B2/13	2.15		
3.93	LE6170/A1/2/4	2.37	2.45	0.05
	LE6170/A1/2/13	2.54		
4.91	LE6170/A1/2/5	2.37	2.78	0.18
	LE6169/A1/B4/2	2.64		
	LE6169/A1/B1/13	3.33		
5.89	LE6170/A1/2/6	2.71	3.02	0.10
	LE6169/A1/B1/4	3.33		
	LE6169/A1/B1/5	3.04		
6.87	LE6170/A1/2/7	2.88	3.14	0.15
	LE6169/A1/B4/3	3.91		
	LE6169/A1/B1/6	3.92		
	LE6169/A1/A4/2	3.04		
	LE6169/A1/A4/3	3.33		
	LE6169/A1/B2/2	2.74		
	LE6169/A1/B2/4	2.74		
	LE6169/A1/B2/6	3.33		
	LE6169/A1/B2/10	2.74		
	LE6169/A1/B2/14	2.74		
7.85	LE6169/A1/B1/7	4.51	4.12	0.08
	LE6169/A1/B1/8	3.92		
	LE6169/A1/B1/9	3.92		
8.83	LE6169/A1/B4/4	2.85	4.06	0.26
	LE6169/A1/B1/11	4.81		
	LE6169/A1/B1/10	4.51		

Table 5.2. Maximum Central Displacement for Impacted CFRP Plates.

Incident Impact Energy U_i (J)	Specimen	Front Face Damage Radius r_f (mm)	Mean r_f (mm)	C of V
0	-	0	0	-
0.98	LE5932/A1/5/7	0.00	0.00	-
	LE6170/A1/1/17	0.00		
	LE6170/A1/1/18	0.00		
	LE6170/A1/2/1	0.00		
	LE6170/A1/2/10	0.00		
1.96	LE5932/A1/5/8	0.57	0.20	1.55
	LE5932/A1/5/16	0.60		
	LE6170/A1/1/19	0.00		
	LE6170/A1/1/20	0.00		
	LE6170/A1/2/2	0.00		
	LE6170/A1/2/11	0.00		
2.94	LE5932/A1/5/9	0.83	0.58	1.33
	LE5932/A1/5/17	0.84		
	LE6170/A1/1/21	0.00		
	LE6170/A1/1/22	0.00		
	LE6170/A1/2/3	0.00		
	LE6170/A1/2/12	0.00		
	LE6169/A1/B4/1	2.00		
	LE6169/A1/B1/12	0.00		
	LE6169/A1/A4/4	1.51		
3.93	LE5932/A1/5/10	0.91	0.57	1.12
	LE5932/A1/5/18	1.21		
	LE6170/A1/1/23	0.00		
	LE6170/A1/1/24	0.00		
	LE6170/A1/2/4	0.00		
	LE6170/A1/2/13	1.28		

Table 5.3. Front Face Damage Radius for Impacted Specimens.

Incident Impact Energy U_i (J)	Specimen	Front Face Damage Radius r_f (mm)	Mean r_f (mm)	C of V
4.91	LE5932/A1/5/11	1.53	1.15	0.79
	LE6170/A1/1/25	1.26		
	LE6170/A1/1/26	1.55		
	LE6170/A1/2/5	0.00		
	LE6170/A1/2/14	1.16		
	LE6169/A1/B4/2	2.56		
	LE6169/A1/B1/13	0.00		
5.89	LE5932/A1/5/12	2.04	1.73	0.20
	LE6170/A1/1/27	1.83		
	LE6170/A1/1/28	1.82		
	LE6170/A1/2/6	1.24		
6.87	LE5932/A1/5/13	2.45	2.42	0.53
	LE6170/A1/1/29	2.52		
	LE6170/A1/1/30	2.23		
	LE6170/A1/2/7	1.32		
	LE6169/A1/B4/3	3.28		
	LE6169/A1/B1/14	0.00		
	LE6169/A1/A4/2	3.70		
	LE6169/A1/A4/3	3.84		
7.85	LE5932/A1/5/14	2.60	2.54	0.12
	LE6170/A1/1/31	2.81		
	LE6170/A1/2/8	2.22		
8.83	LE5932/A1/5/15	2.77	3.18	0.30
	LE6170/A1/1/32	3.07		
	LE6170/A1/2/9	2.17		
	LE6169/A1/B4/4	3.17		
	LE6169/A1/B1/15	4.73		

Table 5.3A Front Face Damage Radius for Impacted Specimens.

Incident Impact Energy U_i (J)	Specimen	Residual Indentation Depth δ_r (mm)	Mean δ_r (mm)	C of V
0	-	0	0	-
0.98	LE6170/A1/1/7	0.00	0.00	-
	LE6170/A1/1/18	0.00		
	LE6170/A1/2/1	0.00		
	LE6170/A1/2/10	0.00		
1.96	LE6170/A1/1/19	0.00	0.00	-
	LE6170/A1/1/20	0.00		
	LE6170/A1/2/2	0.00		
	LE6170/A1/2/11	0.00		
2.94	LE6170/A1/1/21	0.04	0.02	1.12
	LE6170/A1/1/22	0.05		
	LE6170/A1/2/3	0.03		
	LE6170/A1/2/12	0.04		
	LE6169/A1/B4/1	0.00		
	LE6169/A1/B1/12	0.00		
	LE6169/A1/A4/4	0.00		
3.93	LE6170/A1/1/23	0.07	0.07	0.08
	LE6170/A1/1/24	0.06		
	LE6170/A1/2/4	0.07		
	LE6170/A1/2/13	0.07		
4.91	LE6170/A1/1/25	0.09	0.08	0.13
	LE6170/A1/1/26	0.09		
	LE6170/A1/2/5	0.08		
	LE6170/A1/2/14	0.09		
	LE6169/A1/B4/2	0.07		
	LE6169/A1/B1/13	0.07		

Table 5.4. Front Face Residual Indentation Depth

for Impacted Specimens.

Incident Impact Energy U_i (J)	Specimen	Residual Indentation Depth δ_r (mm)	Mean δ_r (mm)	C of V
5.89	LE6170/A1/1/27	0.15	0.12	0.20
	LE6170/A1/1/28	0.11		
	LE6170/A1/2/6	0.11		
6.87	LE6170/A1/1/29	0.23	0.17	0.29
	LE6170/A1/1/30	0.23		
	LE6170/A1/2/7	0.15		
	LE6169/A1/B4/3	0.19		
	LE6169/A1/B1/14	0.10		
	LE6169/A1/A4/2	0.15		
	LE6169/A1/A4/3	0.14		
7.85	LE6170/A1/1/31	0.27	0.28	0.04
	LE6170/A1/2/8	0.28		
8.83	LE6170/A1/1/32	0.29	0.33	0.12
	LE6170/A1/2/9	0.34		
	LE6169/A1/B4/4	0.30		
	LE6169/A1/B1/15	0.38		

Table 5.4*A* Front Face Residual Indentation Depth for Impacted Specimens.

Incident Impact Energy U_i (J)	Specimen	Back Face 0° Crack Length l_c^0 (mm)	Mean 0° l_c^0 (mm)	C of V
0	-	0	0	-
0.98	LE5932/A1/5/7	0.00	0.00	-
	LE6170/A1/1/17	0.00		
	LE6170/A1/1/18	0.00		
	LE6170/A1/2/1	0.00		
	LE6170/A1/2/10	0.00		
1.96	LE5932/A1/5/8	0.00	2.41	1.56
	LE5932/A1/5/16	0.00		
	LE6170/A1/1/19	0.00		
	LE6170/A1/1/20	8.11		
	LE6170/A1/2/2	6.32		
	LE6170/A1/2/11	0.00		
2.94	LE5932/A1/5/9	7.15	6.78	0.46
	LE5932/A1/5/17	3.35		
	LE6170/A1/1/21	10.49		
	LE6170/A1/1/22	11.65		
	LE6170/A1/2/3	8.96		
	LE6170/A1/2/12	7.04		
	LE6169/A1/B4/1	2.91		
	LE6169/A1/B1/12	5.59		
	LE6169/A1/A4/4	3.84		
3.93	LE5932/A1/5/10	5.80	9.46	0.37
	LE5932/A1/5/18	4.92		
	LE6170/A1/1/23	11.14		
	LE6170/A1/1/24	10.31		
	LE6170/A1/2/4	10.17		
	LE6170/A1/2/13	14.40		

Table 5.5. 0° Back Face Crack Lengths for Impacted Specimens.

Incident Impact Energy U_i (J)	Specimen	Back Face 0° Crack Length l_c^0 (mm)	Mean 0° l_c^0 (mm)	C of V
4.91	LE5932/A1/5/11	11.31	12.98	0.26
	LE6170/A1/1/25	17.14		
	LE6170/A1/1/26	15.09		
	LE6170/A1/2/5	14.05		
	LE6170/A1/2/14	15.70		
	LE6169/A1/B4/2	7.71		
	LE6169/A1/B1/13	9.83		
5.89	LE5932/A1/5/12	9.97	17.16	0.28
	LE6170/A1/1/27	19.38		
	LE6170/A1/1/28	19.64		
	LE6170/A1/2/6	19.65		
6.87	LE5932/A1/5/13	11.17	14.83	0.34
	LE6170/A1/1/29	20.92		
	LE6170/A1/1/30	20.38		
	LE6170/A1/2/7	19.66		
	LE6169/A1/B4/3	15.87		
	LE6169/A1/B1/14	12.78		
	LE6169/A1/A4/2	8.63		
	LE6169/A1/A4/3	9.20		
7.85	LE5932/A1/5/14	14.46	20.02	0.24
	LE6170/A1/1/31	22.92		
	LE6170/A1/2/8	22.67		
8.83	LE5932/A1/5/15	10.53	19.51	0.29
	LE6170/A1/1/32	22.75		
	LE6170/A1/2/9	24.70		
	LE6169/A1/B4/4	17.29		
	LE6169/A1/B1/15	22.27		

Table 5.5A 0° Back Face Crack Lengths for Impacted Specimens.

Incident Impact Energy U_i (J)	Specimen	Back Face 90° Crack Length l_c^{90} (mm)	Mean 90° l_c^{90} (mm)	C of V
0	-	0	0	-
0.98	LE5932/A1/5/7	0.00	0.00	-
	LE6170/A1/1/17	0.00		
	LE6170/A1/1/18	0.00		
	LE6170/A1/2/1	0.00		
	LE6170/A1/2/10	0.00		
1.96	LE5932/A1/5/8	0.00	1.32	1.73
	LE5932/A1/5/16	0.00		
	LE6170/A1/1/19	0.00		
	LE6170/A1/1/20	2.33		
	LE6170/A1/2/2	5.56		
	LE6170/A1/2/11	0.00		
2.94	LE5932/A1/5/9	2.73	5.26	0.55
	LE5932/A1/5/17	2.48		
	LE6170/A1/1/21	8.94		
	LE6170/A1/1/22	8.73		
	LE6170/A1/2/3	7.22		
	LE6170/A1/2/12	7.73		
	LE6169/A1/B4/1	4.92		
	LE6169/A1/B1/12	3.03		
	LE6169/A1/A4/4	1.60		
3.93	LE5932/A1/5/10	3.91	9.34	0.46
	LE5932/A1/5/18	6.64		
	LE6170/A1/1/23	12.92		
	LE6170/A1/1/24	6.82		
	LE6170/A1/2/4	15.30		
	LE6170/A1/2/13	10.44		

Table 5.6. 90° Back Face Crack Lengths for Impacted Specimens.

Incident Impact Energy U_i (J)	Specimen	Back Face 90° Crack Length l_c^{90} (mm)	Mean 90° l_c^{90} (mm)	C of V
4.91	LE5932/A1/5/11	5.67	12.03	0.39
	LE6170/A1/1/25	19.19		
	LE6170/A1/1/26	17.03		
	LE6170/A1/2/5	8.76		
	LE6170/A1/2/14	10.96		
	LE6169/A1/B4/2	11.12		
	LE6169/A1/B1/13	11.50		
5.89	LE5932/A1/5/12	6.03	17.04	0.46
	LE6170/A1/1/27	21.38		
	LE6170/A1/1/28	23.59		
	LE6170/A1/2/6	17.15		
6.87	LE5932/A1/5/13	11.14	15.43	0.30
	LE6170/A1/1/29	19.83		
	LE6170/A1/1/30	21.55		
	LE6170/A1/2/7	19.57		
	LE6169/A1/B4/3	14.65		
	LE6169/A1/B1/14	14.75		
	LE6169/A1/A4/2	13.69		
	LE6169/A1/A4/3	8.23		
7.85	LE5932/A1/5/14	9.70	16.92	0.37
	LE6170/A1/1/31	21.27		
	LE6170/A1/2/8	19.80		
8.83	LE5932/A1/5/15	9.64	19.46	0.30
	LE6170/A1/1/32	22.87		
	LE6170/A1/2/9	24.77		
	LE6169/A1/B4/4	19.21		
	LE6169/A1/B1/15	20.82		

Table 5.6 90° Back Face Crack Lengths for Impacted Specimens.

Incident Impact Energy U_i (J)	Specimen	X-Ray Damage Area A_s (mm^2)	Mean A_s (mm^2)	C of V
0	-	0	0	-
0.98	LE5932/A1/5/7	0	0	-
	LE6170/A1/1/18	0		
	LE6170/A1/1/17	0		
	LE6170/A1/2/1	0		
	LE6170/A1/2/10	0		
1.96	LE5932/A1/5/8	0	9	1.38
	LE5932/A1/5/16	31		
	LE6170/A1/1/19	0		
	LE6170/A1/1/20	7		
	LE6170/A1/2/2	15		
	LE6170/A1/2/11	0		
2.94	LE5932/A1/5/9	49	64	0.30
	LE5932/A1/5/17	55		
	LE6170/A1/1/22	57		
	LE6170/A1/1/21	76		
	LE6170/A1/2/3	50		
	LE6170/A1/2/12	56		
	LE6169/A1/B4/1	102		
3.93	LE5932/A1/5/10	82	90	0.10
	LE5932/A1/5/18	84		
	LE6170/A1/1/23	98		
	LE6170/A1/1/24	100		
	LE6170/A1/2/4	79		
	LE6170/A1/2/13	94		

Table 5.7. X-Ray Damage Area for Impacted Specimens.

Incident Impact Energy U_i (J)	Specimen	X-Ray Damage Area A_s (mm^2)	Mean A_s (mm^2)	C of V
4.91	LE5932/A1/5/11	133	147	0.11
	LE6170/A1/1/26	154		
	LE6170/A1/1/25	147		
	LE6170/A1/2/5	134		
	LE6170/A1/2/14	137		
	LE6169/A1/B4/2	175		
5.89	LE5932/A1/5/12	159	198	0.18
	LE6170/A1/1/27	237		
	LE6170/A1/1/28	215		
	LE6170/A1/2/6	180		
6.87	LE5932/A1/5/13	191	238	0.16
	LE6170/A1/1/30	265		
	LE6170/A1/1/29	280		
	LE6170/A1/2/7	247		
	LE6169/A1/B4/3	206		
7.85	LE5932/A1/5/14	216	248	0.11
	LE6170/A1/1/31	270		
	LE6170/A1/2/8	258		
8.83	LE5932/A1/5/15	251	306	0.13
	LE6170/A1/1/32	323		
	LE6170/A1/2/9	310		
	LE6169/A1/B4/4	341		

Table 5.7A X-Ray Damage Area for Impacted Specimens.

Incident Impact Energy U_i (J)	Specimen	C-Scan Damage Area A_c (mm^2)	Mean A_c (mm^2)	C of V
0	-	0	0	-
0.98	LE5932/A1/5/7	0	0	-
	LE6169/A1/1/1	0		
1.96	LE5932/A1/5/8	0	12	1.73
	LE5932/A1/5/16	0		
	LE6169/A1/1/2	36		
2.94	LE5932/A1/5/9	93	98	0.05
	LE5932/A1/5/17	100		
	LE6169/A1/1/3	102		
3.93	LE5932/A1/5/10	134	135	0.08
	LE5932/A1/5/18	125		
	LE6169/A1/1/4	146		
4.91	LE5932/A1/5/11	174	197	0.16
	LE6169/A1/1/5	219		
5.89	LE5932/A1/5/12	198	230	0.19
	LE6169/A1/1/6	261		
6.87	LE5932/A1/5/13	230	274	0.22
	LE6169/A1/1/7	317		
7.85	LE5932/A1/5/14	261	285	0.12
	LE6169/A1/1/8	309		
8.83	LE5932/A1/5/15	290	328	0.16
	LE6169/A1/1/9	366		

Table 5.8. C-Scan Damage Area for Impacted Specimens.

Specimen	σ_{ut} (MPa)	ϵ_{ut} ($\mu\epsilon$)	E_{ut} (GPa)	ν_{xy}
LE5932/A1/5/1	439.1	8996	47.6	0.30
LE5932/A1/5/2	437.2	-	-	-
LE5932/A1/5/3	428.2	-	-	-
LE6170/A1/1/1	408.2	-	-	-
LE6170/A1/1/2	371.5	-	-	-
LE6170/A1/1/3	428.0	-	-	-
LE6170/A1/1/4	419.5	8830	46.8	0.28
LE6170/A1/1/14	397.9	8267	47.9	0.31
LE6170/A1/1/15	414.4	8029	48.1	0.25
LE6169/A1/1/10	413.4	-	-	-
LE6169/A1/1/11	426.3	-	-	-
LE6169/A1/1/16	432.0	9059	46.8	0.32
LE6169/A1/1/17	417.6	8308	49.1	0.38
LE6170/A1/2/15	417.5	-	-	-
LE6169/A1/B4/5	420.6	-	-	-
LE6169/A1/B1/16	445.9	-	-	-
LE6169/A1/A4/5	455.7	-	-	-
Mean	421.9	8582	47.7	0.31
C of V	0.045	0.051	0.018	0.141

Table 6.1. Tensile Test Results for Undamaged Specimens.

Specimen	U_i (J)	σ_{rt} (MPa)	Mean σ_{rt} (Mpa)	C of V
LE6169/A1/1/1		429.5		
LE6170/A1/1/18	0.98	411.5	409.5	0.051
LE6170/A1/2/1		387.5		
LE6170/A1/1/19		418.9		
LE6170/A1/1/20	1.96	384.3	402.9	0.043
LE6170/A1/2/2		405.5		
LE6169/A1/1/3		337.0		
LE6170/A1/1/22	2.94	293.6	344.9	0.161
LE6169/A1/B4/1		404.1		
LE6170/A1/1/23		278.1		
LE6170/A1/1/24	3.93	286.8	275.7	0.045
LE6170/A1/2/4		262.1		
LE6169/A1/1/5		256.9		
LE6170/A1/1/26	4.91	249.5	258.5	0.038
LE6170/A1/2/5		269.0		
LE6170/A1/1/27		236.7		
LE6170/A1/1/28	5.89	238.7	251.0	0.092
LE6169/A1/B1/4		277.7		
LE6169/A1/1/7		234.0		
LE6170/A1/1/30	6.87	225.3	244.6	0.073
LE6169/A1/B4/3		256.4		
LE6169/A1/B1/14		262.5		
LE6170/A1/1/31		214.0		
LE6170/A1/2/8	7.85	209.5	222.2	0.082
LE6169/A1/B1/7		243.1		
LE6169/A1/1/9		213.1		
LE6170/A1/2/9		212.4		
LE6169/A1/B1/10	8.83	242.6	232.1	0.076
LE6169/A1/B1/15		245.8		
LE6169/A1/A4/1		246.5		
LE6170/A1/1/8	12.7 mm	187.6		
LE6170/A1/1/9	ϕ Hole	184.3	187.1	0.014
LE6170/A1/1/10		189.4		

Table 6.2. Tensile Test Results for Impacted Specimens.

Specimen	σ_{cc} (MPa)	ϵ_{cc} ($\mu\epsilon$)	E_{cc} (GPa)
LE5932/A1/5/4	366.0	-	-
LE5932/A1/5/5	302.2	-	-
LE5932/A1/5/6	384.8	-	-
LE6170/A1/1/5	390.8	-	-
LE6170/A1/1/6	405.8	-	-
LE6170/A1/1/7	398.1	-	-
LE6170/A1/1/16	464.7	13516	48.1
LE6169/A1/1/13	457.9	-	-
LE6169/A1/1/14	437.3	-	-
LE6169/A1/1/15	435.4	-	-
LE6169/A1/1/18	455.3	12788	48.9
LE6169/A1/1/19	455.5	14330	43.6
LE6170/A1/2/16	445.6	-	-
LE6169/A1/B4/6	433.1	-	-
LE6169/A1/B1/17	411.8	-	-
Mean	416.3	13545	46.9
C of V	0.105	0.057	0.061

Table 6.3. Compressive Test Results for Undamaged Specimens.

Specimen	U_i (J)	σ_{rc} (MPa)	Mean σ_{rc} (Mpa)	C of V
LE6170/A1/1/17		463.4		
LE6170/A1/2/10	0.98	445.0	439.3	0.062
LE6169/A1/B1/1		409.4		
LE6169/A1/1/2		441.2		
LE6170/A1/2/11	1.96	448.4	443.6	0.009
LE6169/A1/B1/2		441.1		
LE6170/A1/1/21		332.0		
LE6170/A1/2/3	2.94	312.7	323.0	0.030
LE6170/A1/2/12		324.3		
LE6169/A1/1/4		292.8		
LE6170/A1/2/13	3.93	290.2	283.9	0.047
LE6169/A1/B1/3		268.6		
LE6170/A1/1/25		266.7		
LE6169/A1/B4/2	4.91	269.1	267.7	0.005
LE6170/A1/2/14		267.2		
LE6169/A1/1/6		261.7		
LE6170/A1/2/6	5.89	241.2	248.9	0.045
LE6169/A1/B1/5		243.8		
LE6170/A1/1/29		236.8		
LE6170/A1/2/7	6.87	231.0	238.1	0.033
LE6169/A1/B1/6		246.5		
LE6169/A1/1/8		246.2		
LE6169/A1/B1/8	7.85	225.6	230.7	0.059
LE6169/A1/B1/9		220.2		
LE6170/A1/1/32		218.0		
LE6169/A1/B4/4	8.83	224.6	221.1	0.015
LE6169/A1/B1/11		220.7		
LE6170/A1/1/11	12.7 mm	225.0		
LE6170/A1/1/12	ϕ Hole	231.5	224.9	0.030
LE6170/A1/1/13		218.2		

Table 6.4. Compressive Test Results for Impacted Specimens.

Specimen	σ_{max} (MPa)	$\frac{\sigma_{max}}{\sigma_{ult}}$	N_f	
LE6169/A1/B2/17	348.1	0.825	66500	
LE6169/A1/B1/20	348.1	0.825	110600	
LE6169/A1/1/24	348.1	0.825	153680	
LE6170/A1/2/18	348.1	0.825	28440	
LE6169/A1/A4/9	348.1	0.825	25100	
LE6169/A1/1/21	337.5	0.80	8196	
LE6170/A1/2/19	337.5	0.80	153419	
LE6169/A1/B4/10	337.5	0.80	100000	
LE6170/A1/1/33	327.0	0.775	40900	
LE6169/A1/1/22	316.4	0.75	28225	
LE6169/A1/A4/7	316.4	0.75	6953	
LE6170/A1/2/17	316.4	0.75	251900	
LE6169/A1/B1/19	316.4	0.75	187620	
LE6169/A1/A2/17	305.9	0.725	627300	
LE6169/A1/A4/8	295.3	0.70	380800	
LE6169/A1/B1/18	284.8	0.675	298300	
LE6169/A1/1/23	274.2	0.65	136920	
LE6169/A1/A2/16	274.2	0.65	978300	
LE6169/A1/A2/18	274.2	0.65	1000000	*
LE6170/A1/1/34	274.2	0.65	1000000	*
LE6169/A1/B2/16	274.2	0.65	1000000	*
LE6169/A1/B4/9	274.2	0.65	853800	
LE6169/A1/A3/16	253.1	0.60	1000000	*
LE6169/A1/B2/22	211.0	0.50	1000000	*
LE6169/A1/A2/22	168.8	0.40	1000000	*
LE6169/A1/B1/25	126.6	0.30	1000000	*
LE6170/A1/2/26	84.4	0.20	1000000	*
LE6170/A1/2/25	42.2	0.10	1000000	*

* Run-out

Table 7.1. Zero-Tension Fatigue S-N Data for Undamaged Specimens.

Specimen	σ_{max} (MPa)	$\frac{\sigma_{max}}{\sigma_{ult}}$	N_f	
LE6169/A1/A4/4	275.9	0.80	27080	
LE6169/A1/B2/6	275.9	0.80	8771	
LE6169/A1/B2/14	275.9	0.80	8338	
LE6169/A1/A3/5	275.9	0.80	18071	
LE6169/A1/A3/9	267.3	0.775	26842	
LE6169/A1/A2/1	258.7	0.75	32070	
LE6169/A1/A3/11	258.7	0.75	20043	
LE6169/A1/B2/4	241.4	0.70	40129	
LE6169/A1/A2/3	224.2	0.65	98770	
LE6169/A1/A2/5	206.9	0.60	317180	
LE6169/A1/B2/8	206.9	0.60	198150	
LE6169/A1/A2/11	189.7	0.55	500000	*
LE6169/A1/A3/1	175.9	0.51	1000000	*
LE6169/A1/B2/2	172.5	0.50	927870	
LE6169/A1/B2/10	172.5	0.50	1000000	*
LE6169/A1/A3/13	162.1	0.47	1000000	*
LE6169/A1/A2/13	155.2	0.45	1000000	*
LE6169/A1/A3/7	148.3	0.43	1000000	*
LE6169/A1/B2/12	120.7	0.35	1000000	*
LE6169/A1/A2/15	86.2	0.25	1000000	*
LE6169/A1/A3/15	69.0	0.20	1000000	*
LE6169/A1/A3/3	51.7	0.15	1000000	*

* Run-out

Table 7.2. Zero-Tension Fatigue S-N Data for 2.94J Impact Specimens.

Specimen	σ_{max} (MPa)	$\frac{\sigma_{max}}{\sigma_{ult}}$	N_f
LE6169/A1/A4/2	195.7	0.80	77470
LE6169/A1/B2/7	195.7	0.80	25291
LE6169/A1/B2/15	195.7	0.80	27962
LE6169/A1/A3/8	195.7	0.80	74304
LE6169/A1/A3/10	189.6	0.775	66671
LE6169/A1/A2/2	183.5	0.75	118650
LE6169/A1/A3/12	183.5	0.75	90620
LE6169/A1/B2/5	171.2	0.70	153940
LE6169/A1/A2/4	159.0	0.65	543680
LE6169/A1/A2/6	146.8	0.60	630920
LE6169/A1/B2/9	146.8	0.60	1000000 *
LE6169/A1/A3/2	137.0	0.56	1000000 *
LE6169/A1/A2/12	134.5	0.55	1000000 *
LE6169/A1/A3/6	129.6	0.53	1000000 *
LE6169/A1/B2/3	122.3	0.50	600130
LE6169/A1/B2/11	122.3	0.50	1000000 *
LE6169/A1/A2/14	110.1	0.45	1000000 *
LE6169/A1/B2/13	85.6	0.35	1000000 *
LE6169/A1/B2/1	61.2	0.25	1000000 *
LE6169/A1/A3/14	48.9	0.20	1000000 *
LE6169/A1/A3/4	36.7	0.15	1000000 *

* Run-out

Table 7.3. Zero-Tension Fatigue S-N Data for 6.87J Impact Specimens.

Specimen	σ_{max} (MPa)	$\frac{\sigma_{max}}{\sigma_{ult}}$	N_f	
LE6169/A1/B3/10	232.1	1.00	830	
LE6169/A1/B3/8	220.5	0.95	10700	
LE6169/A1/B3/14	217.0	0.935	16270	
LE6169/A1/B3/12	214.7	0.925	1000000	*
LE6169/A1/B3/4	208.9	0.90	1000000	*
LE6169/A1/B3/2	185.7	0.80	1000000	*

* Run-out.

Table 7.4. Zero-Tension Fatigue S-N Data for 8.83J Impact Specimens.

Specimen	σ_{max} (MPa)	$\frac{\sigma_{max}}{\sigma_{ult}}$	N_f	
LE6169/A1/B2/21	187.1	1.00	1000000	*
LE6169/A1/B2/20	187.1	1.00	1000000	*
LE6170/A1/2/22	186.2	0.995	2890	
LE6169/A1/A2/21	186.2	0.995	1000000	*
LE6170/A1/2/20	185.2	0.99	1000000	*
LE6169/A1/B1/21	184.3	0.985	1000000	*
LE6170/A1/1/38	183.4	0.98	67820	
LE6169/A1/B1/22	183.4	0.98	1000000	*
LE6170/A1/1/36	183.4	0.98	1280	
LE6170/A1/1/37	182.4	0.975	140	**
LE6169/A1/B1/23	182.4	0.975	1000000	*
LE6169/A1/B1/24	181.5	0.97	1000000	*
LE6169/A1/A2/20	181.5	0.97	1000000	*
LE6170/A1/1/35	181.5	0.97	384580	
LE6169/A1/A2/19	177.7	0.95	1000000	*
LE6170/A1/2/21	168.4	0.90	1000000	*
LE6170/A1/2/23	149.7	0.80	1000000	*
LE6170/A1/2/24	121.6	0.65	1000000	*

* Run-out. ** Run-up Failure.

Table 7.5. Zero-Tension Fatigue S-N Data for Specimens with a 12.7mm Diameter Drilled Hole.

Specimen	Hole Diameter ϕ_h (mm)	σ_{rt} (MPa)	Mean σ_{rt} (MPa)	C of V
LE6170/A1/2/27	2.5	312.0	311.2	0.007
LE6170/A1/2/28		312.9		
LE6170/A1/2/29		308.8		
LE6170/A1/2/30	5.0	274.9	268.3	0.030
LE6170/A1/2/31		259.2		
LE6170/A1/2/32		270.8		
LE6170/A1/2/33	10.0	220.6	232.0	0.071
LE6170/A1/2/34		224.4		
LE6169/A1/A2/23		251.0		
LE6170/A1/1/8	12.7	187.6	187.1	0.014
LE6170/A1/1/9		184.3		
LE6170/A1/1/10		189.4		
LE6169/A1/A2/30	15.0	199.2	210.7	0.048
LE6169/A1/A2/31		214.7		
LE6169/A1/A2/32		218.1		
LE6169/A1/A2/27	20.0	182.8	175.5	0.036
LE6169/A1/A2/28		171.9		
LE6169/A1/A2/29		171.9		
LE6169/A1/A2/33	25.0	143.9	142.3	0.024
LE6169/A1/B2/23		138.4		
LE6169/A1/B2/24		144.5		
LE6169/A1/B2/25	30.0	114.1	117.4	0.036
LE6169/A1/B2/26		115.9		
LE6169/A1/B2/27		122.1		
LE6169/A1/A2/24	38.5	71.2	67.6	0.059
LE6169/A1/A2/25		68.3		
LE6169/A1/A2/26		63.3		

Table 7.6. Tensile Test Results for Specimens with Centrally Drilled Holes.

Specimen	Hole Diameter ϕ_h (mm)	σ_{max} (MPa)	$\frac{\sigma_{max}}{\sigma_{rt}}$	N_f	
LE6169/A1/B2/29	2.5	311.2	1.00	258750	
LE6169/A1/B2/30	2.5	311.2	1.00	367010	
LE6169/A1/A3/17	10.0	232.0	1.00	1000000	*
LE6169/A1/A3/18	10.0	232.0	1.00	161980	
LE6169/A1/B1/26	25.0	142.3	1.00	660	**
LE6169/A1/B2/28	25.0	142.3	1.00	358980	
LE6169/A1/B1/27	38.5	67.6	1.00	5930	
LE6169/A1/B1/28	38.5	67.6	1.00	19500	

* Run-out. ** Run-up Failure.

Table 7.7. Zero-Tension Fatigue S-N Data for Specimens with Centrally Drilled Holes.

n	$\frac{n}{N_f}$	$\frac{E_{at}}{E_{rt}}$	A_d (mm^2)	A_m (mm^2)	
0	0	1.00	50	50	
4000	0.46	0.59	133	2509	*
8000	0.91	0.80	199	4539	*
8771	1.00	0.00	-	-	

* Damage reached edges of specimen.

Table 7.8. Changes in Localised Stiffness and Growth of Impact Damage Under Fatigue Loading. Specimen LE6169/A1/B2/6, 2.94J, $\frac{\sigma_{max}}{\sigma_{rt}}$=0.80.

n	$\frac{n}{N_f}$	$\frac{E_{at}}{E_{rt}}$	A_d (mm^2)	A_m (mm^2)	
0	0	1.00	164	164	
12000	0.47	0.54	269	2183	*
24000	0.95	0.67	655	4410	*
25291	1.00	0.00	-	-	

* Damage reached edges of specimen.

Table 7.9. Changes in Localised Stiffness and Growth of Impact Damage Under Fatigue Loading. Specimen LE6169/A1/B2/7, 6.87J, $\frac{\sigma_{max}}{\sigma_{rt}}$=0.80.

n	$\frac{n}{N_f}$	$\frac{E_{at}}{E_{rt}}$	A_d (mm^2)	A$_m$ (mm^2)	
0	0	1.00	45	45	
2000	0.24	0.93	75	4124	*
4000	0.48	0.82	146	4482	*
6000	0.72	0.88	207	4651	*
8000	0.96	0.61	617	5000	**
8338	1.00	0.00	-	-	

* Damage reached edges of specimen.

** Damage over full width and gauge length of specimen.

Table 7.10. Changes in Localised Stiffness and Growth of Impact Damage Under Fatigue Loading. Specimen LE6169/A1/B2/14, 2.94J, $\frac{\sigma_{max}}{\sigma_{rt}}$=0.80.

n	$\frac{n}{N_f}$	$\frac{E_{at}}{E_{rt}}$	A_d (mm^2)	A$_m$ (mm^2)	
0	0	1.00	168	168	
6000	0.22	0.82	266	4618	*
12000	0.43	0.73	370	4662	*
18000	0.64	0.79	472	4795	*
24000	0.86	0.61	836	5000	**
27962	1.00	0.00	-	-	

* Damage reached edges of specimen.

** Damage over full width and gauge length of specimen.

Table 7.11. Changes in Localised Stiffness and Growth of Impact Damage Under Fatigue Loading. Specimen LE6169/A1/B2/15, 6.87J, $\frac{\sigma_{max}}{\sigma_{rt}}$=0.80.

n	$\frac{n}{N_f}$	$\frac{E_{at}}{E_{rt}}$	A_d (mm^2)	A_m (mm^2)	
0	0	1.00	62	62	
10000	0.25	1.20	87	2351	*
20000	0.50	1.30	213	4444	*
30000	0.75	0.65	1015	5000	**
40000	1.00	0.66	1050	5000	**
40129	1.00	0.00	-	-	

* Damage reached edges of specimen.

** Damage over full width and gauge length of specimen.

Table 7.12. Changes in Localised Stiffness and Growth of Impact Damage Under Fatigue Loading. Specimen LE6169/A1/B2/4, 2.94J, $\frac{\sigma_{max}}{\sigma_{rt}}$=0.70.

n	$\frac{n}{N_f}$	$\frac{E_{at}}{E_{rt}}$	A_d (mm^2)		A_m (mm^2)	
0	0	1.00	197		197	
50000	0.33	0.85	266		1307	*
100000	0.65	0.71	580		2750	*
150000	0.97	0.35	2501	*	4882	*
153940	1.00	0.00	-		-	

* Damage reached edges of specimen.

Table 7.13. Changes in Localised Stiffness and Growth of Impact Damage Under Fatigue Loading. Specimen LE6169/A1/B2/5, 6.87J, $\frac{\sigma_{max}}{\sigma_{rt}}$=0.70.

n	$\frac{n}{N_f}$	$\frac{E_{at}}{E_{vt}}$	A_d (mm^2)	A_m (mm^2)	
0	0	1.00	16	16	
50000	0.25	0.93	16	3925	*
100000	0.51	0.97	18	5000	**
150000	0.76	0.68	-	5000	**
198150	1.00	0.00	-	-	

* Damage reached edges of specimen.

** Damage over full width and gauge length of specimen.

Table 7.14. Changes in Localised Stiffness and Growth of Impact Damage Under Fatigue Loading. Specimen LE6169/A1/B2/8, 2.94J, $\frac{\sigma_{max}}{\sigma_{vt}}$=0.60.

n	$\frac{E_{at}}{E_{vt}}$	A_d (mm^2)		A_m (mm^2)	
0	1.00	134		134	
150000	0.74	155		3102	*
300000	0.72	251		3470	*
450000	0.67	350		4590	*
600000	0.64	616		5000	**
750000	0.60	1621	*	5000	**
900000	0.39	2424	*	5000	**
1000000	0.24	3982	*	5000	**

Specimen run-out at 10^6 cycles.

* Damage reached edges of specimen.

** Damage over full width and gauge length of specimen.

Table 7.15. Changes in Localised Stiffness and Growth of Impact Damage Under Fatigue Loading. Specimen LE6169/A1/B2/9, 6.87J, $\frac{\sigma_{max}}{\sigma_{vt}}$=0.60.

n	$\frac{E_{ai}}{E_{ri}}$	A_d (mm^2)		A_m (mm^2)	
0	1.00	69		69	
100000	1.06	77		3511	*
200000	1.13	209		4667	*
300000	0.75	2214	*	5000	**
400000	0.44	3832	*	5000	**
500000	0.30	4845	*	5000	**

Specimen run-out at 5×10^5 cycles.

* Damage reached edges of specimen.

** Damage over full width and gauge length of specimen.

Table 7.16. Changes in Localised Stiffness and Growth of Impact Damage Under Fatigue Loading. Specimen LE6169/A1/A2/11, 2.94J, $\frac{\sigma_{max}}{\sigma_{rt}}$=0.55.

n	$\frac{E_{ai}}{E_{ri}}$	A_d (mm^2)	A_m (mm^2)	
0	1.00	174	174	
100000	1.02	181	2561	*
200000	1.00	212	3621	*
300000	0.93	229	3915	*
400000	0.98	243	4212	*
500000	0.90	287	4440	*
600000	0.91	240	4569	*
700000	0.70	442	4729	*
800000	0.68	459	4765	*
900000	0.63	546	4931	*
1000000	0.44	716	5000	**

Specimen run-out at 10^6 cycles.

* Damage reached edges of specimen.

** Damage over full width and gauge length of specimen.

Table 7.17. Changes in Localised Stiffness and Growth of Impact Damage Under Fatigue Loading. Specimen LE6169/A1/A2/12, 6.87J, $\frac{\sigma_{max}}{\sigma_{rt}}$=0.55.

n	$\frac{E_{at}}{E_{rt}}$	A_d (mm^2)		A_m (mm^2)	
0	1.00	79		79	
200000	0.81	60		3482	*
400000	0.54	2126	*	4695	*
600000	0.43	3294	*	5000	**
800000	0.27	5000	**	5000	**
1000000	0.31	5000	**	5000	**

Specimen run-out at 10^6 cycles.

* Damage reached edges of specimen.

** Damage over full width and gauge length of specimen.

Table 7.18. Changes in Localised Stiffness and Growth of Impact Damage Under Fatigue Loading. Specimen LE6169/A1/B2/10, 2.94J, $\frac{\sigma_{max}}{\sigma_{rt}}$=0.50.

n	$\frac{E_{at}}{E_{rt}}$	A_d (mm^2)	A_m (mm^2)	
0	1.00	139	139	
200000	1.50	175	2665	*
400000	1.45	224	3338	*
600000	0.83	234	3899	*
800000	1.00	321	4868	*
1000000	0.70	368	4928	*

Specimen run-out at 10^6 cycles.

* Damage reached edges of specimen.

Table 7.19. Changes in Localised Stiffness and Growth of Impact Damage Under Fatigue Loading. Specimen LE6169/A1/B2/11, 6.87J, $\frac{\sigma_{max}}{\sigma_{rt}}$=0.50.

n	$\frac{n}{N_f}$	$\frac{E_{at}}{E_{rt}}$	A_d (mm^2)		A_m (mm^2)	
0	0	1.00	56		56	
200000	0.22	0.86	71		3768	*
400000	0.43	0.79	147		5000	**
600000	0.65	0.48	5000	**	5000	**
800000	0.86	0.56	5000	**	5000	**
927870	1.00	0.00	-		-	

* Damage reached edges of specimen.

** Damage over full width and gauge length of specimen.

Table 7.20. Changes in Localised Stiffness and Growth of Impact Damage Under Fatigue Loading. Specimen LE6169/A1/B2/2, 2.94J, $\frac{\sigma_{max}}{\sigma_{rt}}$=0.50.

n	$\frac{n}{N_f}$	$\frac{E_{at}}{E_{rt}}$	A_d (mm^2)	A_m (mm^2)	
0	0	1.00	186	186	
200000	0.33	0.95	213	1128	*
400000	0.67	0.52	262	2846	*
600000	1.00	0.85	295	4715	*
600130	1.00	0.00	-	-	

* Damage reached edges of specimen.

Table 7.21. Changes in Localised Stiffness and Growth of Impact Damage Under Fatigue Loading. Specimen LE6169/A1/B2/3, 6.87J, $\frac{\sigma_{max}}{\sigma_{rt}}$=0.50.

n	$\frac{E_{at}}{E_{vt}}$	A_d (mm^2)	A_m (mm^2)	
0	1.00	75	75	
100000	0.92	36	1351	
200000	1.11	39	3072	*
300000	0.71	37	3626	*
400000	0.48	46	3957	*
691700	0.63	33	4138	*
800000	0.32	45	4643	*
1000000	0.71	43	4843	*

Specimen run-out at 10^6 cycles.

* Damage reached edges of specimen.

Table 7.22. Changes in Localised Stiffness and Growth of Impact Damage Under Fatigue Loading. Specimen LE6169/A1/A2/13, 2.94J, $\frac{\sigma_{max}}{\sigma_{vt}}$=0.45.

n	$\frac{E_{at}}{E_{vt}}$	A_d (mm^2)	A_m (mm^2)	
0	1.00	184	184	
100000	1.14	164	2326	*
209680	1.37	169	2445	*
300000	1.13	170	2715	*
400000	1.13	192	2901	*
600000	0.80	180	3432	*
887000	0.78	204	3687	*
1000000	0.81	193	3814	*

Specimen run-out at 10^6 cycles.

* Damage reached edges of specimen.

Table 7.23. Changes in Localised Stiffness and Growth of Impact Damage Under Fatigue Loading. Specimen LE6169/A1/A2/14, 6.87J, $\frac{\sigma_{max}}{\sigma_{vt}}$=0.45.

n	$\frac{E_{sat}}{E_{ref}}$	A_d (mm^2)	A_m (mm^2)	
0	1.00	70	70	
200000	0.86	62	1865	*
400000	0.96	64	3048	*
774690	0.90	60	5000	**
800000	0.93	59	5000	**
1000000	0.89	54	5000	**

Specimen run-out at 10^6 cycles.

* Damage reached edges of specimen.

** Damage over full width and gauge length of specimen.

Table 7.24. Changes in Localised Stiffness and Growth of Impact Damage Under Fatigue Loading. Specimen LE6169/A1/B2/12, 2.94J, $\frac{\sigma_{max}}{\sigma_{ref}}$=0.35.

n	$\frac{E_{sat}}{E_{ref}}$	A_d (mm^2)	A_m (mm^2)	
0	1.00	171	171	
200000	0.87	153	552	
400000	0.92	166	2669	*
600000	0.89	155	3987	*
800000	0.93	151	5000	**
1000000	0.54	164	5000	**

Specimen run-out at 10^6 cycles.

* Damage reached edges of specimen.

** Damage over full width and gauge length of specimen.

Table 7.25. Changes in Localised Stiffness and Growth of Impact Damage Under Fatigue Loading. Specimen LE6169/A1/B2/13, 6.87J, $\frac{\sigma_{max}}{\sigma_{ref}}$=0.35.

n	$\frac{E_{at}}{E_{vt}}$	A_d (mm^2)	A_m (mm^2)
0	1.00	72	72
1000000	0.93	46	621

Specimen run-out at 10^6 cycles.

Table 7.26. Changes in Localised Stiffness and Growth of Impact Damage Under Fatigue Loading. Specimen LE6169/A1/A2/15, 2.94J, $\frac{\sigma_{max}}{\sigma_{vt}}$=0.25.

n	$\frac{E_{at}}{E_{vt}}$	A_d (mm^2)	A_m (mm^2)
0	1.00	162	162
1000000	1.02	148	547

Specimen run-out at 10^6 cycles.

Table 7.27. Changes in Localised Stiffness and Growth of Impact Damage Under Fatigue Loading. Specimen LE6169/A1/B2/1, 6.87J, $\frac{\sigma_{max}}{\sigma_{vt}}$=0.25.

n	$\frac{E_{at}}{E_{rt}}$	A_d (mm^2)	A_m (mm^2)
0	1.00	49	49
1000000	1.03	47	47

Specimen run-out at 10^6 cycles.

Table 7.28. Changes in Localised Stiffness and Growth of Impact Damage Under Fatigue Loading. Specimen LE6169/A1/A3/15, 2.94J, $\frac{\sigma_{max}}{\sigma_{rt}}$=0.20.

n	$\frac{E_{at}}{E_{rt}}$	A_d (mm^2)	A_m (mm^2)
0	1.00	187	187
1000000	1.04	188	188

Specimen run-out at 10^6 cycles.

Table 7.29. Changes in Localised Stiffness and Growth of Impact Damage Under Fatigue Loading. Specimen LE6169/A1/A3/14, 6.87J, $\frac{\sigma_{max}}{\sigma_{rt}}$=0.20.

$\frac{\sigma_{max}}{\sigma_{rt}}$	$\frac{E_{at}}{E_{rt}}$	
	2.94J Impact	6.87J Impact
0.60	*	0.24
0.55	*	0.44
0.50	0.31	0.70
0.45	0.71	0.81
0.35	0.89	0.54
0.25	0.93	1.02
0.20	1.03	1.04

* Specimen failed before run-out.

Table 7.30. Change in Stiffness Ratio for Impacted Specimens under Zero-Tension Fatigue Loading after 10^6 Cycles.

$\frac{\sigma_{max}}{\sigma_{rt}}$	$A_{m_{10^6}} - A_{m_0}$ (mm^2)	
	2.94J Impact	6.87J Impact
0.60	*	4866
0.55	*	4826
0.50	4921	4789
0.45	4768	3630
0.35	4930	4829
0.25	549	385
0.20	-2	1

* Specimen failed before run-out.

Table 7.31. Micro-Damage Growth for Impacted Specimens Under Zero-Tension Fatigue Loading over 10^6 Cycles.

n	$\frac{n}{N_f}$	A_d (mm^2)
0	0	37
2000	0.11	57
4000	0.22	70
6000	0.33	105
8000	0.44	128
10000	0.55	164
12000	0.66	252
14000	0.78	233
16000	0.89	293
18000	1.00	690

Table 7.32. Growth of Delamination under Fatigue Loading.

Specimen LE6169/A1/A3/5, 2.94J, $\frac{\sigma_{max}}{\sigma_{rt}}$=0.80.

n	$\frac{n}{N_f}$	A_d (mm^2)
0	0	147
7000	0.09	222
14000	0.19	230
21000	0.28	321
28000	0.38	465
35000	0.47	599
42000	0.57	714
49000	0.66	828
56000	0.75	839
63000	0.85	1000

Table 7.33. Growth of Delamination under Fatigue Loading.

Specimen LE6169/A1/A3/8, 6.87J, $\frac{\sigma_{max}}{\sigma_{rt}}$=0.80.

n	$\frac{n}{N_f}$	A_d (mm^2)
0	0	47
3000	0.11	71
6000	0.22	90
9000	0.34	90
12000	0.45	149
15000	0.56	203
18000	0.67	252
21000	0.78	251
24000	0.89	402

Table 7.34. Growth of Delamination under Fatigue Loading.

Specimen LE6169/A1/A3/9, 2.94J, $\frac{\sigma_{max}}{\sigma_{rt}}$=0.775.

n	$\frac{n}{N_f}$	A_d (mm^2)
0	0	136
11000	0.17	215
22000	0.33	333
33000	0.50	540
44000	0.66	858
55000	0.83	1131

Table 7.35. Growth of Delamination under Fatigue Loading.

Specimen LE6169/A1/A3/10, 6.87J, $\frac{\sigma_{max}}{\sigma_{rt}}$=0.775.

n	$\frac{n}{N_f}$	A_d (mm^2)
0	0	50
5000	0.25	90
10000	0.50	108
15000	0.75	276
20000	1.00	922

Table 7.36. Growth of Delamination under Fatigue Loading.

Specimen LE6169/A1/A3/11, 2.94J, $\frac{\sigma_{max}}{\sigma_{rt}}$=0.75.

n	$\frac{n}{N_f}$	A_d (mm^2)
0	0	157
15000	0.17	225
30000	0.33	390
45000	0.50	549
60000	0.67	900
75000	0.83	1263

Table 7.37. Growth of Delamination under Fatigue Loading.

Specimen LE6169/A1/A3/12, 6.87J, $\frac{\sigma_{max}}{\sigma_{rt}}$=0.75.

$\frac{\sigma_{max}}{\sigma_{rt}}$	$A_{d_{10^6}} - A_{d_0}$ (mm^2)	
	2.94J Impact	6.87J Impact
0.60	*	3848
0.55	*	542
0.50	4921	229
0.45	-32	9
0.35	-16	-7
0.25	-26	-14
0.20	-2	1

* Specimen failed before run-out.

Table 7.38. Delamination Growth for Impacted Specimens Under Zero-Tension Fatigue Loading over 10^6 Cycles.

Specimen	σ_{max} (MPa)	$\frac{\sigma_{max}}{\sigma_{ot}}$	σ_{rt} (MPa)	$\frac{\sigma_{rt}}{\sigma_{ot}}$	
-	0.00	0.00	421.9	1.00	*
LE6170/A1/2/25	42.2	0.10	432.5	1.03	
LE6170/A1/2/26	84.4	0.20	417.3	0.99	
LE6169/A1/B1/25	126.6	0.30	485.7	1.15	
LE6169/A1/A2/22	168.8	0.40	487.1	1.16	
LE6169/A1/B2/22	211.0	0.50	470.7	1.12	
LE6169/A1/A3/16	243.1	0.60	442.1	1.05	
LE6170/A1/1/34	274.2	0.65	386.9	0.92	
LE6169/A1/A2/18	274.2	0.65	419.7	1.00	
LE6169/A1/B2/16	274.2	0.65	366.8	0.87	
-	293.2	0.69	0.000	0.00	**

* Static Tensile Result. ** Result taken from S-N Curve.

Table 7.39. Residual Tensile Strength after 10^6 Cycles

Zero-Tension Fatigue for Undamaged Specimens.

Specimen	σ_{max} (MPa)	$\frac{\sigma_{max}}{\sigma_{rt}}$	σ_{rt} (MPa)	$\frac{\sigma_{rt}}{\sigma_{rt}}$
-	0.00	0.00	344.9	1.00 *
LE6169/A1/A3/3	51.7	0.15	470.4	1.36
LE6169/A1/A3/15	69.0	0.20	434.2	1.26
LE6169/A1/A2/15	86.2	0.25	419.1	1.22
LE6169/A1/B2/12	120.7	0.35	347.3	1.01
LE6169/A1/A3/7	148.3	0.43	436.9	1.27
LE6169/A1/A2/13	155.2	0.45	386.6	1.12
LE6169/A1/A3/13	162.1	0.47	467.4	1.36
LE6169/A1/B2/10	172.5	0.50	236.3	0.69
LE6169/A1/A3/1	175.9	0.51	435.5	1.26
-	175.9	0.51	0.000	0.00 **

* Static Tensile Result. ** Result taken from S-N Curve.

Table 7.40. Residual Tensile Strength after 10^6 Cycles

Zero-Tension Fatigue for 2.94J Impact Specimens.

Specimen	σ_{max} (MPa)	$\frac{\sigma_{max}}{\sigma_{rt}}$	σ_{rt} (MPa)	$\frac{\sigma_{rt}}{\sigma_{rt}}$	
-	0.00	0.00	244.6	1.00	*
LE6169/A1/A3/4	36.7	0.15	314.3	1.29	
LE6169/A1/A3/14	48.9	0.20	265.1	1.08	
LE6169/A1/B2/1	61.1	0.25	265.4	1.09	
LE6169/A1/B2/13	85.6	0.35	236.8	0.97	
LE6169/A1/A2/14	110.1	0.45	256.1	1.05	
LE6169/A1/B2/11	122.3	0.50	254.1	1.04	
LE6169/A1/A3/6	129.6	0.53	288.3	1.18	
LE6169/A1/A2/12	134.5	0.55	230.4	0.94	
LE6169/A1/A3/2	137.0	0.56	282.1	1.15	
-	137.0	0.56	0.000	0.00	**
LE6169/A1/B2/9	146.8	0.60	189.3	0.77	

* Static Tensile Result. ** Result taken from S-N Curve.

Table 7.41. Residual Tensile Strength after 10^6 Cycles

Zero-Tension Fatigue for 6.87J Impact Specimens.

Specimen	σ_{max} (MPa)	$\frac{\sigma_{max}}{\sigma_{rt}}$	σ_{rt} (MPa)	$\frac{\sigma_{rt}}{\sigma_{rt}}$	
-	0.00	0.00	187.1	1.00	*
LE6170/A1/2/24	121.6	0.65	209.5	1.12	
LE6170/A1/2/23	149.7	0.80	210.7	1.13	
LE6170/A1/2/21	168.4	0.90	206.8	1.11	
LE6169/A1/A2/19	177.7	0.95	236.0	1.26	
LE6169/A1/B1/24	181.5	0.97	227.3	1.22	
LE6169/A1/A2/20	181.5	0.97	231.9	1.24	
-	181.5	0.97	0.000	0.00	**
LE6169/A1/B1/23	182.4	0.975	224.1	1.20	
LE6169/A1/B1/22	183.4	0.98	220.0	1.18	
LE6169/A1/B1/21	184.3	0.985	232.2	1.24	
LE6170/A1/2/20	185.2	0.99	203.7	1.09	
LE6169/A1/A2/21	186.2	0.995	240.4	1.29	
LE6169/A1/B2/20	187.1	1.00	227.9	1.22	
LE6169/A1/B2/21	187.1	1.00	231.6	1.24	

* Static Tensile Result. ** Result taken from S-N Curve.

Table 7.42. Residual Tensile Strength after 10^6 Cycles Zero-Tension Fatigue for Specimens with a 12.7mm Diameter Drilled Hole.

Specimen	U_i (J)	$\frac{\sigma_{rt}}{\sigma_{ut}}$	r_f (mm)	δ_r (mm)	l_c^{mean} (mm)	A_a (mm^2)	A_c (mm^2)
LE6169/A1/1/1		1.02	-	-	-	-	0
LE6170/A1/1/18	0.98	0.98	0.00	0.00	0.00	0	-
LE6170/A1/2/1		0.92	0.00	0.00	0.00	0	-
LE6170/A1/1/19		0.99	0.00	0.00	0.00	0	-
LE6170/A1/1/20	1.96	0.91	0.00	0.00	5.22	7	-
LE6170/A1/2/2		0.96	0.00	0.00	5.94	15	-
LE6169/A1/1/3		0.80	-	-	-	-	102
LE6170/A1/1/22	2.94	0.70	0.00	0.05	10.19	57	-
LE6169/A1/B4/1		0.96	2.00	0.00	3.92	102	-
LE6170/A1/1/23		0.66	0.00	0.07	12.03	98	-
LE6170/A1/1/24	3.93	0.68	0.00	0.06	8.57	100	-
LE6170/A1/2/4		0.62	0.00	0.07	12.74	79	-
LE6169/A1/1/5		0.61	-	-	-	-	219
LE6170/A1/1/26	4.91	0.59	1.55	0.09	16.06	154	-
LE6170/A1/2/5		0.64	0.00	0.08	11.41	134	-
LE6170/A1/1/27		0.56	1.83	0.15	20.38	237	-
LE6170/A1/1/28	5.89	0.57	1.82	0.11	21.62	215	-
LE6169/A1/B1/4		0.66	-	-	-	-	-
LE6169/A1/1/7		0.55	-	-	-	-	317
LE6170/A1/1/30	6.87	0.53	2.23	0.23	21.00	265	-
LE6169/A1/B4/3		0.61	3.28	0.19	15.26	206	-
LE6169/A1/B1/14		0.62	0.00	0.10	13.77	-	-
LE6170/A1/1/31		0.51	2.81	0.27	22.10	270	-
LE6170/A1/2/8	7.85	0.50	2.22	0.28	21.24	258	-
LE6169/A1/B1/7		0.58	-	-	-	-	-
LE6169/A1/1/9		0.51	-	-	-	-	366
LE6170/A1/2/9		0.50	2.17	0.34	24.74	310	-
LE6169/A1/B1/10	8.83	0.58	-	-	-	-	-
LE6169/A1/B1/15		0.58	4.73	0.38	21.55	-	-
LE6169/A1/A4/1		0.58	-	-	-	-	-

Table 9.1. Correlation of Damage Detection with

Residual Tensile Strength.

Specimen	U_i (J)	$\frac{\sigma_{rc}}{\sigma_{oc}}$	r_f (mm)	δ_r (mm)	l_c^{mean} (mm)	A_s (mm^2)	A_c (mm^2)
LE6170/A1/1/17		1.11	0.00	0.00	0.00	0	-
LE6170/A1/2/10	0.98	1.07	0.00	0.00	0.00	0	-
LE6169/A1/B1/1		0.98	-	-	-	-	-
LE6169/A1/1/2		1.06	-	-	-	-	36
LE6170/A1/2/11	1.96	1.08	0.00	0.00	0.00	0	-
LE6169/A1/B1/2		1.06	-	-	-	-	-
LE6170/A1/1/21		0.80	0.00	0.04	9.72	76	-
LE6170/A1/2/3	2.94	0.75	0.00	0.03	8.09	50	-
LE6170/A1/2/12		0.78	0.00	0.04	7.39	56	-
LE6169/A1/1/4		0.70	-	-	-	-	146
LE6170/A1/2/13	3.93	0.70	1.28	0.07	12.42	94	-
LE6169/A1/B1/3		0.65	-	-	-	-	-
LE6170/A1/1/25		0.64	1.26	0.09	18.17	147	-
LE6169/A1/B4/2	4.91	0.65	2.56	0.07	9.42	175	-
LE6170/A1/2/14		0.64	1.16	0.09	13.33	137	-
LE6169/A1/1/6		0.63	-	-	-	-	261
LE6170/A1/2/6	5.89	0.58	1.24	0.11	18.40	180	-
LE6169/A1/B1/5		0.59	-	-	-	-	-
LE6170/A1/1/29		0.57	2.52	0.23	20.38	280	-
LE6170/A1/2/7	6.87	0.55	1.32	0.15	19.62	247	-
LE6169/A1/B1/6		0.59	-	-	-	-	-
LE6169/A1/1/8		0.59	-	-	-	-	309
LE6169/A1/B1/8	7.85	0.54	-	-	-	-	-
LE6169/A1/B1/9		0.53	-	-	-	-	-
LE6170/A1/1/32		0.52	3.07	0.29	22.81	323	-
LE6169/A1/B4/4	8.83	0.54	3.17	0.30	18.25	341	-
LE6169/A1/B1/11		0.53	-	-	-	-	-

Table 9.2. Correlation of Damage Detection with

Residual Compressive Strength.

U_i (J)	mean $\overline{U_i}$ (Jmm^{-1})	Experimental $\frac{\sigma_{rt}}{\sigma_{ut}}$	Predicted $\frac{\sigma_{rt}}{\sigma_{ut}}$	Percentage Difference
0	0	1.0000	1.0000	0
0.98	0.4206	0.9706	0.9525	-1.86
1.96	0.8388	0.9550	0.9029	-5.46
2.94	1.2427	0.8175	0.8522	4.24
3.93	1.6795	0.6535	0.7937	21.45
4.91	2.0955	0.6127	0.7337	19.75
5.89	2.4789	0.5949	0.6736	13.23
6.87	2.8968	0.5798	0.6014	3.73
7.85	3.3280	0.5267	0.5164	-1.96
8.83	3.7000	0.5501	0.4298	-21.87

Table 9.3. Husman et al [78]. Comparison of Predicted and Experimental Residual Tensile Strength after Impact.

U_i (J)	mean $\overline{U_i}$ (Jmm^{-1})	Experimental $\frac{\sigma_{rc}}{\sigma_{uc}}$	Predicted $\frac{\sigma_{rc}}{\sigma_{uc}}$	Percentage Difference
0	0	1.0000	1.0000	0
0.98	0.4159	1.0552	0.9484	-10.12
1.96	0.8344	1.0656	0.8943	-16.08
2.94	1.2618	0.7759	0.8350	7.62
3.93	1.6655	0.6820	0.7748	13.61
4.91	2.0608	0.6430	0.7109	10.56
5.89	2.5075	0.5979	0.6310	5.54
6.87	2.9005	0.5719	0.5513	-3.60
7.85	3.2727	0.5542	0.4682	-15.52
8.83	3.6800	0.5311	0.3418	-35.64

Table 9.4. Husman et al [78]. Comparison of Predicted and Experimental Residual Compressive Strength after Impact.

U_i (J)	mean $\overline{U_i}$ (Jmm^{-1})	Experimental $\frac{\sigma_{rt}}{\sigma_{ut}}$	Predicted $\frac{\sigma_{rt}}{\sigma_{ut}}$	Percentage Difference
0	0	1.0000	1.0000	0
0.98	0.4206	0.9706	0.8758	-9.77
1.96	0.8388	0.9550	0.7892	-17.36
2.94	1.2427	0.8175	0.7260	-11.19
3.93	1.6795	0.6535	0.6723	2.88
4.91	2.0955	0.6127	0.6308	2.95
5.89	2.4789	0.5949	0.5987	0.64
6.87	2.8968	0.5798	0.5687	-1.91
7.85	3.3280	0.5267	0.5421	2.92
8.83	3.7000	0.5501	0.5219	5.13

Table 9.5. Lal [96], [97]. Comparison of Predicted and Experimental Residual Tensile Strength after Impact.

U_i (J)	mean $\overline{U_i}$ (Jmm^{-1})	Experimental $\frac{\sigma_{rc}}{\sigma_{uc}}$	Predicted $\frac{\sigma_{rc}}{\sigma_{uc}}$	Percentage Difference
0	0	1.0000	1.0000	0
0.98	0.4159	1.0552	0.8775	-16.84
1.96	0.8344	1.0656	0.7908	-25.79
2.94	1.2618	0.7759	0.7243	-6.65
3.93	1.6655	0.6820	0.6748	-1.06
4.91	2.0608	0.6430	0.6350	-1.26
5.89	2.5075	0.5979	0.5976	-0.05
6.87	2.9005	0.5719	0.5697	-0.38
7.85	3.2727	0.5542	0.5464	-1.41
8.83	3.6800	0.5311	0.5240	-1.34

Table 9.6. Lal [96], [97]. Comparison of Predicted and Experimental Residual Compressive Strength after Impact.

U_i (J)	mean $\bar{U}_i$ (Jmm^{-1})	Experimental $\frac{\sigma_{rt}}{\sigma_{ot}}$	Predicted $\frac{\sigma_{rt}}{\sigma_{ot}}$	Percentage Difference
0	0	1.0000	1.0000	0
0.98	0.4206	0.9706	1.0000	3.03
1.96	0.8388	0.9550	0.8666	-9.26
2.94	1.2427	0.8175	0.7581	-7.27
3.93	1.6795	0.6535	0.6888	5.40
4.91	2.0955	0.6127	0.6400	4.46
5.89	2.4789	0.5949	0.6027	1.31
6.87	2.8968	0.5798	0.5729	-1.19
7.85	3.3280	0.5267	0.5482	4.08
8.83	3.7000	0.5501	0.5273	-4.14

Table 9.7. Caprino [56]. Comparison of Predicted and Experimental Residual Tensile Strength after Impact.

U_i (J)	mean $\bar{U}_i$ (Jmm^{-1})	Experimental $\frac{\sigma_{rc}}{\sigma_{oc}}$	Predicted $\frac{\sigma_{rc}}{\sigma_{oc}}$	Percentage Difference
0	0	1.0000	1.0000	0
0.98	0.4159	1.0552	1.0000	-5.23
1.96	0.8344	1.0656	0.9800	-8.03
2.94	1.2618	0.7759	0.8232	6.10
3.93	1.6655	0.6820	0.7266	6.54
4.91	2.0608	0.6430	0.6603	2.69
5.89	2.5075	0.5979	0.6106	2.12
6.87	2.9005	0.5719	0.5715	-0.07
7.85	3.2727	0.5542	0.5396	-2.63
8.83	3.6800	0.5311	0.5130	-3.41

Table 9.8. Caprino [56]. Comparison of Predicted and Experimental Residual Compressive Strength after Impact.

U_i (J)	mean $\overline{U_i}$ (Jmm^{-1})	Experimental $\frac{\sigma_{rt}}{\sigma_{ut}}$	Predicted $\frac{\sigma_{rt}}{\sigma_{ut}}$	Percentage Difference
0	0	1.0000	1.0000	0
0.98	0.4206	0.9706	0.9024	-7.03
1.96	0.8388	0.9550	0.8099	-15.19
2.94	1.2427	0.8175	0.7431	-9.10
3.93	1.6795	0.6535	0.6867	5.08
4.91	2.0955	0.6127	0.6434	5.01
5.89	2.4789	0.5949	0.6100	2.54
6.87	2.8968	0.5798	0.5789	-0.16
7.85	3.3280	0.5267	0.5514	4.69
8.83	3.7000	0.5501	0.5305	-3.56

Table 9.9. Avva and Padmanabha [80]. Comparison of Predicted and Experimental Residual Tensile Strength after Impact.

U_i (J)	mean $\overline{U_i}$ (Jmm^{-1})	Experimental $\frac{\sigma_{rc}}{\sigma_{uc}}$	Predicted $\frac{\sigma_{rc}}{\sigma_{uc}}$	Percentage Difference
0	0	1.0000	1.0000	0
0.98	0.4159	1.0552	1.0000	-5.23
1.96	0.8344	1.0656	0.9037	-15.19
2.94	1.2618	0.7759	0.7913	1.98
3.93	1.6655	0.6820	0.7163	5.03
4.91	2.0608	0.6430	0.6603	2.69
5.89	2.5075	0.5979	0.6105	2.11
6.87	2.9005	0.5719	0.5749	0.52
7.85	3.2727	0.5542	0.5463	-1.43
8.83	3.6800	0.5311	0.5195	-2.18

Table 9.10. Avva and Padmanabha [80]. Comparison of Predicted and Experimental Residual Compressive Strength after Impact.

U_i (J)	σ_{nt} (MPa)				
	*$n = 0$	$n = 3$	$n = 4$	$n = 5$	$n = 6$
0	421.9	370.6	344.8	319.0	293.2
2.94	344.9	333.7	280.6	227.5	174.4
6.87	244.6	267.6	223.8	180.0	136.2
8.83	232.1	231.1	219.3	208.5	197.2
12.7mm ϕ Hole	187.1	185.5	184.3	183.1	181.9

* Note: for $n = 0$ $\quad \sigma_{nt}\,|_{U_i=0} = \sigma_{ot}$

$\sigma_{nt}\,|_{U_i=\infty} = \sigma_{rt}$

Table 9.11. Fatigue Strengths of Specimens Subjected to Low Velocity Impact and Zero-Tension Fatigue.

Figures

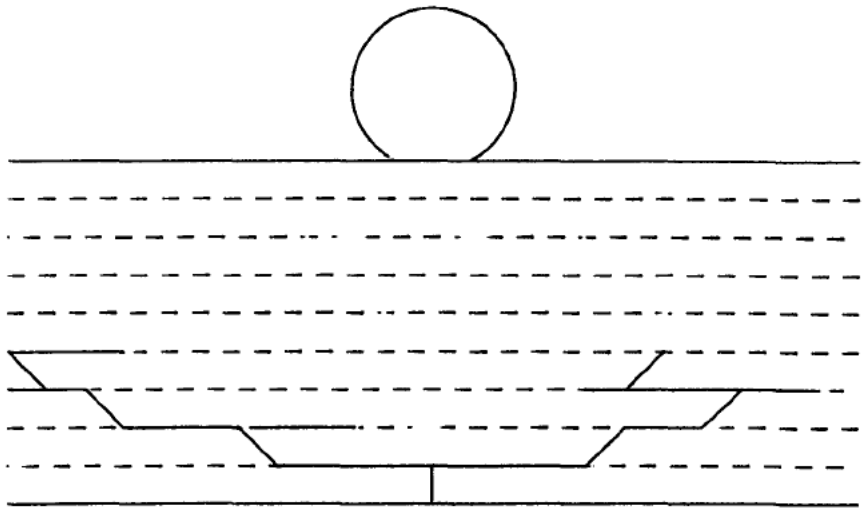

(a) Flexural Stresses

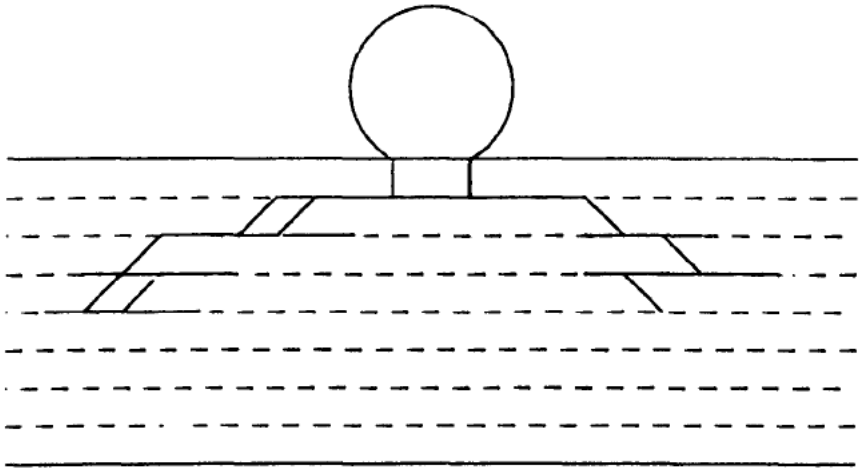

(b) Contact Stresses

Figure 2.1. Schematic Representation of Damage Progression in CFRP due to Impact Loading [22].

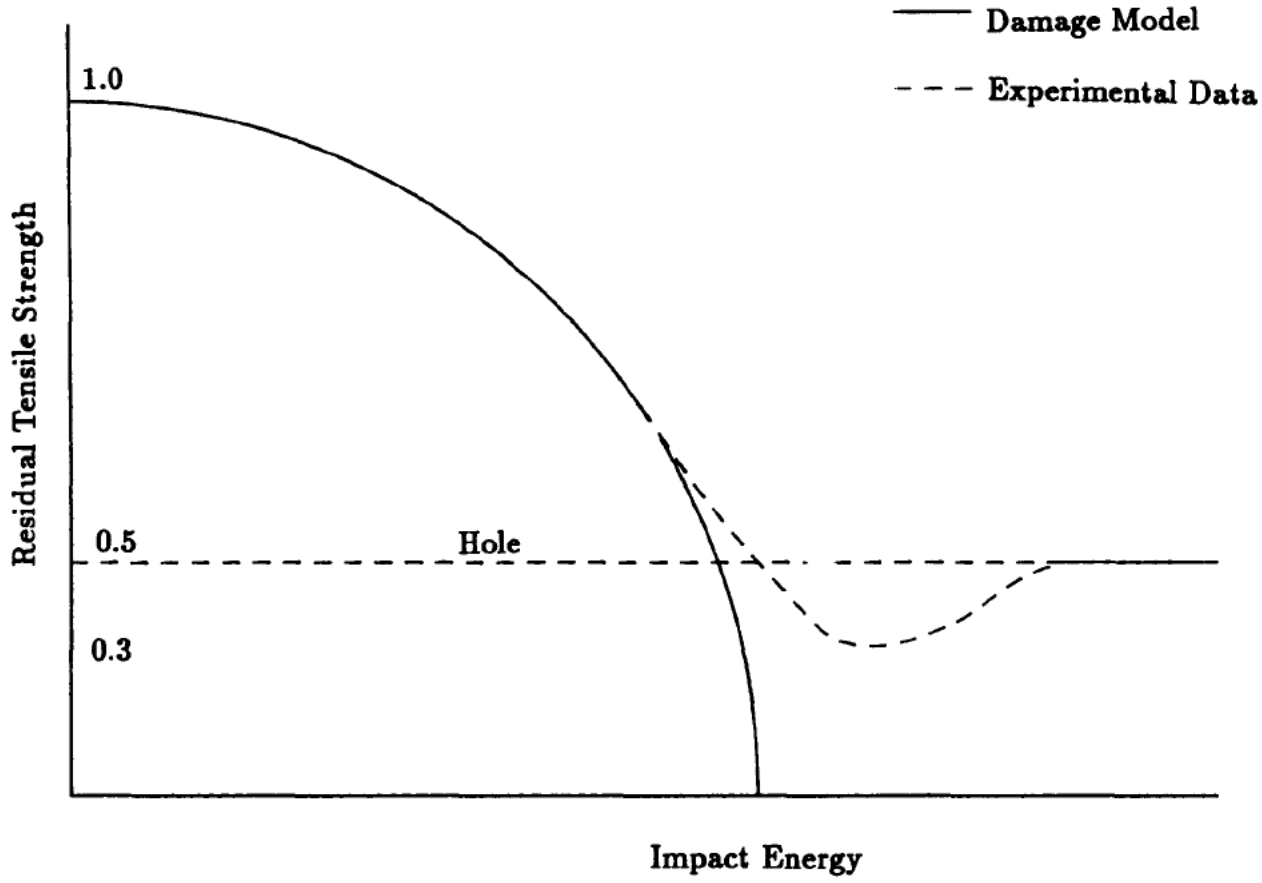

Figure 2.2. Residual Static Strength as a Function of Impact Energy [78].

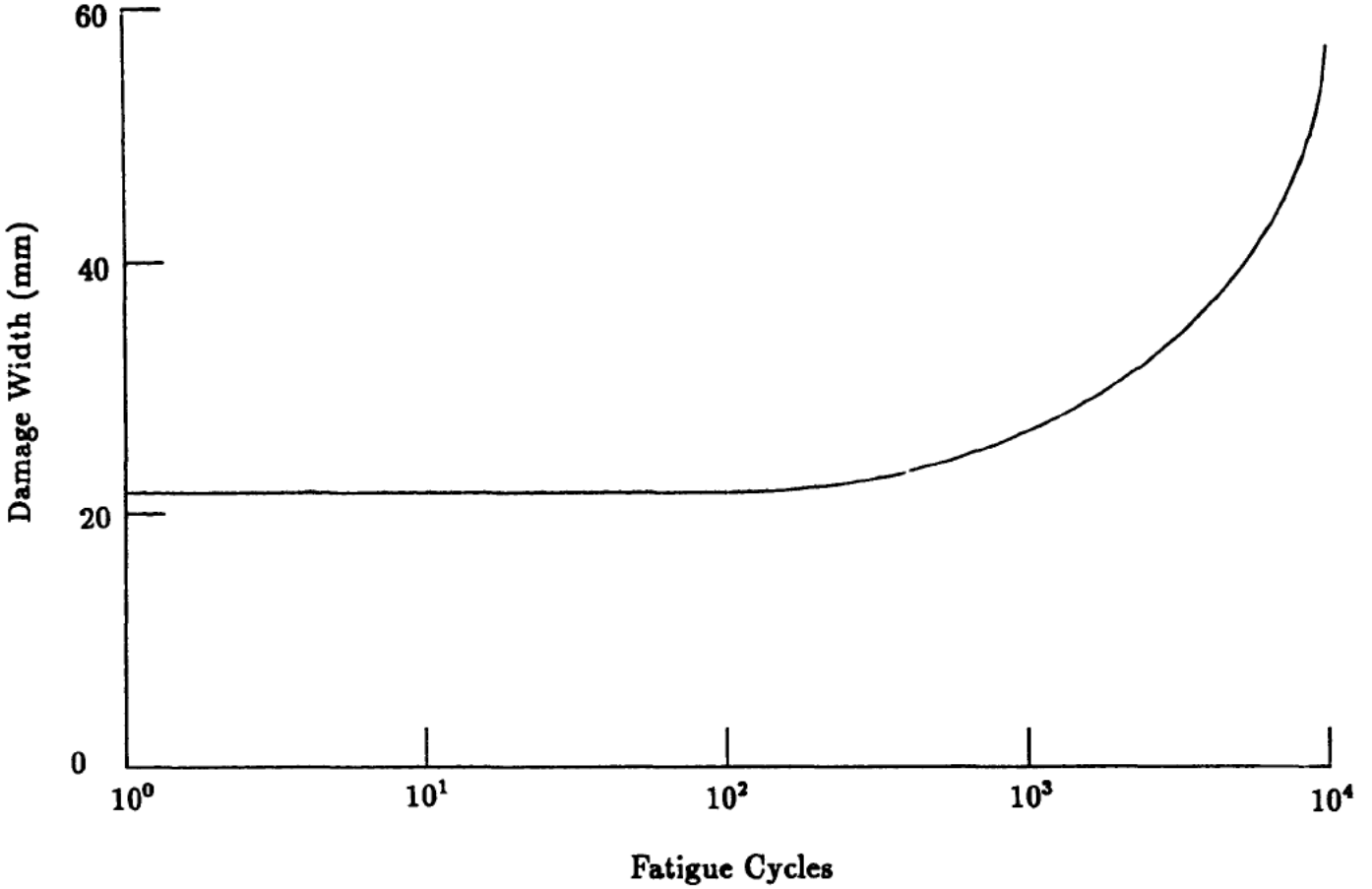

Figure 2.3. Lateral Growth of Damage under

Compressive Fatigue [55].

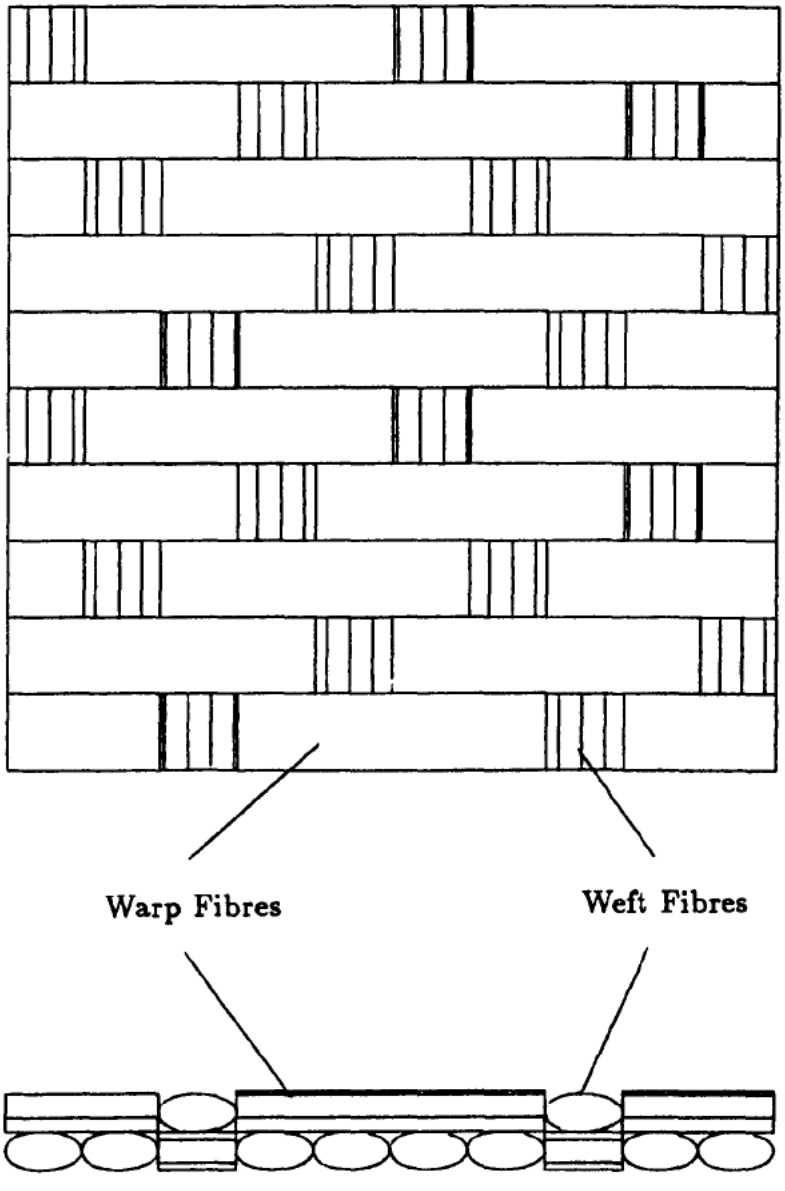

Figure 3.1. Weave Style of

Five - Harness - Satin Woven CFRP.

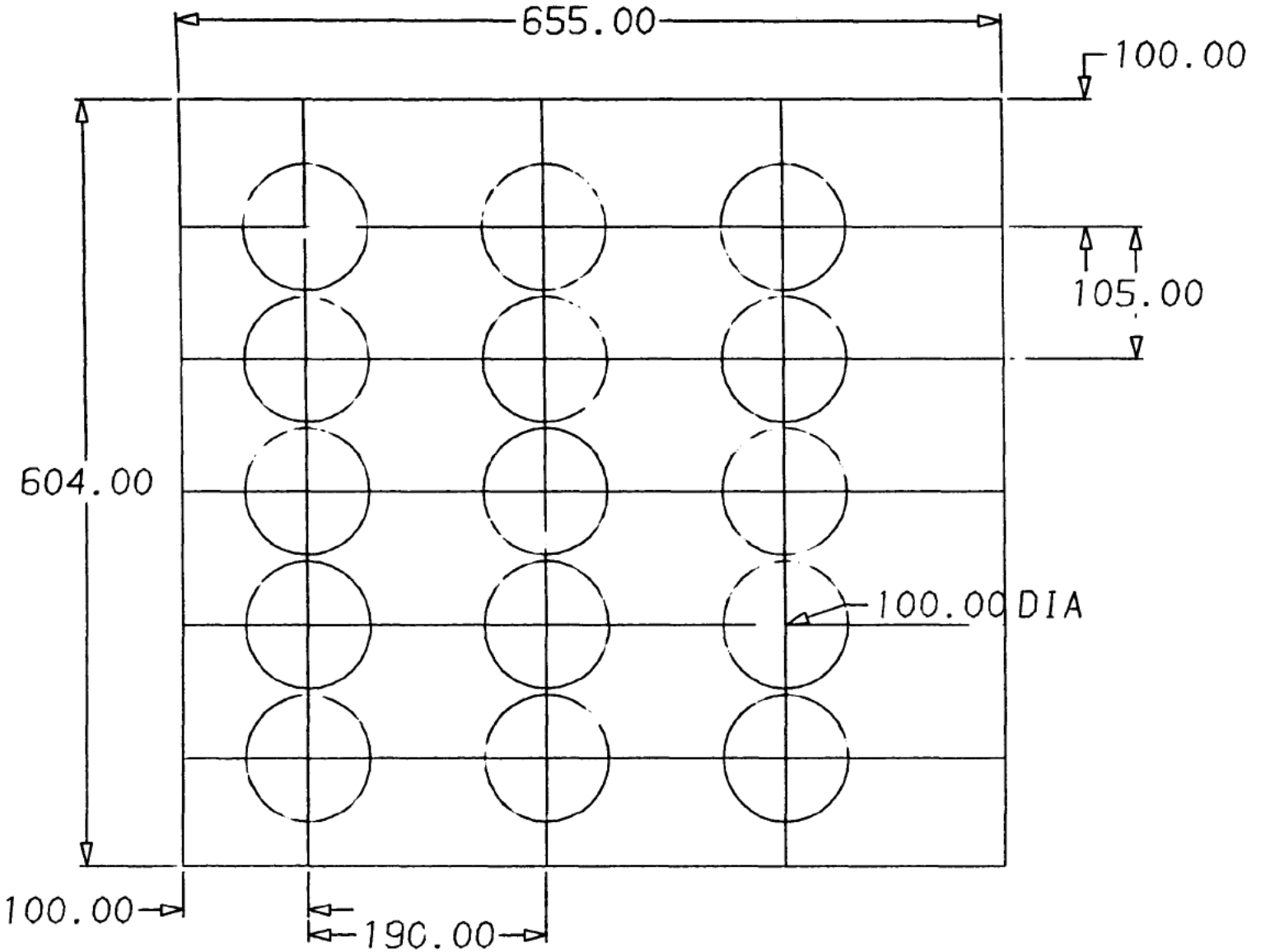

Figure 3.2. Impact Centre Positions for a

Typical CFRP Laminate.

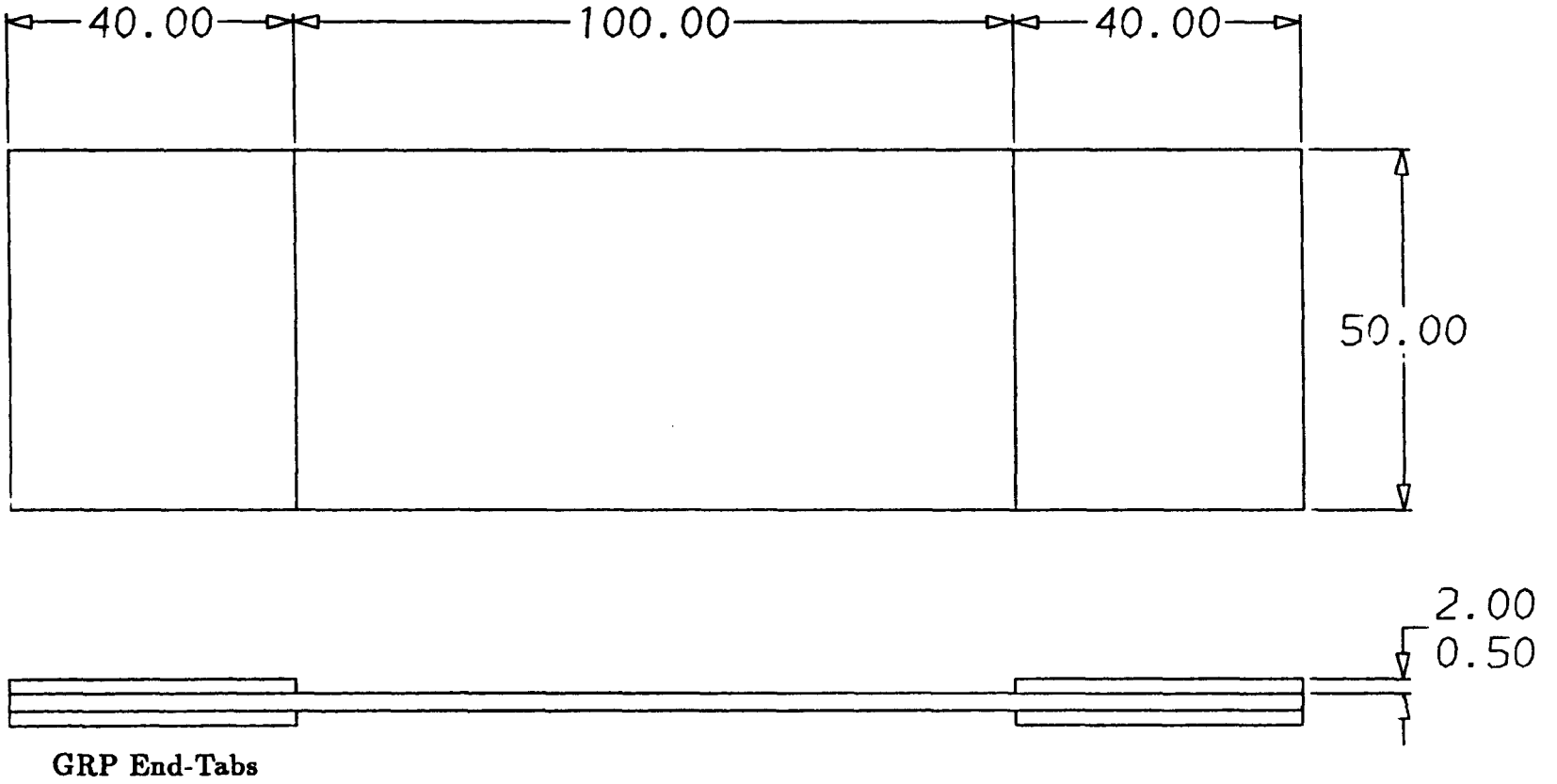

Figure 3.3. Specimen Design for Post-Impact

Static and Fatigue Testing [104].

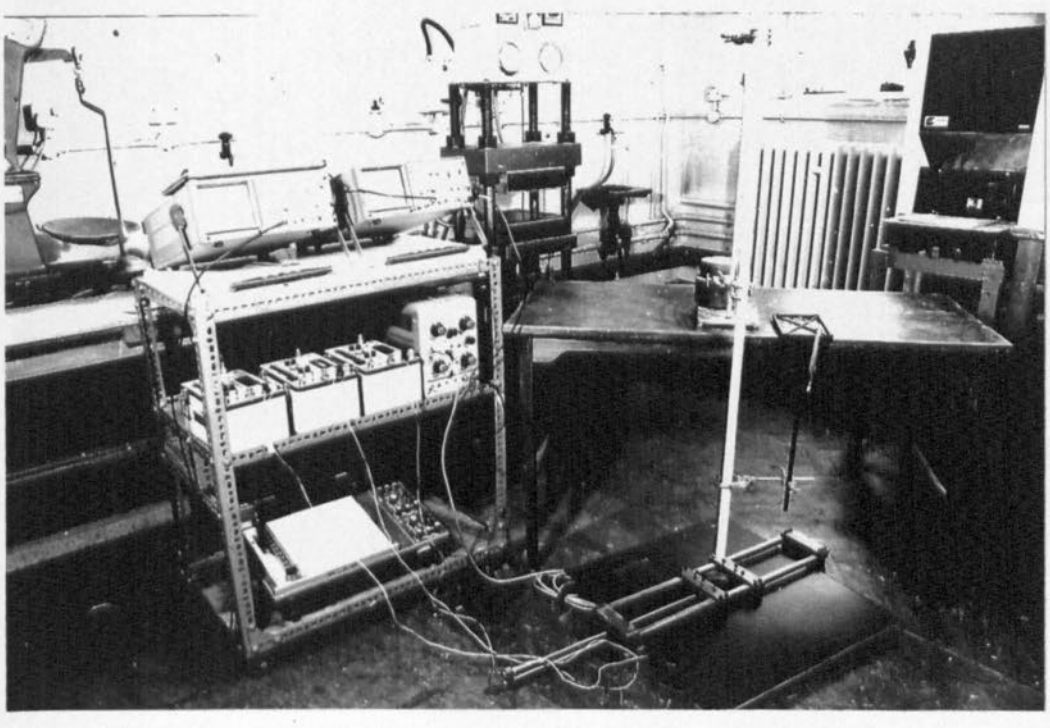

Figure 3.4. Drop - Weight Impact Test Rig.

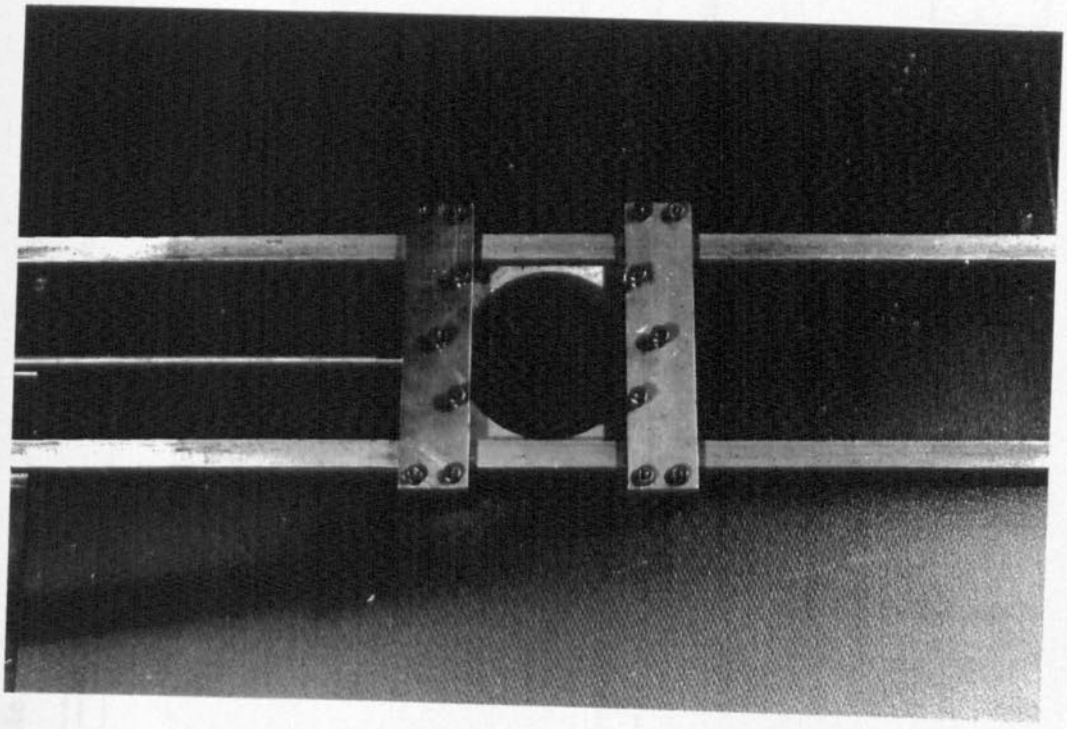

Figure 3.5. Drop - Weight Impact. Clamping Frame.

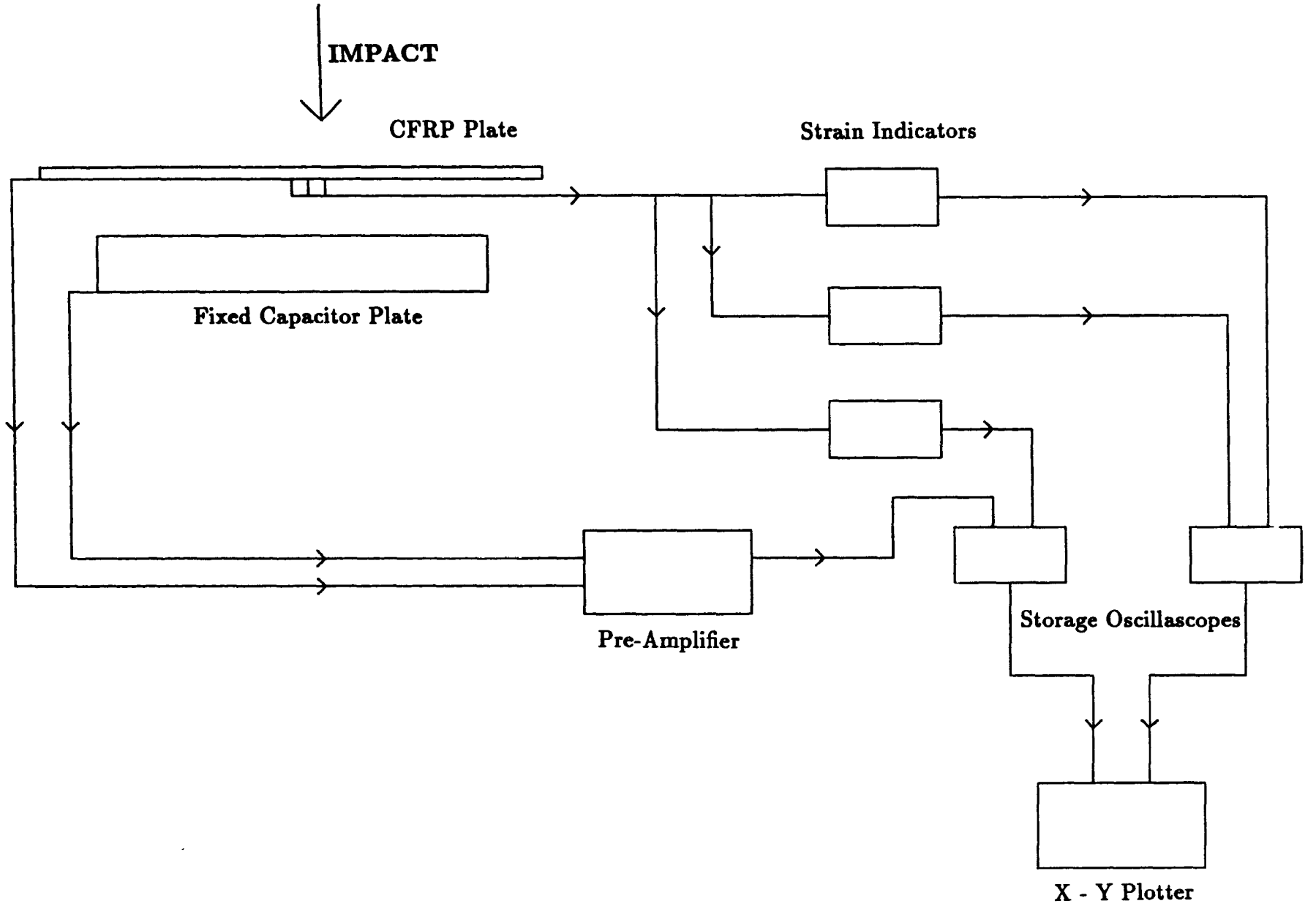

Figure 3.6. Schematic Representation of Instrumentation for Impacting CFRP Laminates.

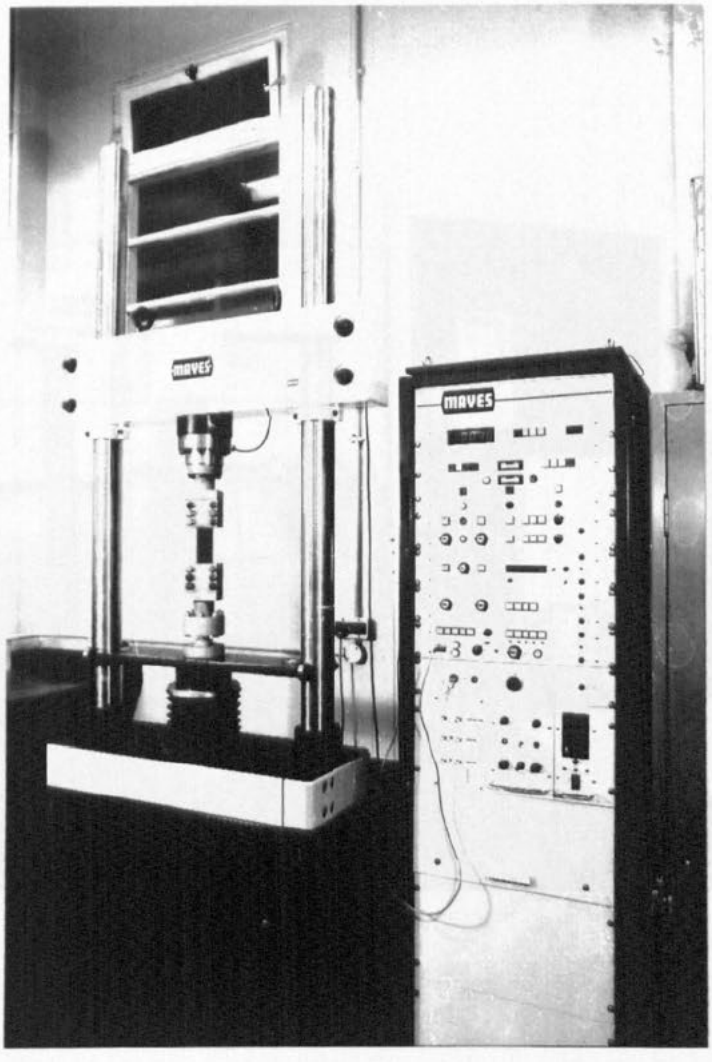

Figure 3.7. Mayes S100 Test Machine.

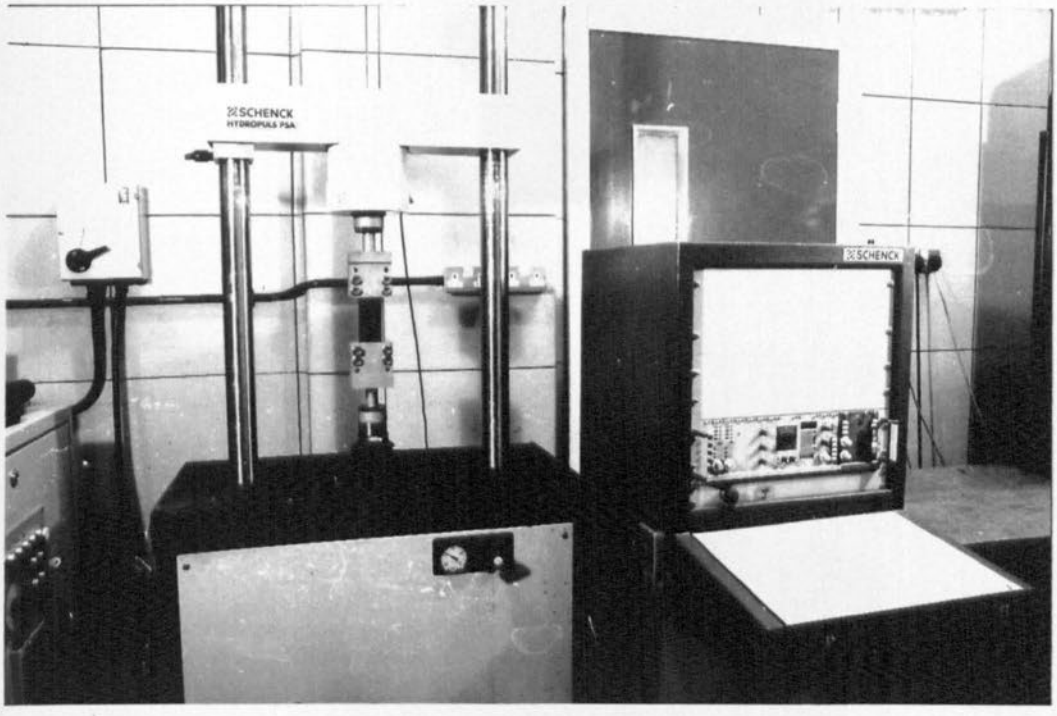

Figure 3.8. Schenck Hydropuls PSA 1006 Test Machine.

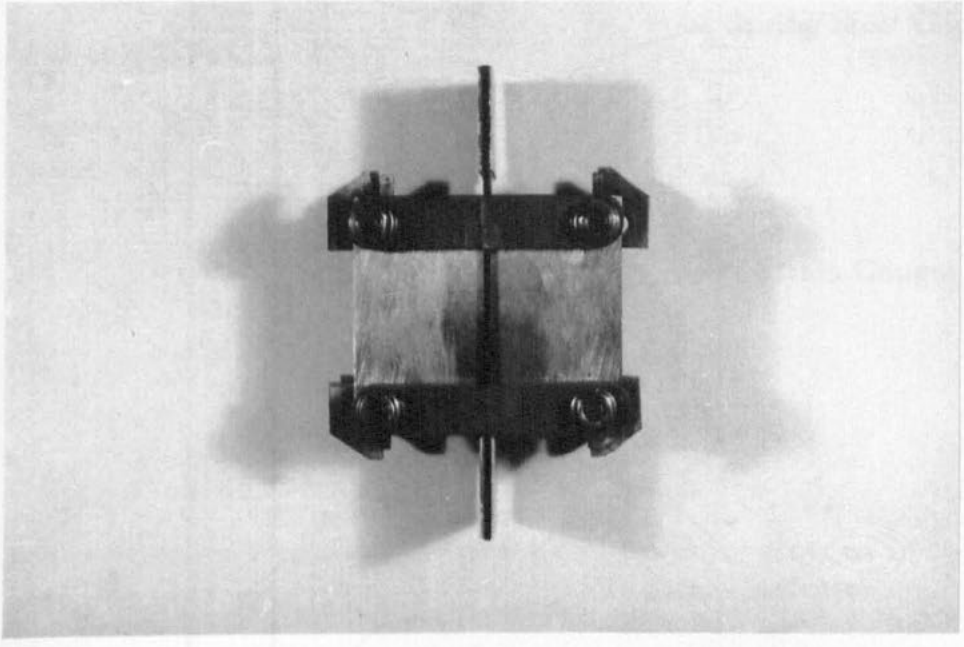

Figure 4.1. Axial Compression Test. Anti - Buckling Guides.

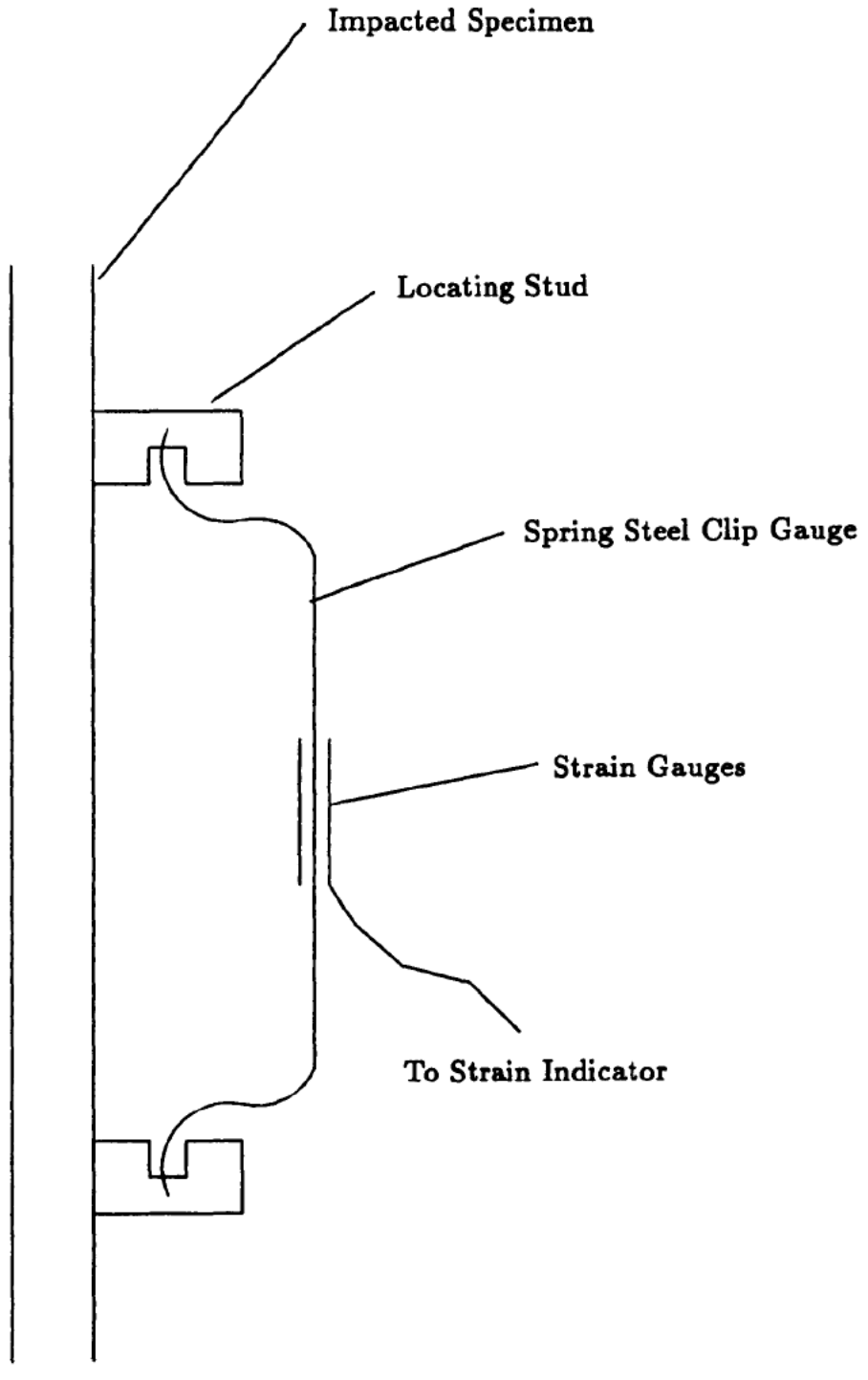

Figure 4.2. Clip Gauge Mounted Across the

Impact Damage Site.

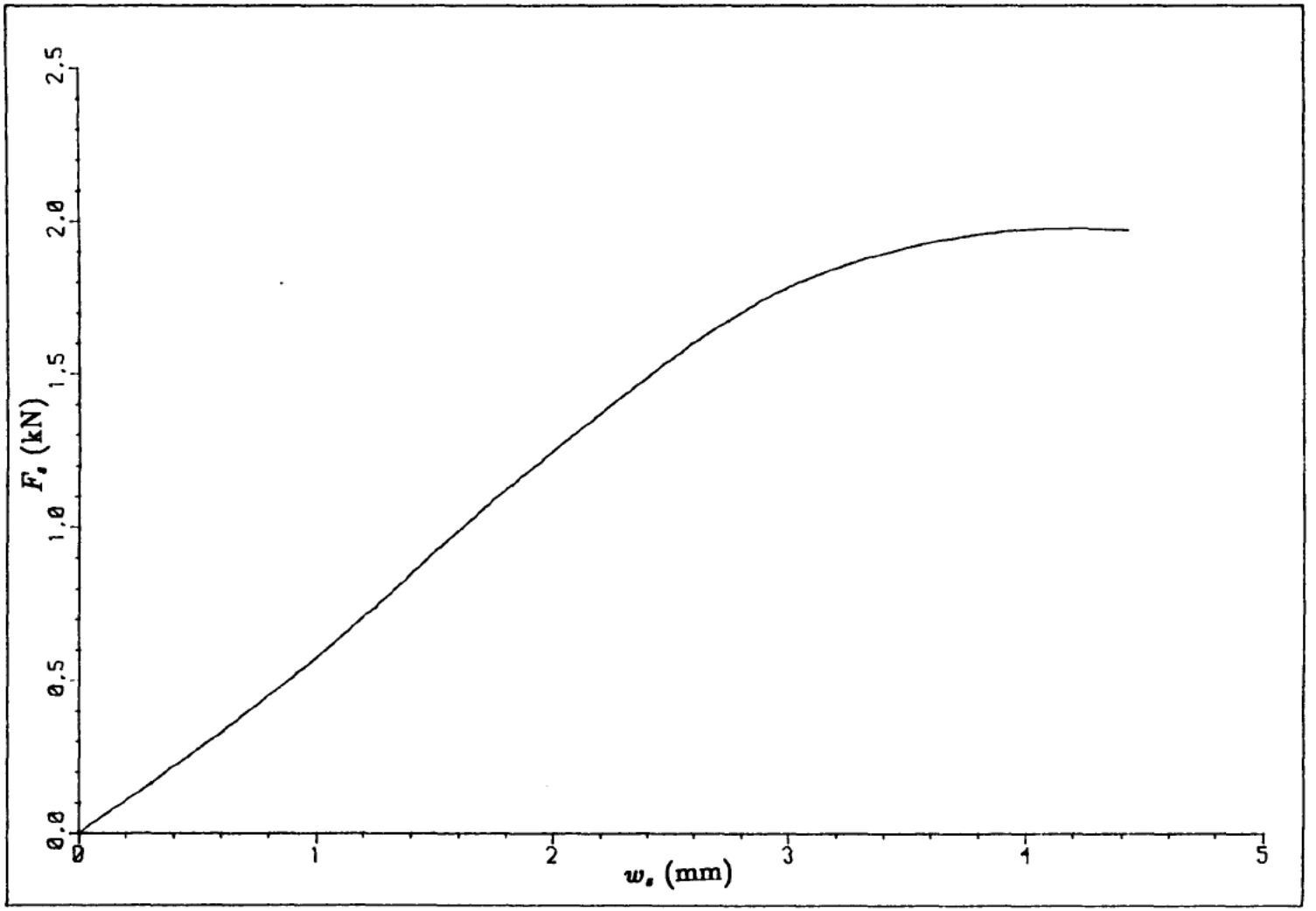

Figure 5.1. Typical Static Load/Deflection Behaviour of Clamped

100mm Diameter CFRP Plate. Specimen LE6169/A1/A4/CAL2.

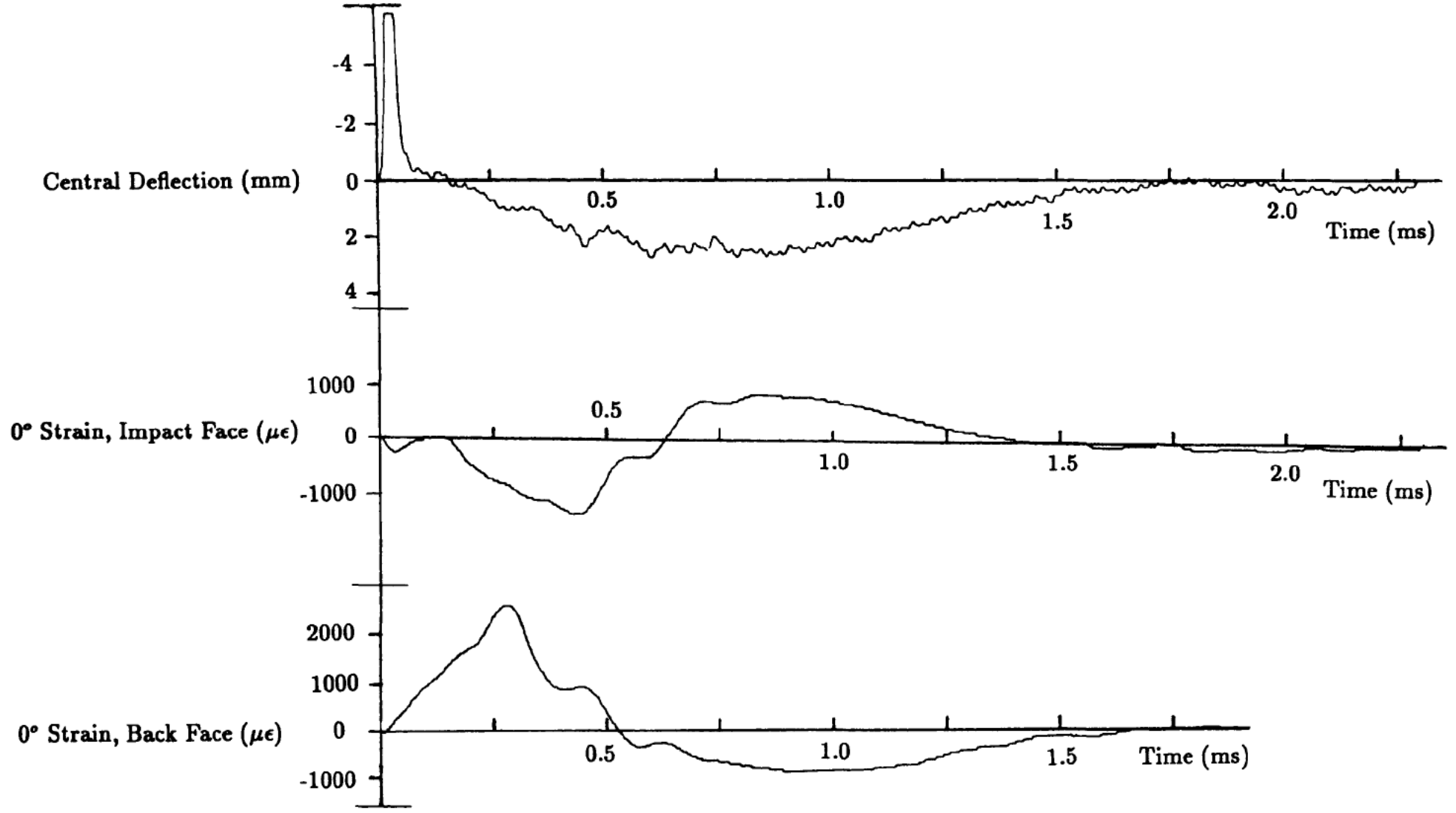

Figure 5.2. Typical Impact Response for Clamped 100mm Diameter

CFRP Plate. Specimen LE6170/A1/2/5. 4.91J Impact.

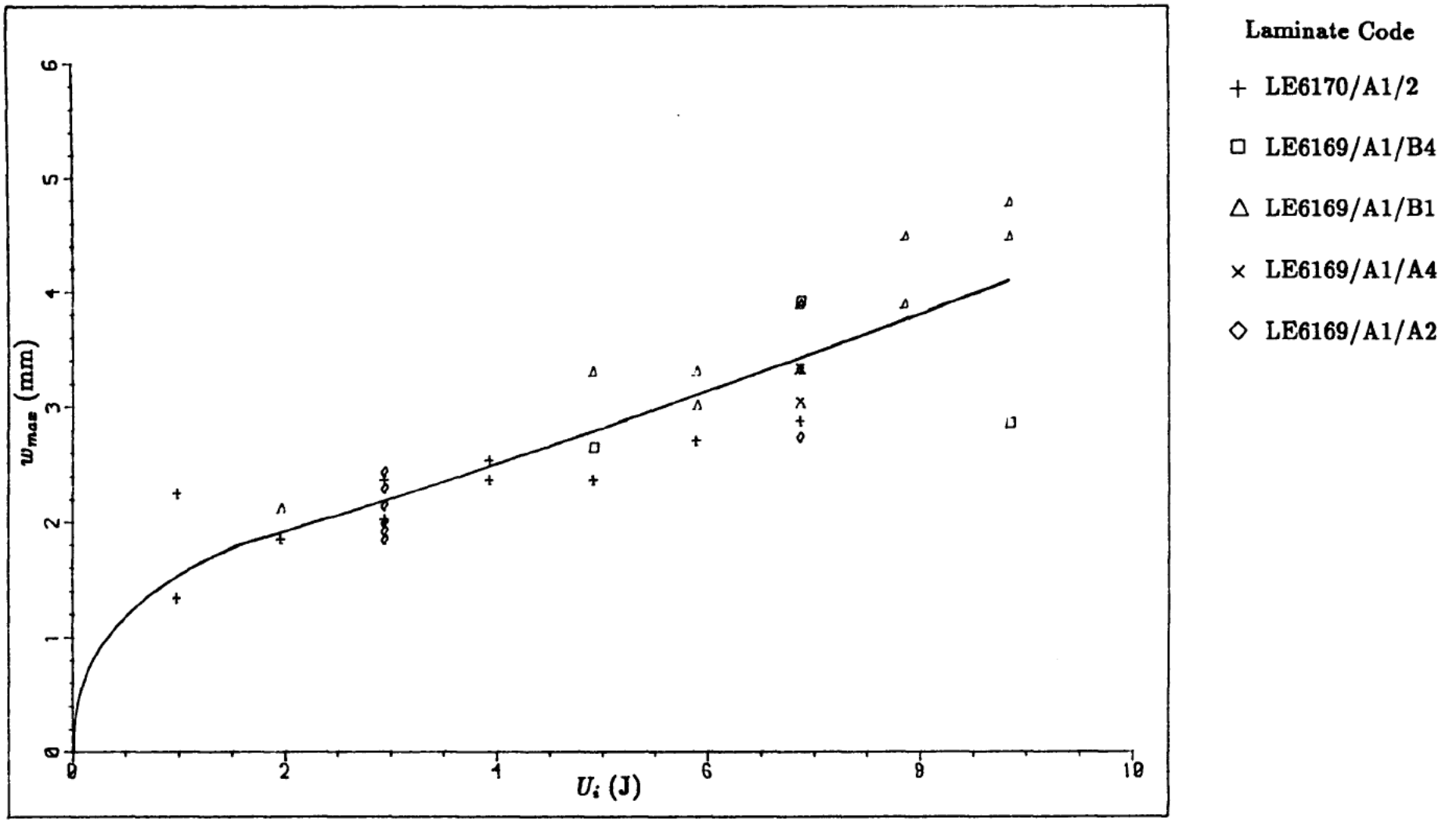

Figure 5.3. The Relationship Between Incident Impact Energy and Maximum Central Displacement for Impacted CFRP Plates.

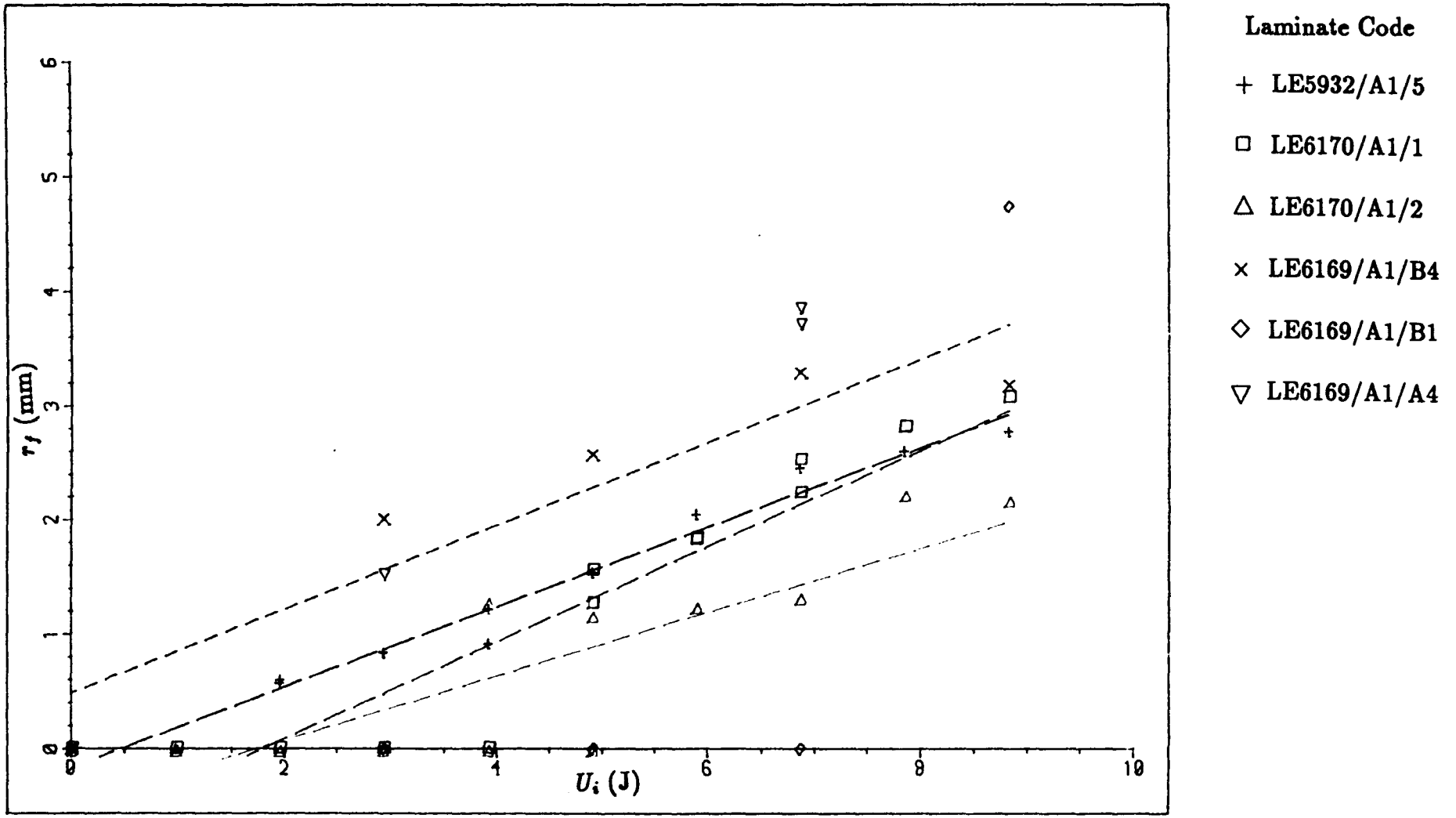

Figure 5.4. The Relationship Between Incident Impact Energy and Front Face Damage Radius for Impacted CFRP.

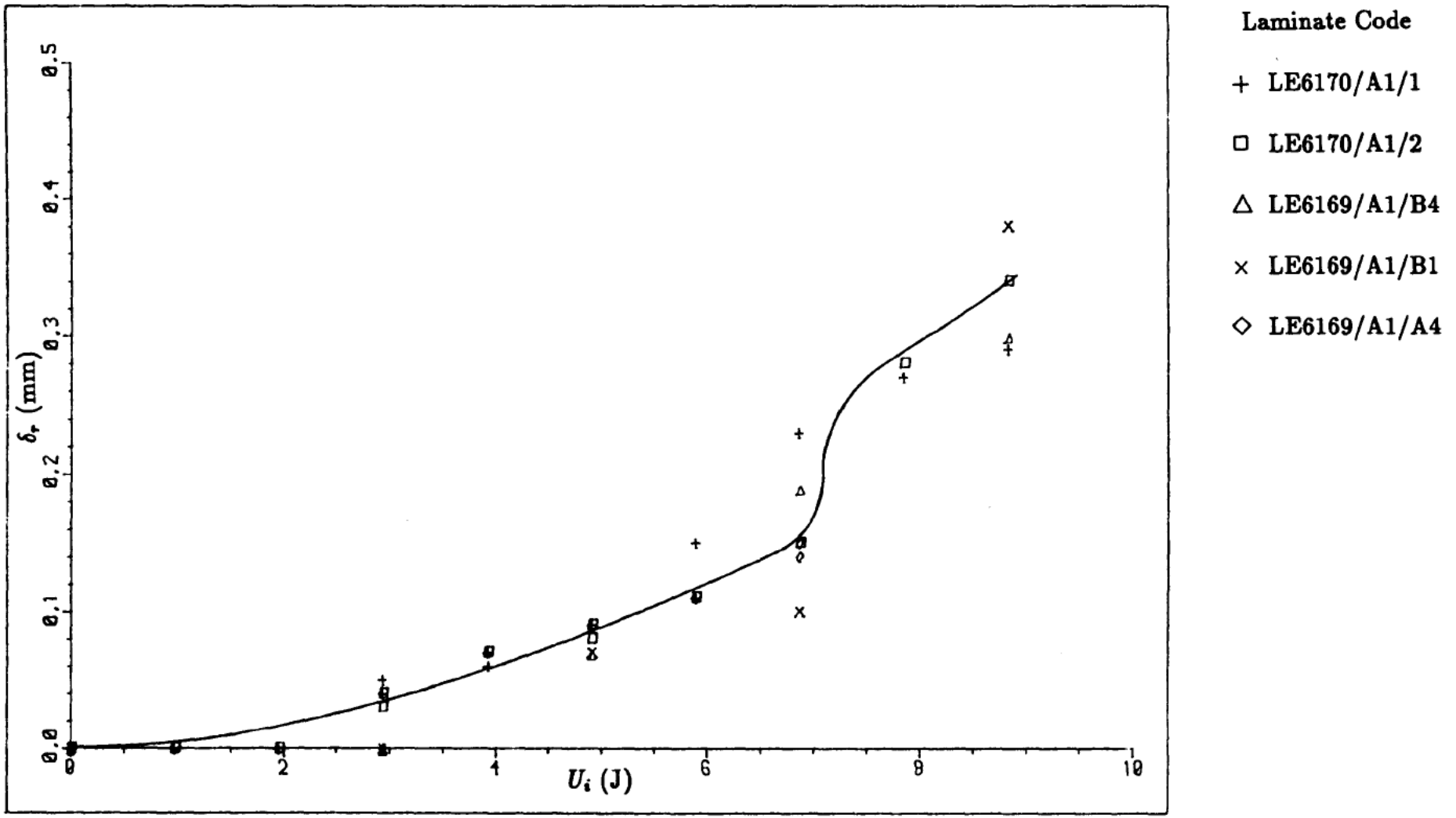

Figure 5.5. The Relationship Between Incident Impact Energy and Residual Indentation Depth for Impacted CFRP.

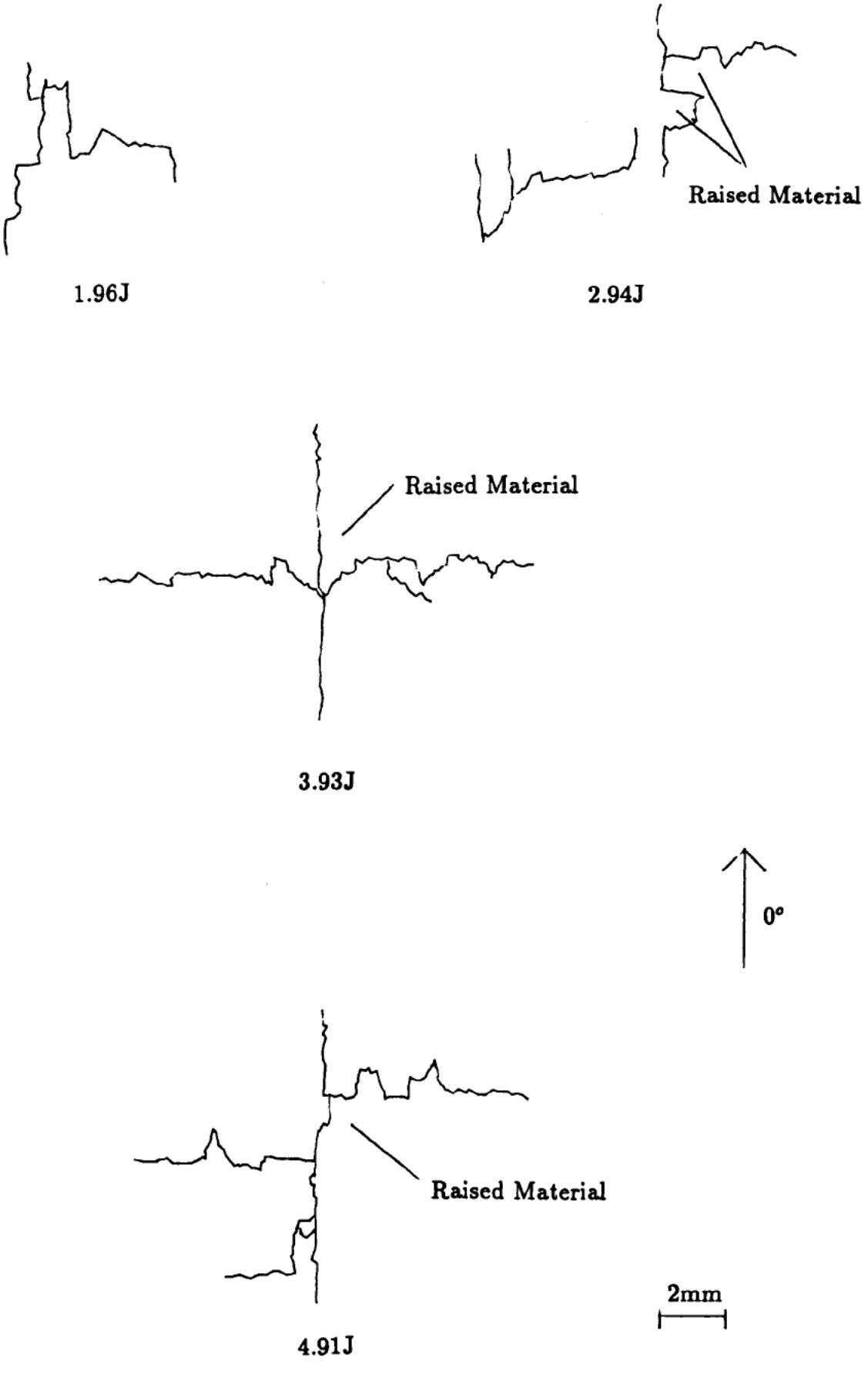

Figure 5.6. Typical Back Face Crack Patterns for

Impacted CFRP. Laminate LE6170/A1/2.

(a)

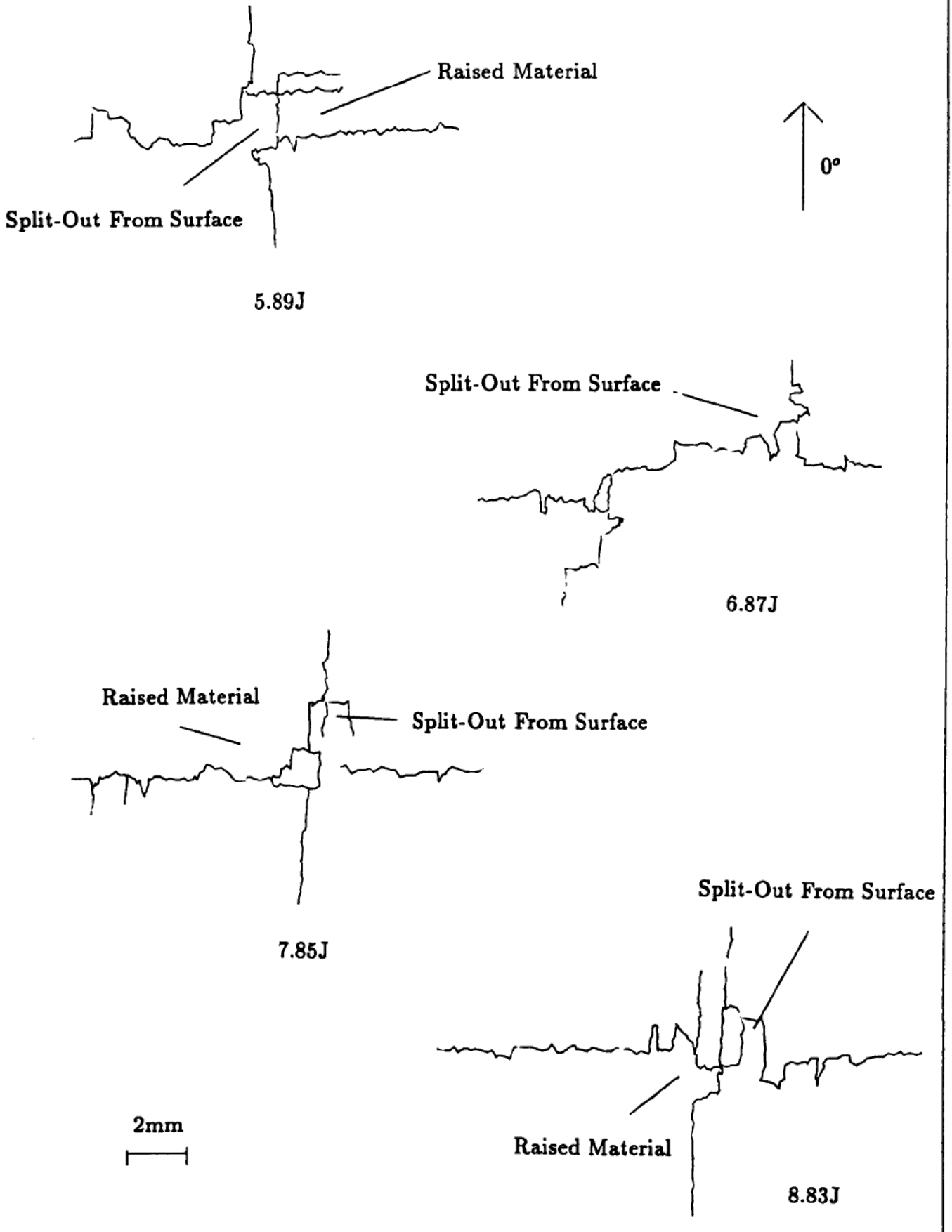

Figure 5.6A Typical Back Face Crack Patterns for

Impacted CFRP. Laminate LE6170/A1/2.

(b)

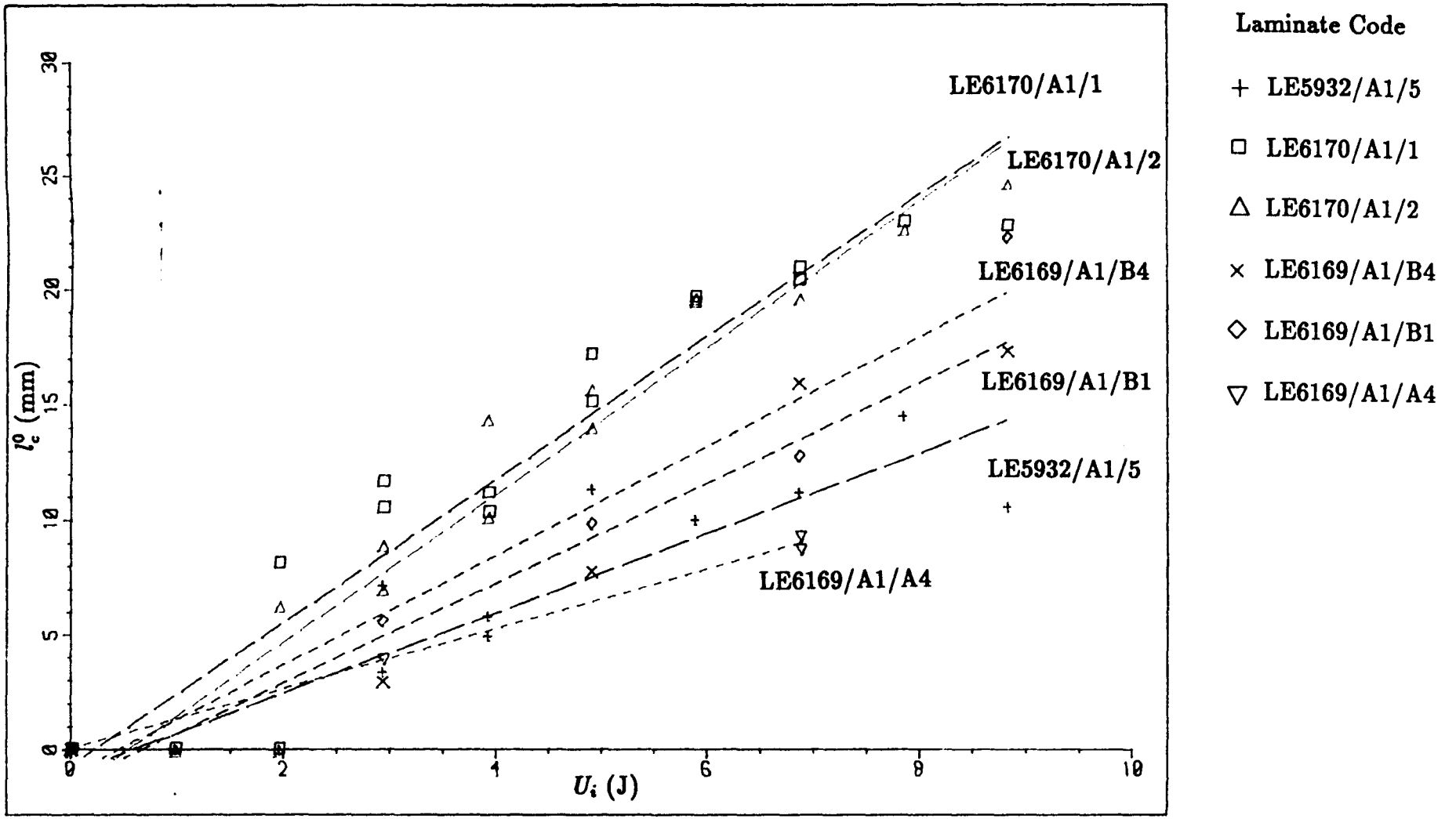

Figure 5.7. The Relationship Between Incident Impact Energy and

0° Split Length in the Back Face for Impacted CFRP.

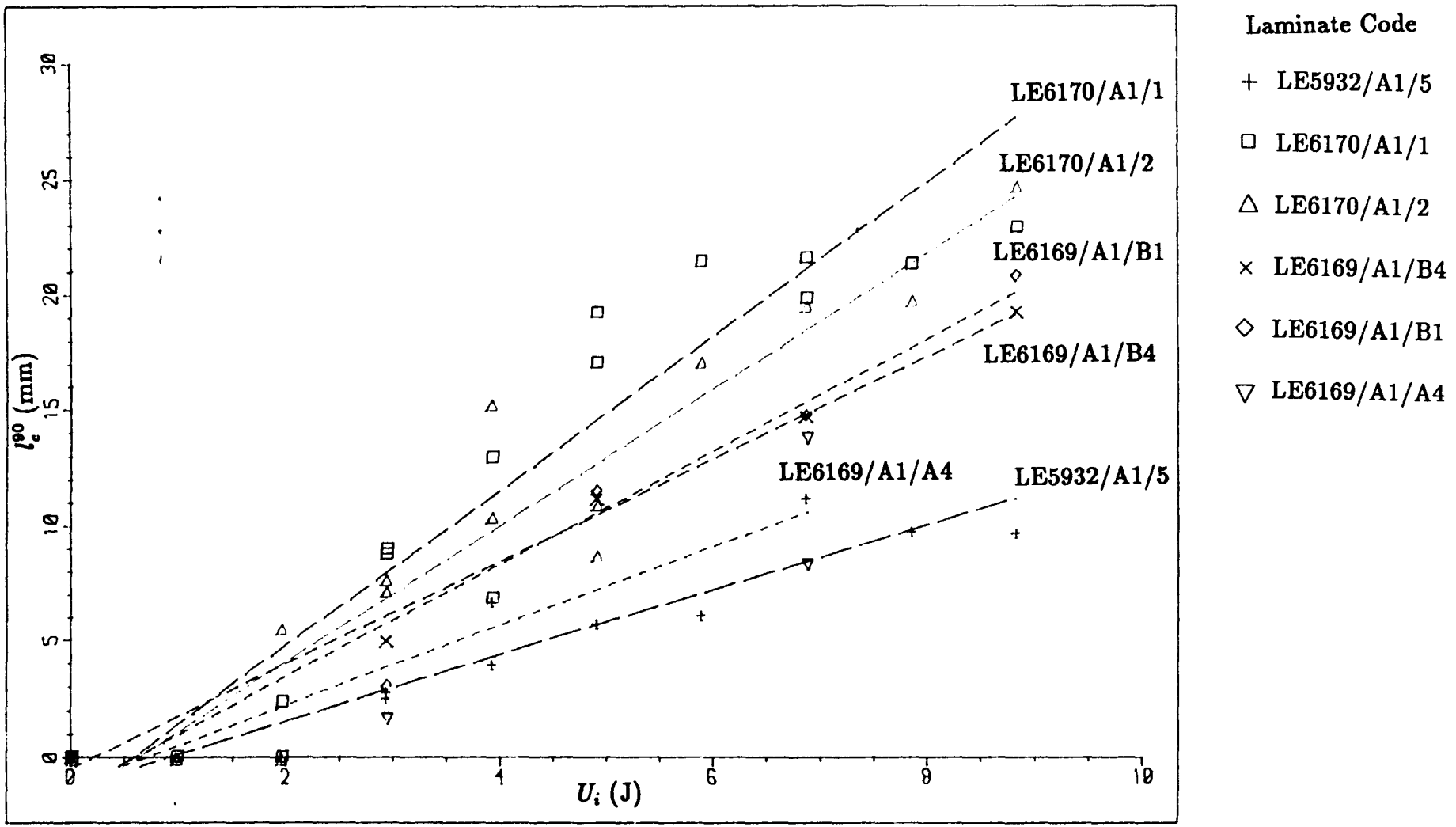

Figure 5.8. The Relationship Between Incident Impact Energy and

90° Split Length in the Back Face for Impacted CFRP.

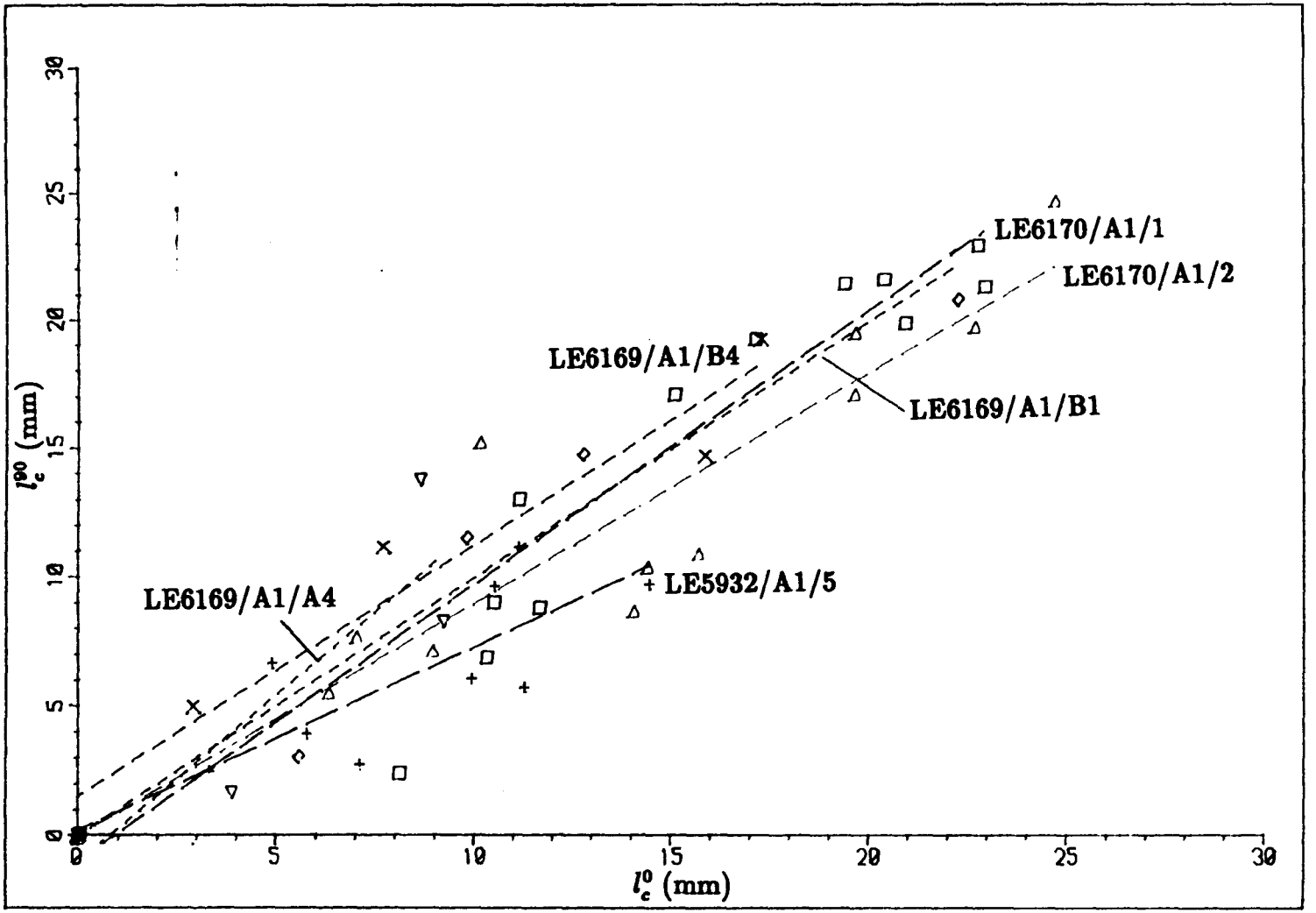

Figure 5.9. The Relationship Between Split Length in the Back Face

in the Two Principle Fibre Directions for Impacted CFRP.

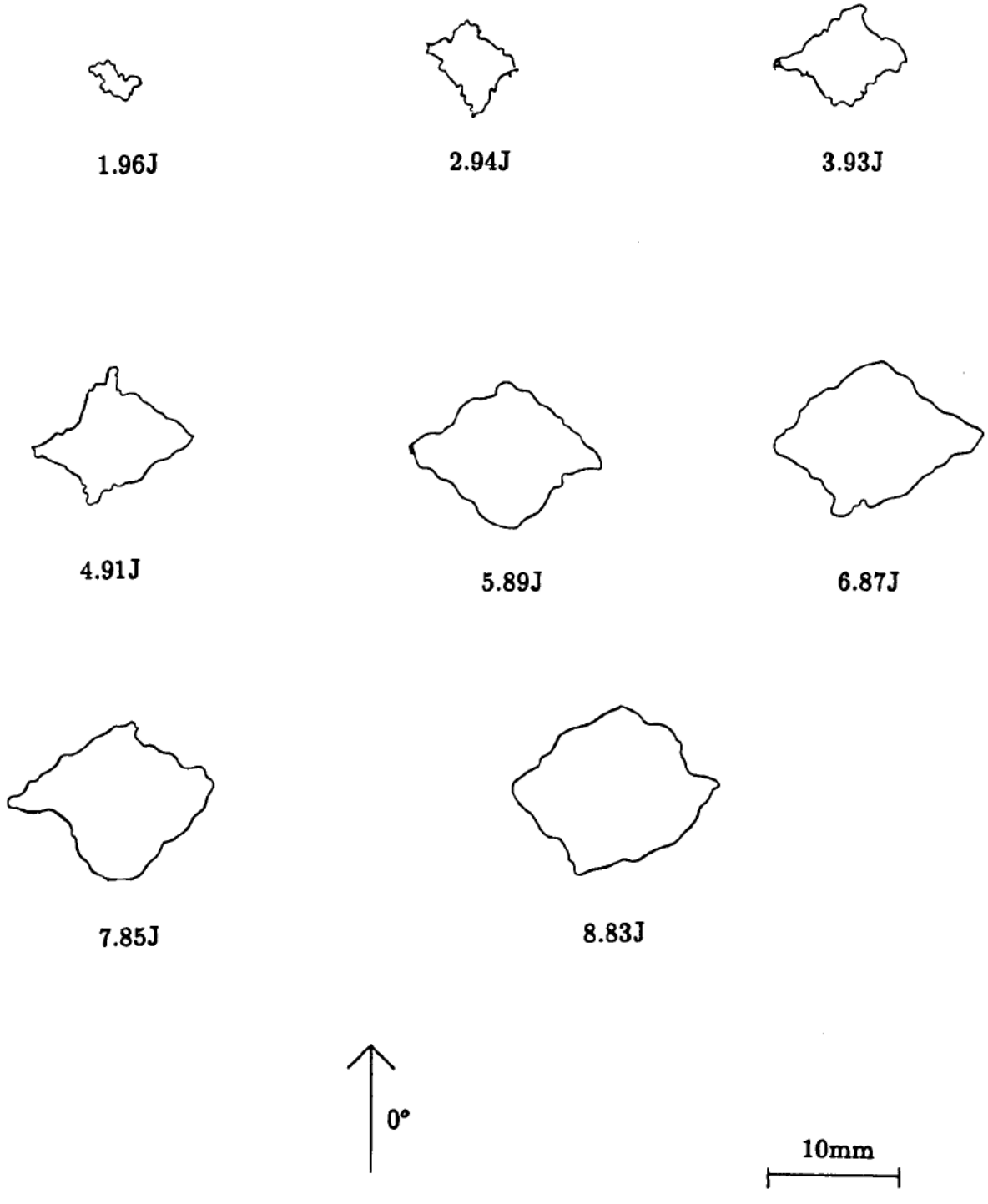

Figure 5.10. Typical C-Scan Areas for Impacted CFRP.

Laminate LE5932/A1/5.

1.96J
LE6170/A1/1/20

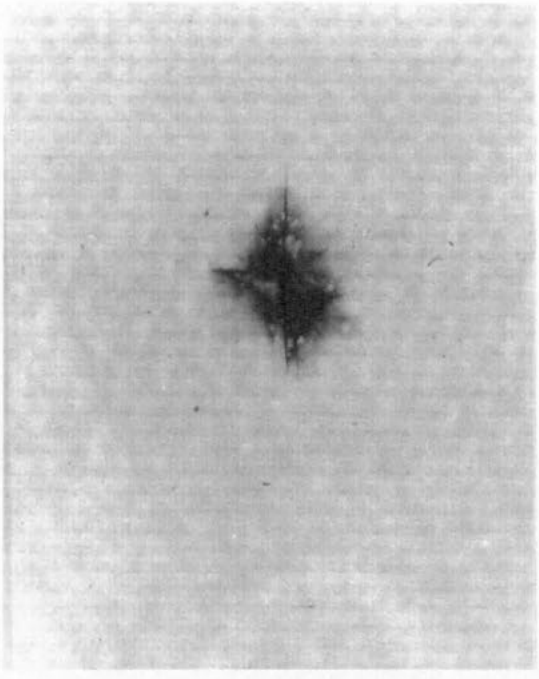

↑ 0°

2.94J
LE6170/A1/1/22

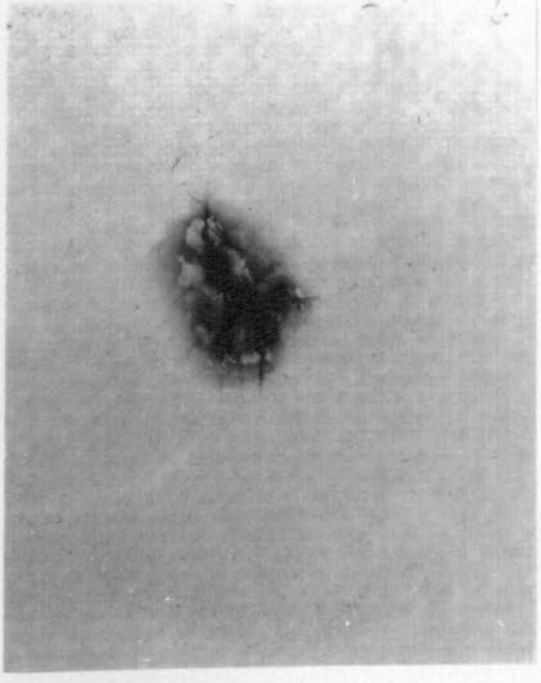

3.93J
LE6170/A1/1/24

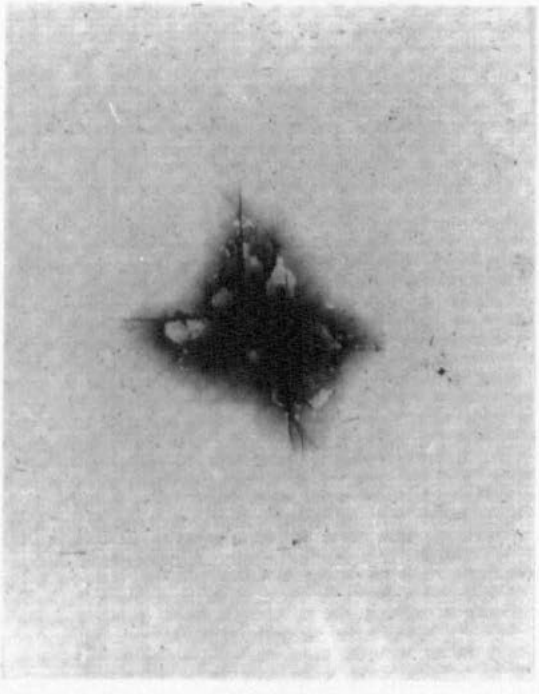

4.91J
LE6170/A1/1/25

Figure 5.11. Typical X-Rays for Impacted Specimens.

(a)

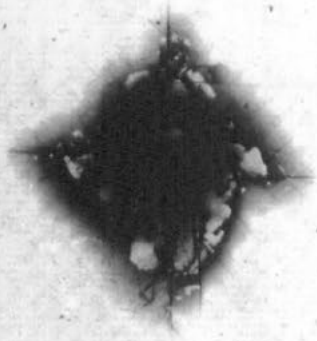

5.89J
LE6170/A1/1/27

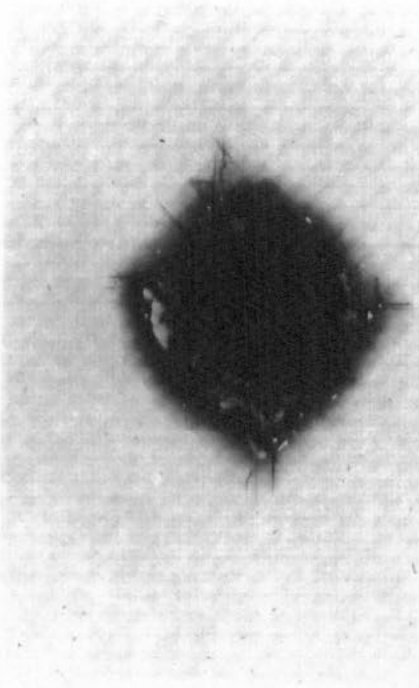

6.87J
LE6170/A1/1/29

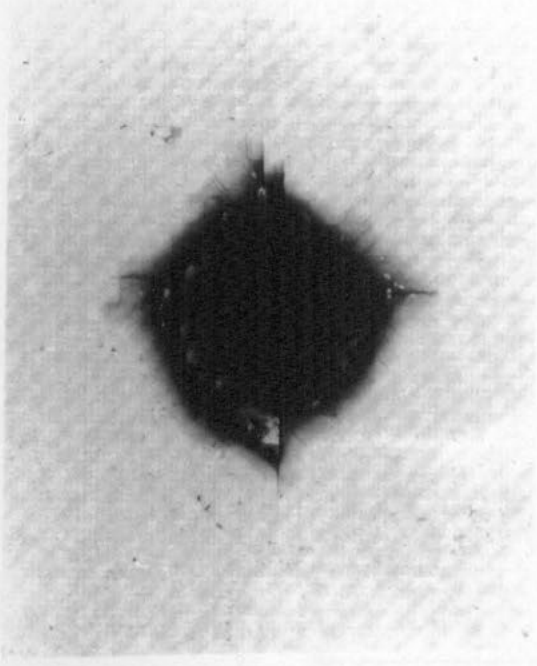

7.85J
LE6170/A1/1/31

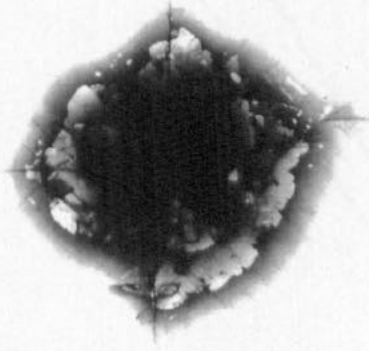

8.83J
LE6170/A1/1/32

Figure 5.11 Typical X-Rays for Impacted Specimens. (b)

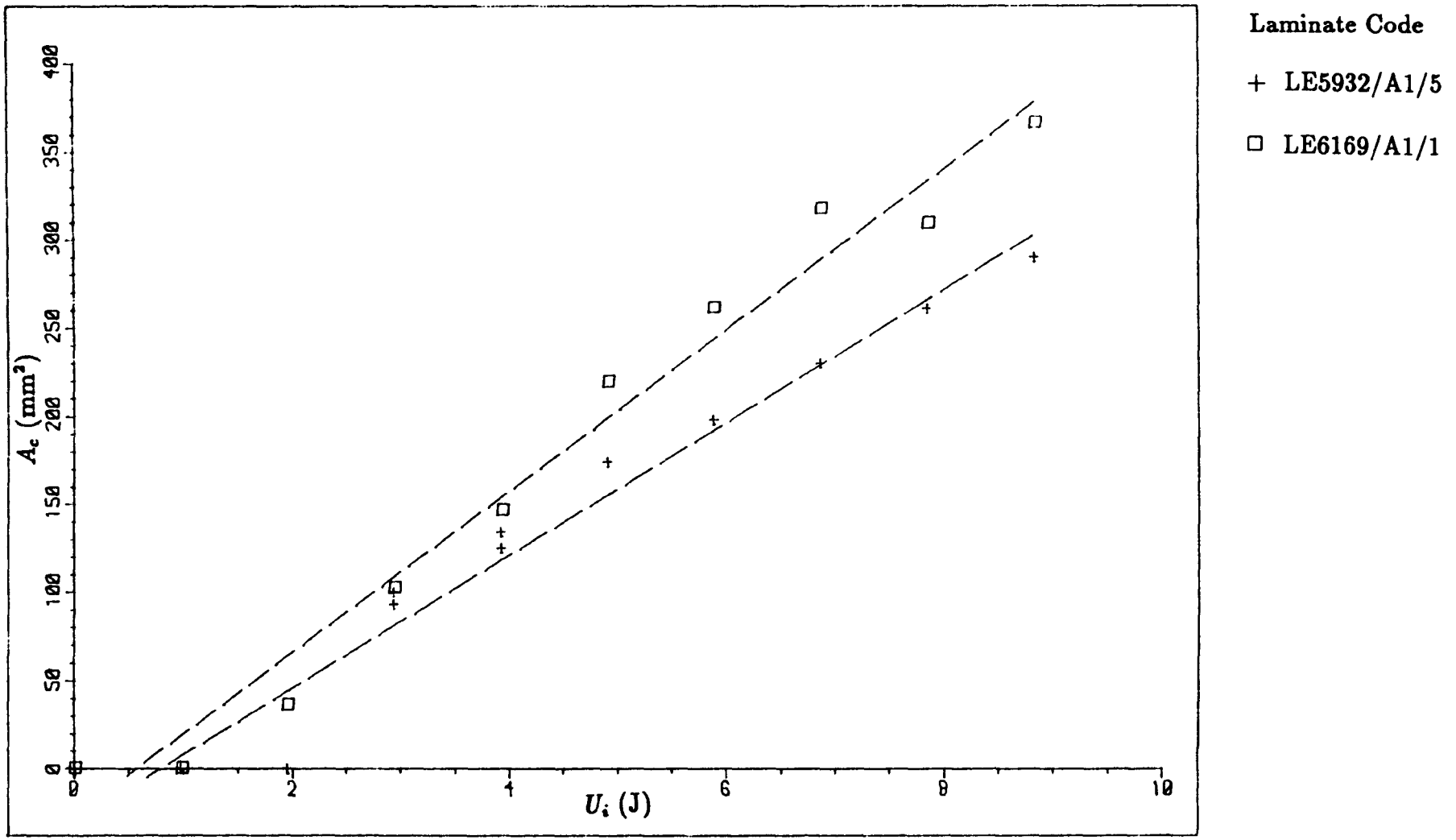

Figure 5.12. The Relationship Between Incident Impact Energy

and C-Scan Damage Area for Impacted CFRP.

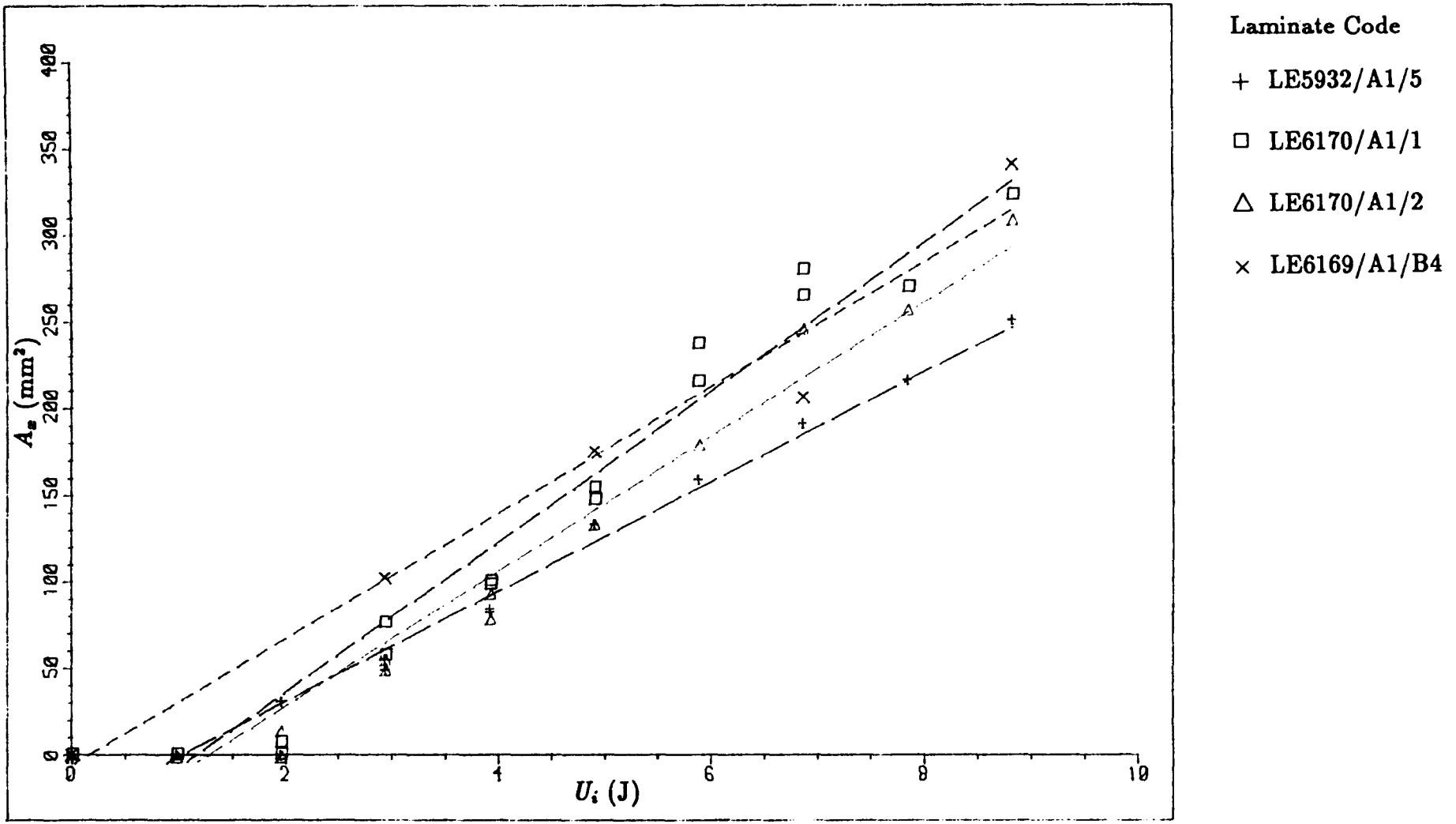

Figure 5.13. The Relationship Between Incident Impact Energy

and X-Ray Damage Area for Impacted CFRP.

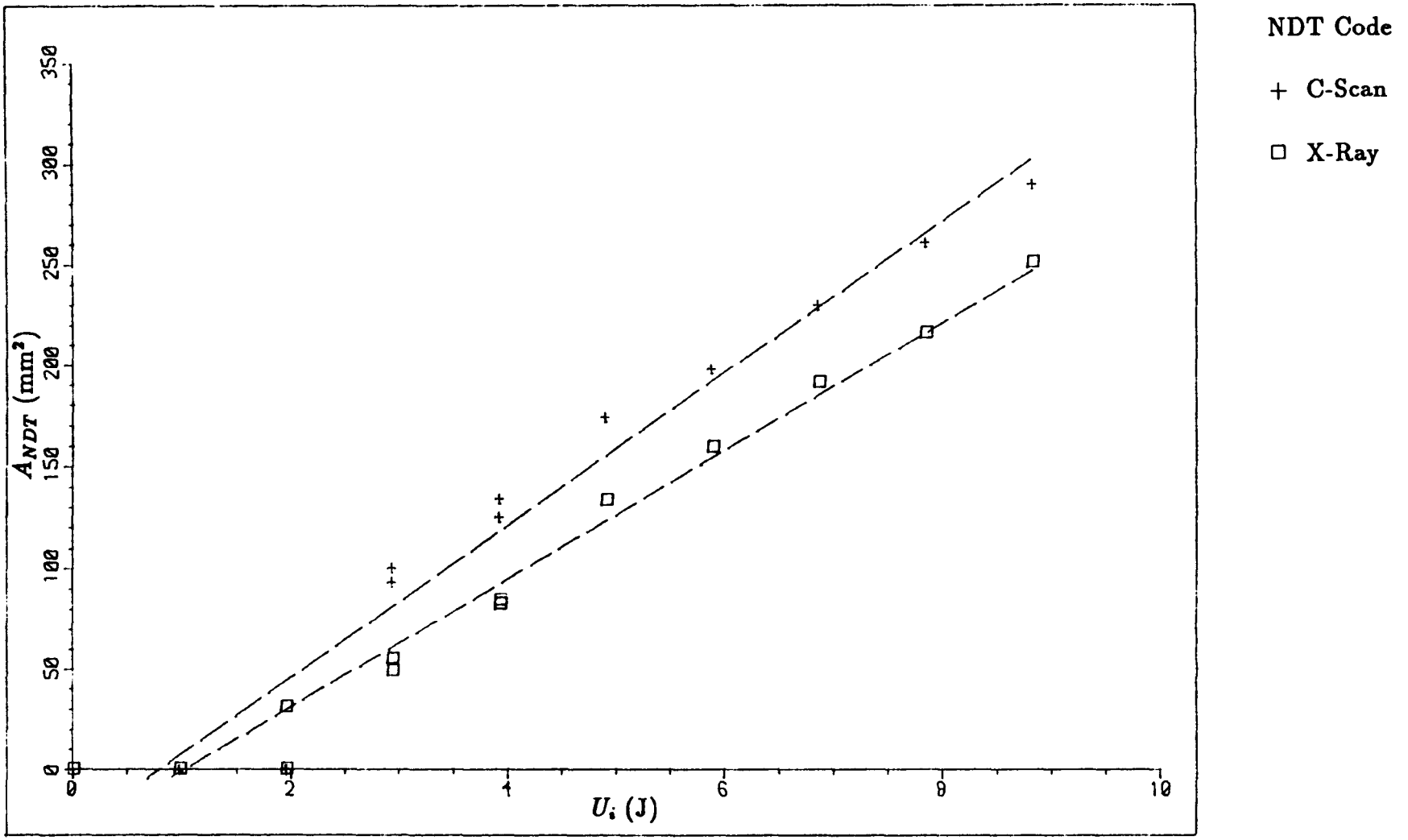

Figure 5.14. Comparison of C-Scan and X-Ray Non-Destructive Test Methods. Laminate LE5932/A1/5.

Impact ↓

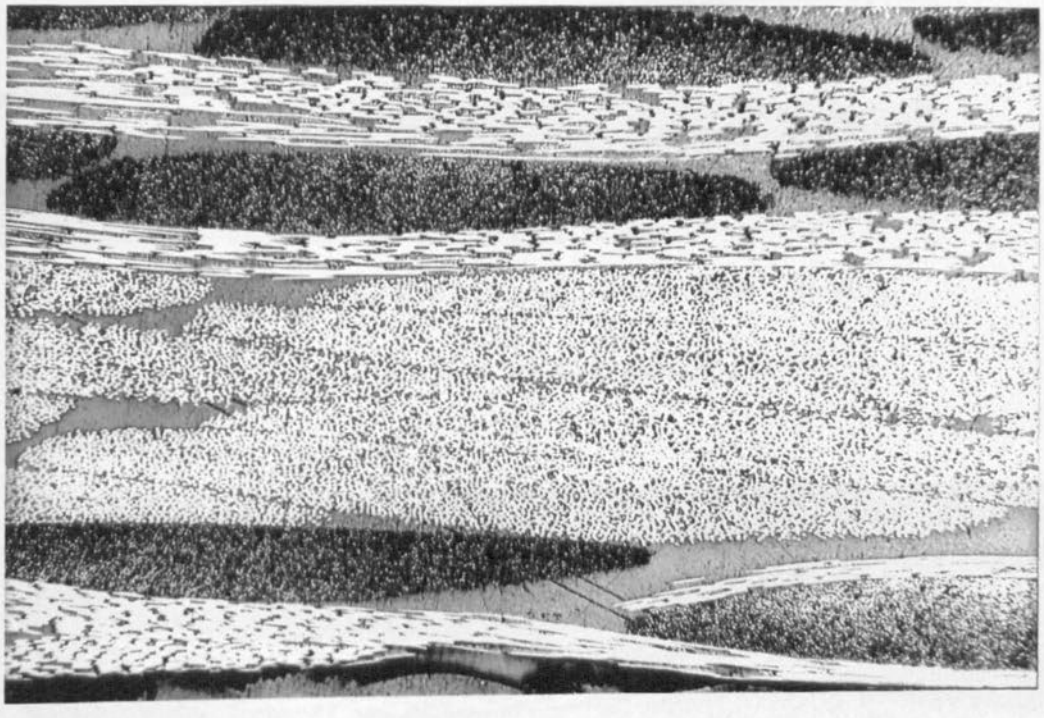

Figure 5.15. Polished Cross-Section of Typical

0.98J Impact. No Damage Visible.

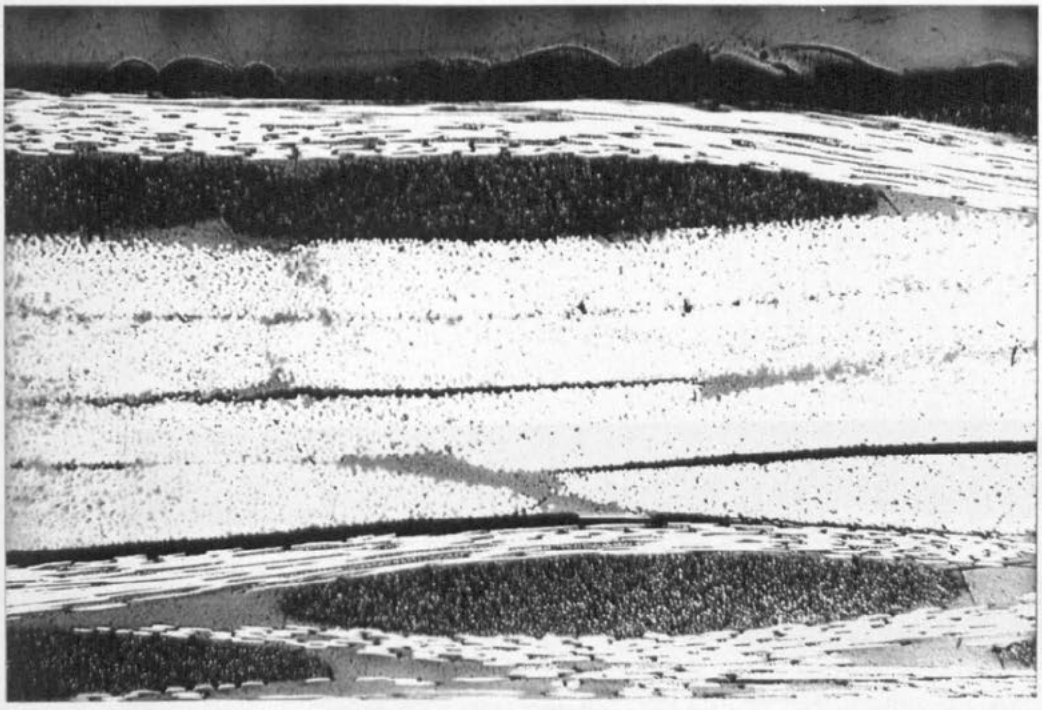

Figure 5.16. 2.94J Impact. Upper Plies Showing

Isolated Delaminations.

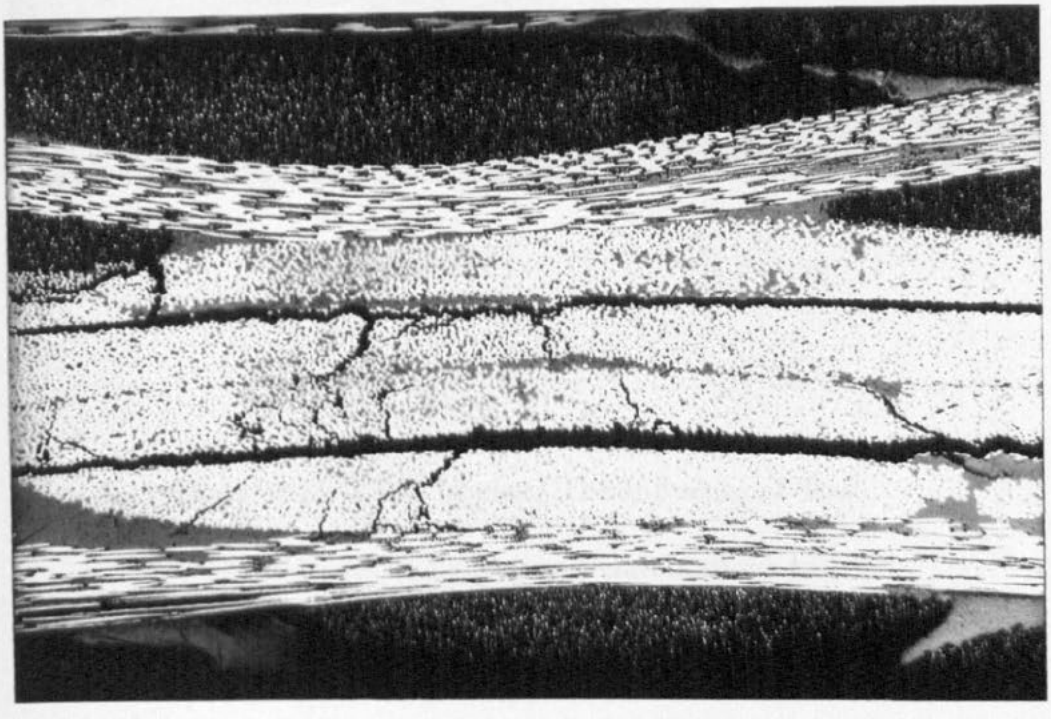

Figure 5.17. 2.94J Impact. Lower Plies Showing

Delaminations and Interconnecting Matrix Cracks.

Impact ↓

Figure 5.18. 2.94J Impact. The Influence of Tow Cross-Overs in Deflecting Delaminations to Adjacent Interfaces.

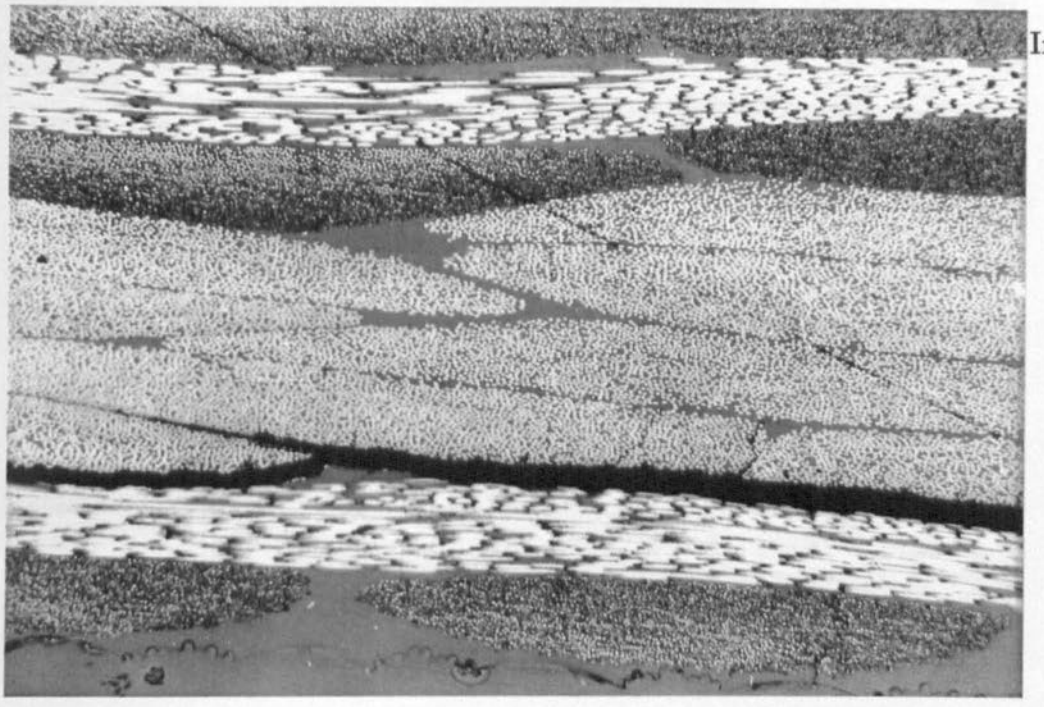

Figure 5.19. 4.91J Impact. Deflection of Delamination into Adjacent ±45° Plies at Tow Cross-Overs.

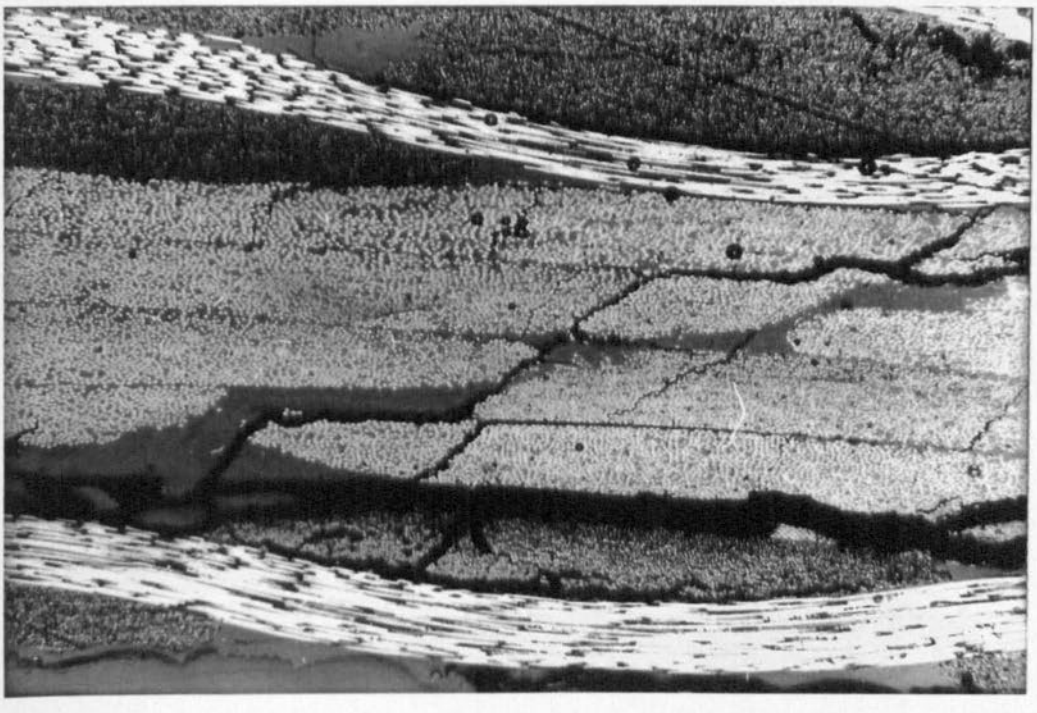

Figure 5.20. 4.91J Impact. Extensive Network of Delaminations and Through-Thickness Matrix Cracks.

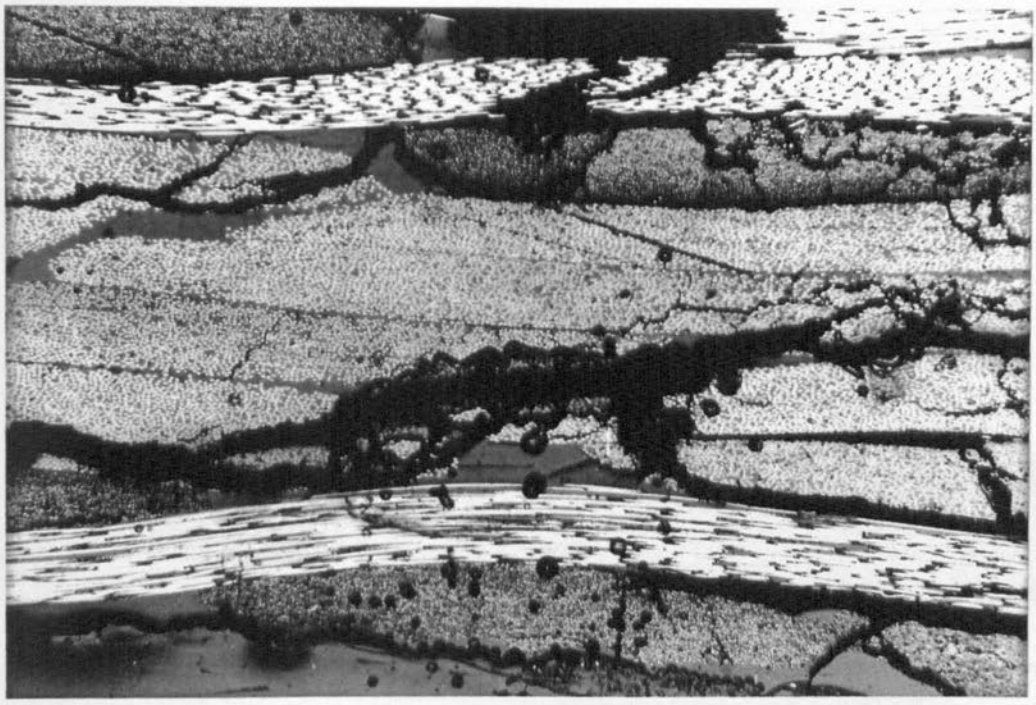

Figure 5.21. 4.91J Impact. Fibre Failure in the Central

$0°/90°$ Plies.

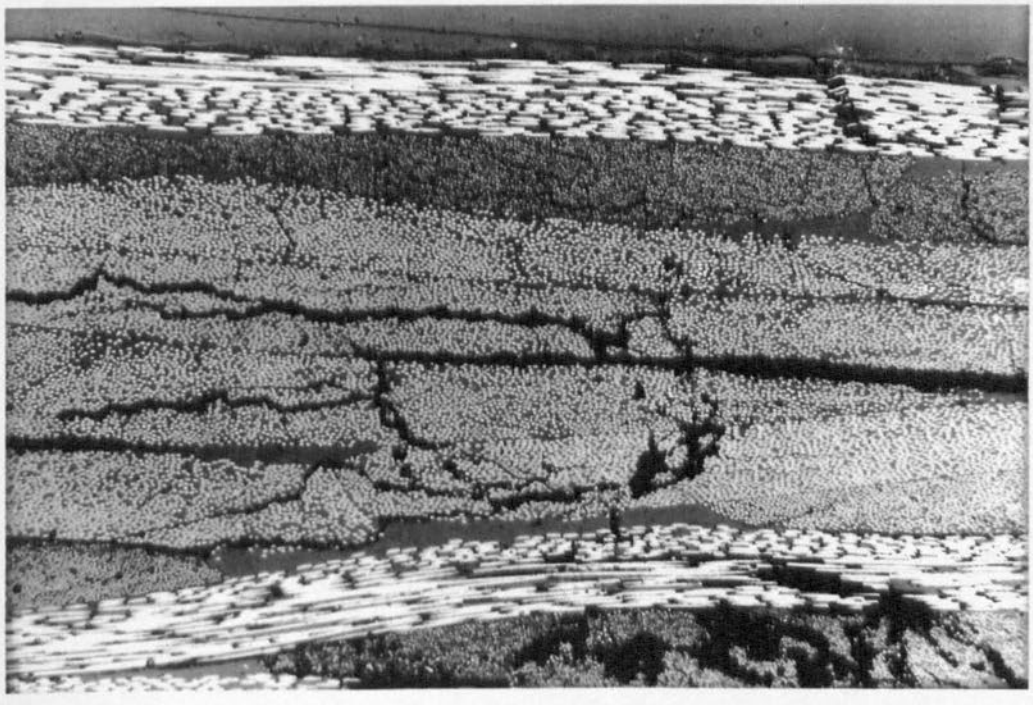

Figure 5.22. 4.91J Impact. Compressive Buckling 'Kink

Zone' on the Impact Face.

Impact ↓

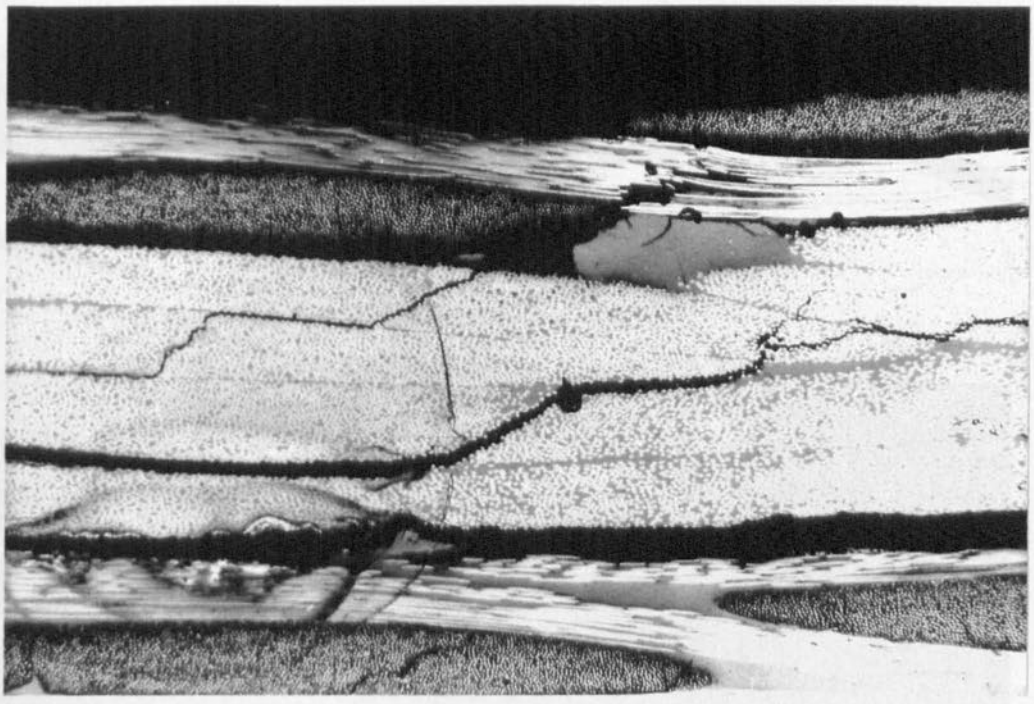

Figure 5.23. 6.87J Impact. Fibre Failure

in the Impact Face Ply.

Impact ↓

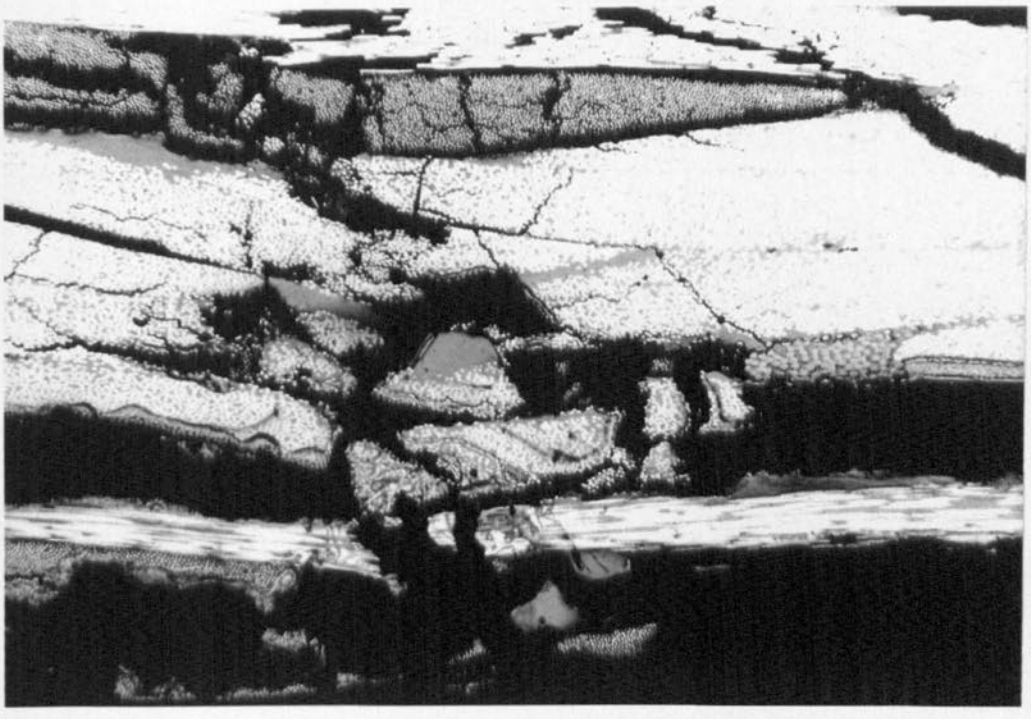

Figure 5.24. 8.83J Impact. Separation and Displacement of Fragments of Material from The Body of The Specimen.

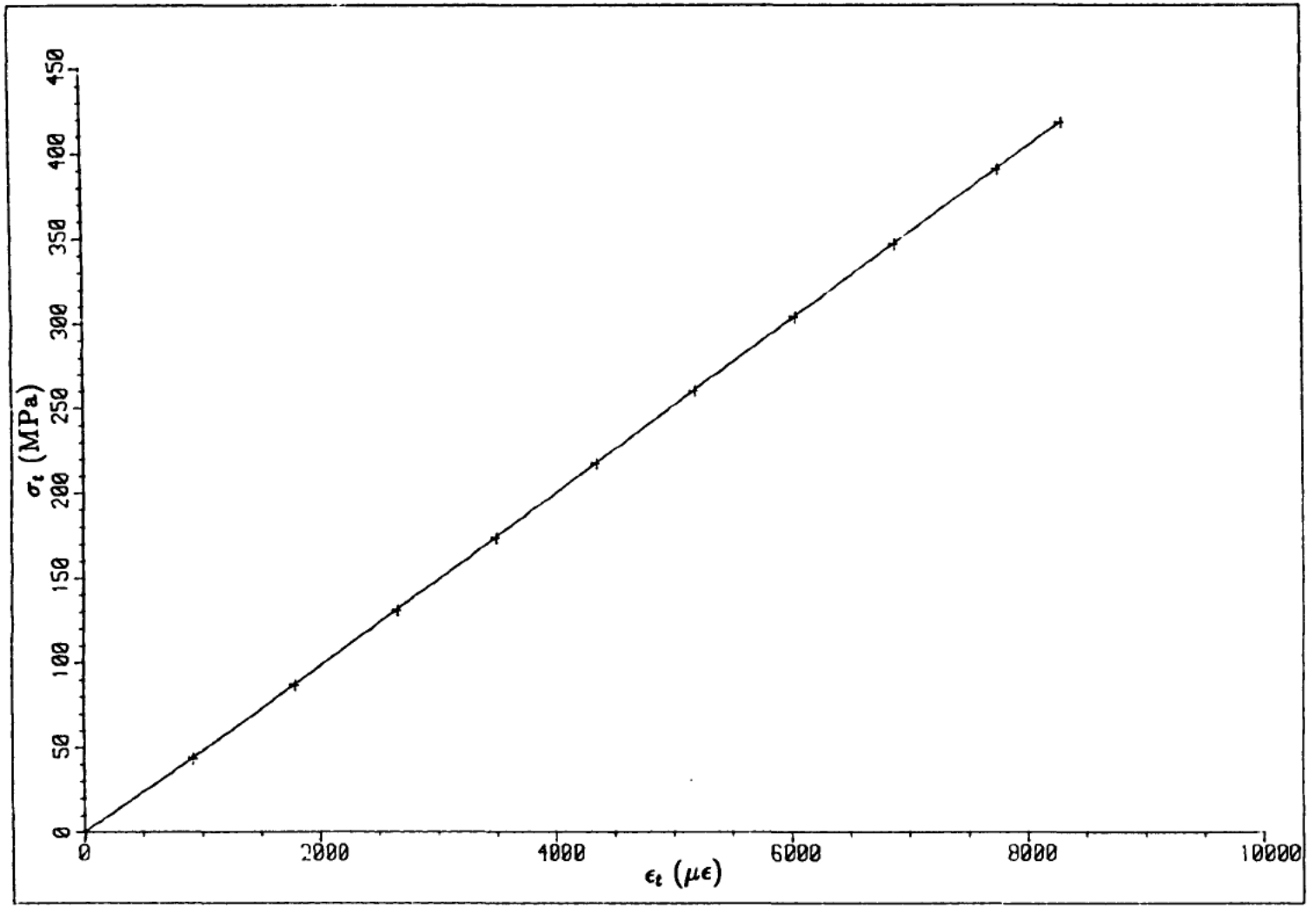

Figure 6.1. Tensile Stress/Strain Behaviour for Undamaged

CFRP. Specimen LE6169/A1/1/17.

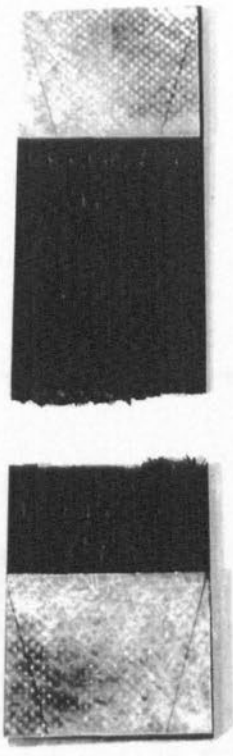

Figure 6.2. Typical Failure of Undamaged Tensile Specimen. LE6170/A1/1/3.

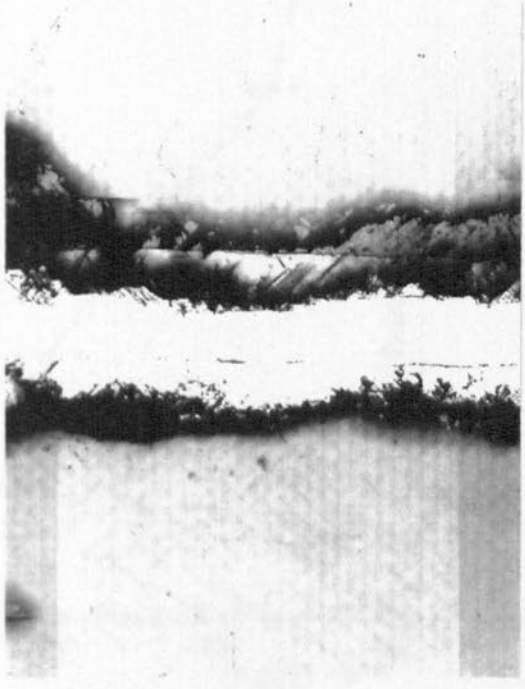

Figure 6.3. X-Ray of Tensile Fracture for Undamaged Specimen. LE6169/A1/1/16.

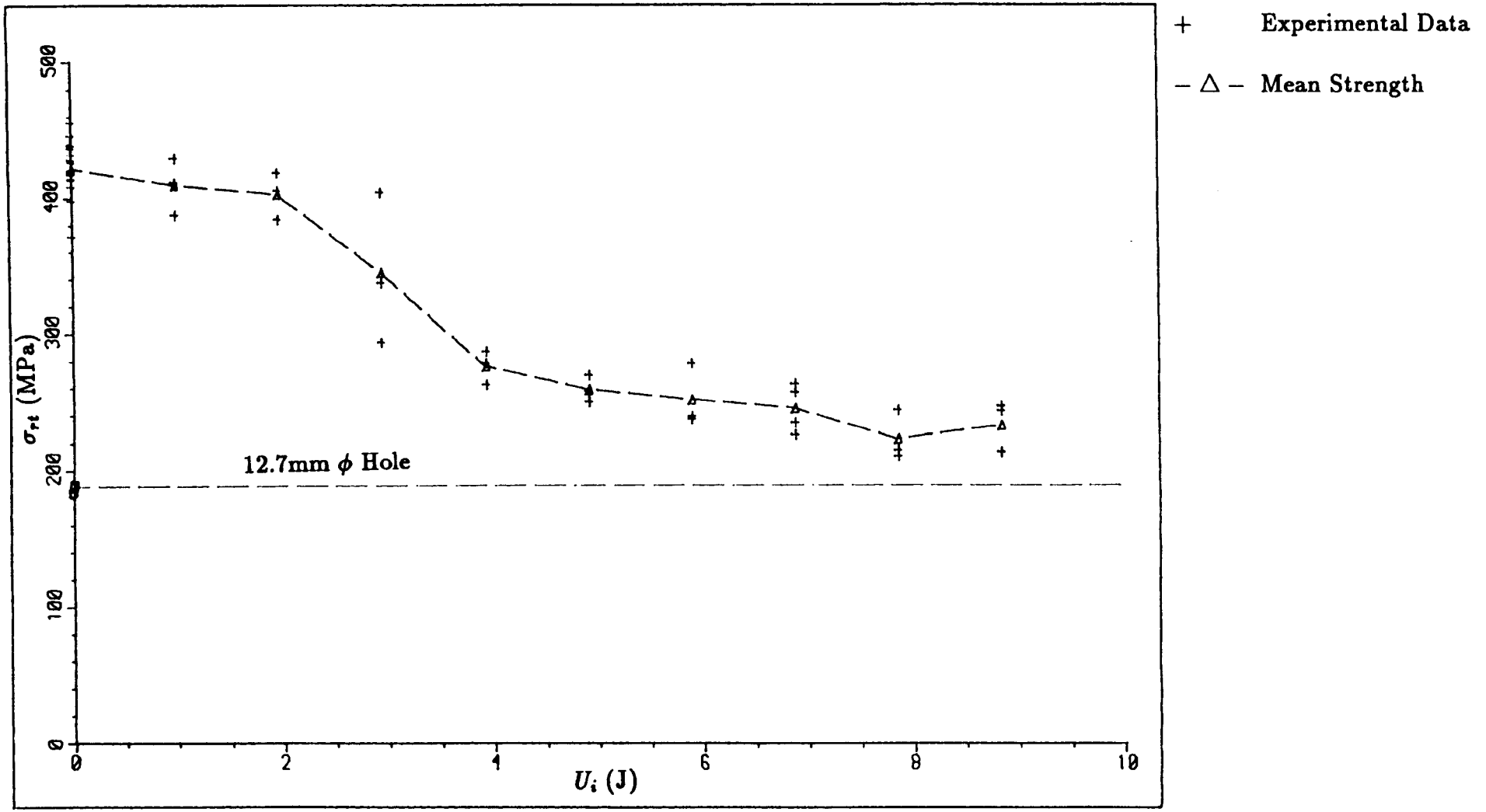

Figure 6.4. The Relationship Between Incident Impact Energy and Residual Tensile Strength for Impacted CFRP.

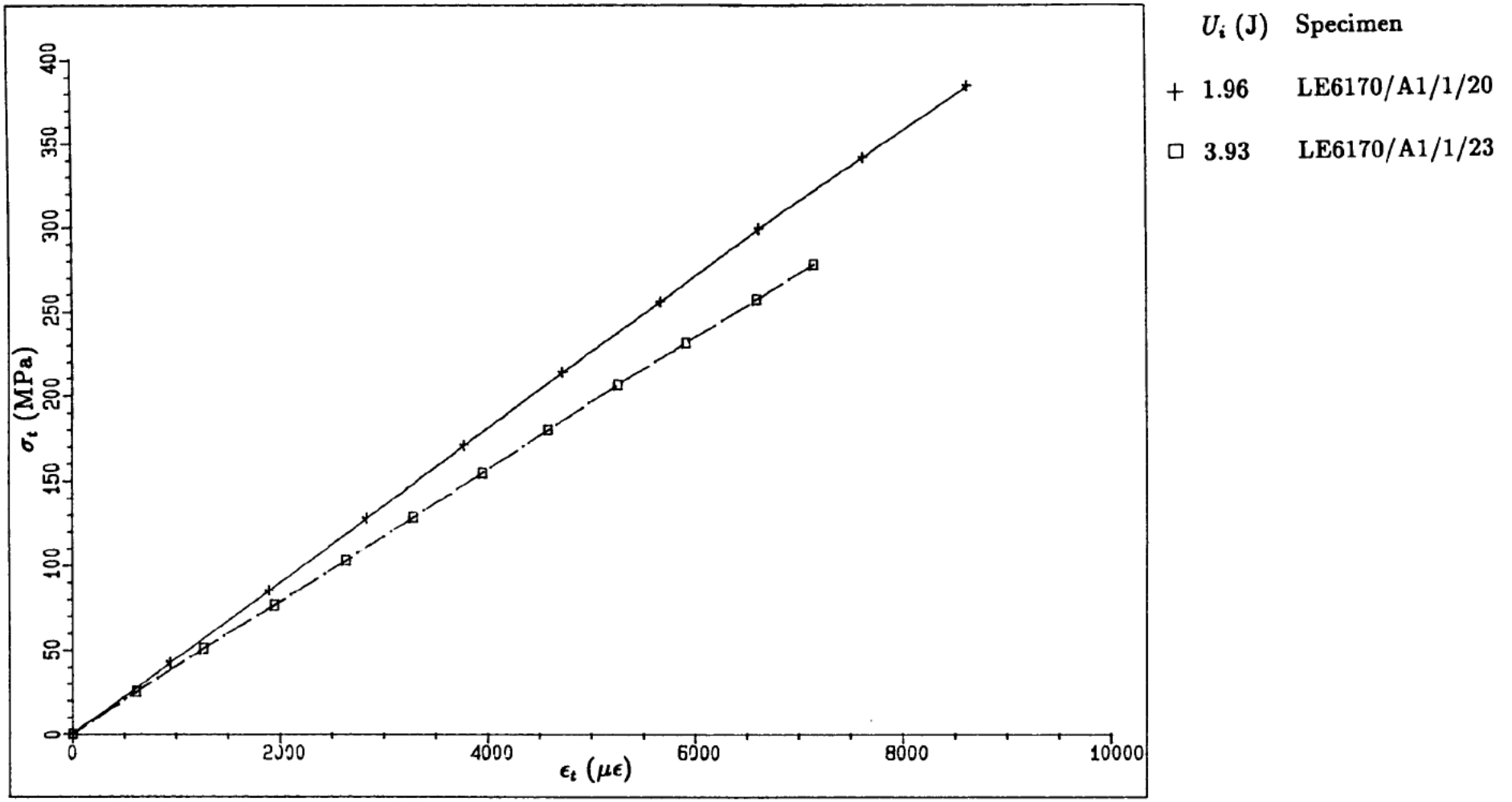

Figure 6.5. Tensile Stress/Strain Behaviour for 1.96J and 3.93J

Impact. Axial Gauge on Back Face Adjacent to Damage.

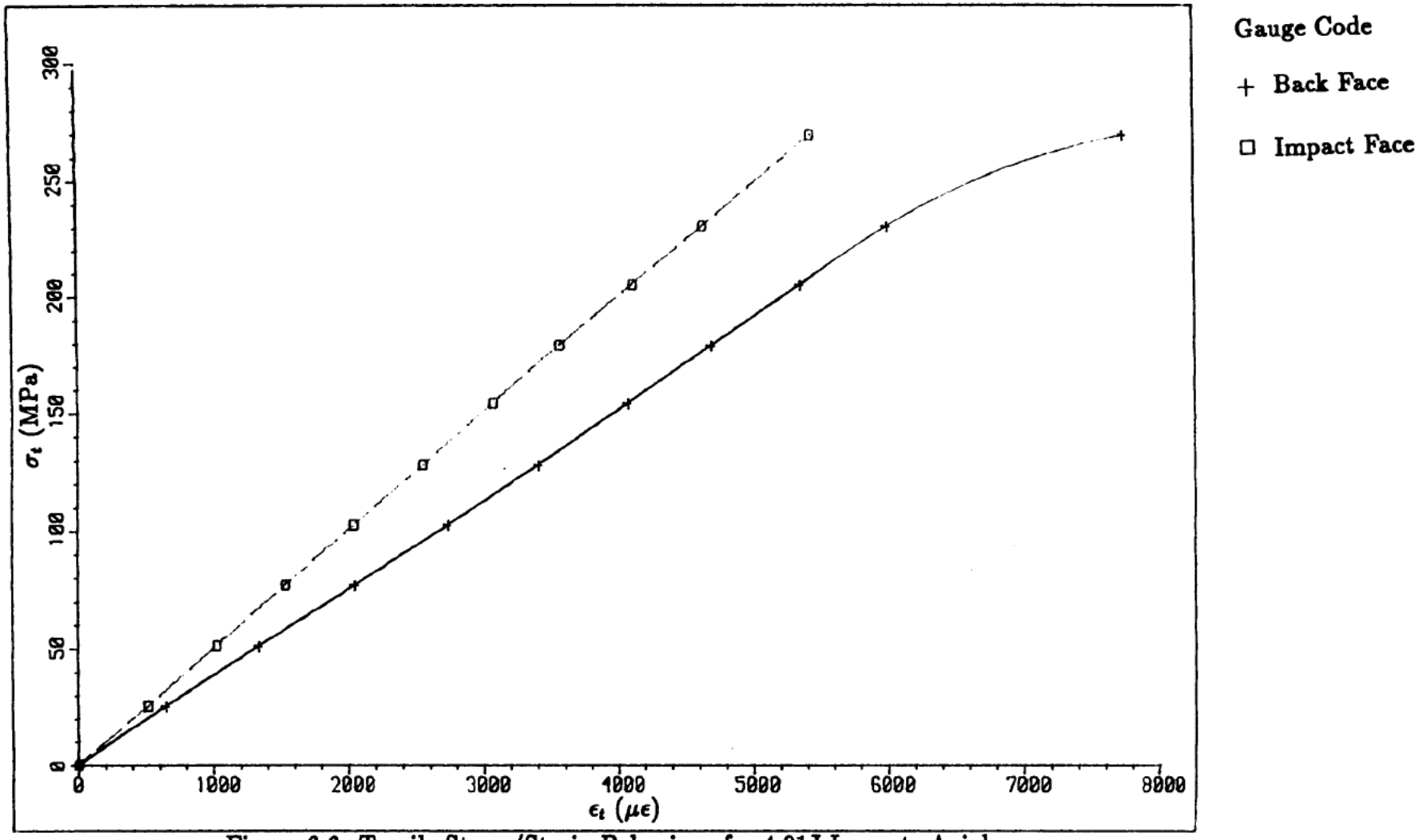

Figure 6.6. Tensile Stress/Strain Behaviour for 4.91J Impact. Axial Gauges on Impact and Back Face Adjacent to Damage. Specimen LE6170/A1/2/5.

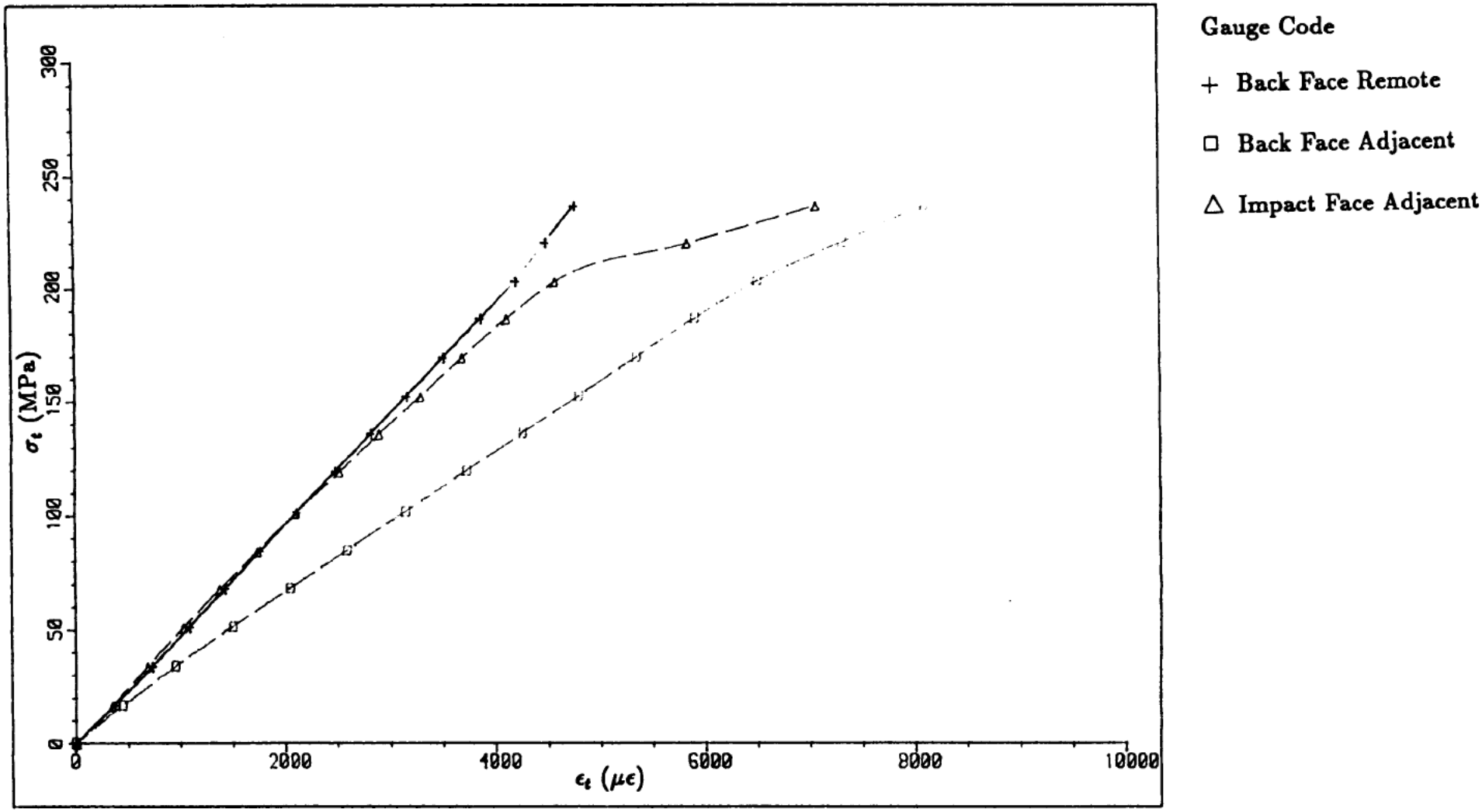

Figure 6.7. Tensile Stress/Strain Behaviour for 5.89J Impact. Axial Gauges on Impact and Back Face. Specimen LE6170/A1/1/27.

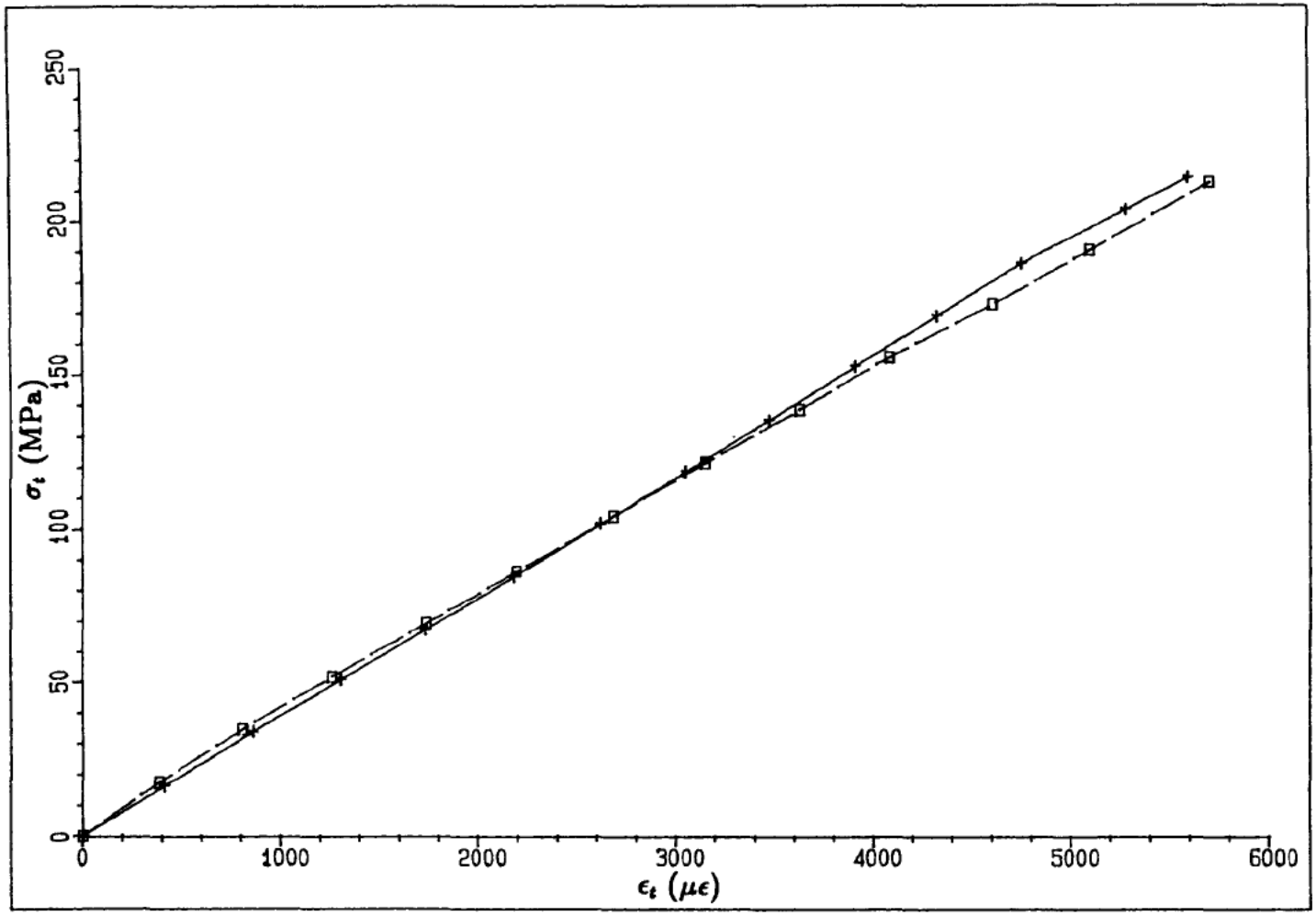

	U_i (J)	Specimen
+	7.85	LE6170/A1/1/31
□	8.83	LE6170/A1/2/9

Figure 6.8. Tensile Stress/Strain Behaviour for 7.85J and 8.83J

Impact. Axial Gauge on Back Face Adjacent to Damage.

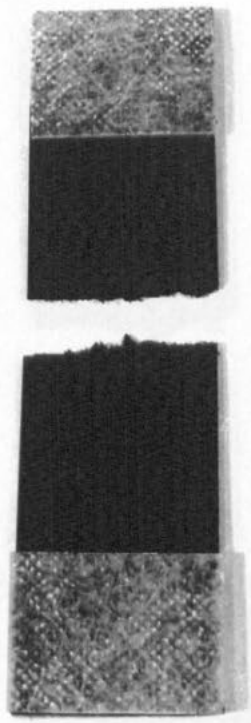

Figure 6.9. Typical Tensile Failure for 4.91J

Impacted Specimen. LE6170/A1/2/5.

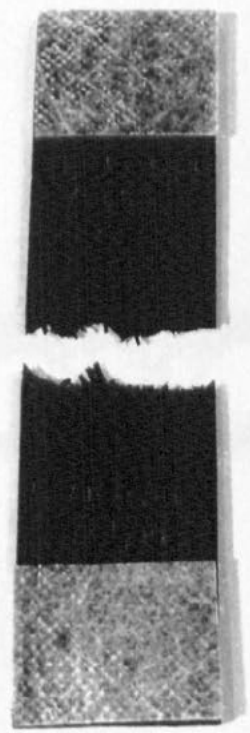

Figure 6.10. Typical Tensile Failure for 6.87J

Impacted Specimen. LE6169/A1/B1/14.

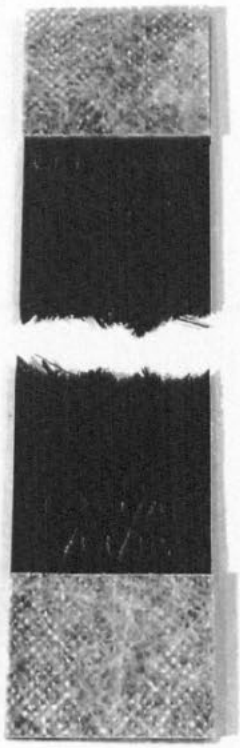

Figure 6.11. Typical Tensile Failure for 8.83J

Impacted Specimen. LE6169/A1/B1/10.

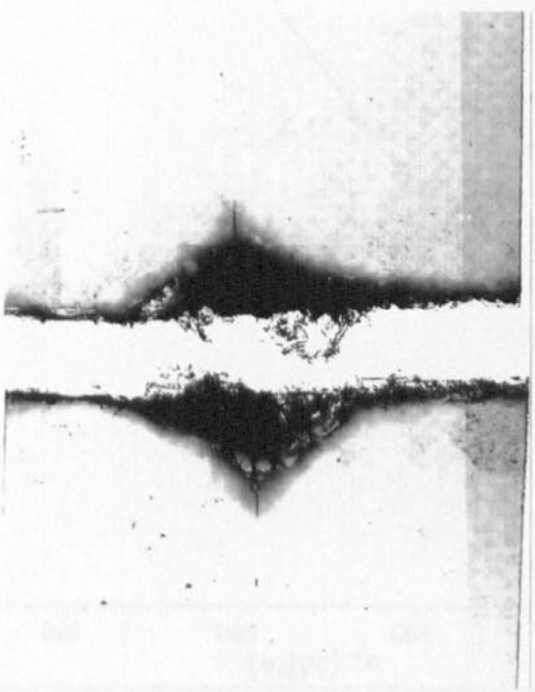

Figure 6.12. X-Ray of Tensile Fracture for 8.83J

Impacted Specimen. LE6169/A1/1/9.

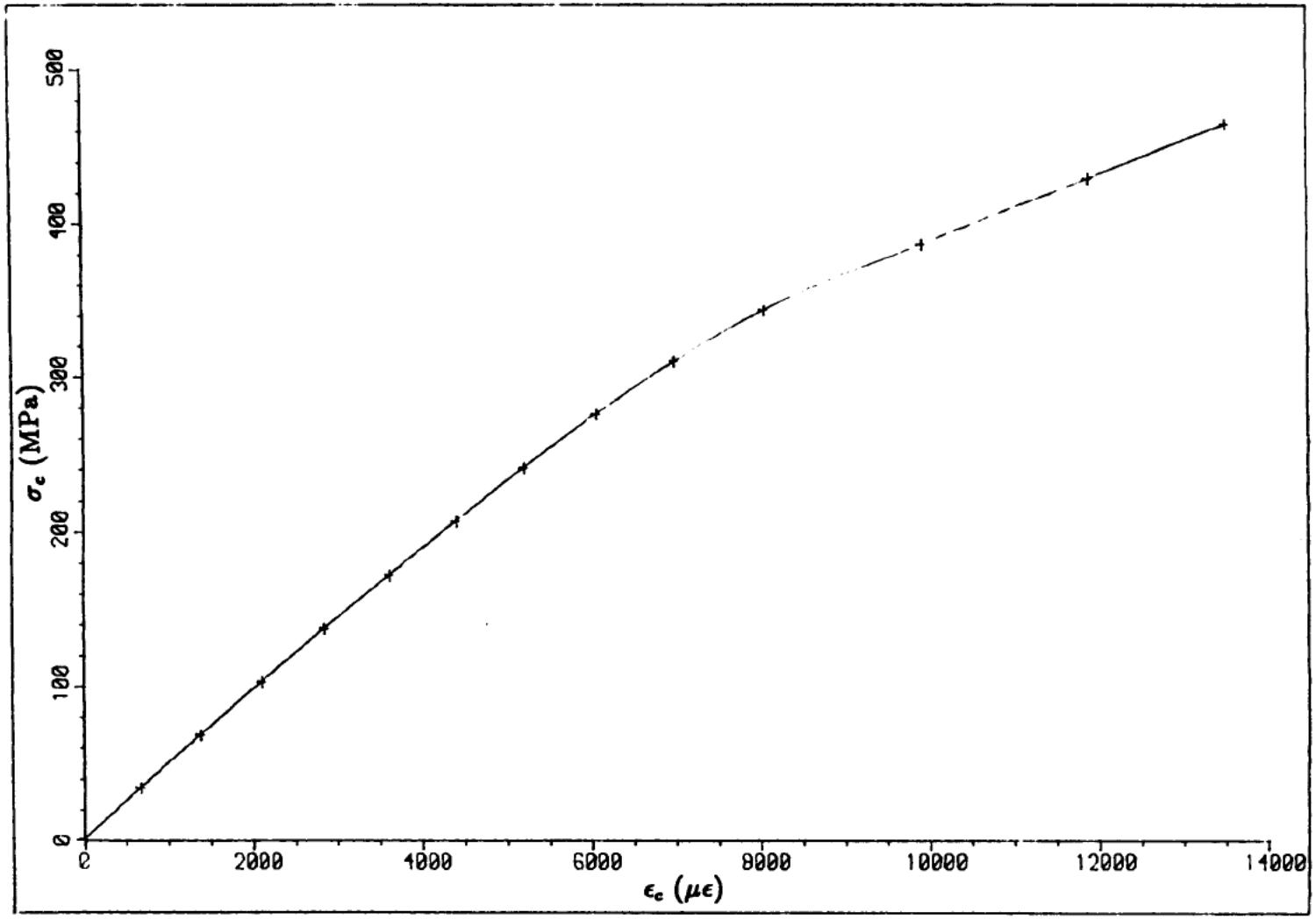

Figure 6.13. Compressive Stress/Strain Behaviour for Undamaged

CFRP. Specimen LE6170/A1/1/16.

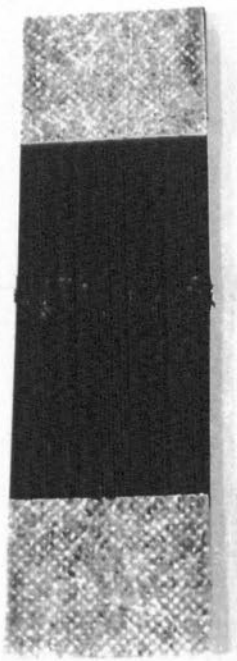

Figure 6.14. Typical Failure of Undamaged Compression Specimen. LE61619/A1/B1/17.

Figure 6.15. X-Ray of Compression Fracture for Undamaged Specimen. LE6169/A1/1/13.

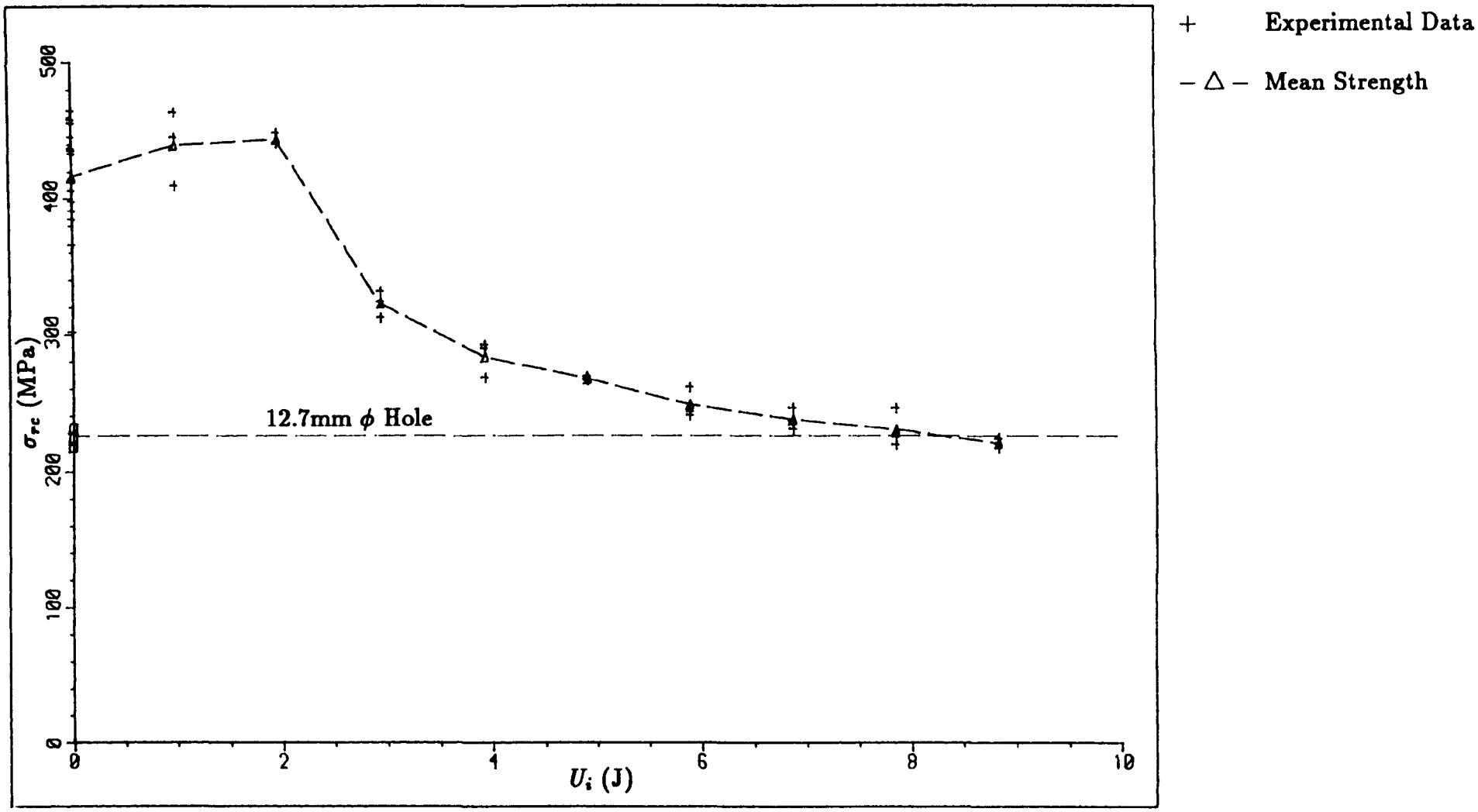

Figure 6.16. The Relationship Between Incident Impact Energy and Residual Compressive Strength for Impacted CFRP.

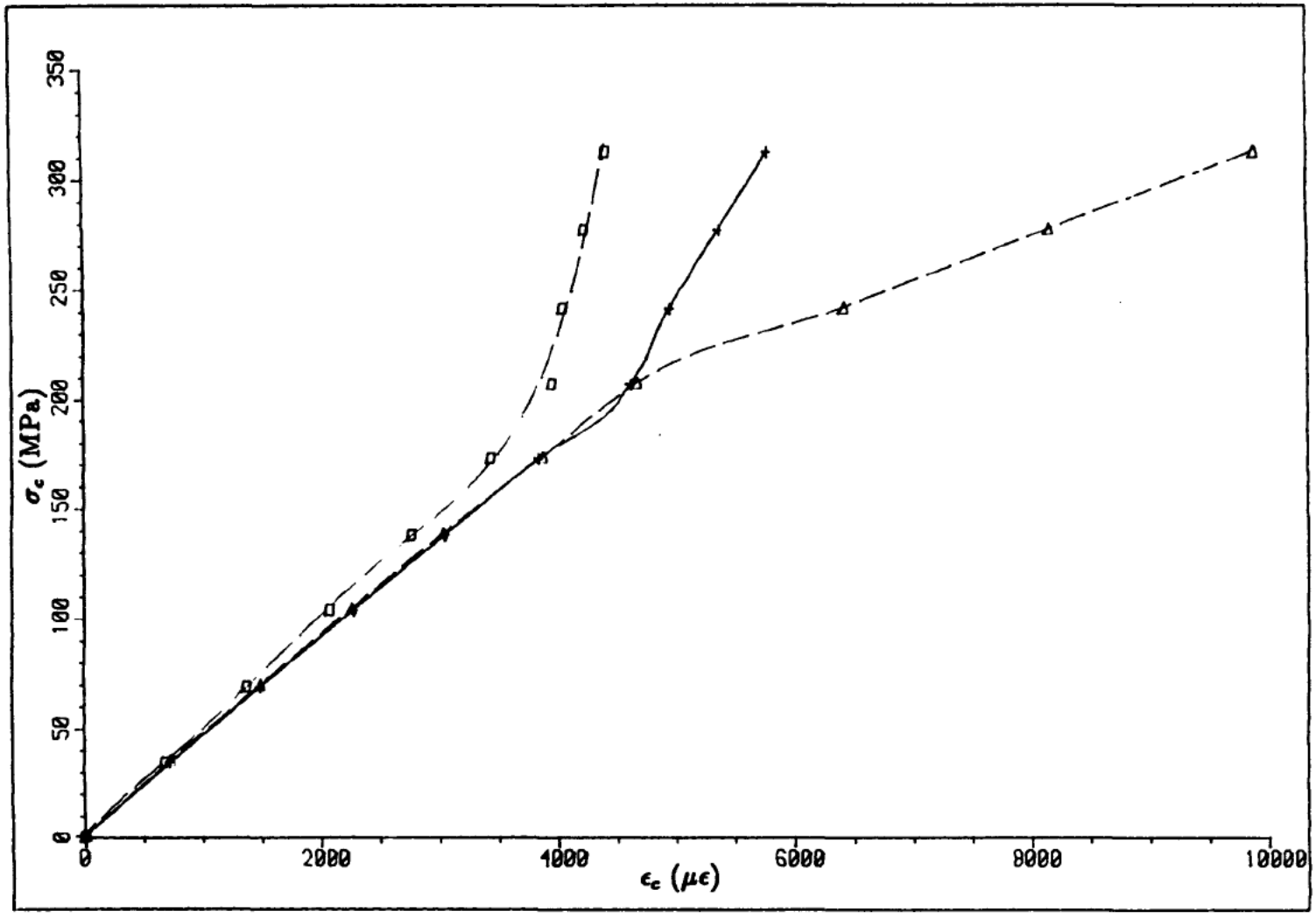

Figure 6.17. Compressive Stress/Strain Behaviour for 2.94J Impact.

Axial Gauges on Impact and Back Faces. Specimen LE6170/A1/2/3.

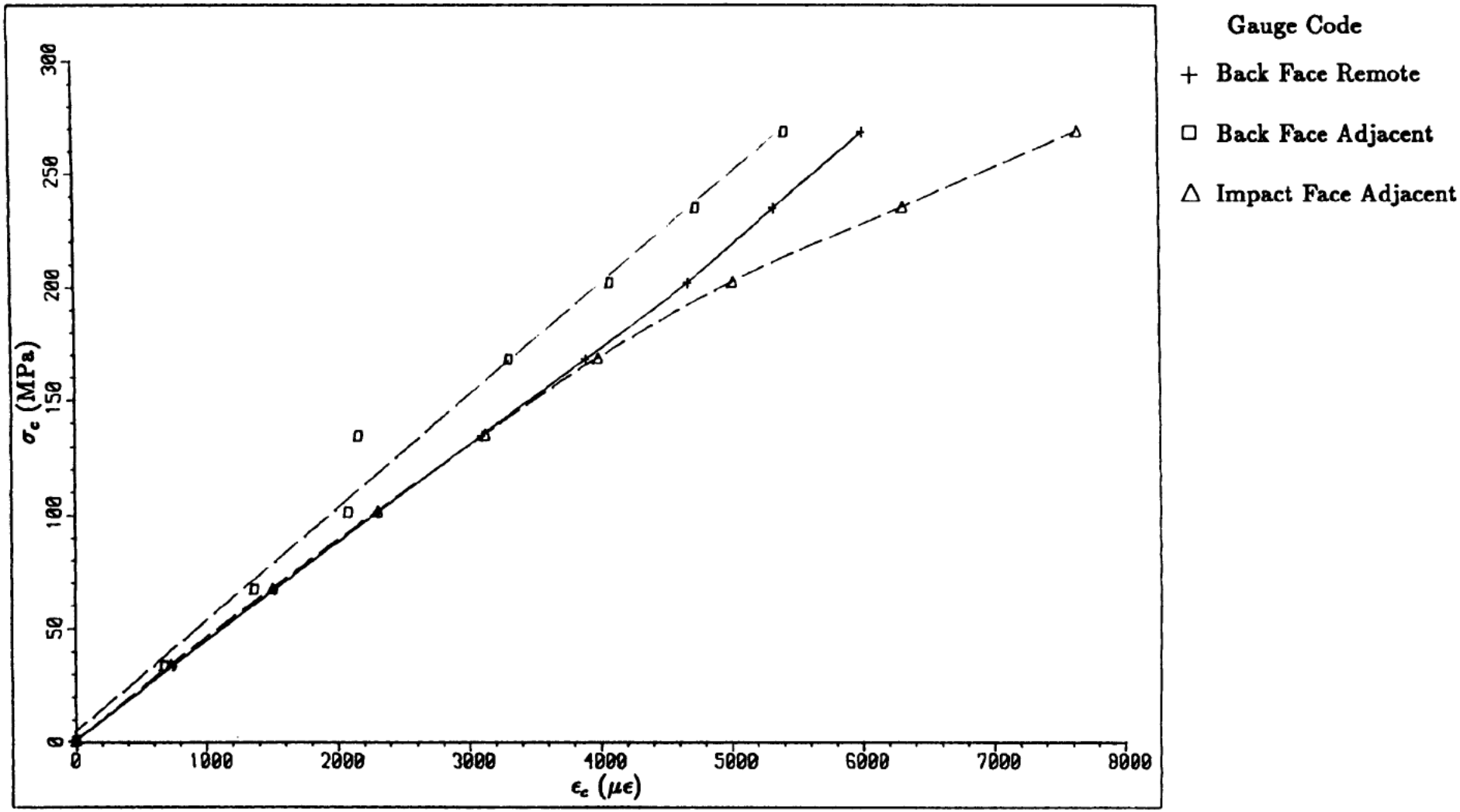

Figure 6.18. Compressive Stress/Strain Behaviour for 3.93J Impact.

Axial Gauges on Impact and Back Faces. Specimen LE6169/A1/B1/3.

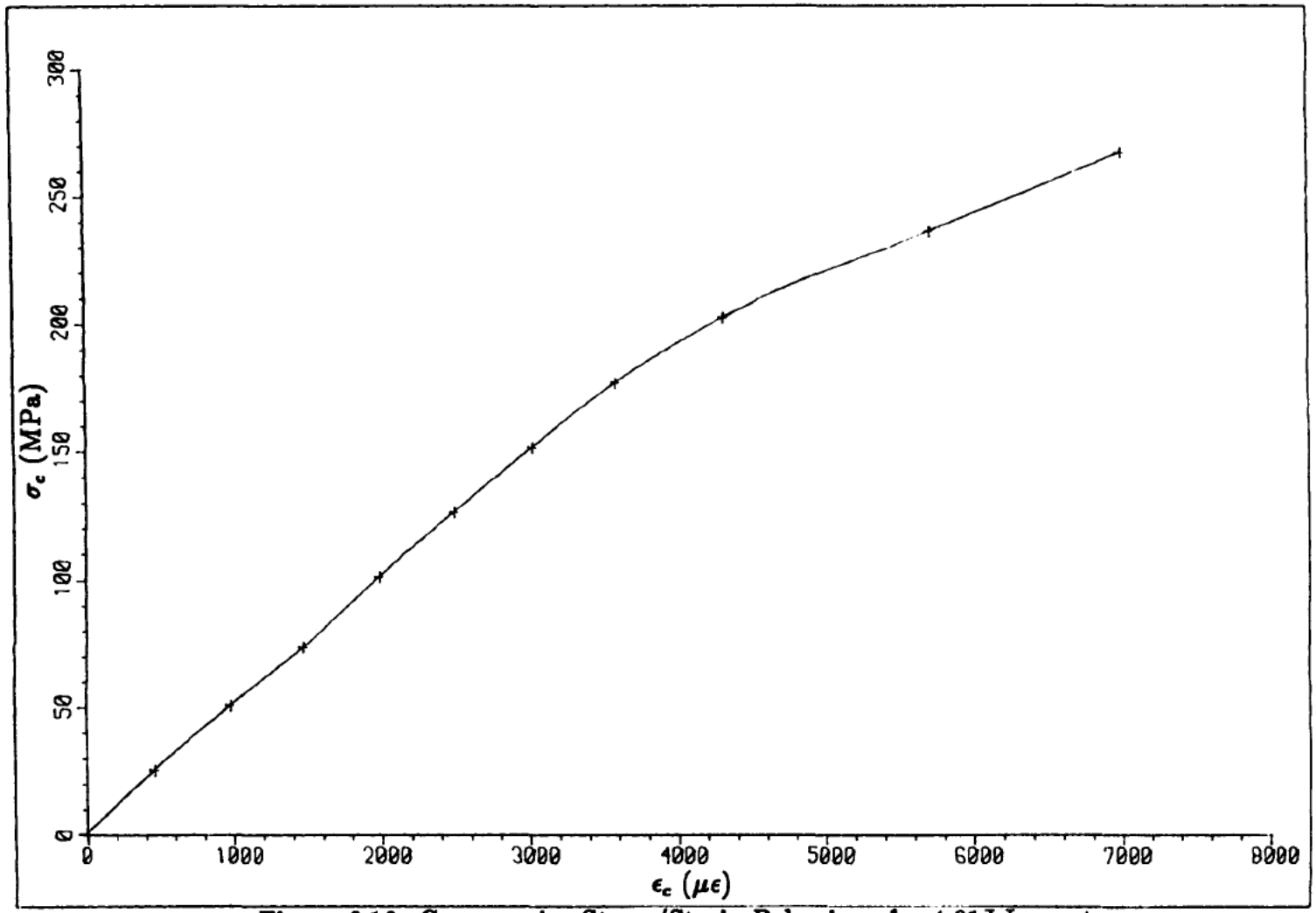

Figure 6.19. Compressive Stress/Strain Behaviour for 4.91J Impact.

Axial Gauge on Back Face Adjacent to Damage. Specimen

LE6170/A1/1/25.

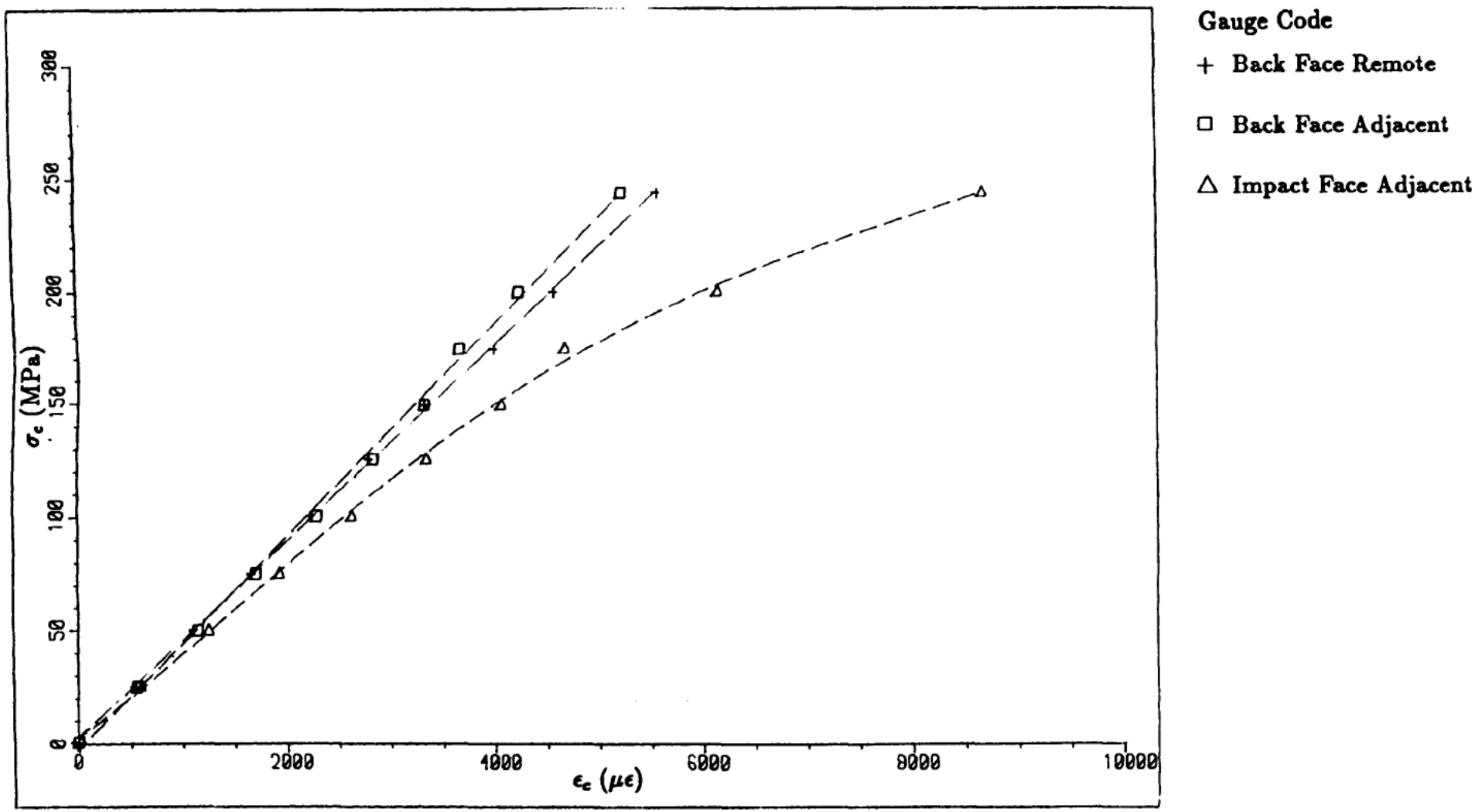

Figure 6.20. Compressive Stress/Strain Behaviour for 5.89J Impact.

Axial Gauges on Impact and Back Faces. Specimen LE6169/A1/B1/5.

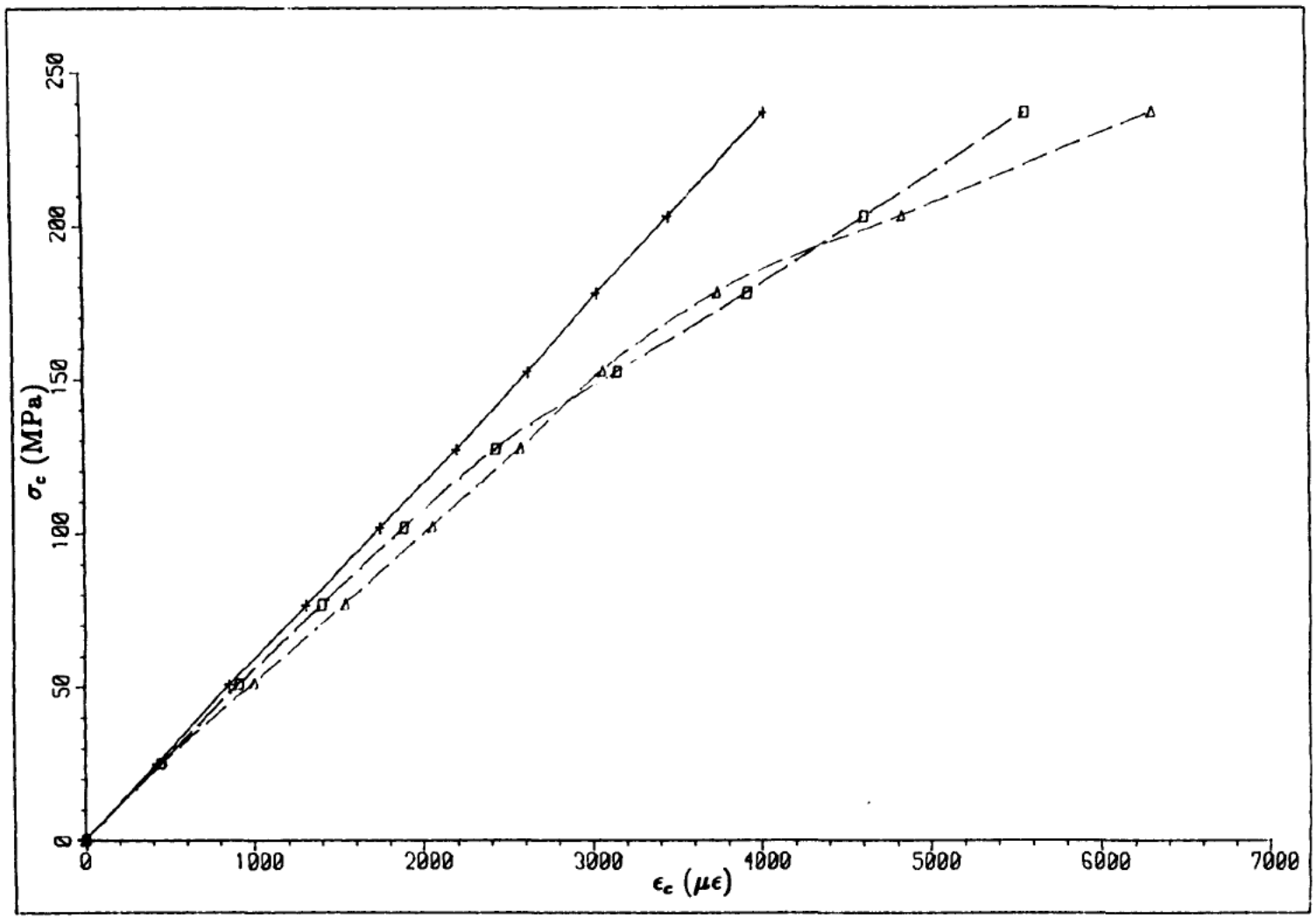

Figure 6.21. Compressive Stress/Strain Behaviour for 6.87J Impact.

Axial Gauges on Impact and Back Faces. Specimen LE6170/A1/1/29.

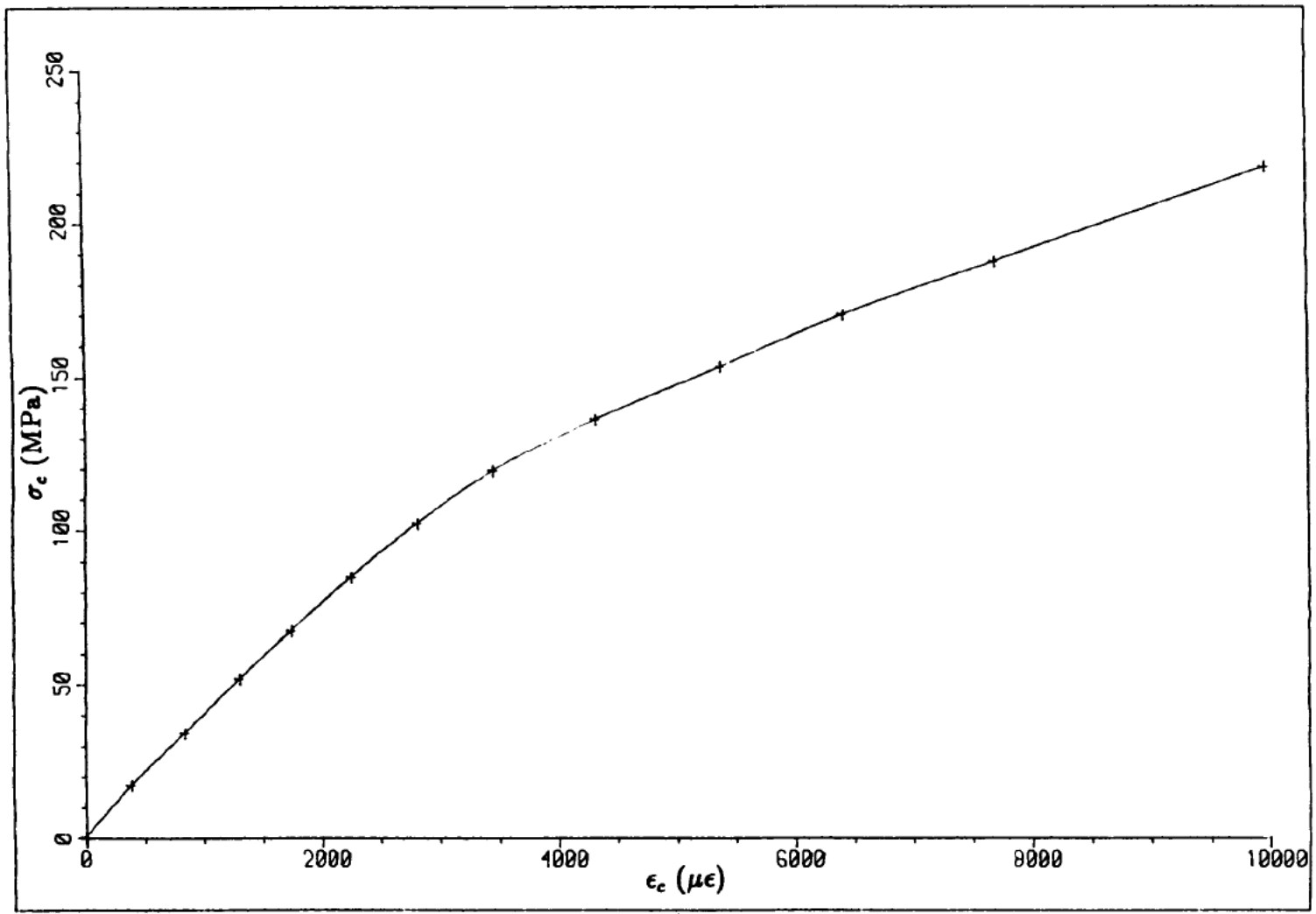

Figure 6.22. Compressive Stress/Strain Behaviour for 8.83J Impact.

Axial Gauge on Back Face Adjacent to Damage. Specimen

LE6170/A1/1/32.

Figure 6.23. Typical Compressive Failure for 8.83J Impacted Specimen. LE6169/A1/B1/11.

Figure 6.24. X-Ray of Compressive Fracture for 7.85J Specimen. LE6169/A1/1/8.

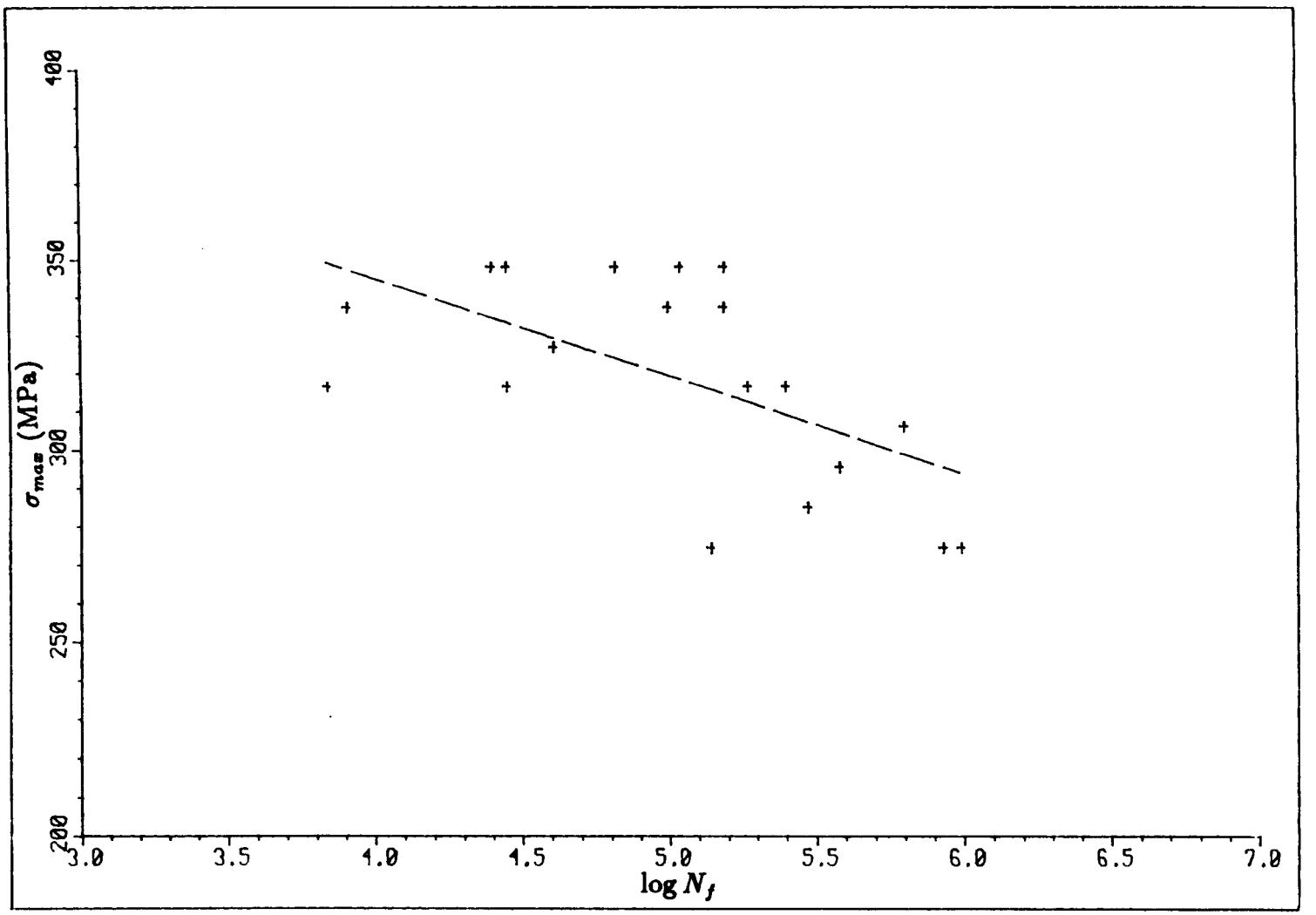

Figure 7.1. Zero-Tension Fatigue S-N Curve for Undamaged CFRP.

$\uparrow F_{applied}$

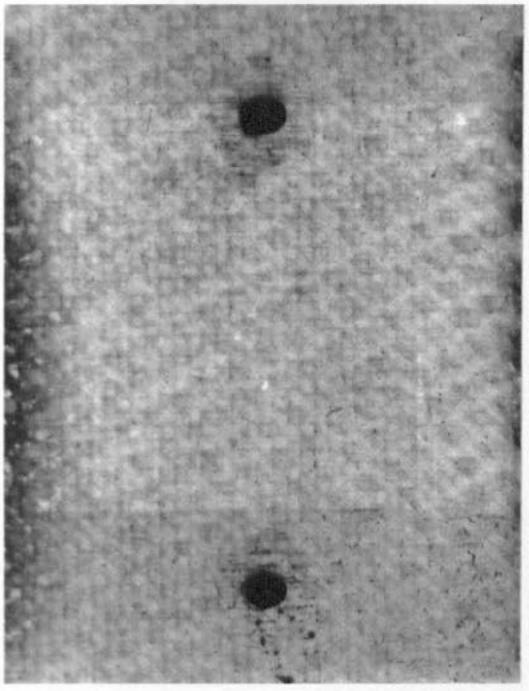

Figure 7.2. Typical X-Ray of Zero-Tension Fatigue Damage in CFRP. Specimen LE6169/A1/1/23, 0J, $\frac{\sigma_{max}}{\sigma_{ot}} = 0.65$, $n = 10^5$.

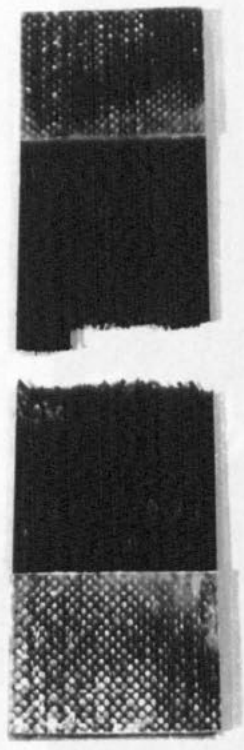

Figure 7.3. Typical High Stress/Low Cycle Zero-Tension Fatigue Failure. Specimen LE6170/A1/2/18, 0J, $\frac{\sigma_{max}}{\sigma_{ot}} = 0.825$, $N_f = 28440$.

Figure 7.4. Typical Low Stress/High Cycle Zero-Tension Fatigue Failure. Specimen LE6169/A1/A2/16, 0J, $\frac{\sigma_{max}}{\sigma_{ot}} = 0.65$, $N_f = 978300$.

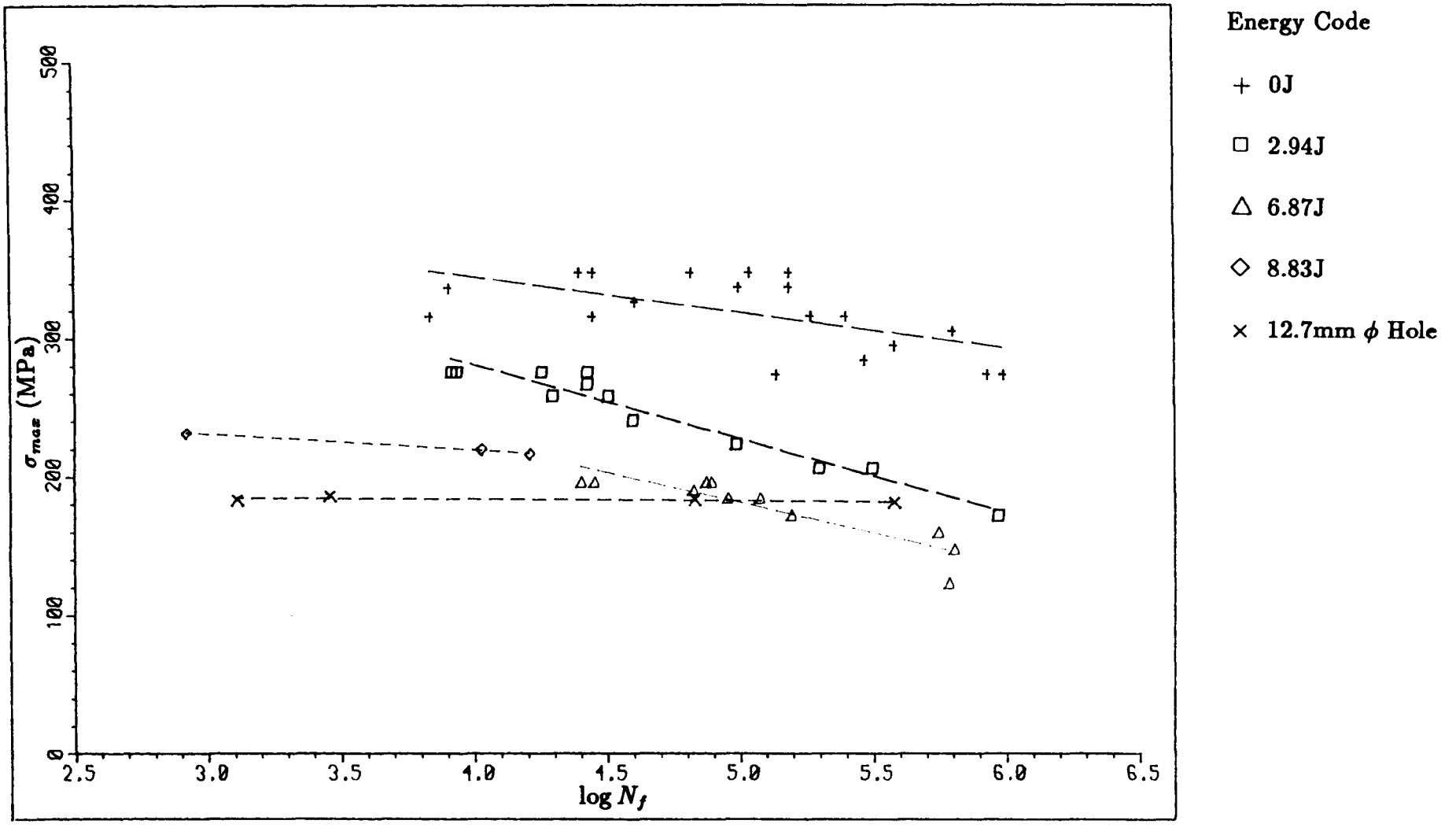

Figure 7.5. Zero-Tension Fatigue S-N Curves for Impacted CFRP.

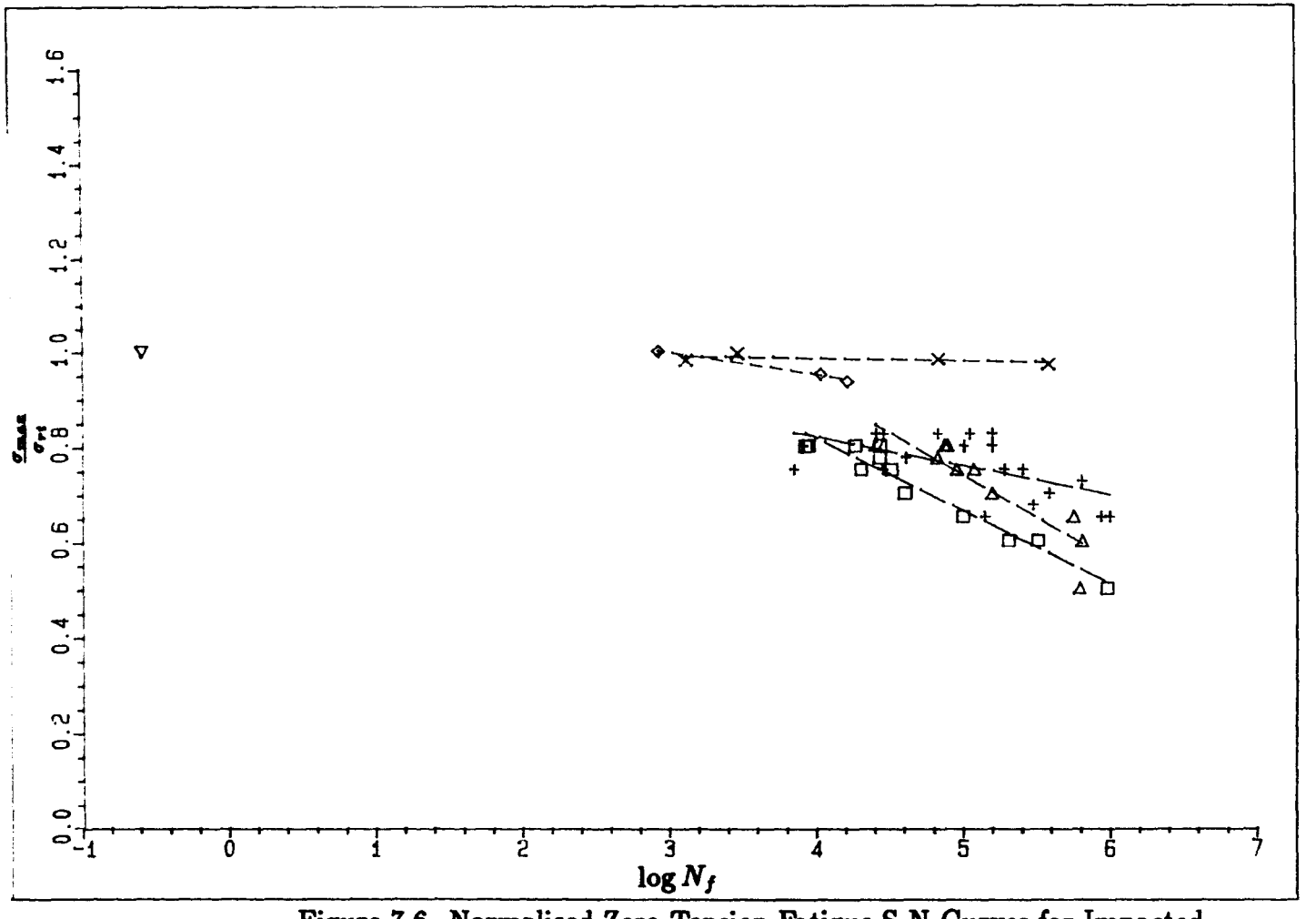

Figure 7.6. Normalised Zero-Tension Fatigue S-N Curves for Impacted CFRP.

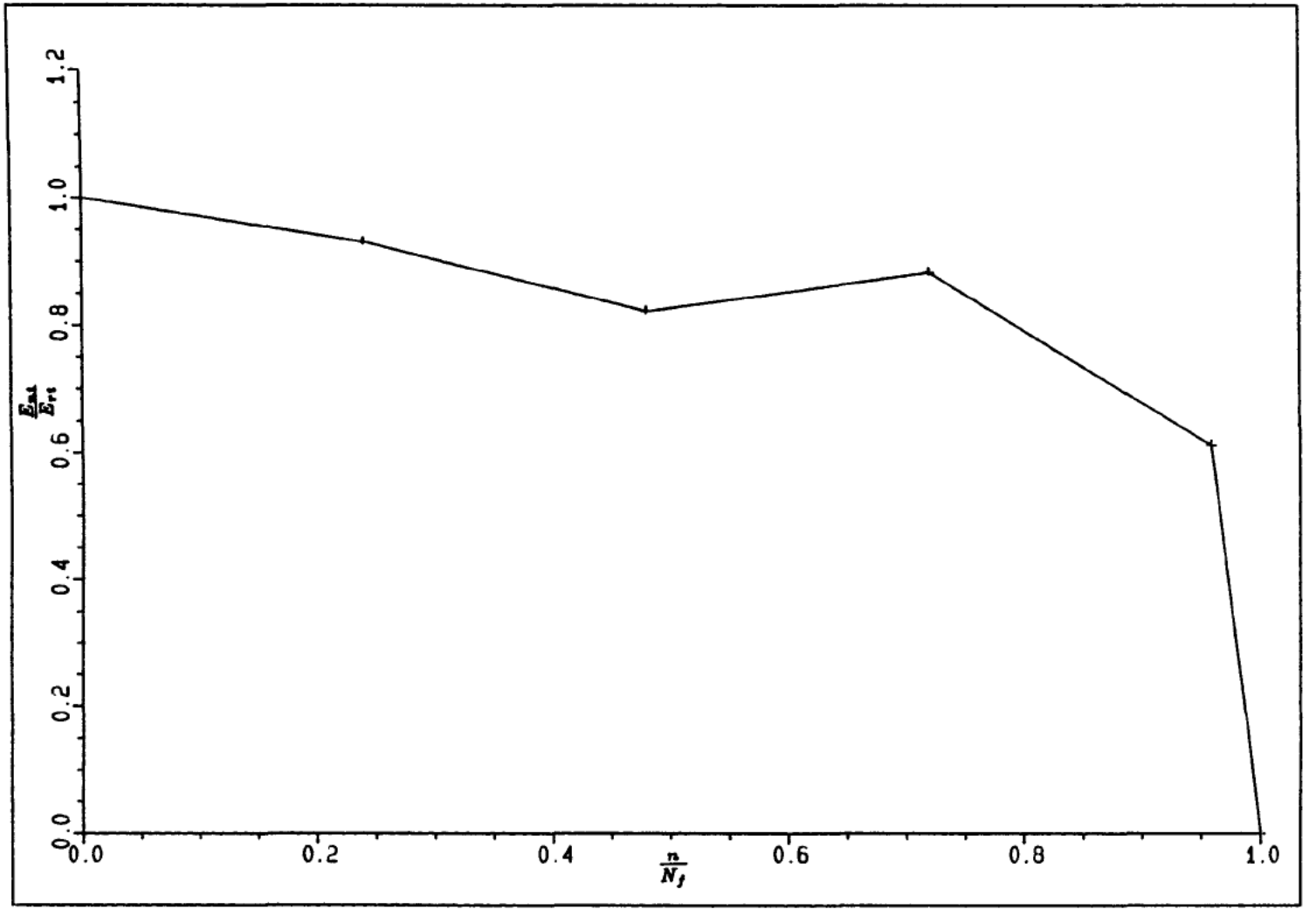

Figure 7.7. Typical Relationship Between Stiffness Ratio and Fatigue Cycle Ratio under Zero-Tension Fatigue Loading.

Specimen LE6169/A1/B2/14, 2.94J, $\frac{\sigma_{max}}{\sigma_{rt}} = 0.80$.

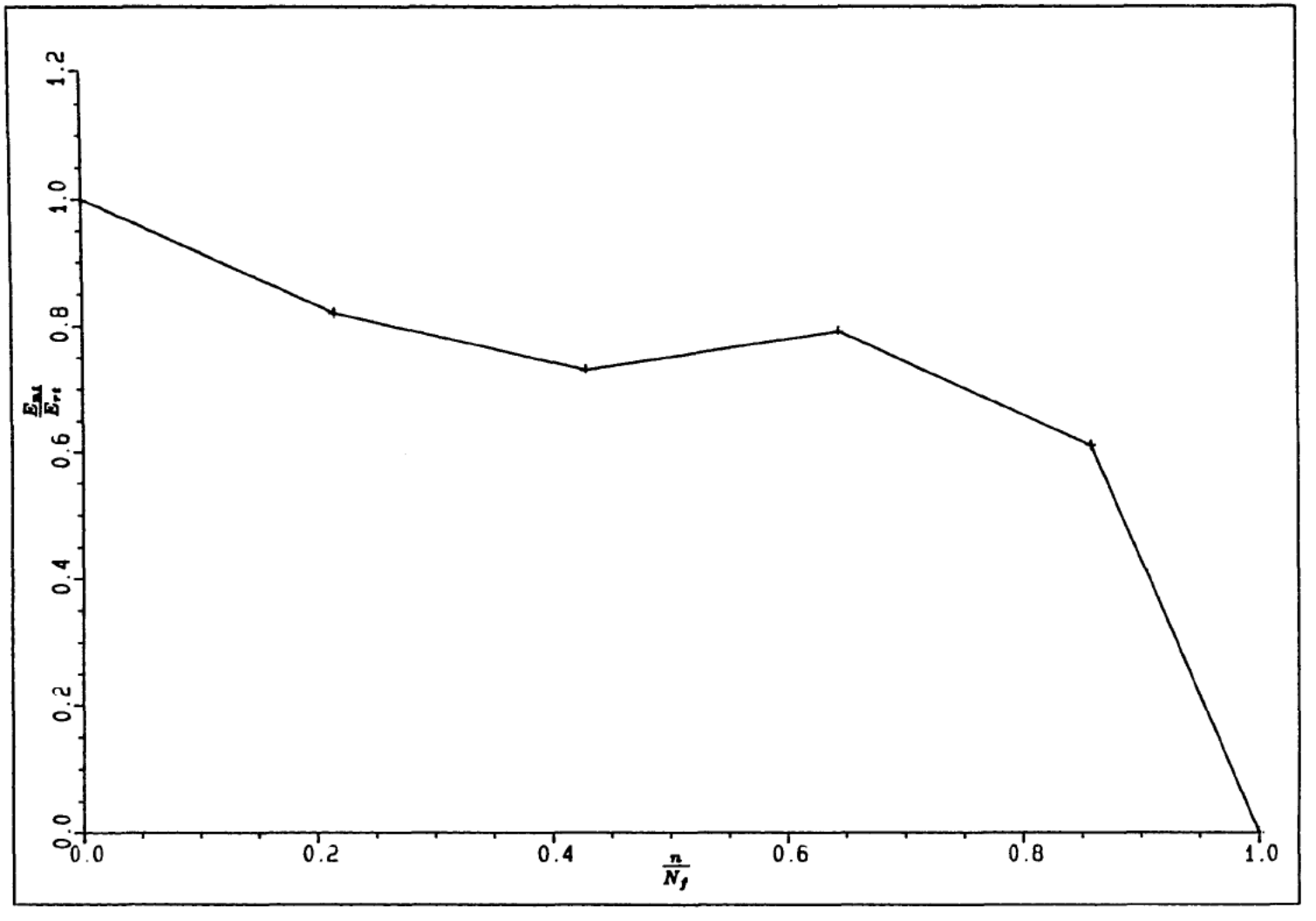

Figure 7.8. Typical Relationship Between Stiffness Ratio and Fatigue Cycle Ratio under Zero-Tension Fatigue Loading.

Specimen LE6169/A1/B2/15, 6.87J, $\frac{\sigma_{max}}{\sigma_{rt}} = 0.80$.

$\uparrow F_{applied}$

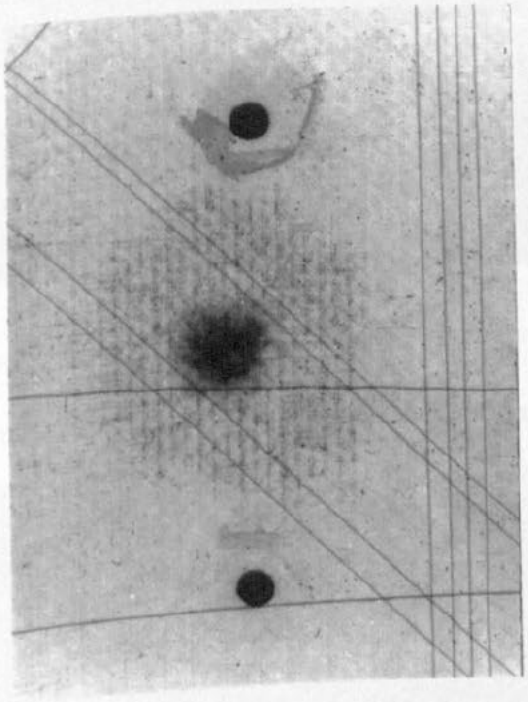

Figure 7.9. Typical X-Ray of Zero-Tension Fatigue Damage.

Specimen LE6169/A1/A2/15, 2.94J, $\frac{\sigma_{max}}{\sigma_{rt}} = 0.25$, $n = 10^6$.

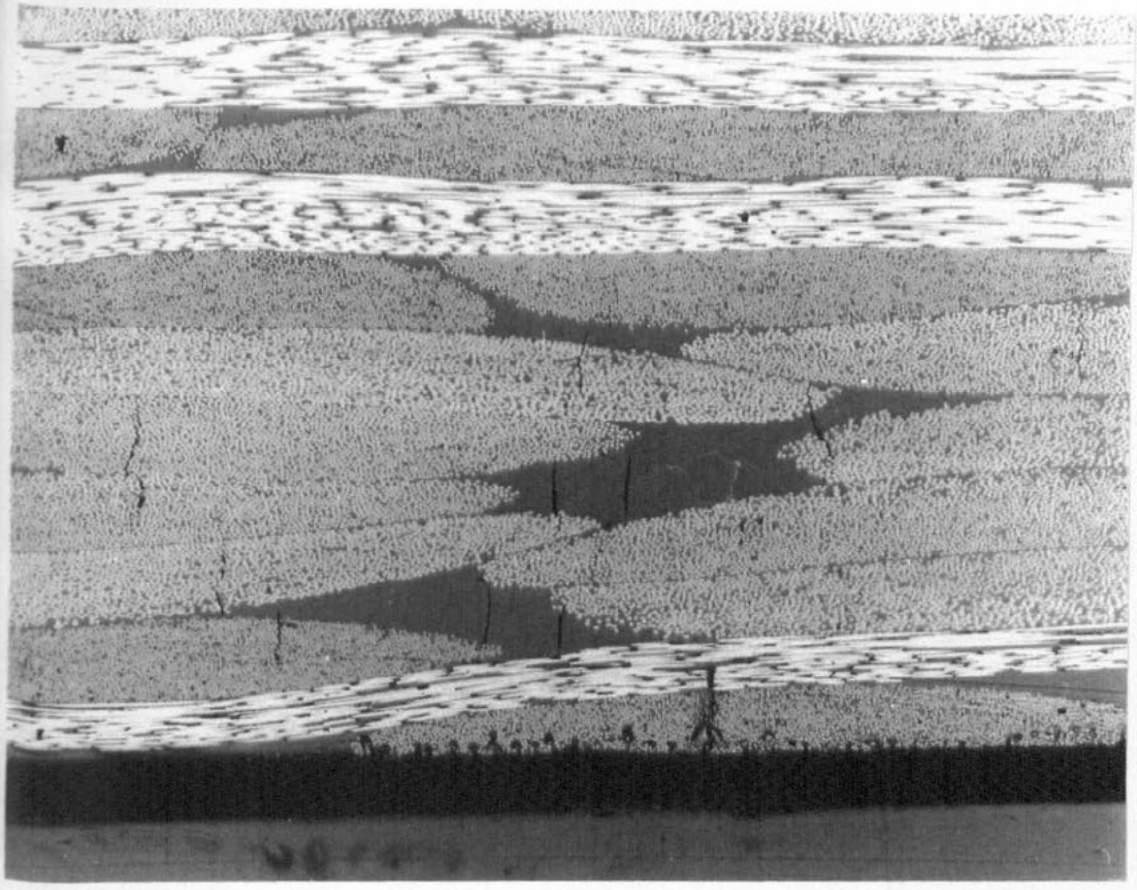

Figure 7.10. Polished Section of Fatigue Damage. Specimen Cut Perpendicular to Loading Direction.

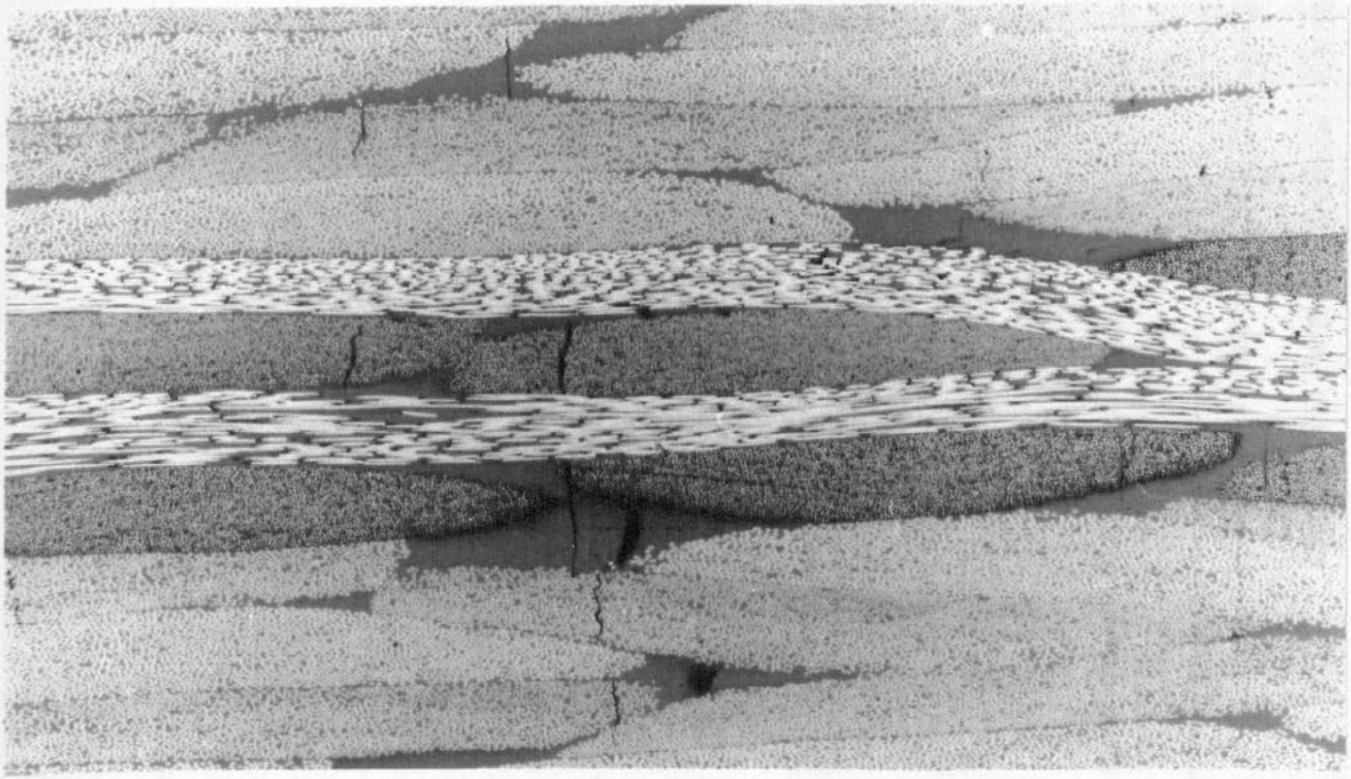

Figure 7.11. Polished Section of Fatigue Damage. Specimen Cut Parallel to Loading Direction.

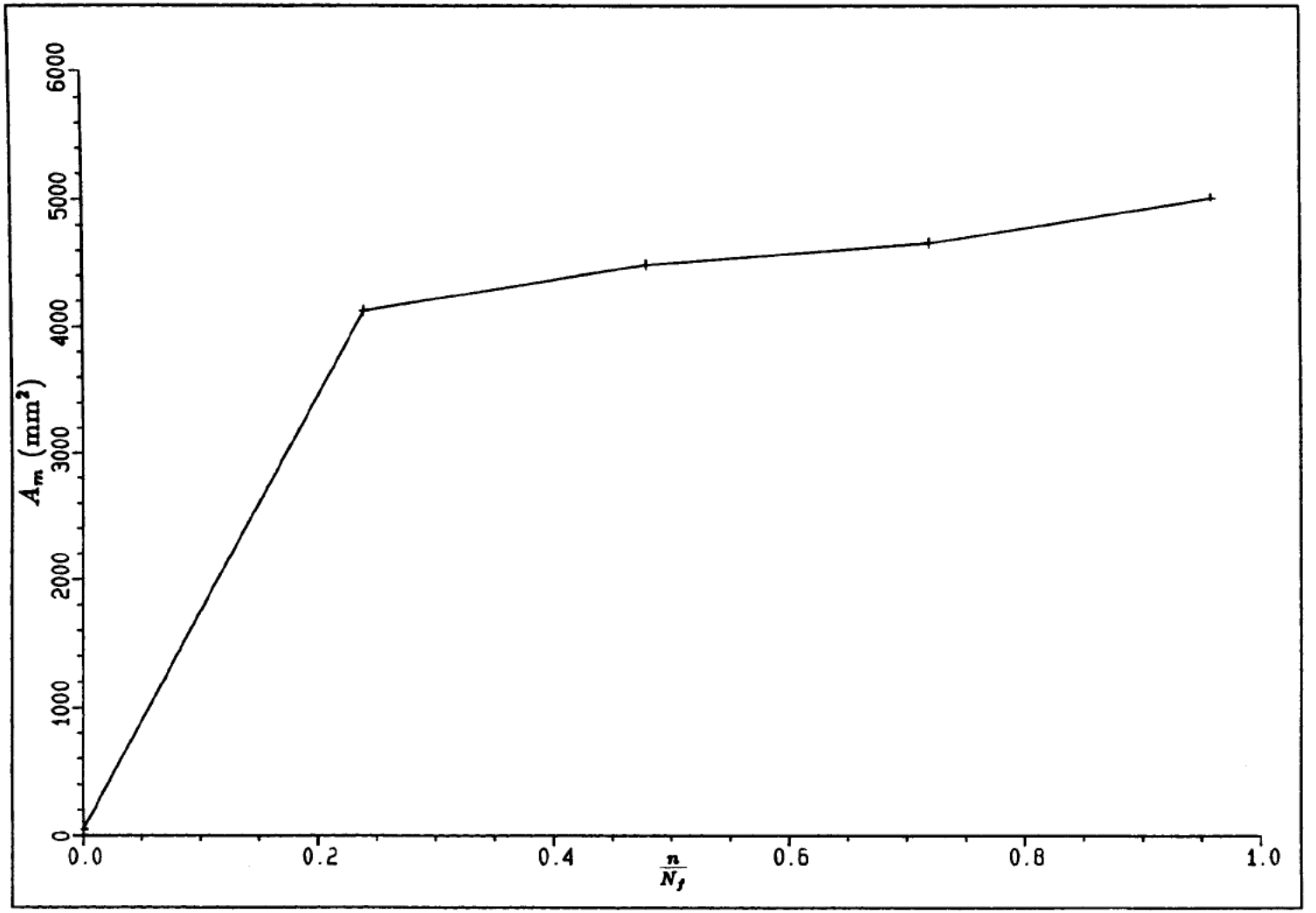

Figure 7.12. Typical Micro-Damage Growth Curve for CFRP under Zero-Tension Fatigue. Specimen LE6169/A1/B2/14, 2.94J, $\frac{\sigma_{max}}{\sigma_{rt}} = 0.80$.

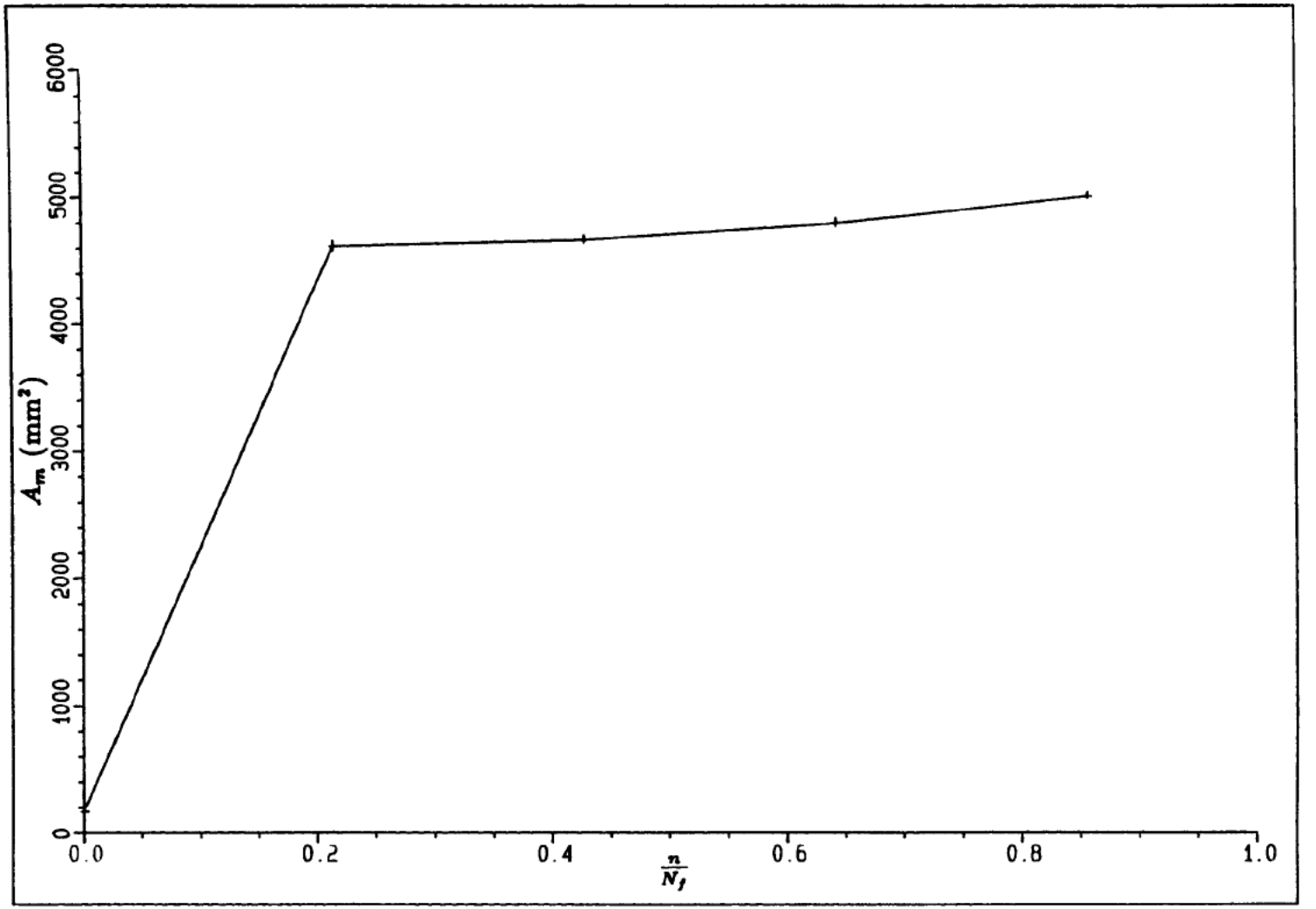

Figure 7.13. Typical Micro-Damage Growth Curve for CFRP under

Zero-Tension Fatigue. Specimen LE6169/A1/B2/15, 6.87J, $\frac{\sigma_{max}}{\sigma_{ut}} = 0.80$.

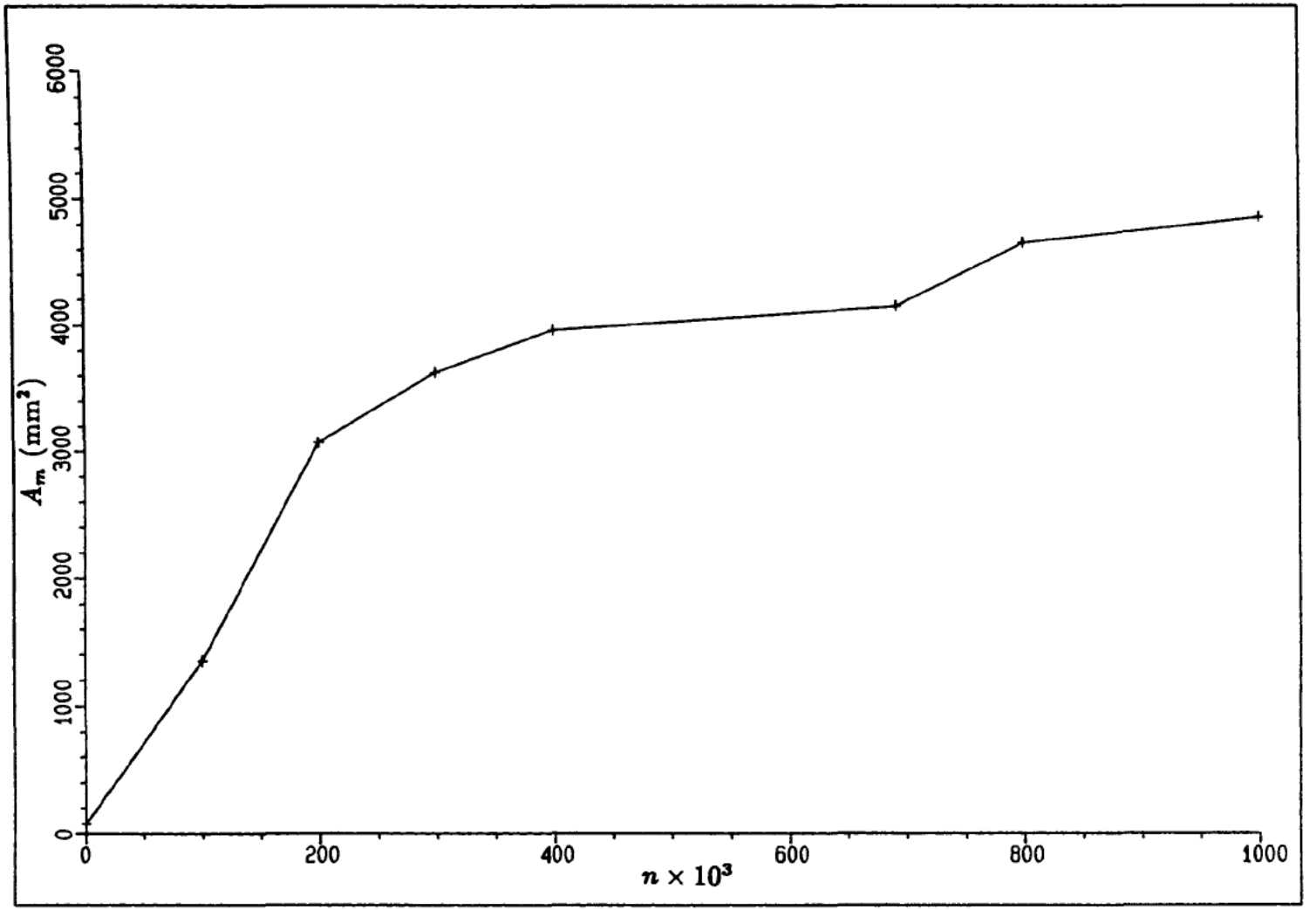

Figure 7.14. Typical Micro-Damage Growth Curve for CFRP under Zero-Tension Fatigue. Specimen LE6169/A1/A2/13, 2.94J, $\frac{\sigma_{max}}{\sigma_{rt}} = 0.45$.

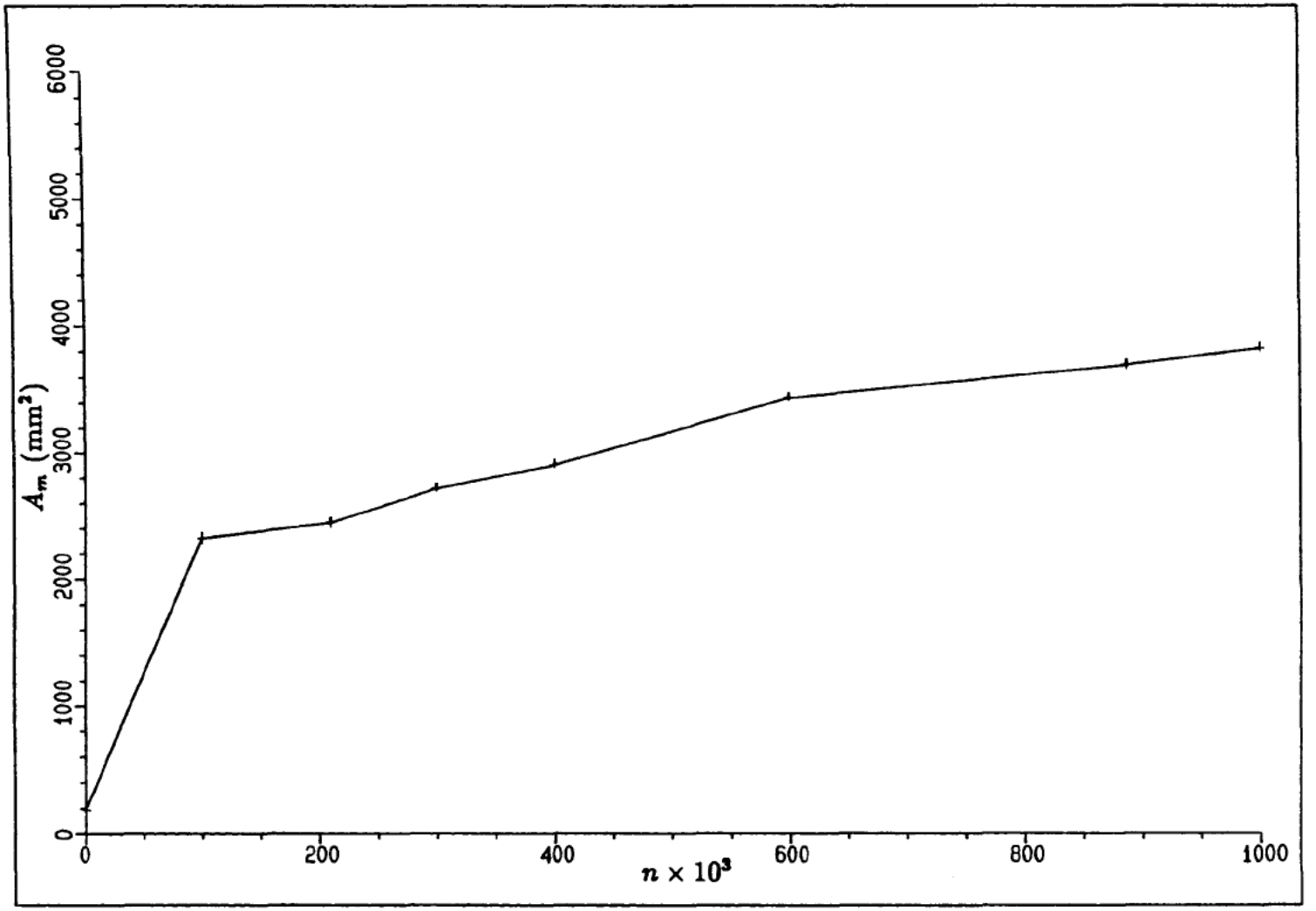

Figure 7.15. Typical Micro-Damage Growth Curve for CFRP under Zero-Tension Fatigue. Specimen LE6169/A1/A2/14, 6.87J, $\frac{\sigma_{max}}{\sigma_{rt}} = 0.45$.

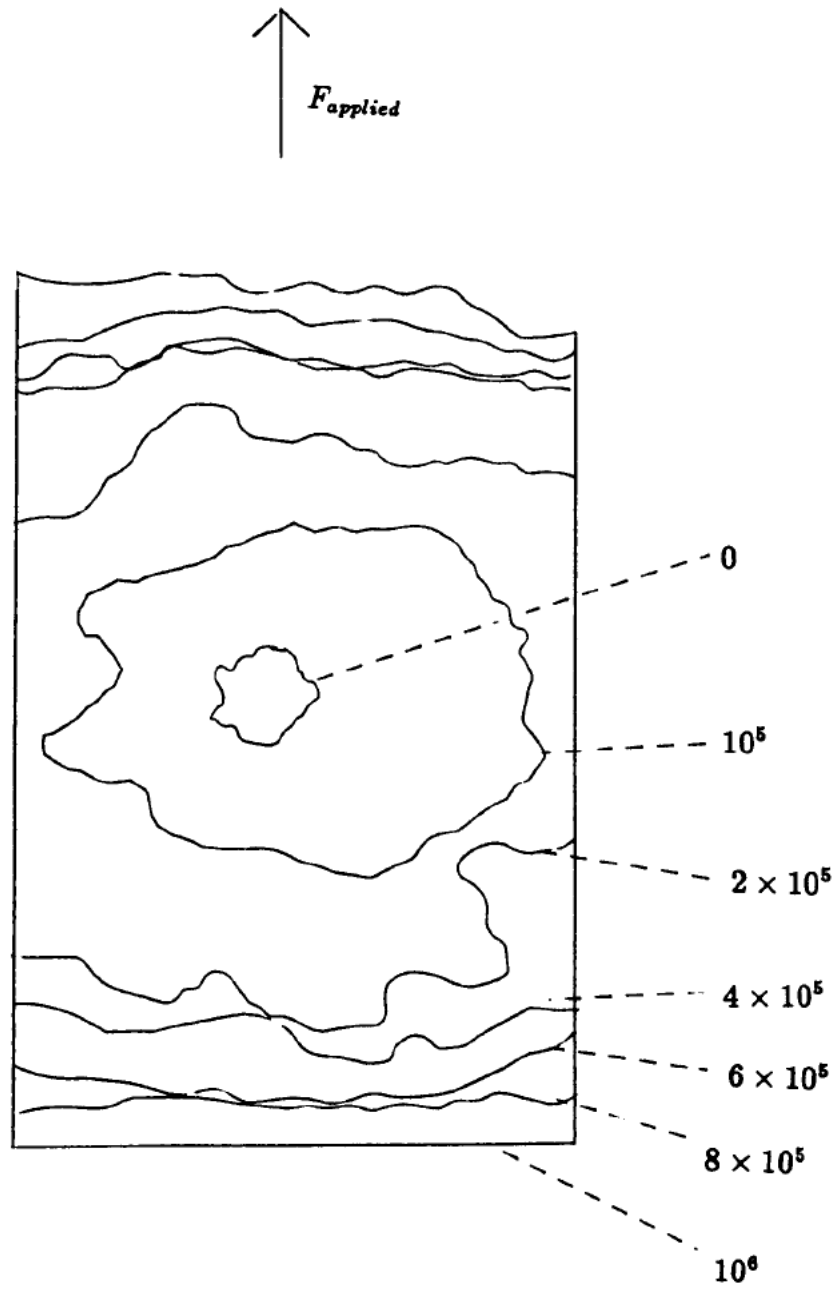

Figure 7.16. Typical Growth of Micro-Damage with Fatigue Cycles. Specimen LE6169/A1/A2/13, 2.94J, $\frac{\sigma_{max}}{\sigma_{rt}} = 0.45$.

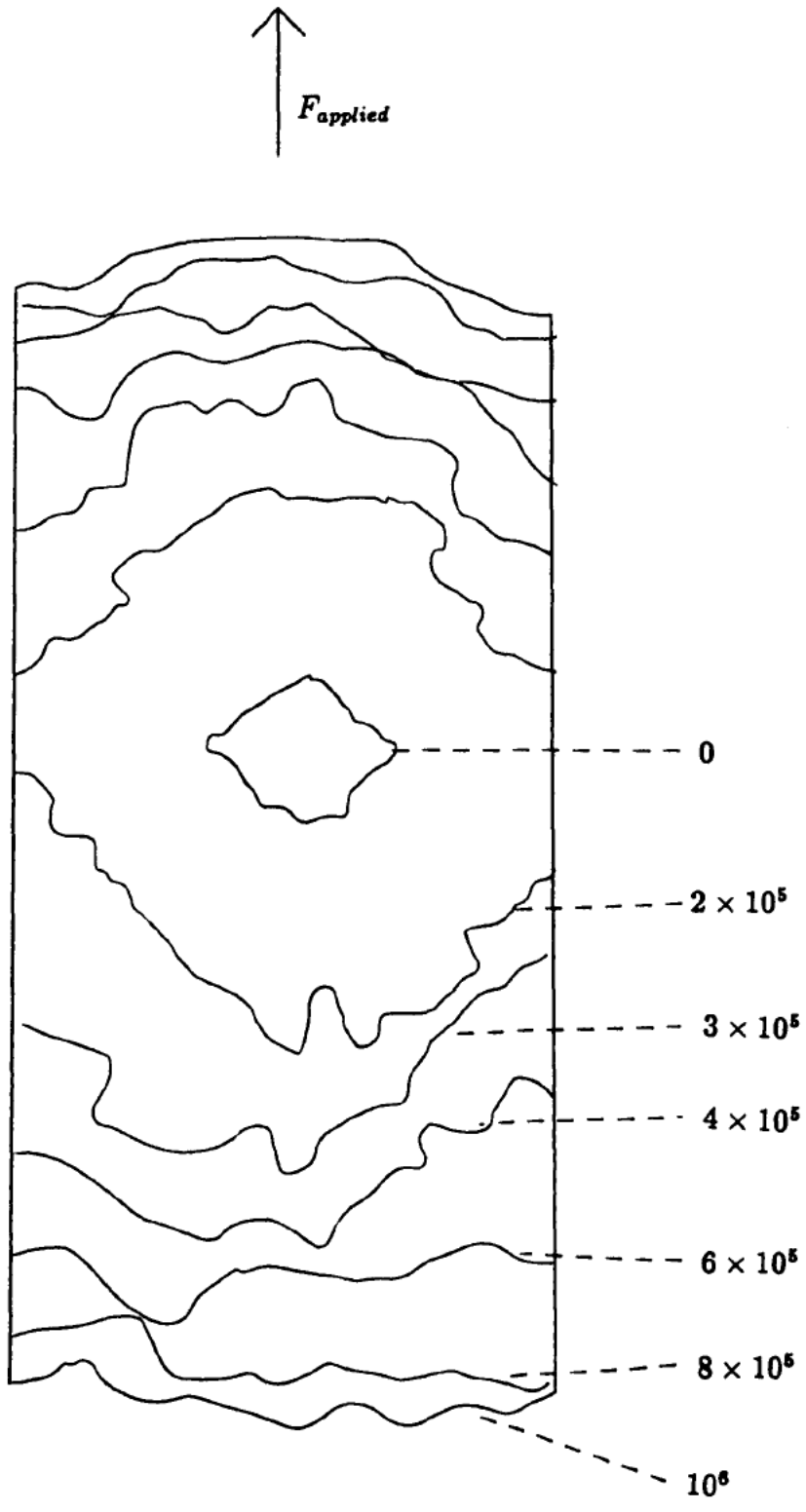

Figure 7.17. Typical Growth of Micro-Damage with Fatigue Cycles. Specimen LE6169/A1/A2/14, 6.87J, $\frac{\sigma_{max}}{\sigma_{rt}} = 0.45$.

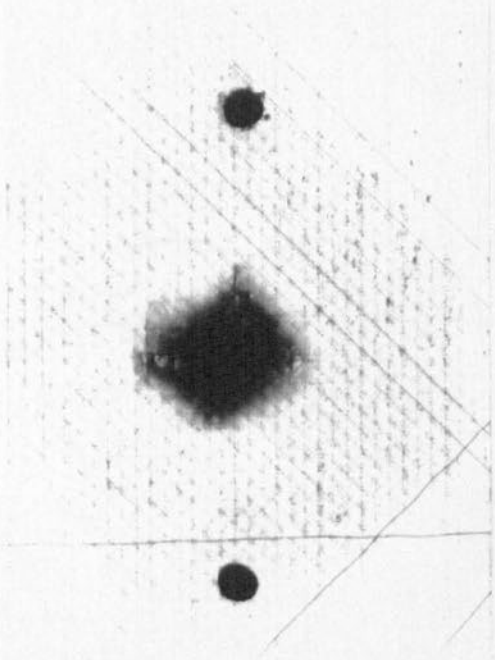

Figure 7.18. Typical X-Ray of Zero-Tension Fatigue Damage.

Specimen LE6169/A1/A2/14, 6.87J, $\frac{\sigma_{max}}{\sigma_{rt}} = 0.45$, $n = 10^5$.

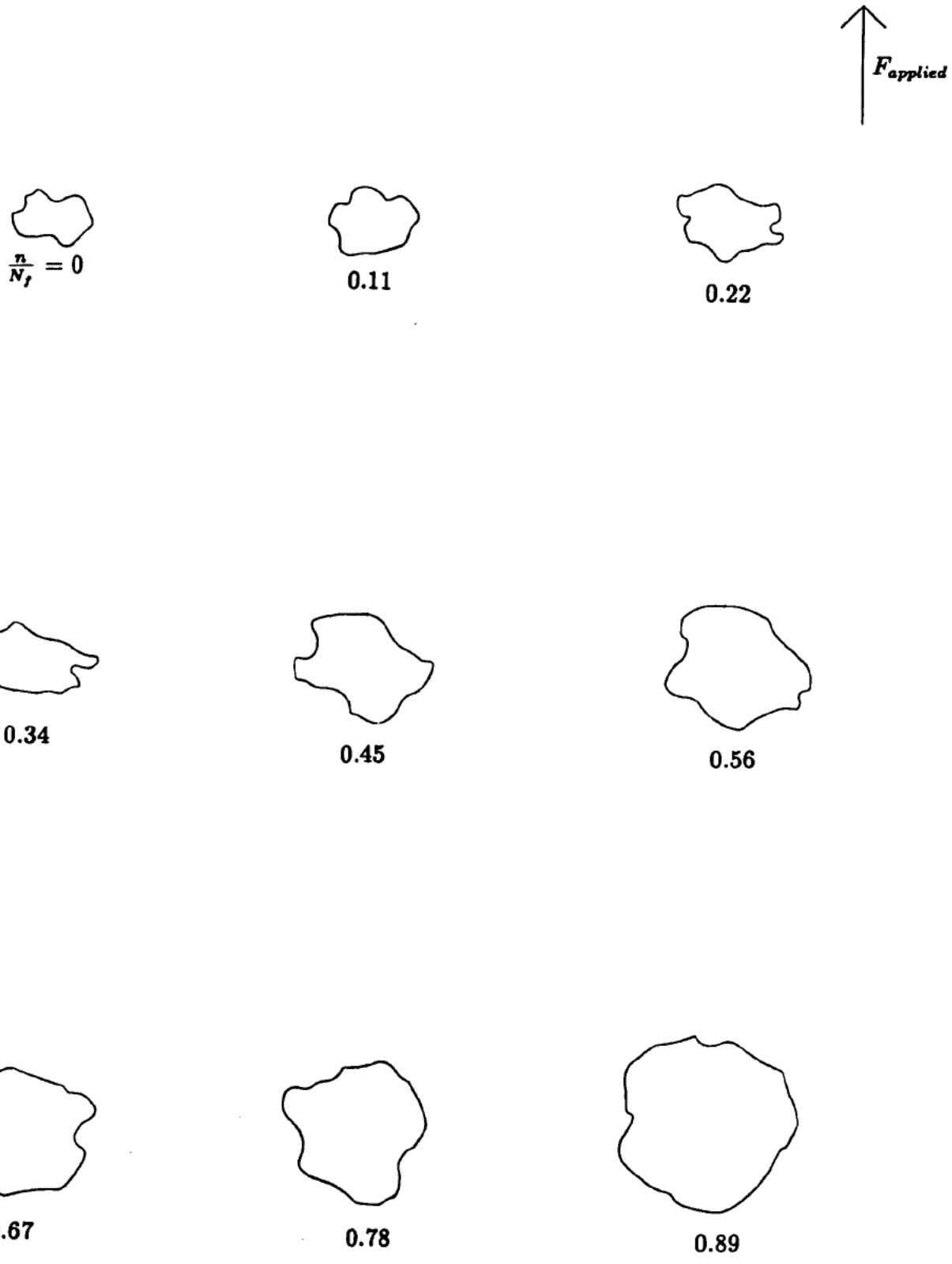

Figure 7.19. The Growth of Delamination with Fatigue Cycles.

Specimen LE6169/A1/A3/9, 2.94J, $\frac{\sigma_{max}}{\sigma_{rt}} = 0.775$.

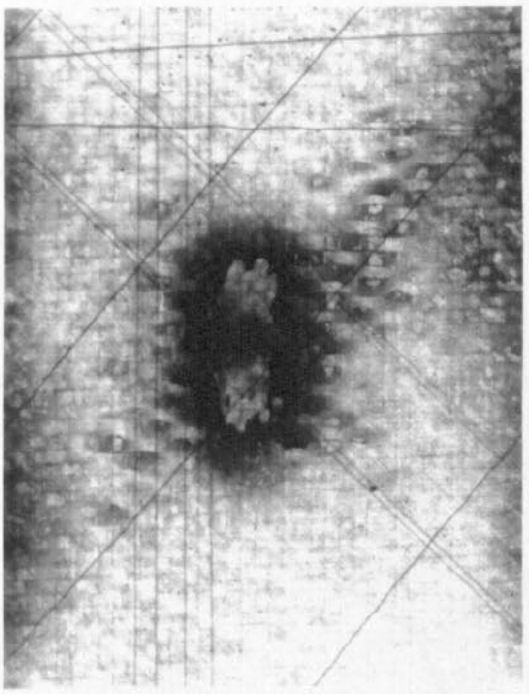

$\uparrow F_{applied}$

Figure 7.20. The Growth of Delamination with Fatigue Cycles. Specimen LE6169/A1/A3/9, 2.94J, $\frac{\sigma_{max}}{\sigma_{rt}} = 0.775$, $\frac{n}{N_f} = 0.89$.

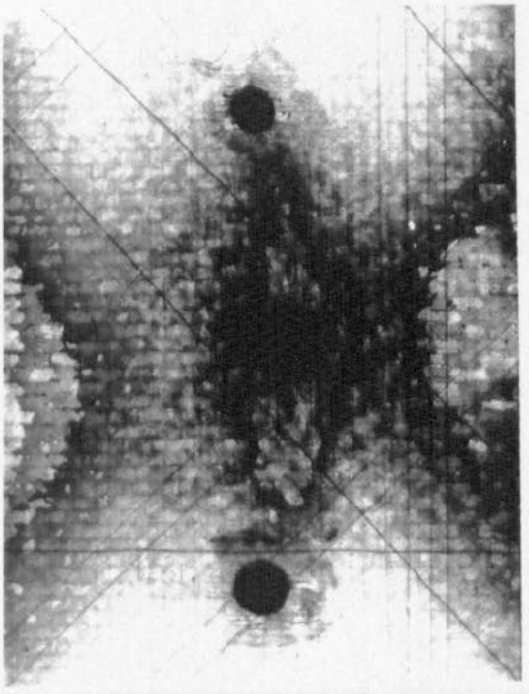

Figure 7.21. The Growth of Delamination with Fatigue Cycles. Specimen LE6169/A1/A2/11, 2.94J, $\frac{\sigma_{max}}{\sigma_{rt}} = 0.55$, $\frac{n}{N_f} = 0.75$.

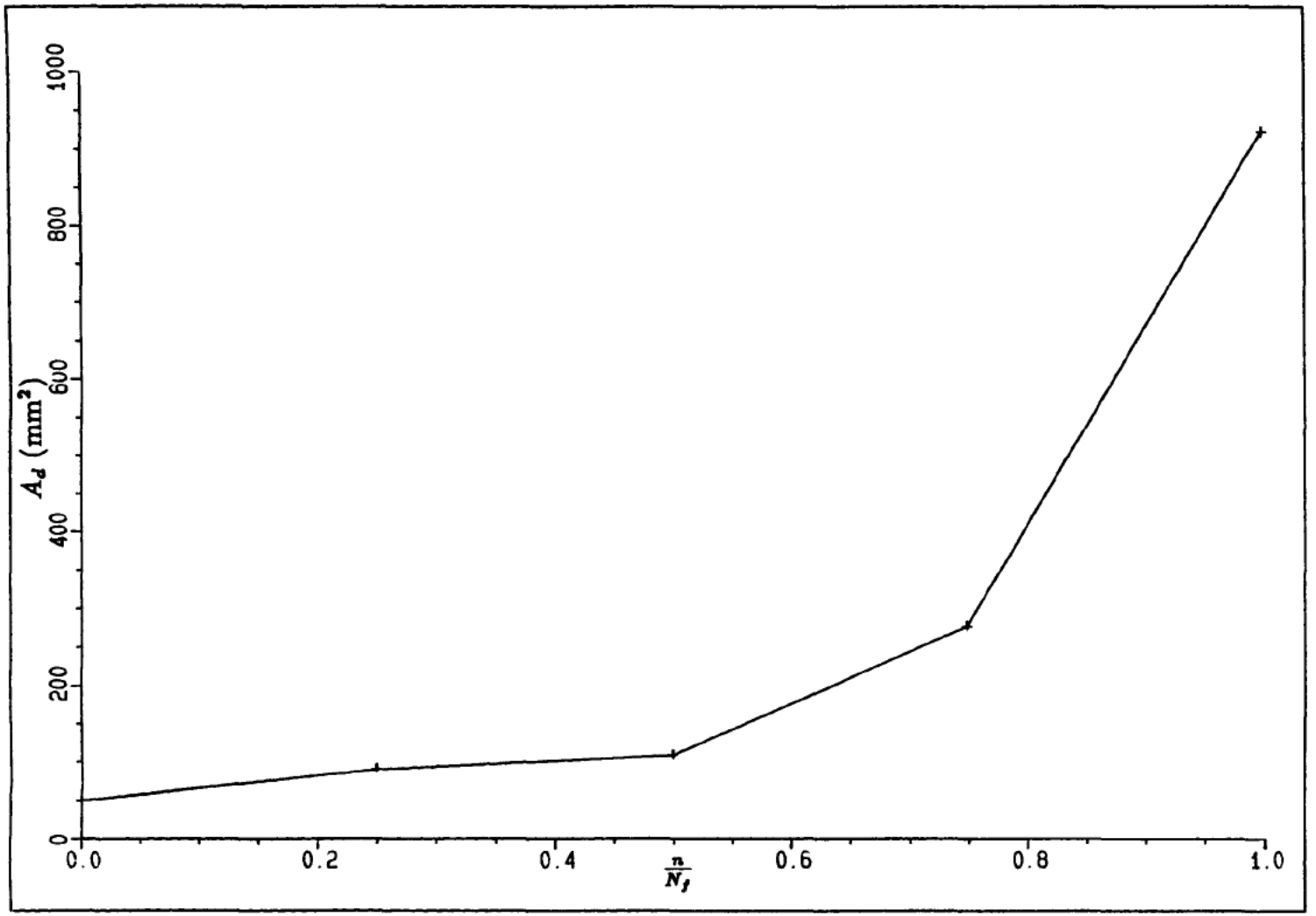

Figure 7.22. Typical Delamination Growth Curve for CFRP under Zero-Tension Fatigue. Specimen LE6169/A1/A3/11, 2.94J, $\frac{\sigma_{max}}{\sigma_{rt}} = 0.75$.

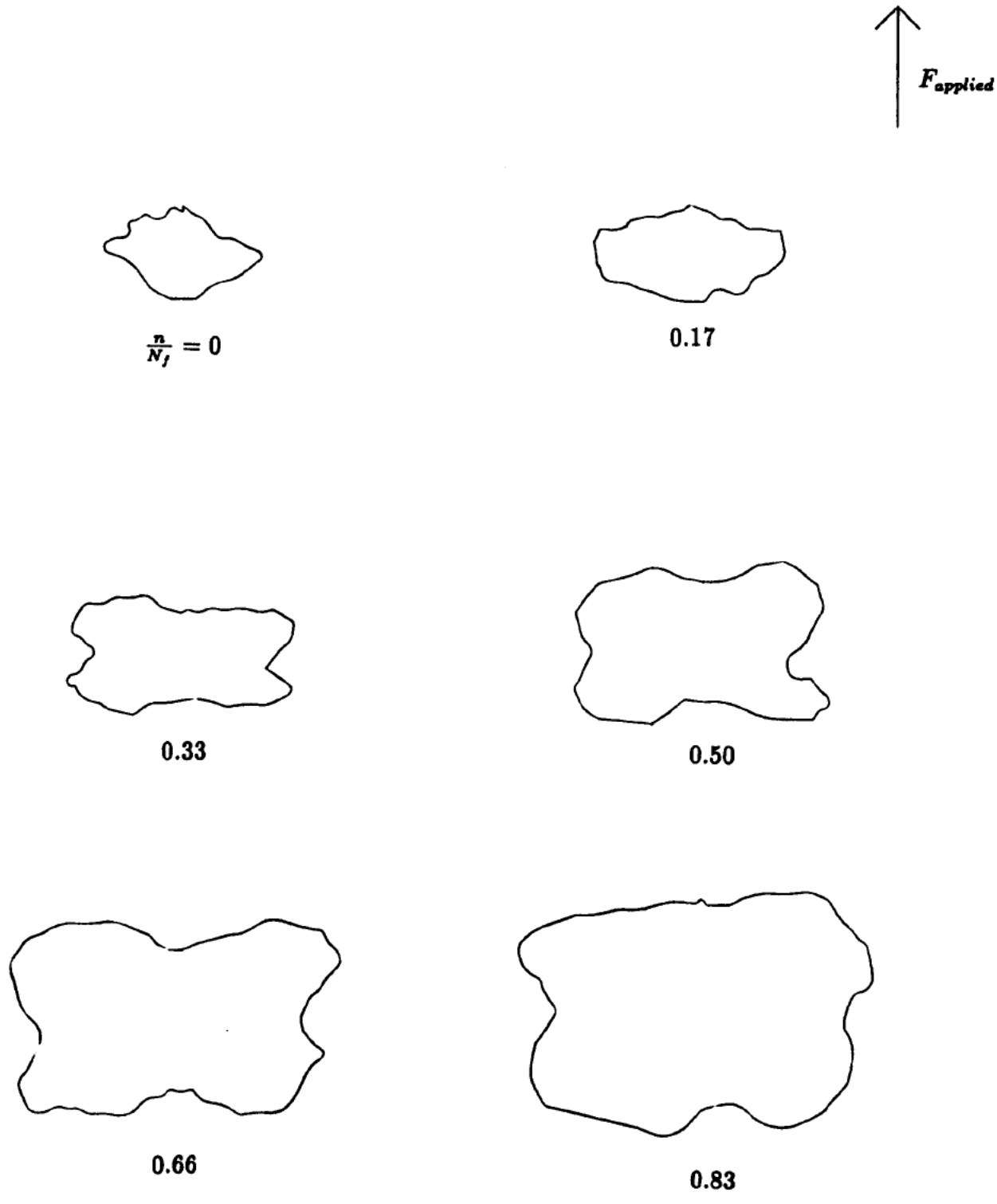

Figure 7.23. The Growth of Delamination with Fatigue Cycles.

Specimen LE6169/A1/A3/10, 6.87J, $\frac{\sigma_{max}}{\sigma_{rt}} = 0.775$.

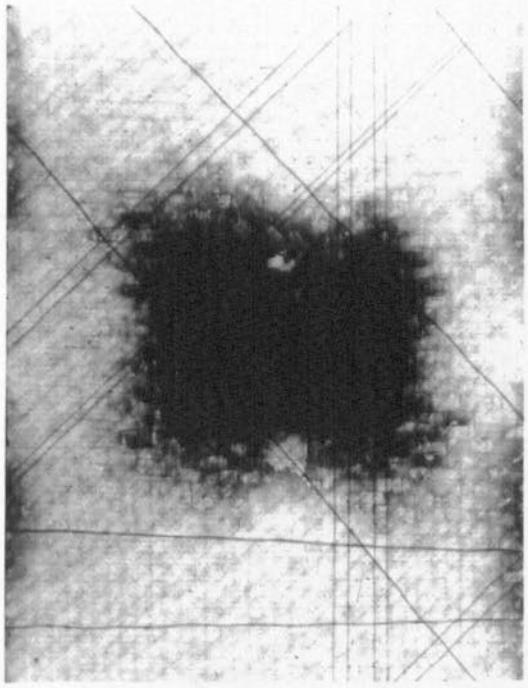

Figure 7.24. The Growth of Delamination with Fatigue Cycles. Specimen LE6169/A1/A3/8, 6.87J, $\frac{\sigma_{max}}{\sigma_{rt}} = 0.80$, $\frac{n}{N_f} = 0.75$.

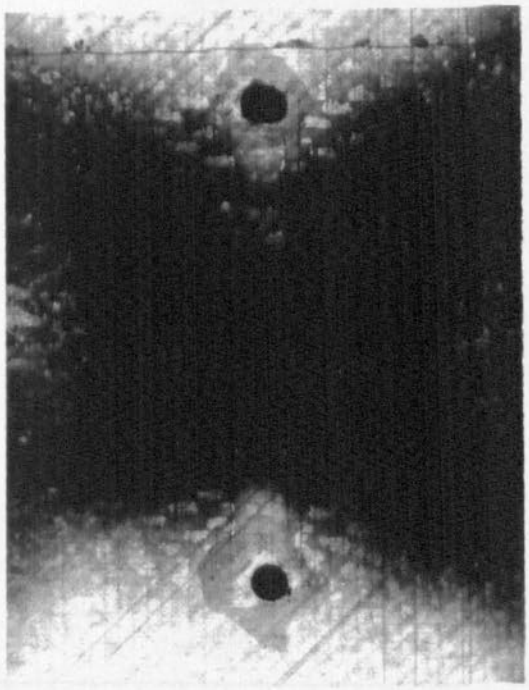

Figure 7.25. The Growth of Delamination with Fatigue Cycles. Specimen LE6169/A1/B2/5, 6.87J, $\frac{\sigma_{max}}{\sigma_{rt}} = 0.70$, $\frac{n}{N_f} = 0.97$.

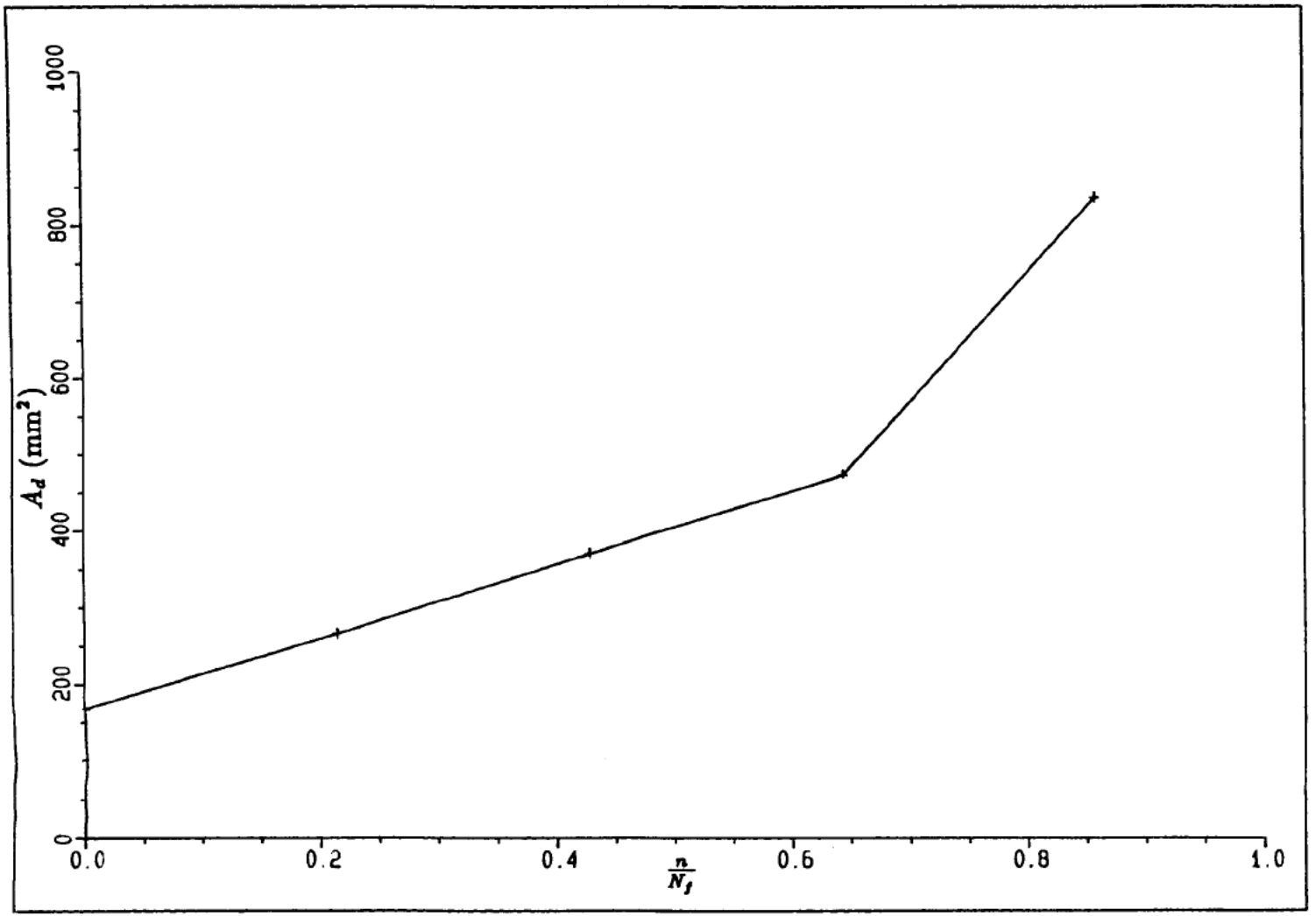

Figure 7.26. Typical Delamination Growth Curve for CFRP under

Zero-Tension Fatigue. Specimen LE6169/A1/B2/15, 6.87J, $\frac{\sigma_{max}}{\sigma_{ri}} = 0.80$.

Figure 7.27. Typical High Stress/Low Cycle Zero-Tension Fatigue Failure. Specimen LE6169/A1/B2/14, 2.94J, $\frac{\sigma_{max}}{\sigma_{rt}} = 0.80$, $N_f = 8338$.

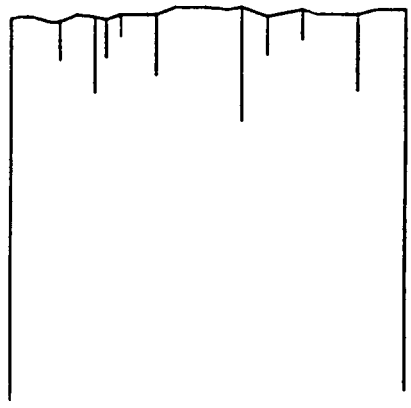

Figure 7.28. Schematic Representation of 0° Fibre Tow Failure Showing Plane Fracture Surface and Matrix Splitting.

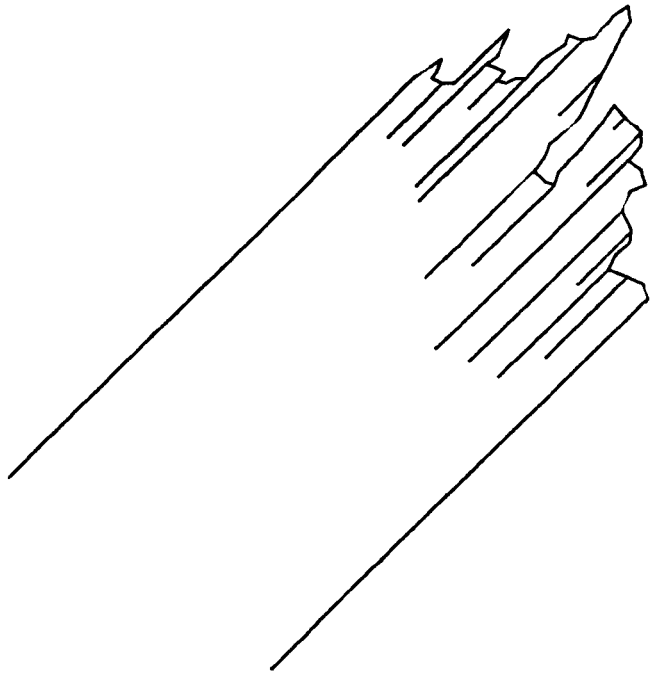

Figure 7.29. Schematic Representation of ±45° Fibre Tow Failure Showing Jagged Fracture Surface with Associated Matrix Splitting.

Figure 7.30. Typical Low Stress/High Cycle Zero-Tension Fatigue Failure. Specimen LE6169/A1/B2/2, 2.94J, $\frac{\sigma_{max}}{\sigma_{rt}} = 0.50$, $N_f = 927870$.

Figure 7.31. Typical High Stress/Low Cycle Zero-Tension Fatigue Failure. Specimen LE6169/A1/B2/7, 6.87J, $\frac{\sigma_{max}}{\sigma_{rt}} = 0.80$, $N_f = 25291$.

Figure 7.32. Typical Low Stress/High Cycle Zero-Tension Fatigue Failure. Specimen LE6169/A1/A2/6, 6.87J, $\frac{\sigma_{max}}{\sigma_{rt}} = 0.60$, $N_f = 630920$.

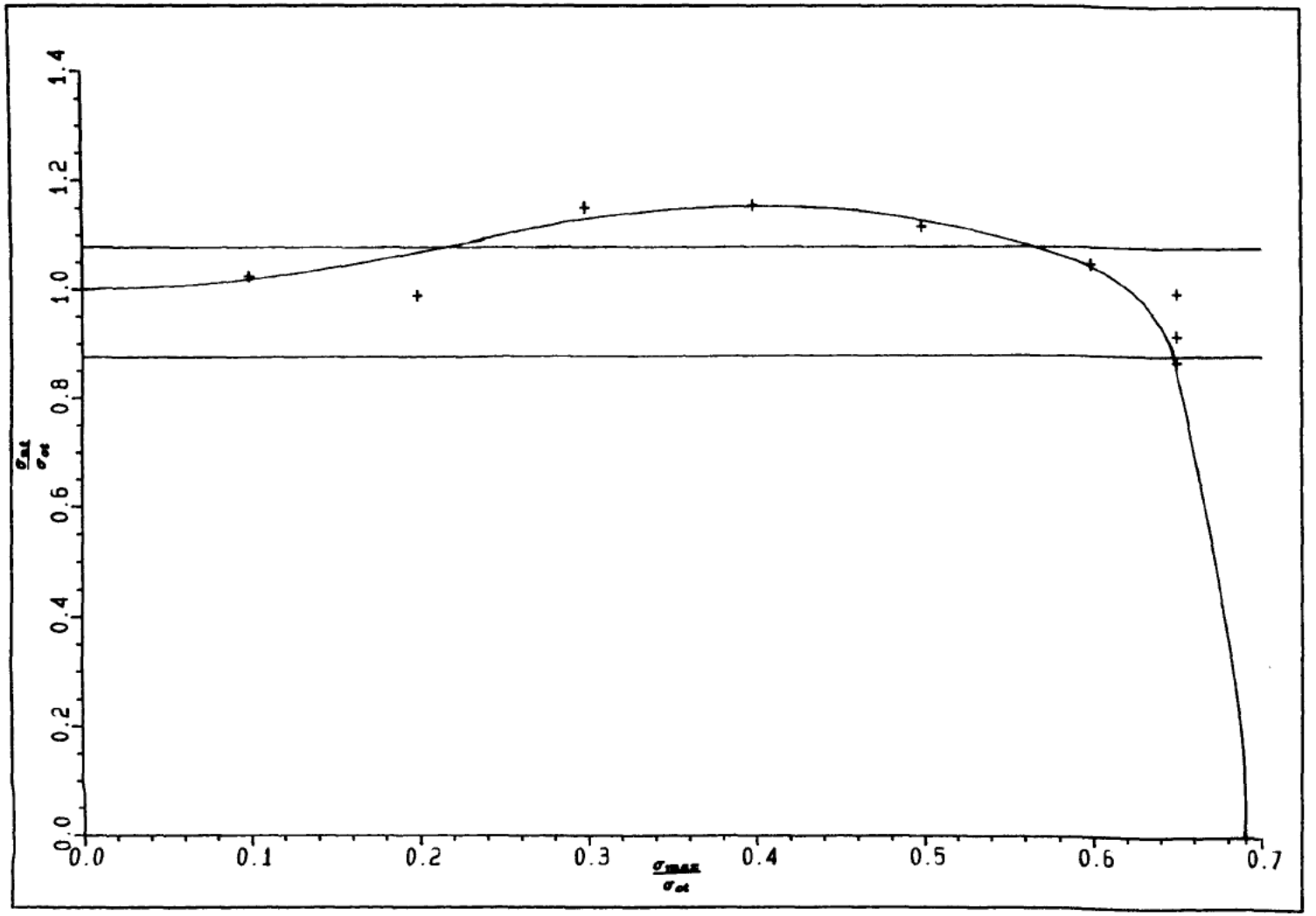

Figure 7.33. The Residual Tensile Strength of Undamaged Specimens

after 10^6 Cycles Zero-Tension Fatigue.

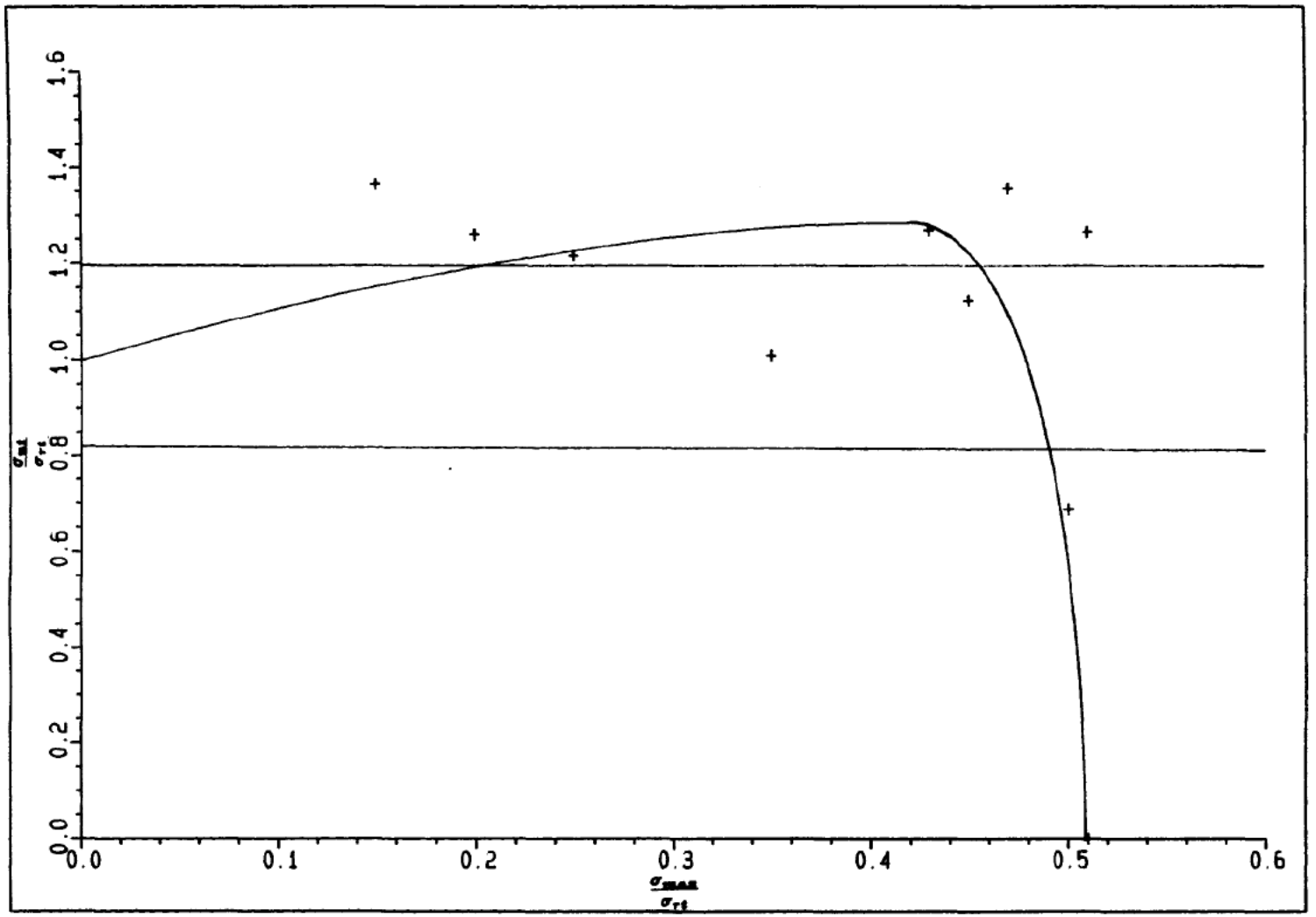

Figure 7.34. The Residual Tensile Strength of 2.94J Impact Specimens after 10^6 Cycles Zero-Tension Fatigue.

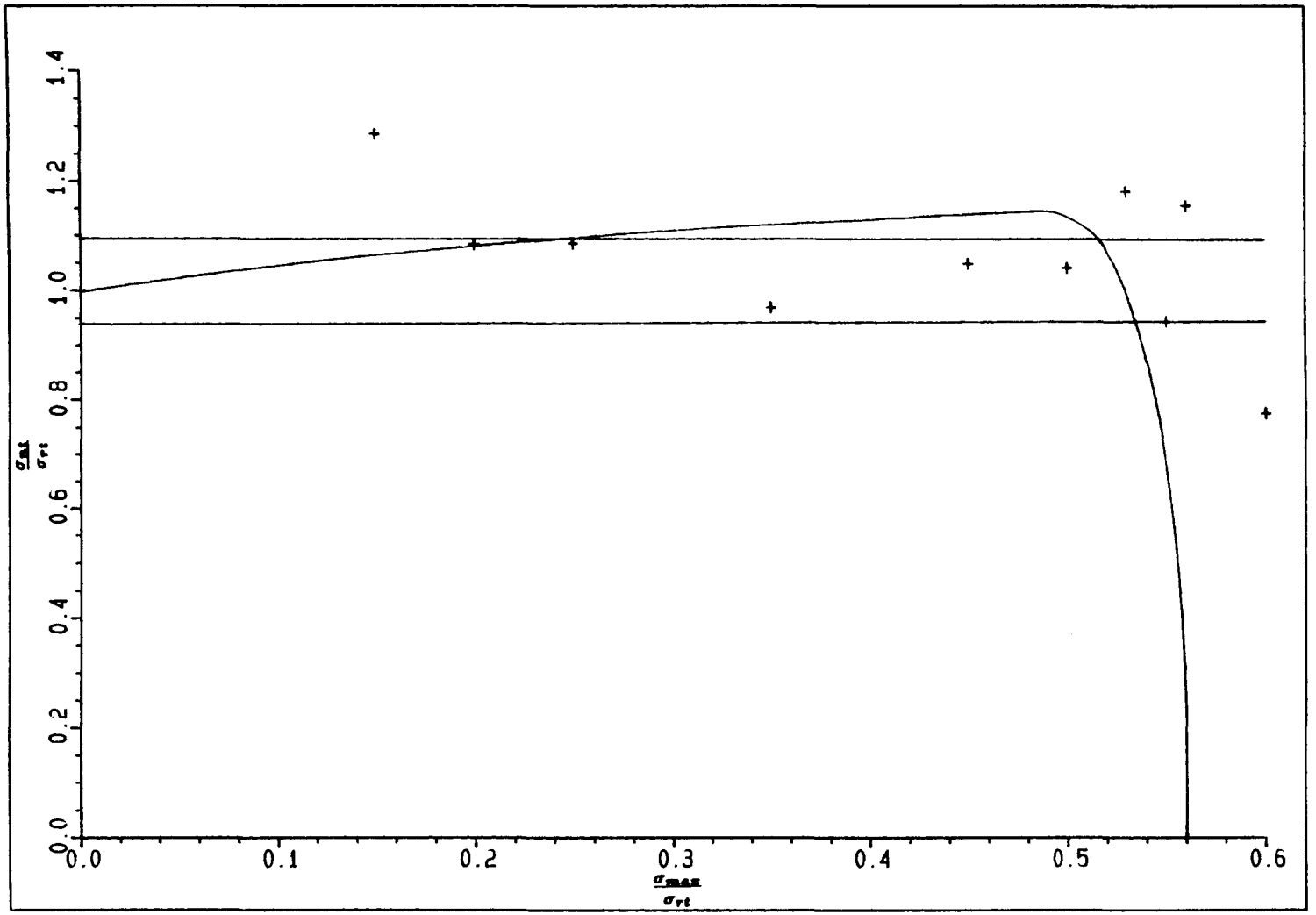

Figure 7.35. The Residual Tensile Strength of 6.87J Impact Specimens after 10^6 Cycles Zero-Tension Fatigue.

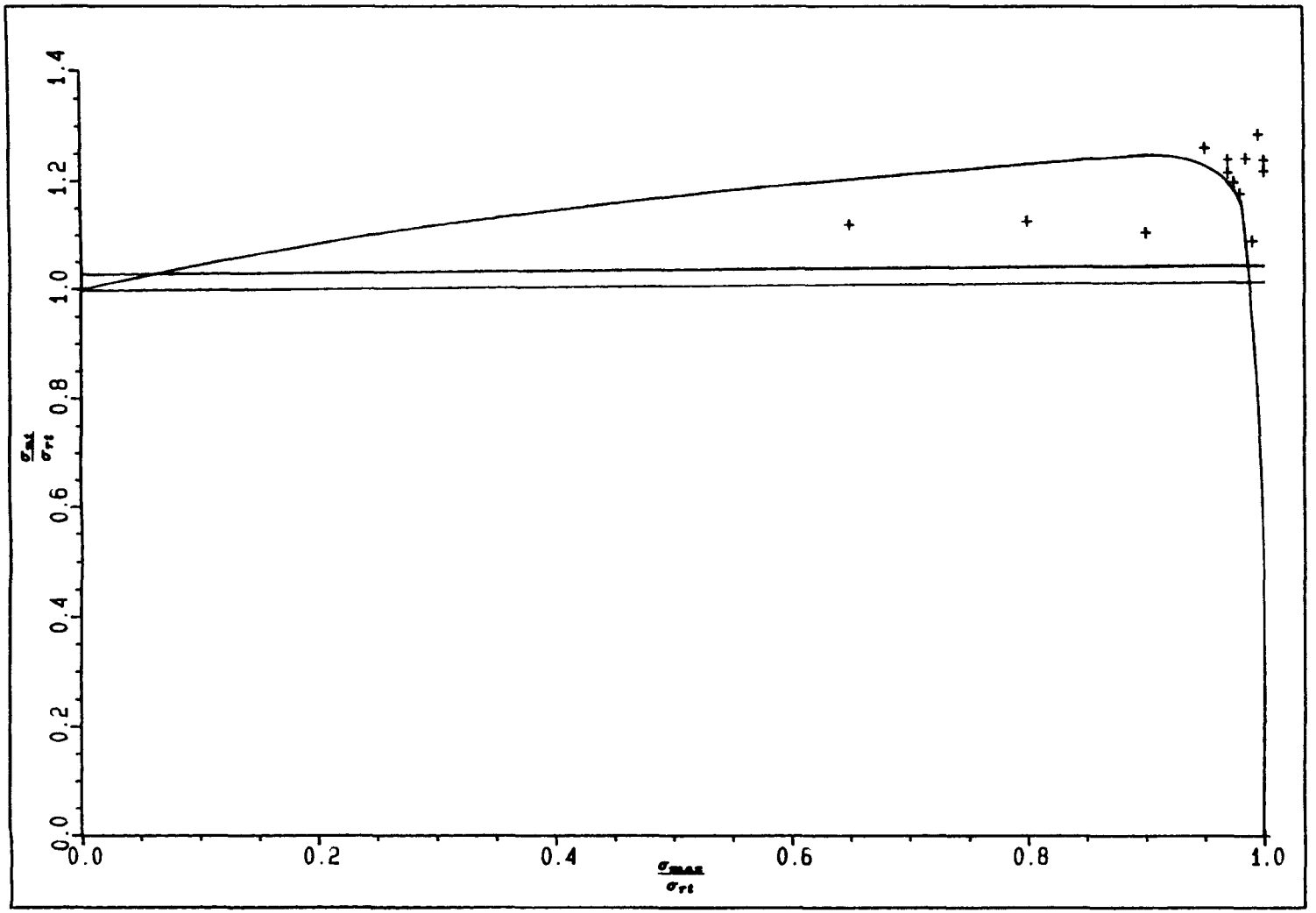

Figure 7.36. The Residual Tensile Strength of Specimens Containing a 12.7mm Diameter Hole after 10^6 Cycles Zero-Tension Fatigue.

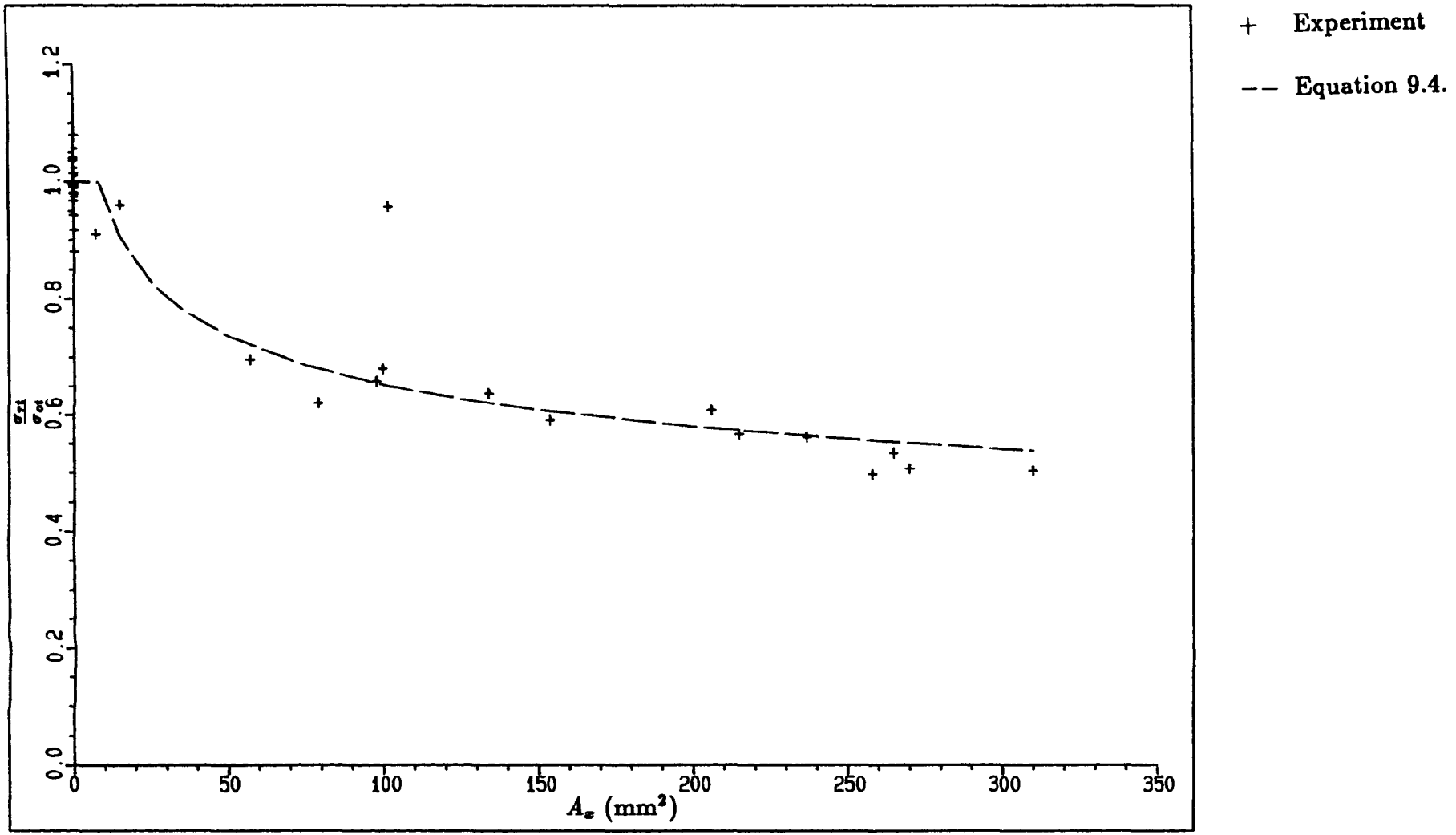

Figure 9.1. The Relationship Between X-Ray Damage Area and Residual Tensile Strength for Impacted CFRP Specimens.

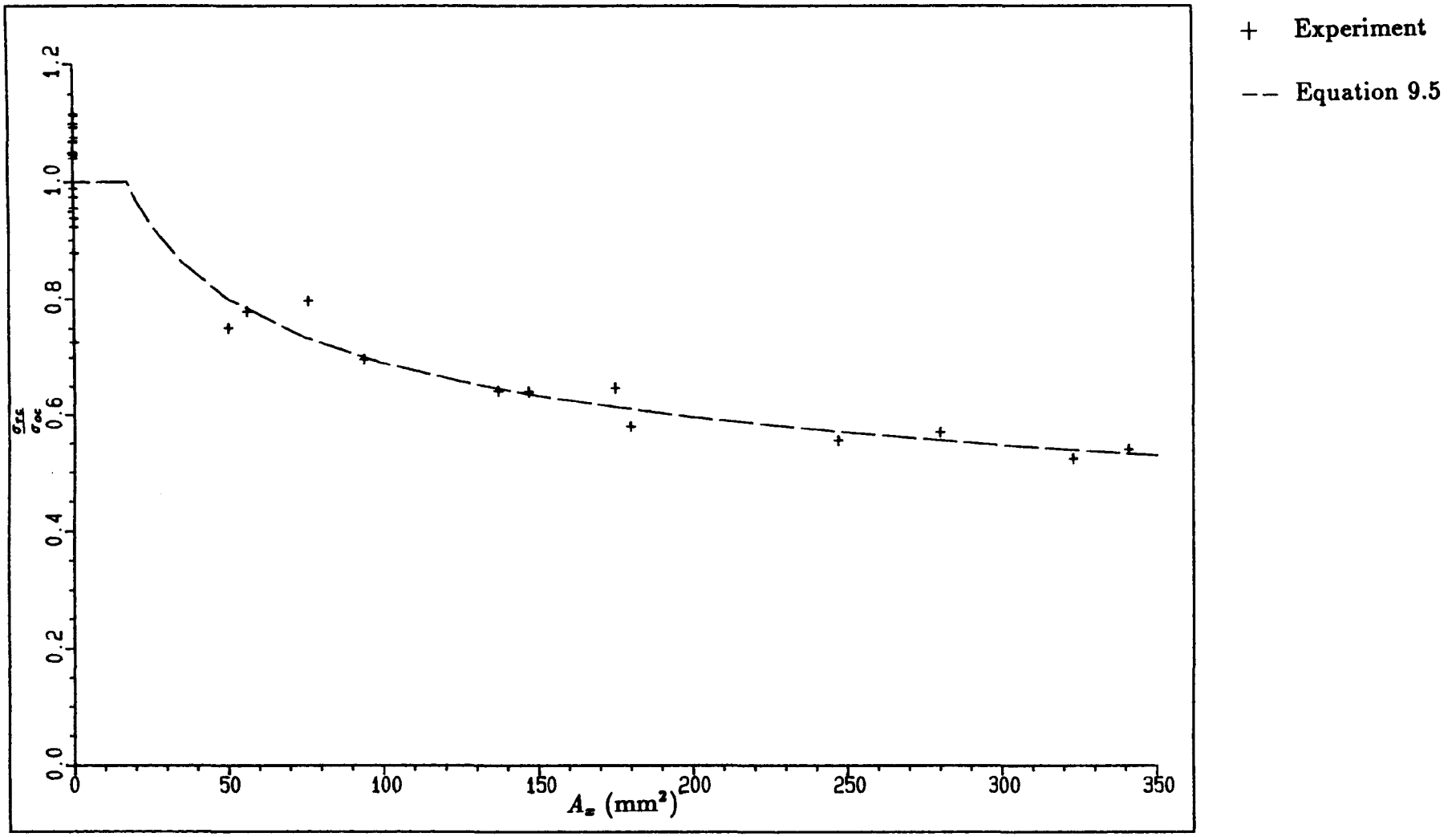

Figure 9.2. The Relationship Between X-Ray Damage Area and Residual Compressive Strength for Impacted CFRP Specimens.

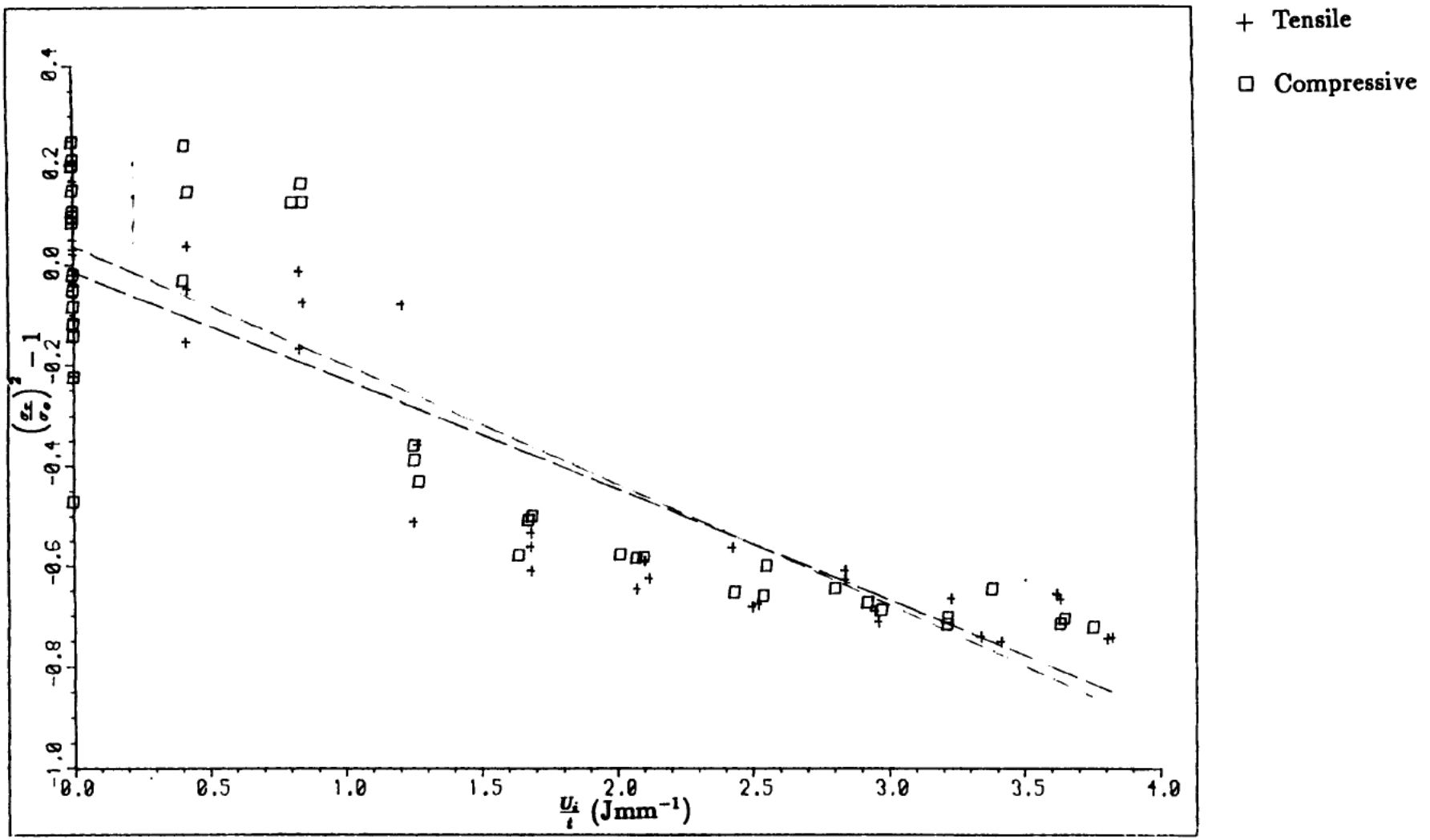

Figure 9.3. Husman Analysis Plot to Determine Empirical Constants.

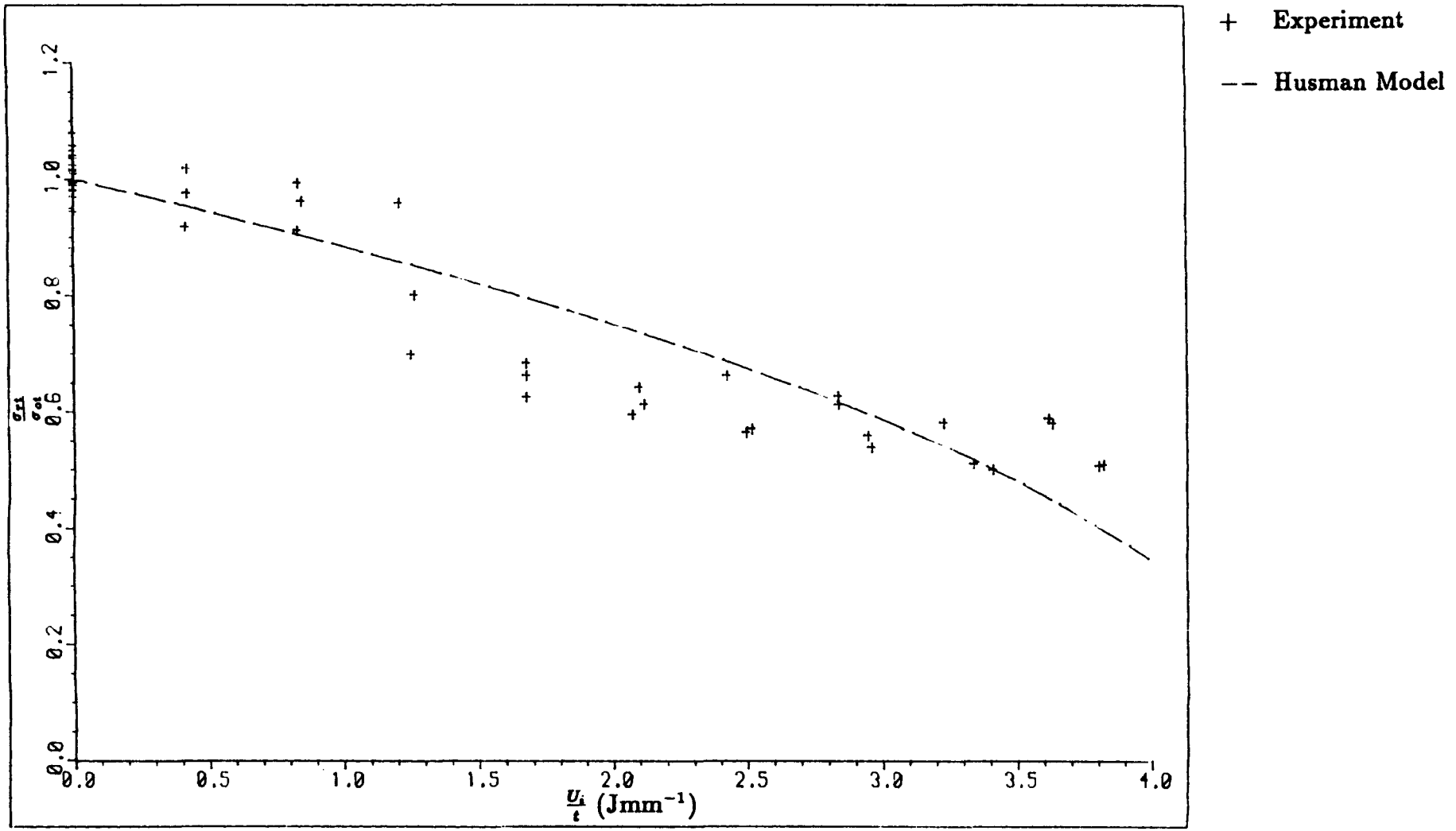

Figure 9.4. Husman Model for the Prediction of Residual Tensile Strength of Impacted Specimens.

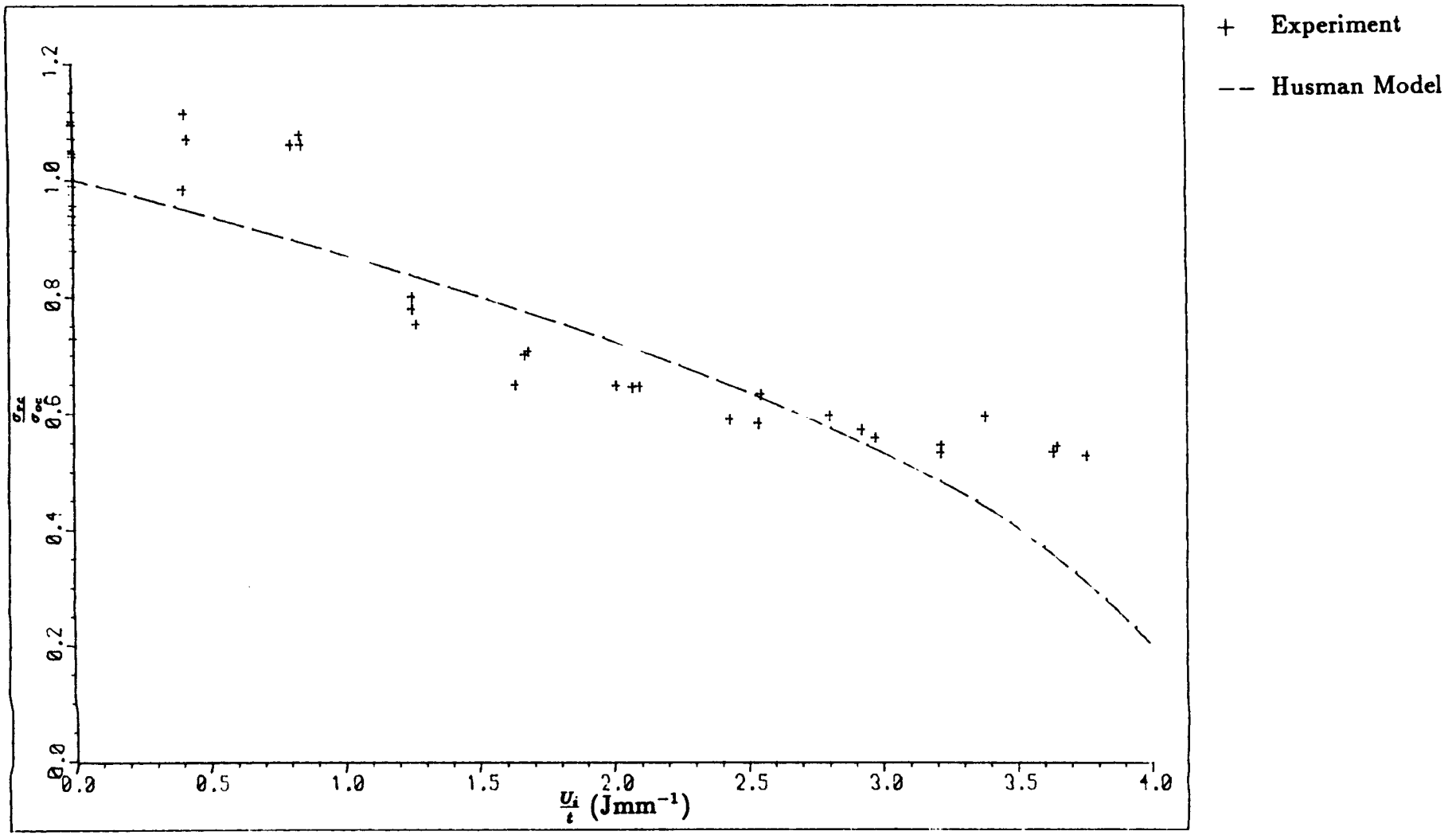

Figure 9.5. Husman Model for the Prediction of Residual

Compressive Strength of Impacted Specimens.

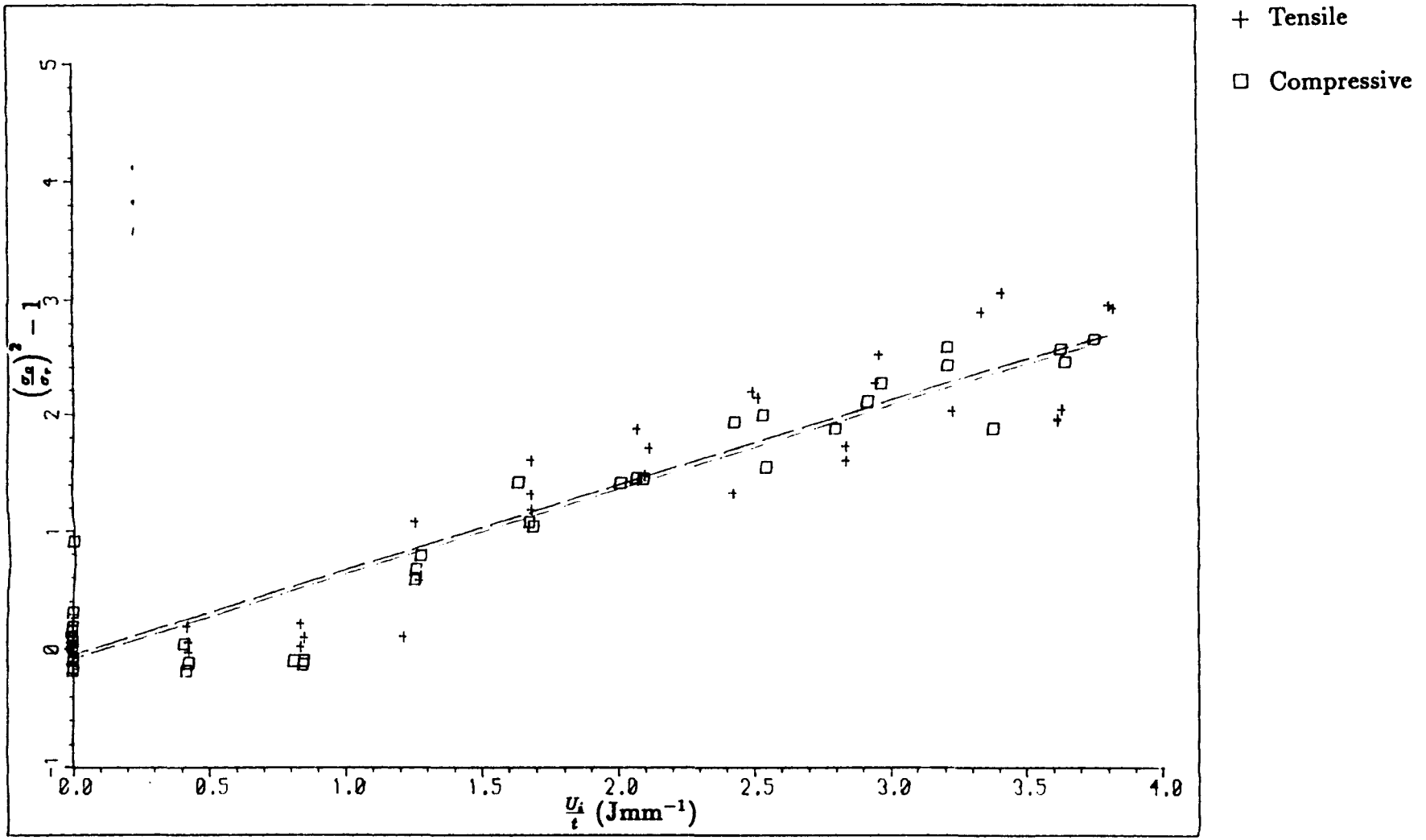

Figure 9.6. Lal Analysis Plot to Determine Empirical Constants.

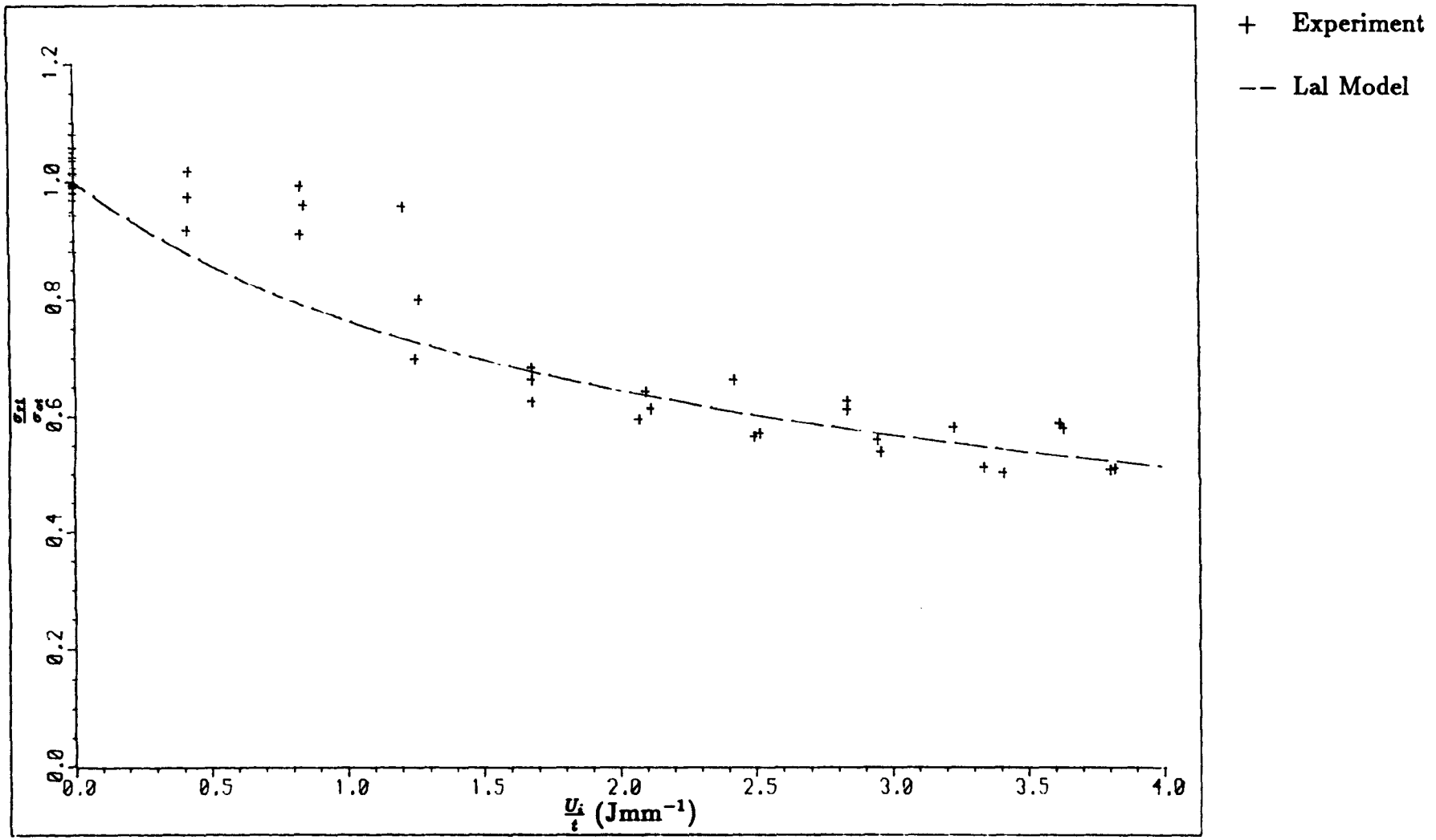

Figure 9.7. Lal Model for the Prediction of Residual

Tensile Strength of Impacted Specimens.

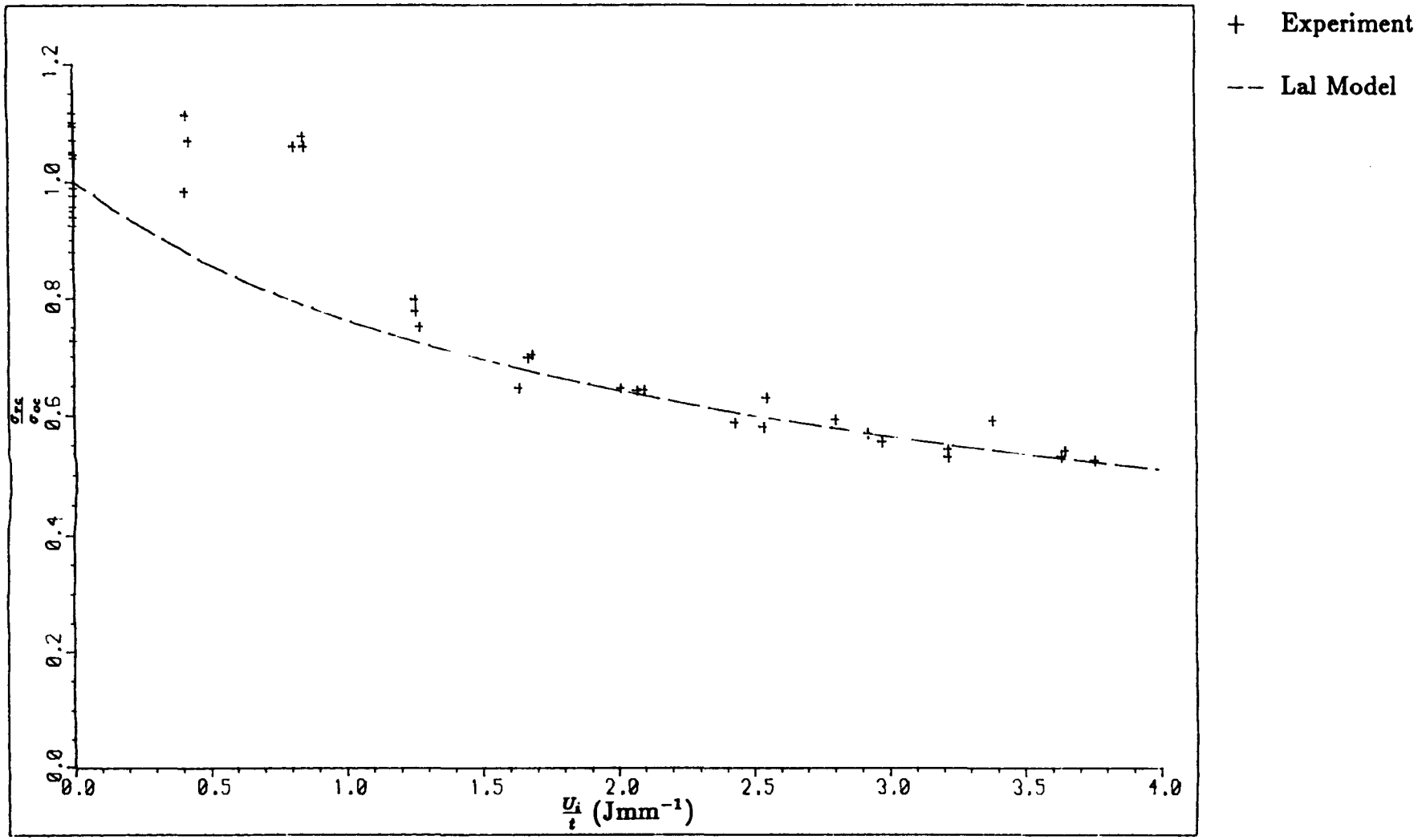

Figure 9.8. Lal Model for the Prediction of Residual

Compressive Strength of Impacted Specimens.

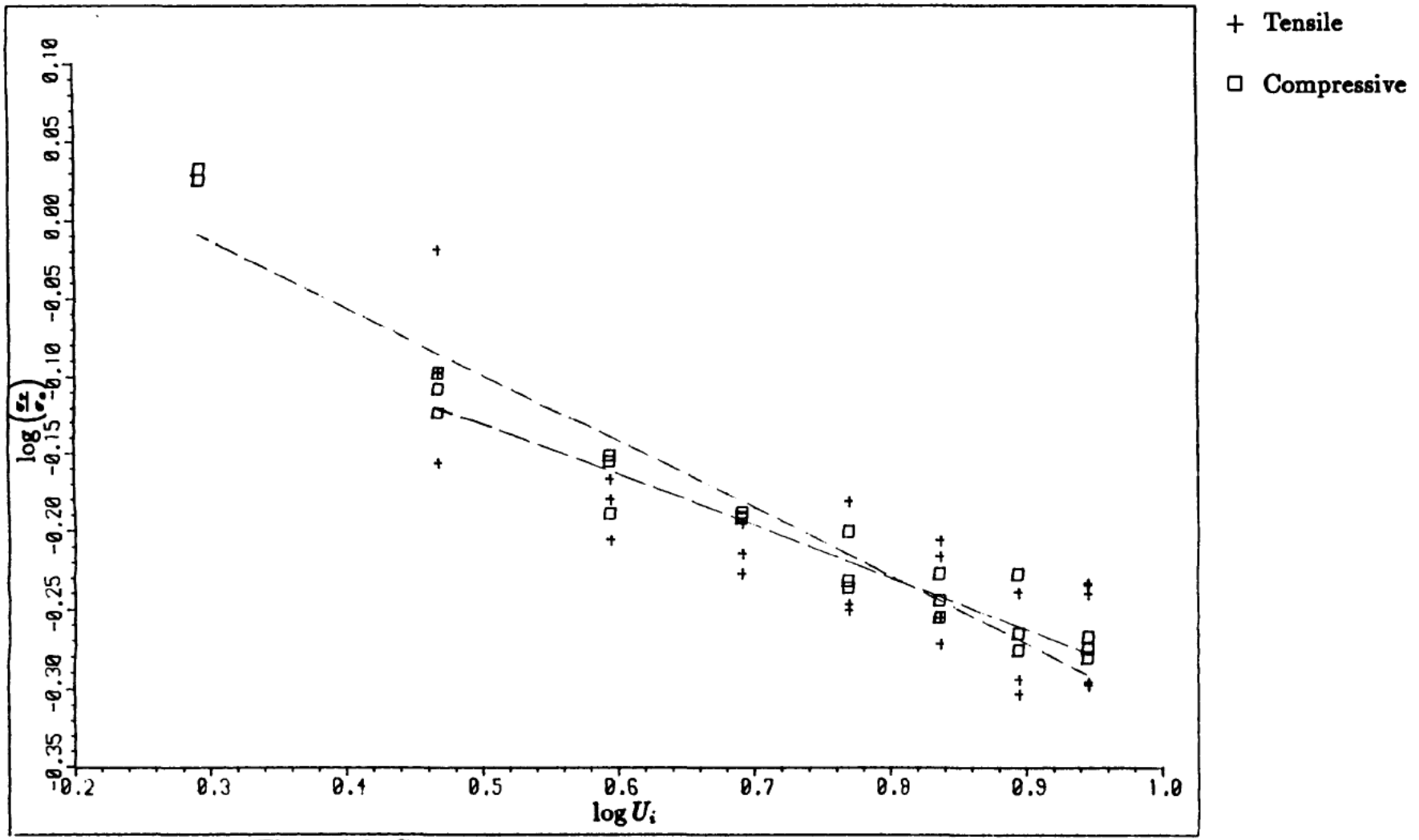

Figure 9.9. Caprino Analysis Plot to Determine Empirical Constants.

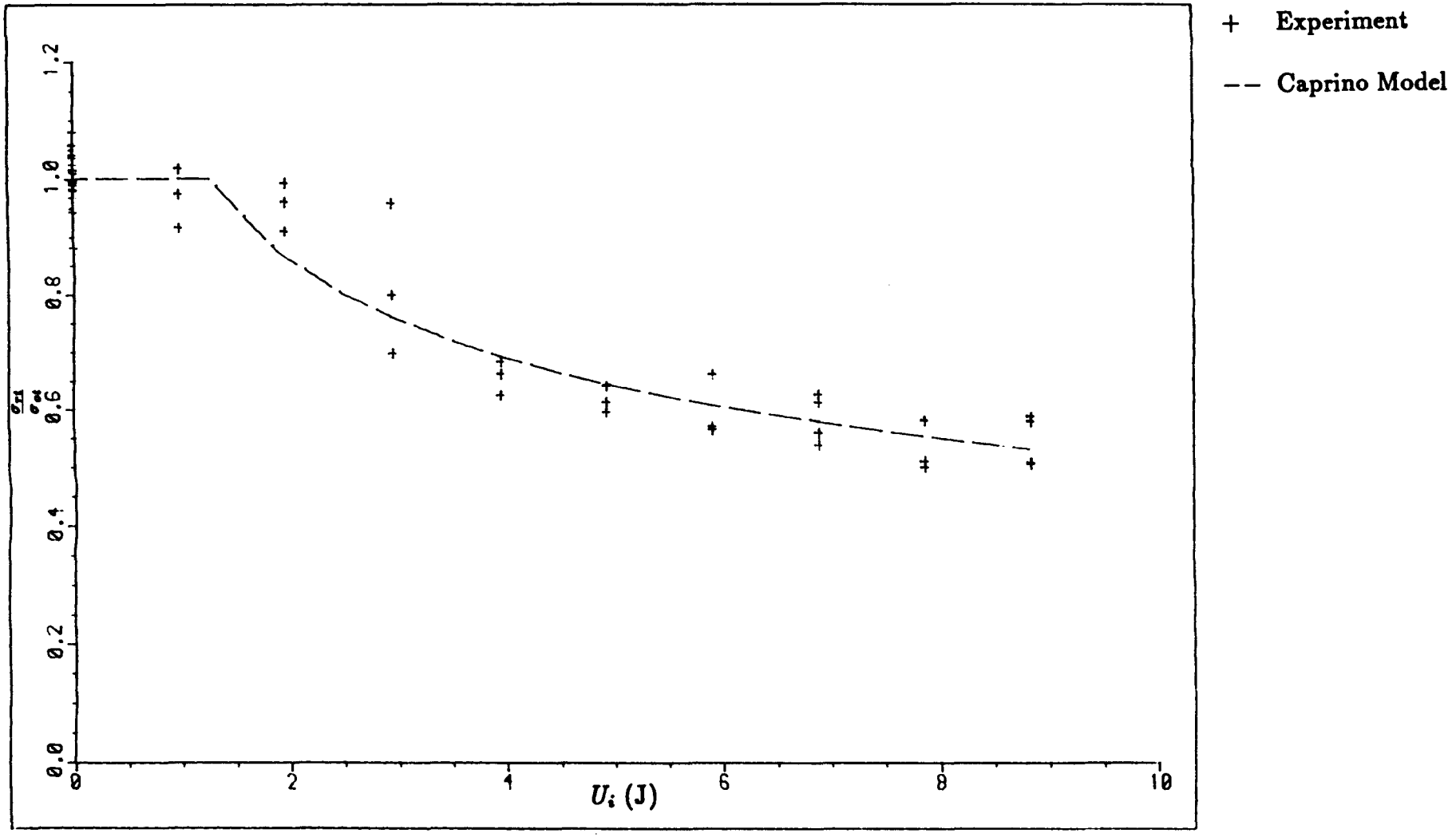

Figure 9.10. Caprino Model for the Prediction of Residual

Tensile Strength of Impacted Specimens.

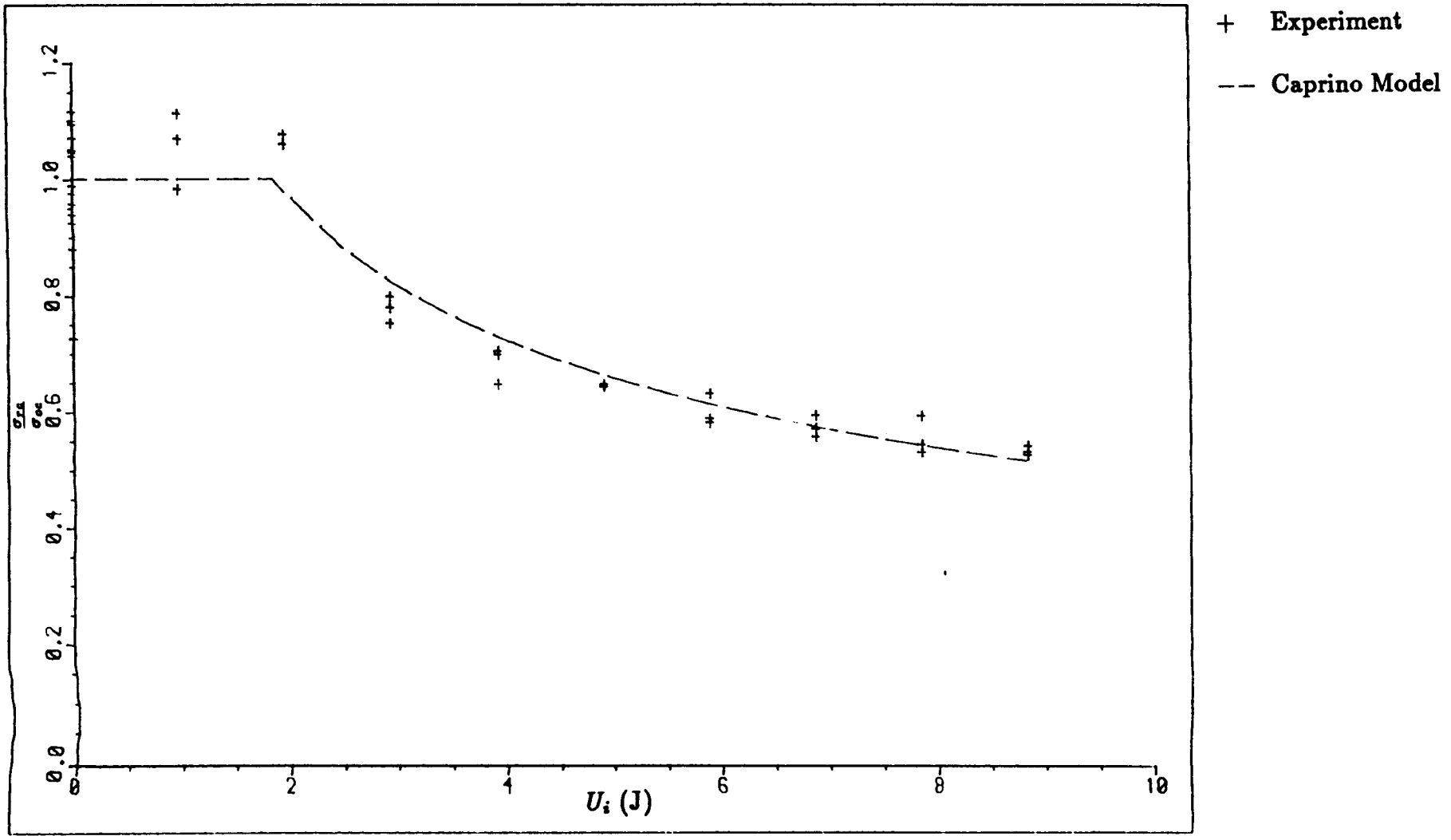

Figure 9.11. Caprino Model for the Prediction of Residual

Compressive Strength of Impacted Specimens.

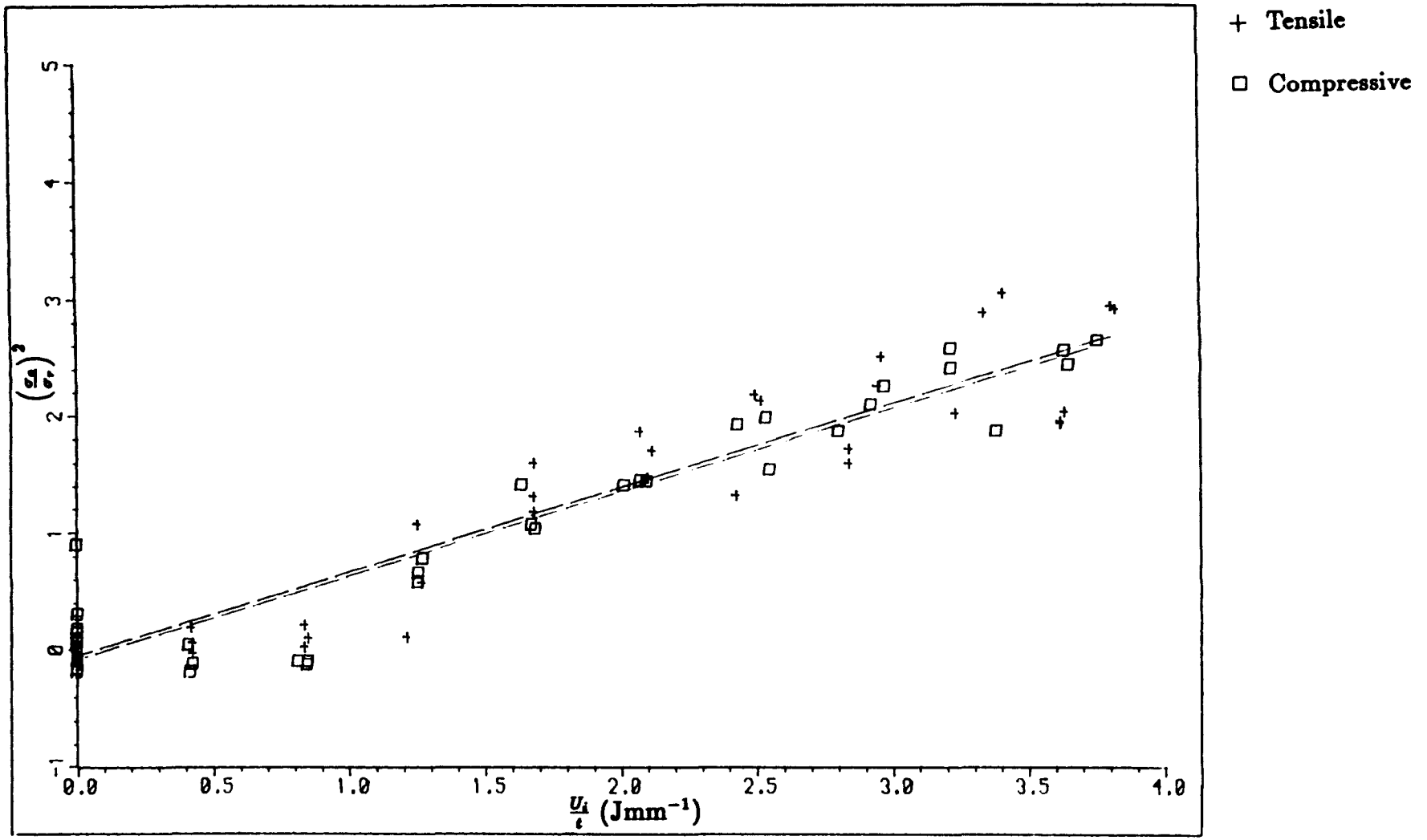

Figure 9.12. Avva Analysis Plot to Determine Empirical Constants.

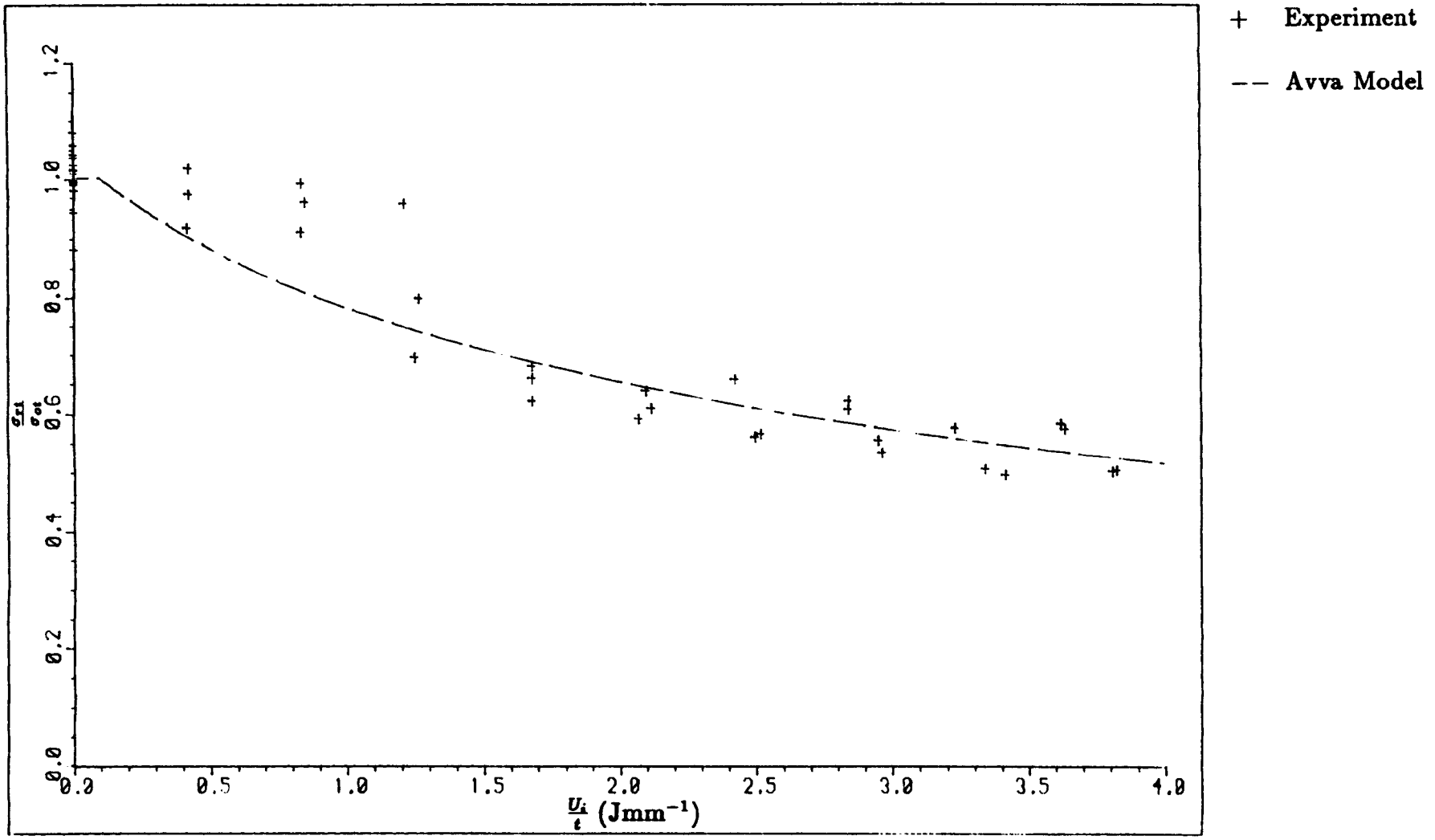

Figure 9.13. Avva Model for the Prediction of Residual

Tensile Strength of Impacted Specimens.

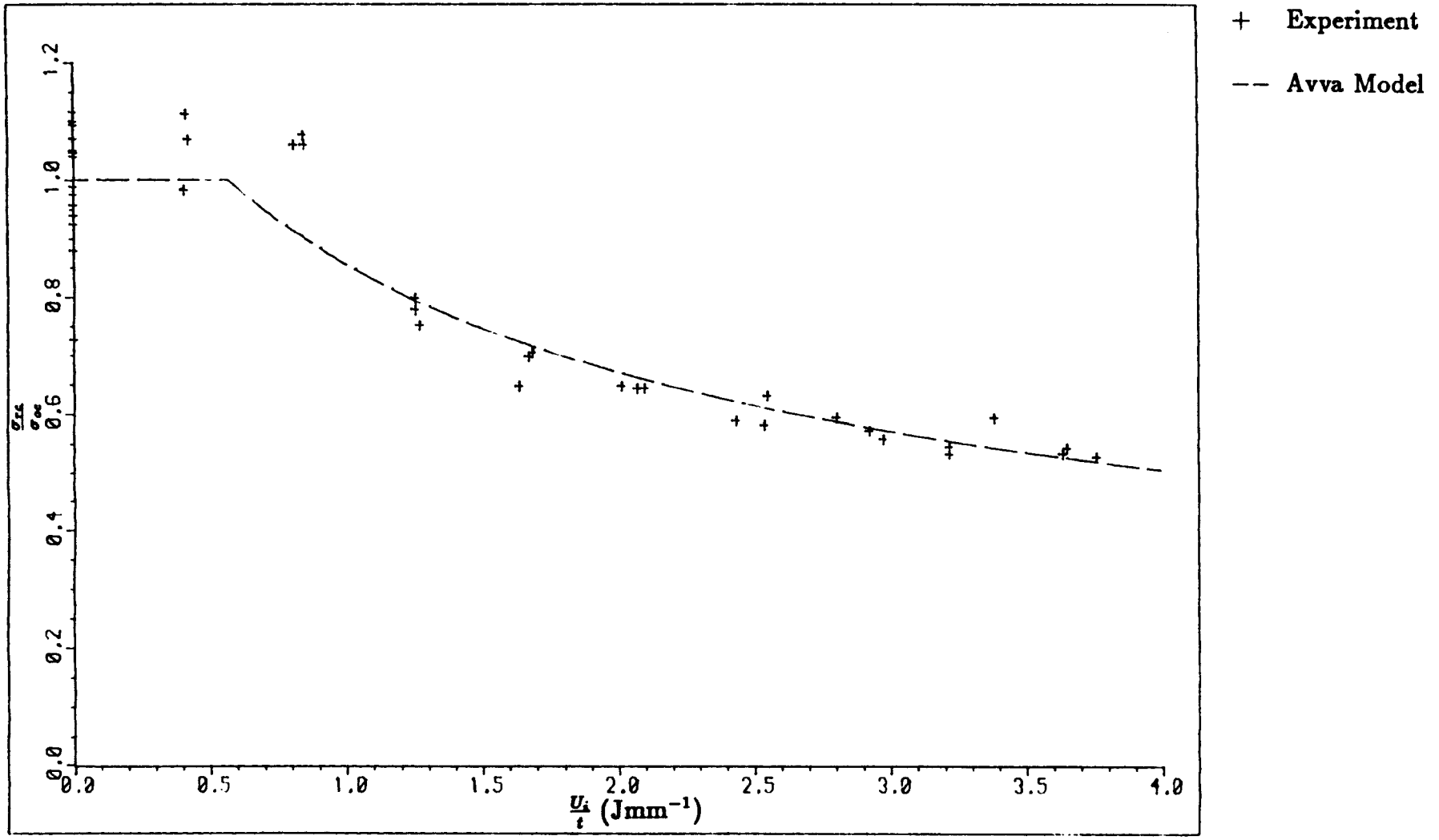

Figure 9.14. Avva Model for the Prediction of Residual

Compressive Strength of Impacted Specimens.

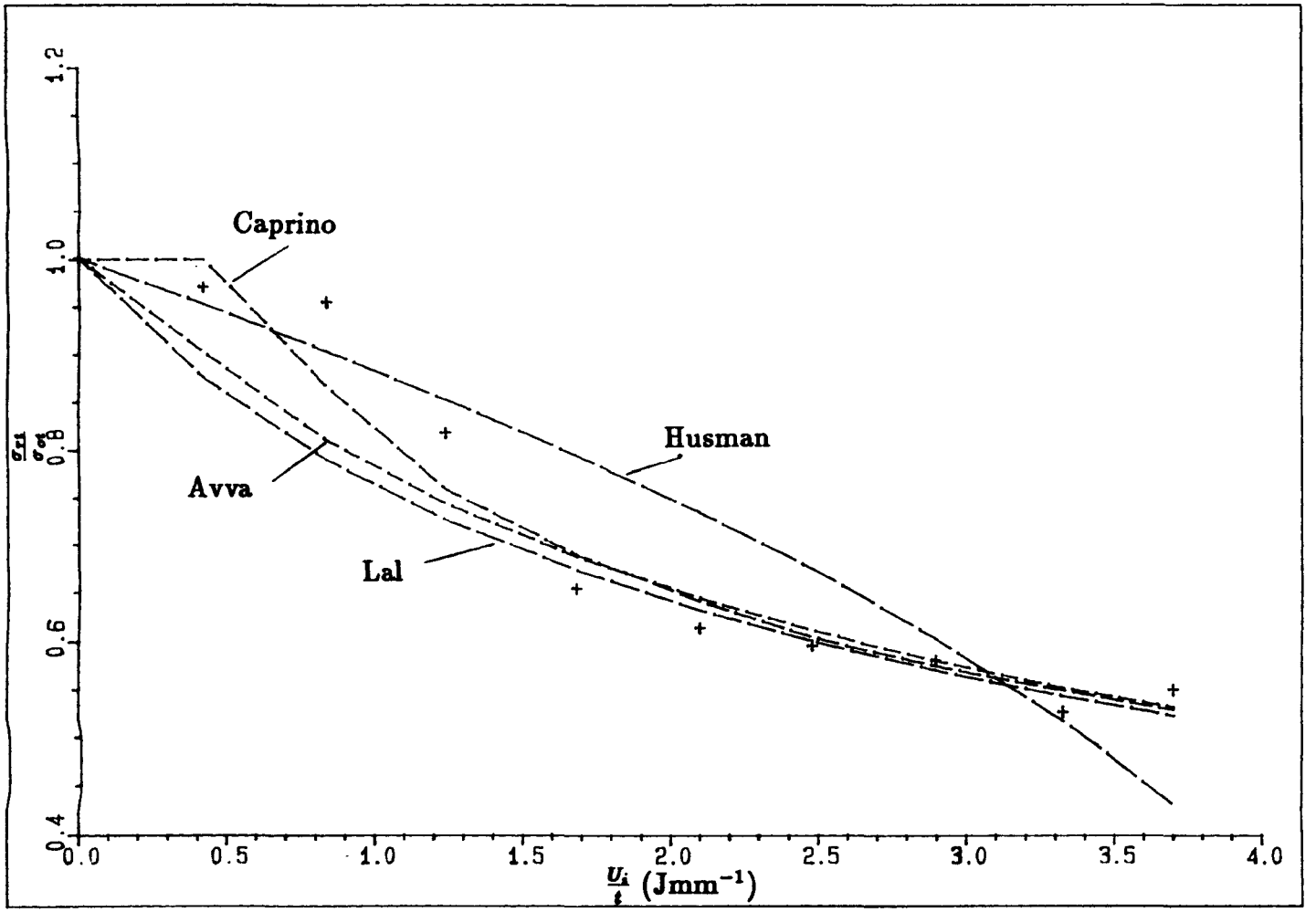

Figure 9.15. Comparison of Equivalent Flaw Models for the Prediction of Residual Tensile Strength of Impacted Specimens.

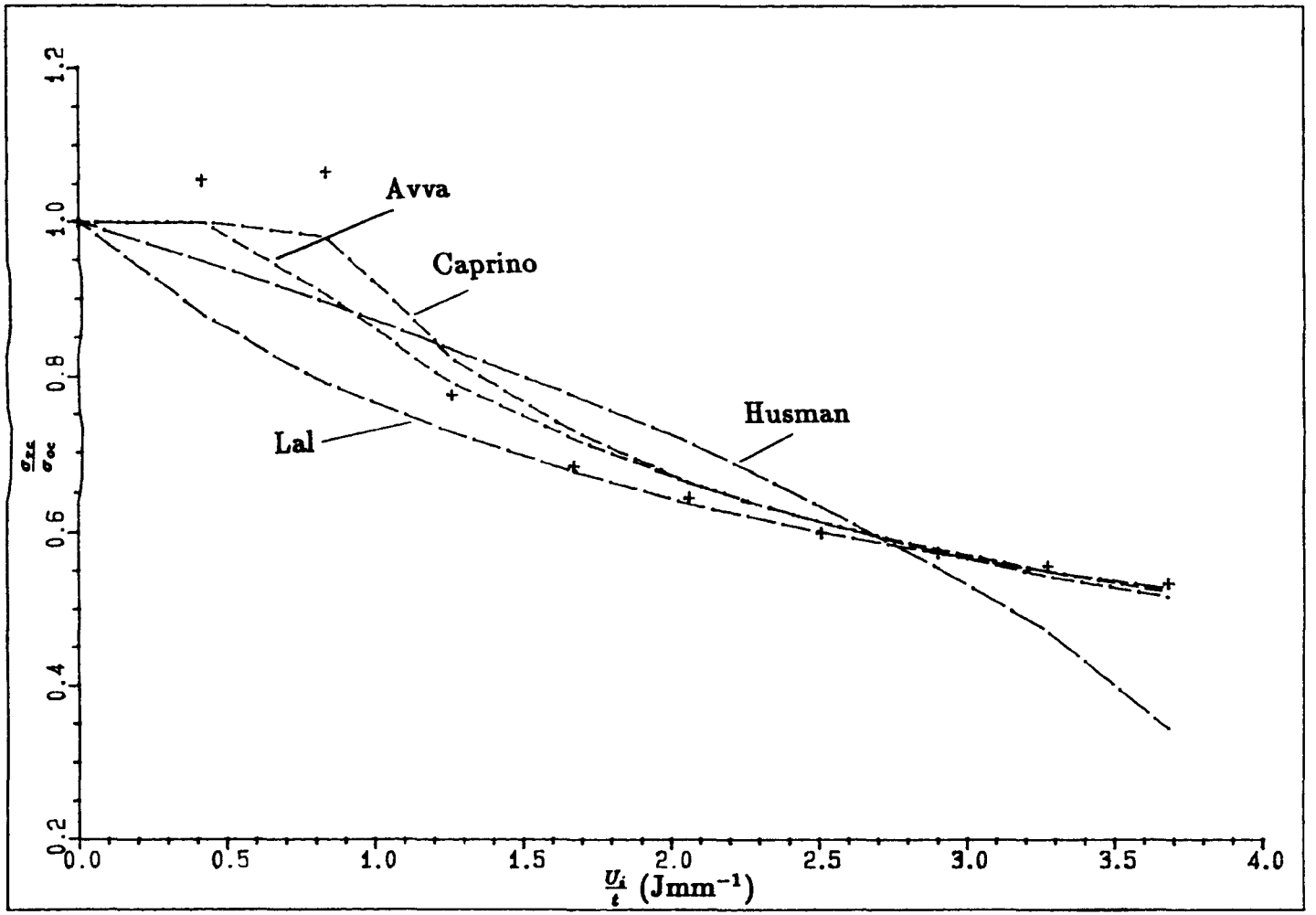

Figure 9.16. Comparison of Equivalent Flaw Models for the Prediction of Residual Compressive Strength of Impacted Specimens.

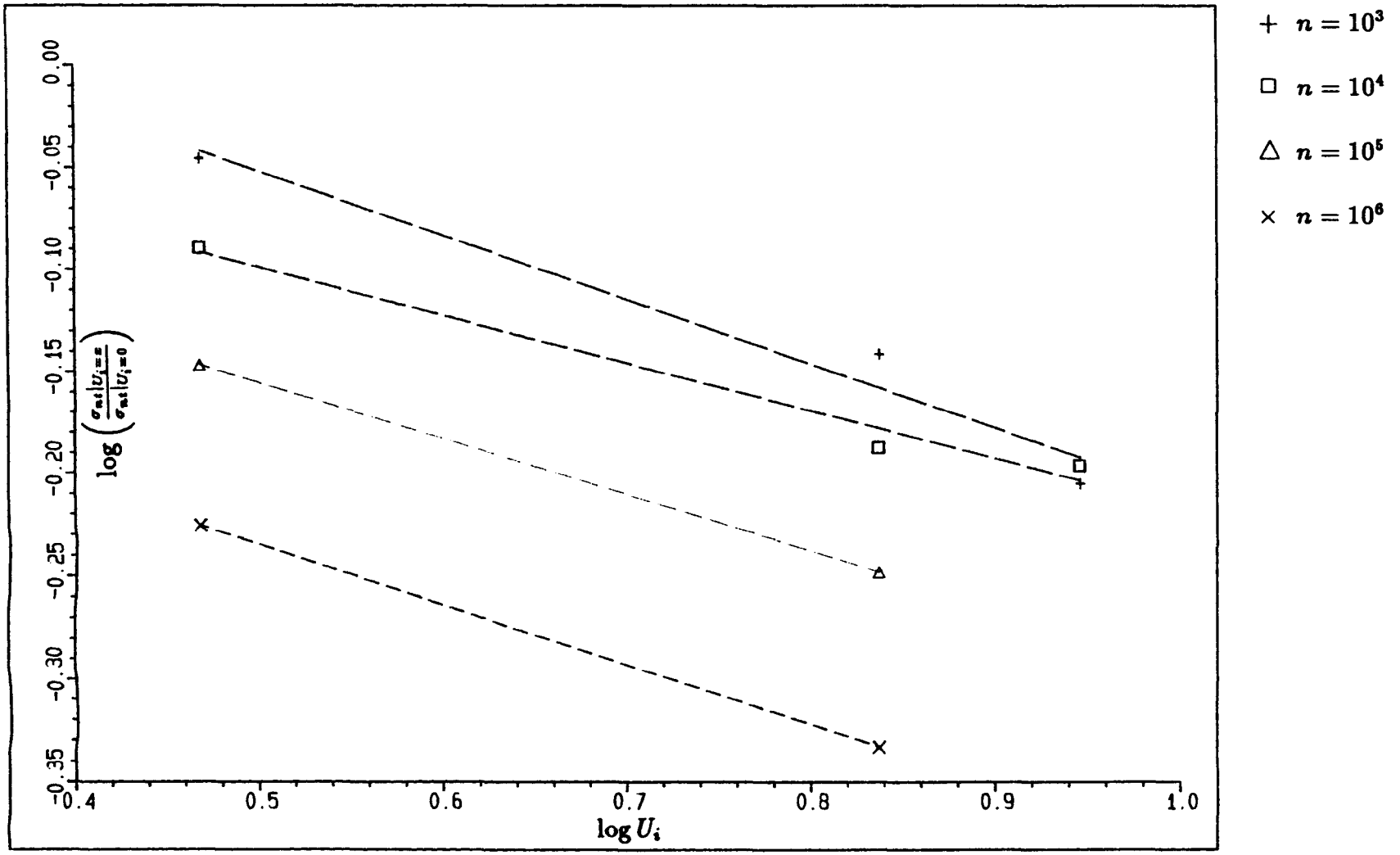

Figure 9.17. Fatigue Model Analysis Plot to Determine

Empirical Consants.

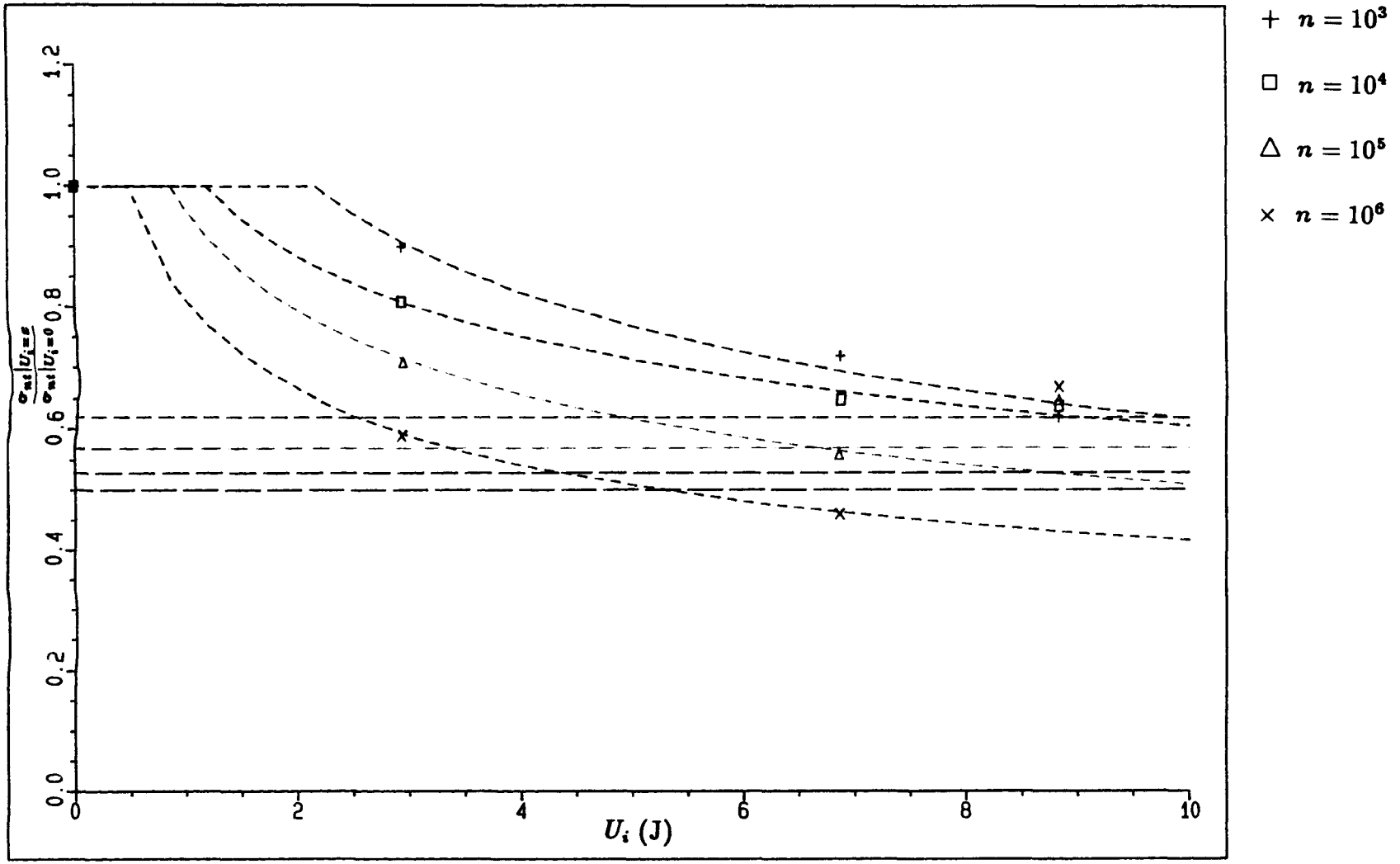

Figure 9.18. Fatigue Model Predictions of Fatigue Strength of Impacted Specimens.

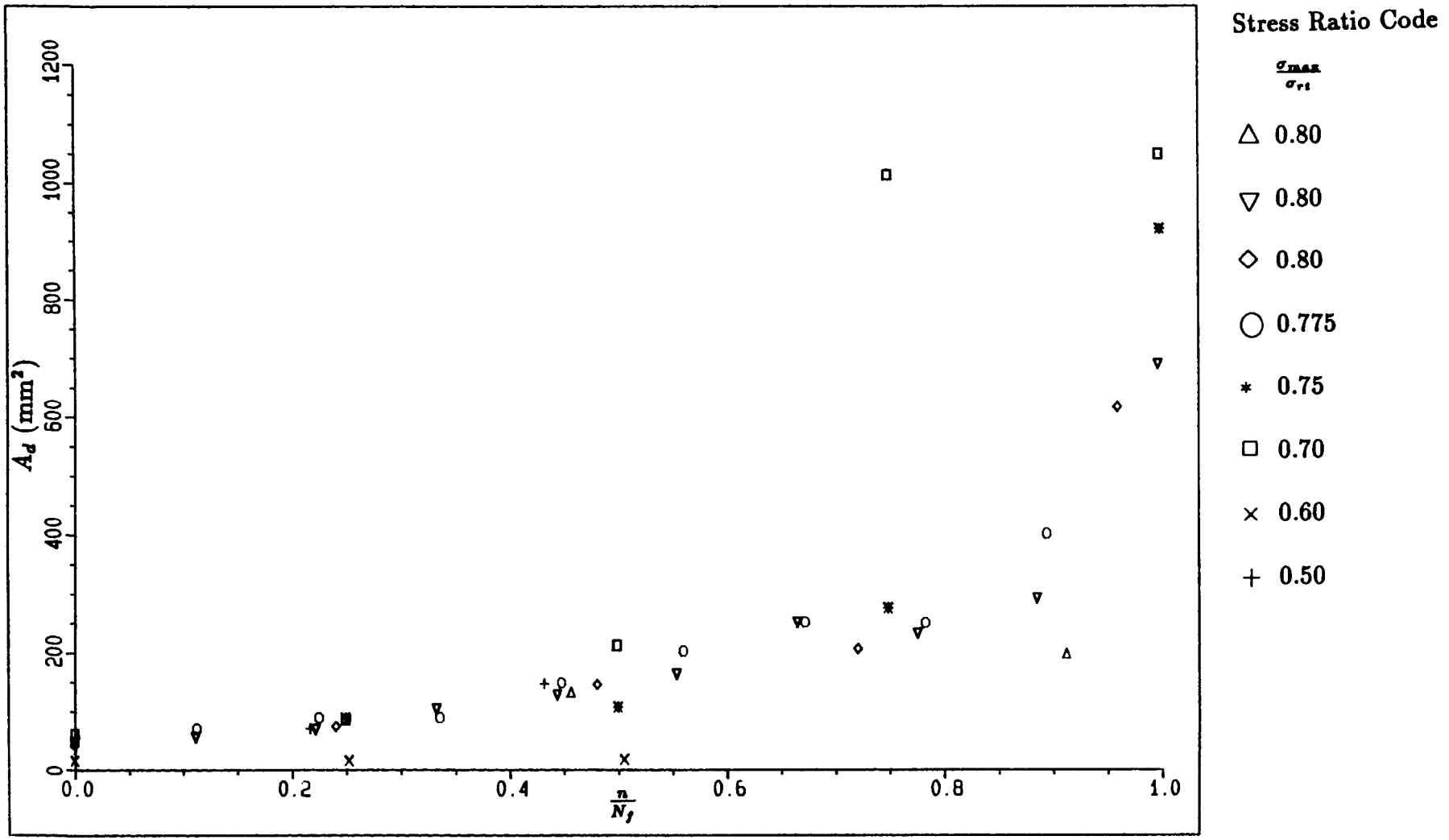

Figure 9.19. The Relationship Between Fatigue Cycle Ratio and Delamination Area for 2.94J Impact Specimens under Zero-Tension Fatigue.

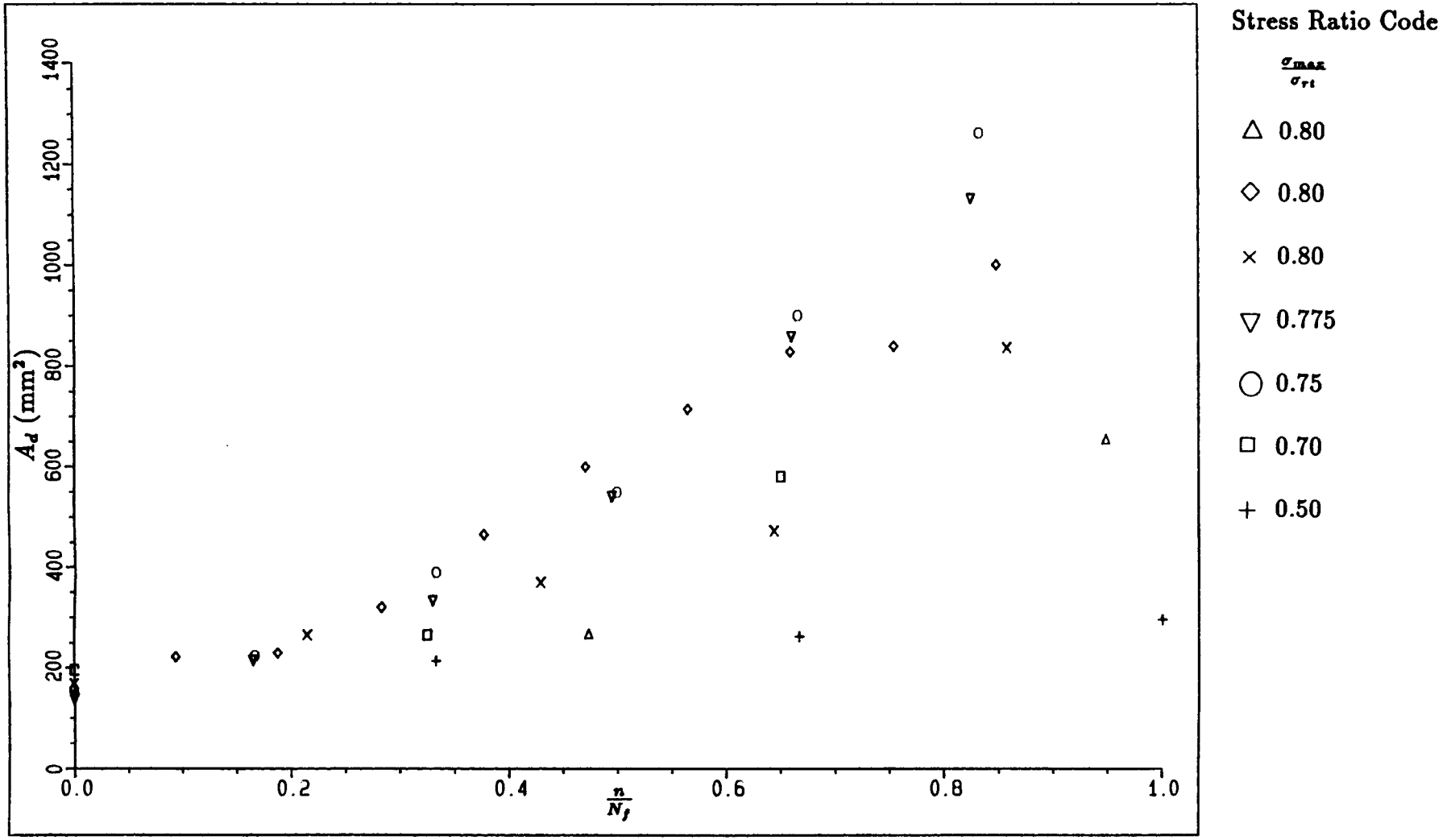

Figure 9.20. The Relationship Between Fatigue Cycle Ratio and Delamination Area for 6.87J Impact Specimens under Zero-Tension Fatigue.

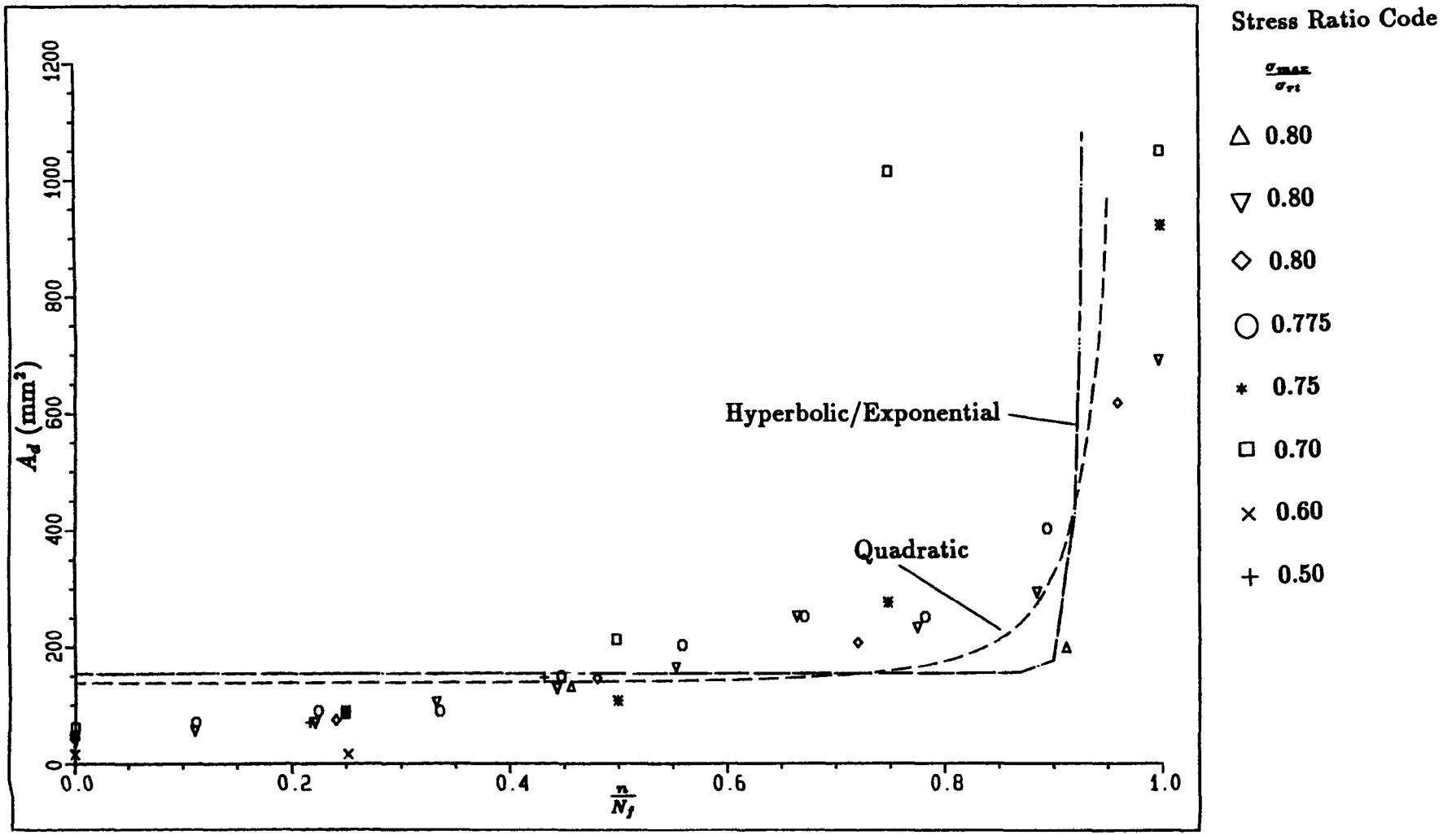

Figure 9.21. Prediction of Delamination Area for 2.94J Impact

Specimens under Zero-Tension Fatigue.

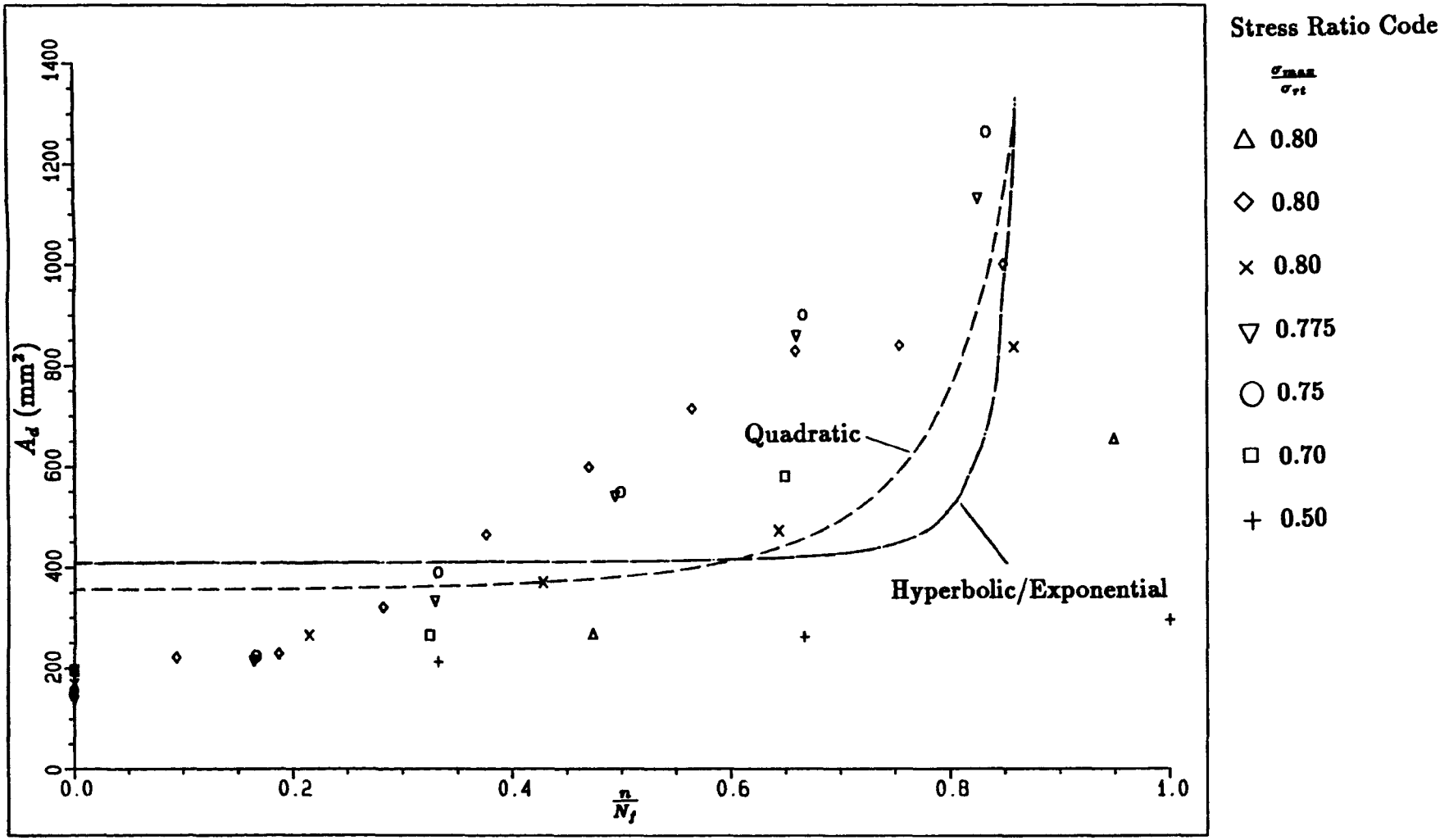

Figure 9.22. Prediction of Delamination Area for 6.87J Impact Specimens under Zero-Tension Fatigue.

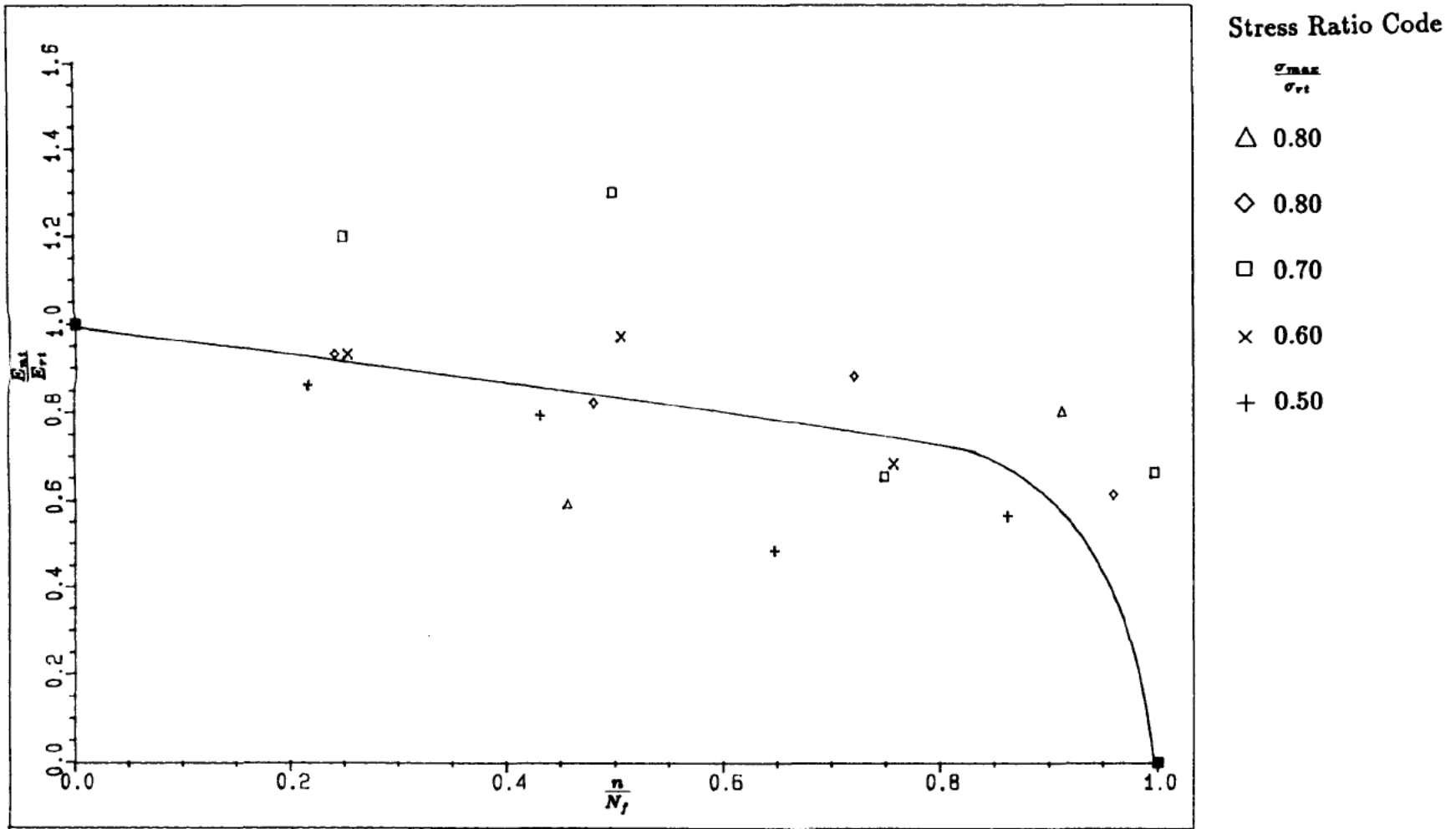

Figure 9.23. The Relationship Between Fatigue Cycle Ratio and Axial Stiffness Ratio for 2.94J Impact Specimens under Zero-Tension Fatigue

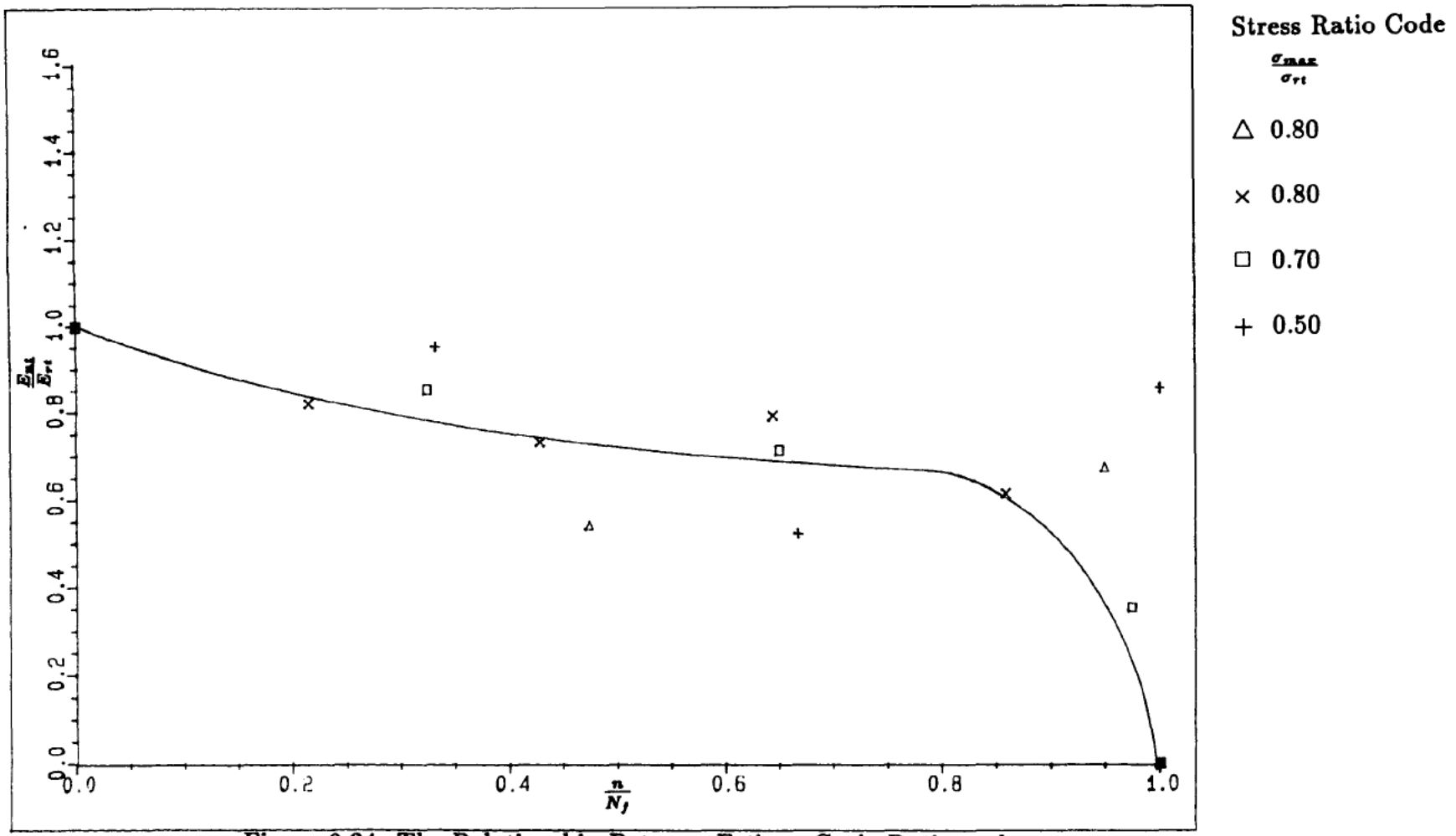

Figure 9.24. The Relationship Between Fatigue Cycle Ratio and Axial Stiffness Ratio for 6.87J Impact Specimens under Zero-Tension Fatigue

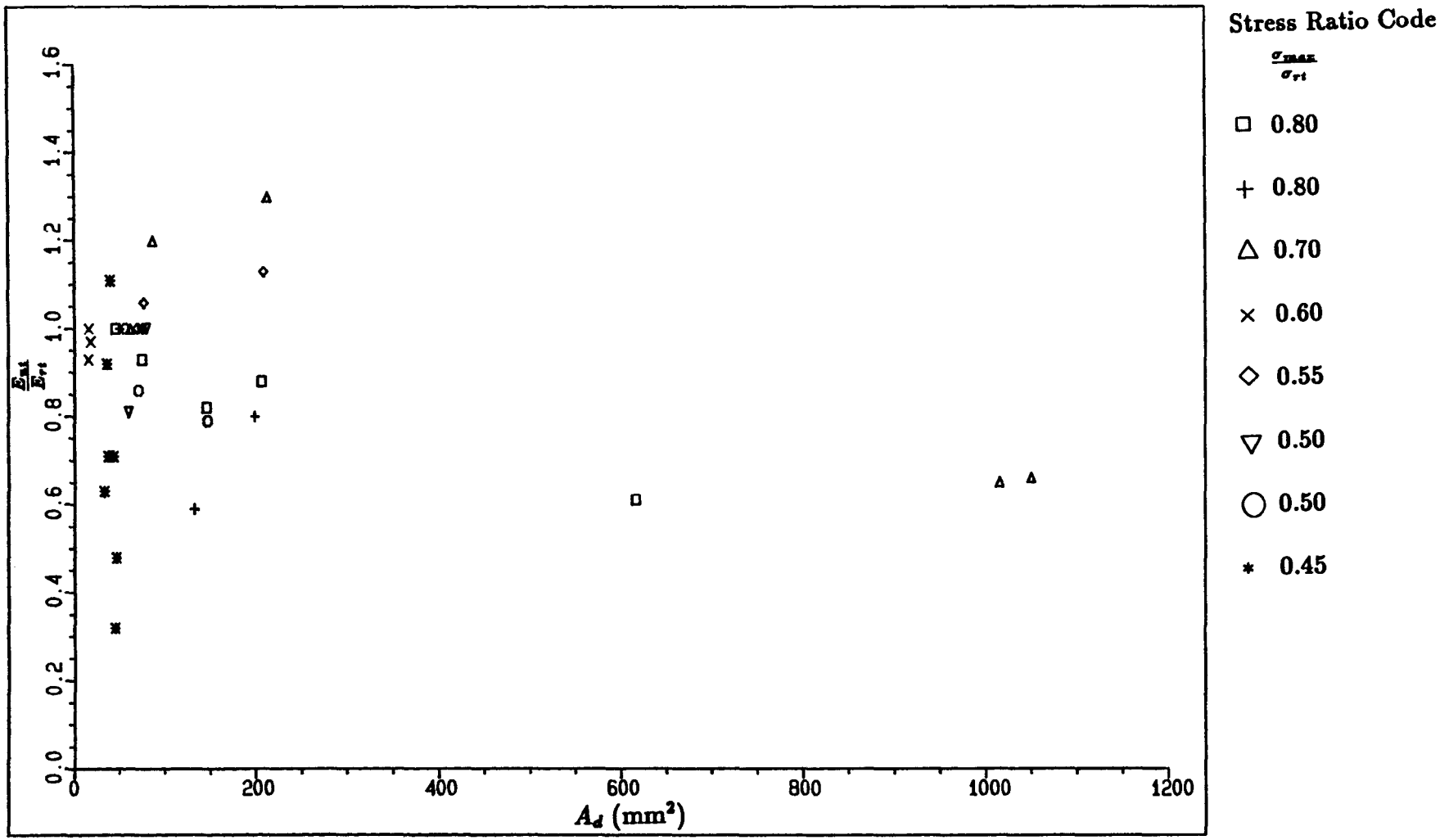

Figure 9.25. The Relationship Between Delamination Area and Axial Stiffness Ratio for 2.94J Impact Specimens under Zero-Tension Fatigue.

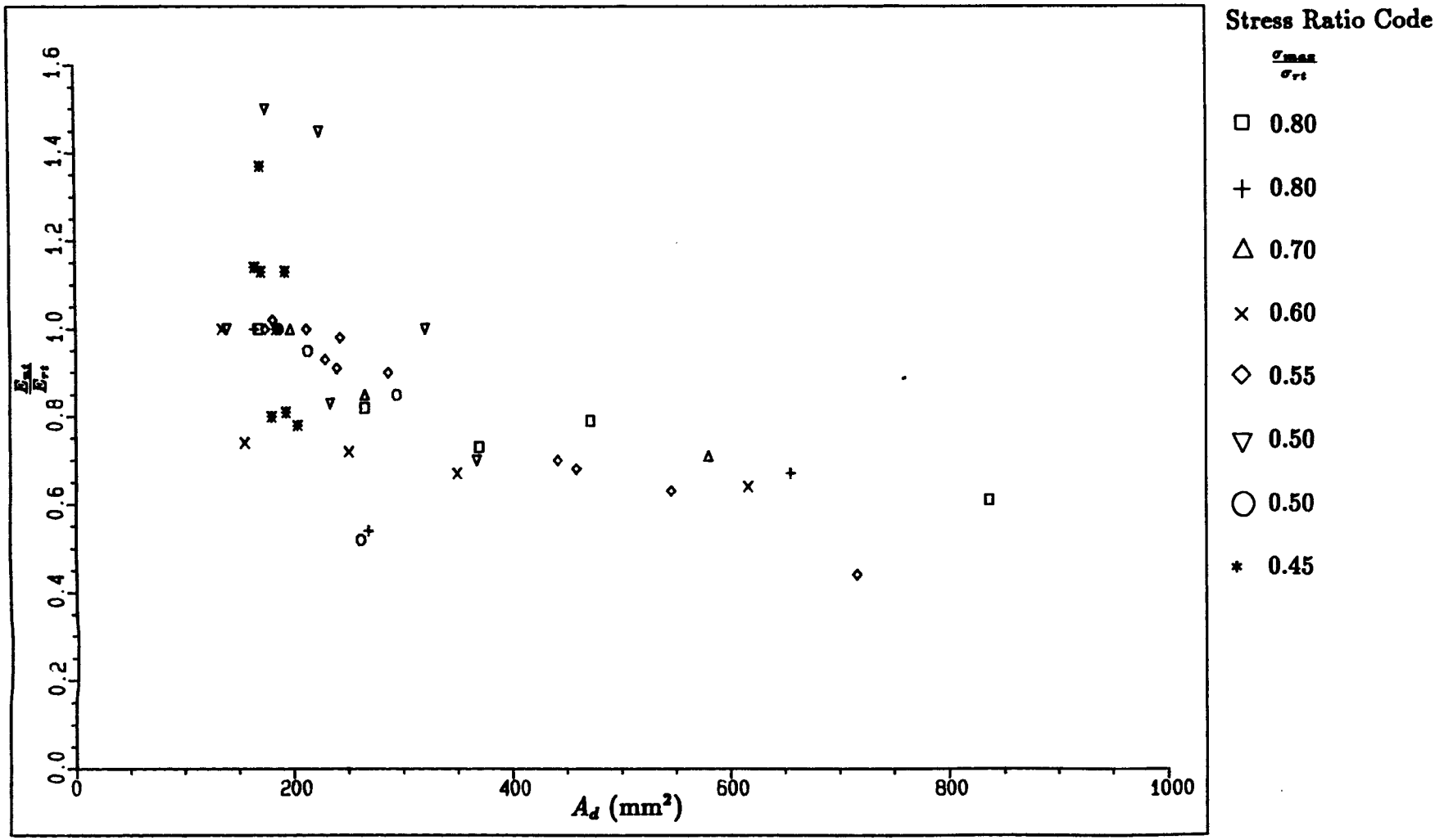

Figure 9.26. The Relationship Between Delamination Area and Axial Stiffness Ratio for 6.87J Impact Specimens under Zero-Tension Fatigue.

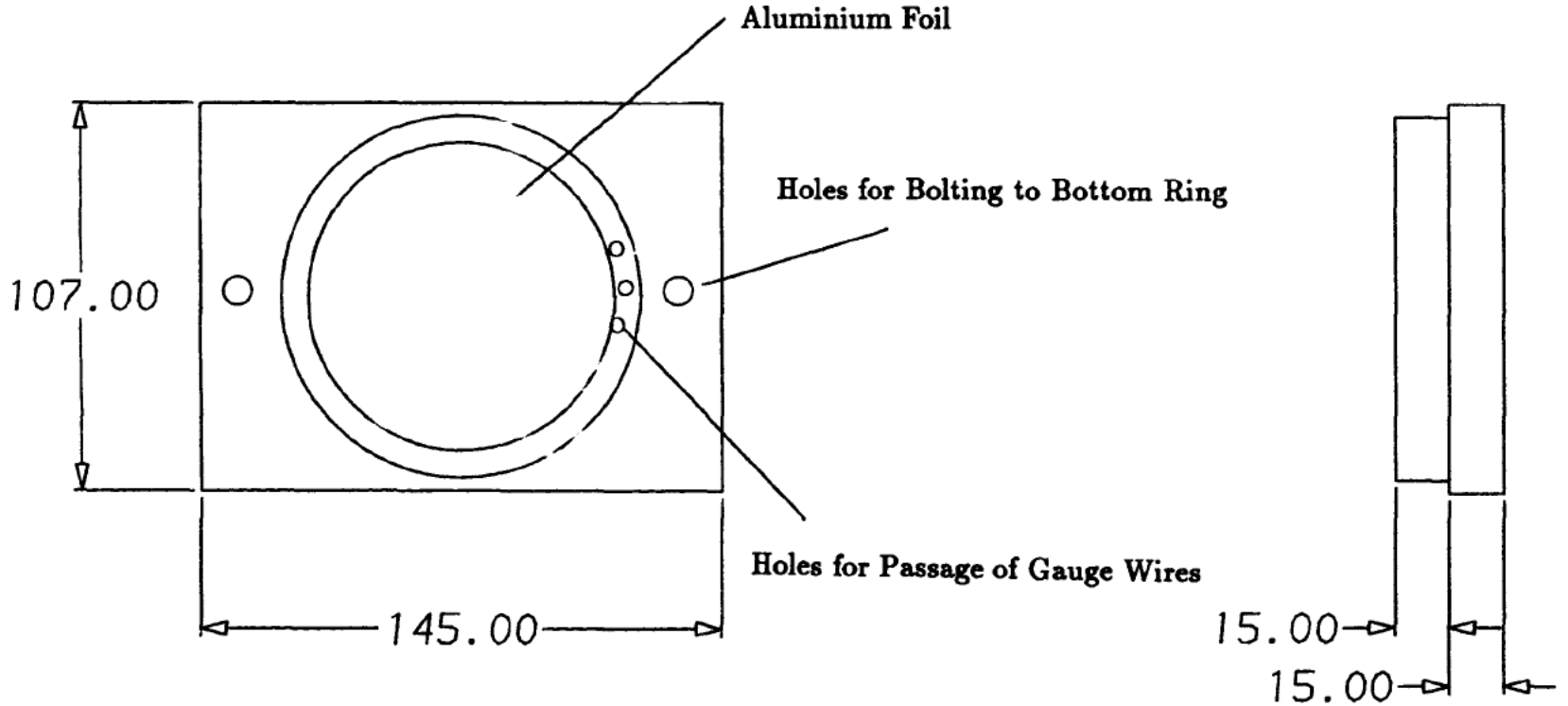

Figure D.1. Capacitance Displacement Transducer Fixed Plate.